PTB bericht
Wissenschaftliche Veröffentlichungen

Diss-24
April 2026

Dissertation

Ziyang Jiao

Hybrid optical and atomic force microscope for micro- and nano-dimensional metrology

ISSN 2941-1297
ISBN 978-3-944659-56-5

DOI 10.7795/110.20260421A

Genauigkeit | Objektivität | Leidenschaft

www.ptb.de

Ziyang Jiao

Hybrid optical and atomic force microscope for micro-and nano-dimensional metrology

Dissertation

PTB-Diss-24

Braunschweig, April 2026

ISSN 2751-6598
ISBN 978-3-944659-56-5

DOI 10.7795/110.20260421A

Empfohlene Zitierweise/recommended citation

Jiao, Z., 2026. *Hybrid optical and atomic force microscope for micro- and nano-dimensional metrology*,
Technische Universität Carolo-Wilhelmina zu Braunschweig.
Braunschweig: Physikalisch-Technische Bundesanstalt.
PTB-Bericht Diss-24. ISBN 978-3-944659-56-5.
Verfügbar unter: https://doi.org/10.7795/110.20260421A

Herausgeber:
Physikalisch-Technische Bundesanstalt
ISNI: 0000 0001 2186 1887

Presse und Öffentlichkeitsarbeit

Bundesallee 100
38116 Braunschweig

Telefon: (05 31) 592-93 21
Telefax: (05 31) 592-92 92
www.ptb.de

Hybrid optical and atomic force microscope for micro- and nano-dimensional metrology

Von der Fakultät für Maschinenbau

der Technischen Universität Braunschweig

zur Erlangung der Würde

eines Doktor-Ingenieurs (Dr.-Ing.)

genehmigte Dissertation

von: Ziyang Jiao

geboren in: Shandong, China

eingereicht am: 13.10.2025

mündliche Prüfung am: 03.03.2026

Vorsitz: Prof. Dr. Georg Garnweitner

Gutachter: Prof. Dr.-Ing. Rainer Tutsch

Gutachter: Prof. Dr.-Ing. habil. Peter Lehmann

Gutachter: Dr.-Ing. Gaoliang Dai

2026

https://doi.org/10.7795/110.20260421A

https://doi.org/10.7795/110.20260421A

献给王焱，我不愿只在梦里见到你
以及焦濂，望你平安顺遂，喜乐安康

Acknowledgments

First and foremost, I would like to express my deepest gratitude to my doctoral supervisors, Dr.-Ing. Gaoliang Dai from Physikalisch-Technische Bundesanstalt (PTB) and Prof. Dr.-Ing. Rainer Tutsch from Technische Universität Braunschweig (TU BS), for their continuous guidance, support, and encouragement throughout the course of my research. Their expertise and insights have been invaluable and have greatly contributed to the development of this dissertation. I would also like to express my sincere appreciation to Prof. Dr. Georg Garnweitner, the chair of the examination committee, and Prof. Dr.-Ing. habil. Peter Lehmann, the reviewer of this work. Their valuable feedback and constructive suggestions have significantly improved the quality of this dissertation.

My heartfelt appreciation goes to my family, especially my wife, Xiaoyu Tian; my father, Yulin Jiao; my mother, Yueling Yang; and my mother-in-law, Mingxia Zhang, for their sacrifices and unconditional love. This achievement would not have been possible without your unwavering support and understanding. Your encouragement kept me motivated and focused, and I am profoundly grateful for your patience and belief in me.

I would also like to extend special thanks to my friends and colleagues at PTB, particularly Dr. Min Xu, Dr. Xiukun Hu, Dr. Jan Thiesler, Mr. André Felgner, Mr. Johannes Degenhardt, Mr. Frank Pohlenz, Mr. Helmut Wolff, and Mr. Radovan Popadic. It has been a great honor and pleasure to work alongside you over the past seven years. Your insightful discussions and generous assistance have been invaluable during both the research and writing stages of this work. My sincere thanks go as well to Mr. Xingyu Rao, Mr. Tianhang Deng and Ms. Ria Mohan, three master's students I had the honor to supervise. Your support and dedication to our work have been remarkable. It has been a pleasure collaborating with you, and I wish you all every success in your future endeavors.

Finally, I am deeply grateful to all my dear friends, especially Mr. Meiyu Zhou, for their constant encouragement, thoughtful advice, and emotional support throughout this journey. Their friendship has been a source of strength and motivation during challenging times.

Braunschweig
Ziyang Jiao

https://doi.org/10.7795/110.20260421A

Abstract

A novel instrument named hybrid microscope (HM) for *in-situ* reference areal surface metrology is presented in this doctoral work. The hybrid in its name indicates that the developed instrument synergically combines different surface measuring modes such as atomic force microscopic mode (AFM) and interference microscopic mode (IM). With these modes in combination, topography can be measured firstly with the IM-mode to have a quick overlook of the sample surface in a large measurement area. Then the instrument is switched to the AFM-mode for measuring with higher resolution whenever and wherever needed. Two of the most essential advantages of this instrument are (I) *in-situ* reference data can be obtained at the very same position without changing and transporting samples from one instrument to another, and (II) the local topography fidelity as well as lateral resolution of the IM measurement results can be enhanced by the AFM measurement results.

The HM is developed on a framework of an optical interference microscope, facilitating the IM measurements through the integration of both phase-shifting interferometric- (PSI) and white-light interferometric- (WLI) techniques. The HM system is employed with Mirau-type objectives manufactured by the company Nikon, with magnifications of 20x and 100x, respectively. These objectives enable high-precision measurements, demonstrated by a low noise level, e.g., the measurement noise of the IM-mode using 20x objective is characterized as low as approximately 0.27 nm (RMS). Furthermore, the IM-mode of the HM exhibits good isotropic bandwidth characteristics, whose angular-dependent relative difference is characterized lower than 8%, and excellent measurement repeatability, where a standard deviation less than 0.5 nm is obtained across five repeated IM measurements.

The AFM-mode is integrated into the HM system without relying on a conventional optical-lever readout system. Instead, by positioning the AFM cantilever within the camera's field of view (FOV) at the objective's focal plane, interference fringe is generated between a measurement light beam reflected from the back side of the AFM cantilever and a reference beam reflected from the reference mirror of the Mirau-objective. The generated interference fringe represents the topography of the back side of the AFM cantilever. During AFM measurements, as the AFM tip interacts with sample surfaces and impacted by tip-sample interaction forces, deflection of the AFM cantilever will be detected from the changes of the interference fringe. More specifically, the phase shift of the fringe represents the z-motion of the AFM tip, and the distortion of the fringe indicates the torsion of the AFM cantilever. In such a way, AFM-mode can be realized in

https://doi.org/10.7795/110.20260421A

a compact but high synergic design manner. The AFM sensor system developed in this study exhibits a lateral measurement resolution comparable to that of commercial AFM instruments (down to 10 nm, depending on the AFM tip used), and a noise level of 0.04 nm, which is both theoretically predicted and experimentally confirmed in this work. The measurement traceability of the HM is ensured by calibrations using nanoscale standards, which were calibrated by a metrological AFM developed at the Physikalisch-Technische Bundesanstalt (PTB).

Application examples are demonstrated in this dissertation, showing a high application potential of the developed HM for reference surface metrology. One of the most potential applications is to offer reference topography data for optical measurement instruments. To demonstrate this application, a set of sample surfaces made of different materials and manufactured by different surface processing techniques are investigated using AFM- and IM-modes of the HM. AFM and IM datasets are then correlated and compared. The results show that the sample structures can not only be resolved with more details by AFM measurements than that of IM, but also the optical artifacts in IM measurements can be easily detected by using the AFM data as a reference. Thus, by using the AFM data as a reference, the topography fidelity of optical measurements can be characterized, which also offers hints for potential improvements of optical measurement techniques.

https://doi.org/10.7795/110.20260421A

Kurzfassung

In dieser Doktorarbeit wird ein neuartiges Instrument namens Hybridmikroskop (HM) für die *in-situ*-Referenzoberflächenmessung vorgestellt. Das Hybrid im Namen weist darauf hin, dass das entwickelte Instrument verschiedene Oberflächenmessmodi wie den Rasterkraftmikroskopie-Modus (AFM) und den Interferenzmikroskopie-Modus (IM) synergetisch kombiniert. Durch die Kombination dieser Modi kann die Topografie zunächst mit dem IM-Modus gemessen werden, um einen schnellen Überblick über die Probenoberfläche in einem großen Messbereich zu erhalten. Anschließend wird das Gerät auf den AFM-Modus umgeschaltet, um jederzeit und überall mit höherer Auflösung zu messen.

Zwei der wichtigsten Vorteile dieses Instruments sind, dass (I) *in-situ*-Referenzdaten an der gleichen Stelle gewonnen werden können, ohne dass die Proben von einem Instrument zum anderen gewechselt und transportiert werden müssen, und (II) die lokale Topographietreue (topography fidelity) sowie die laterale Auflösung der IM-Messergebnisse durch AFM-Messergebnisse verbessert werden können.

Das HM wurde auf der Grundlage eines optischen Interferenzmikroskops entwickelt, das durch die Integration von phasenverschiebender Interferometrie (PSI) und Weißlichtinterferometrie (WLI) IM-Messungen ermöglicht. Das HM-System wird mit Mirau-Objektiven der Firma Nikon mit Vergrößerungen von 20x bzw. 100x eingesetzt. Diese Objektive ermöglichen hochpräzise Messungen, die sich durch ein geringes Rauschen auszeichnen, z. B. ist das Messrauschen des IM-Modus bei Verwendung eines 20x-Objektivs mit ungefähr 0,27 nm (RMS) als sehr gering einzustufen. Darüber hinaus weist der IM-Modus des HM gute isotrope Bandbreiteneigenschaften auf, deren winkelabhängige relative Differenz als < 8% charakterisiert wird, sowie eine ausgezeichnete Messwiederholbarkeit, bei der eine Standardabweichung von < 0,5 nm über fünf wiederholte IM-Messungen erzielt wird.

Der AFM-Modus ist in das HM-System integriert, ohne auf ein herkömmliches „Optical-Lever"-Auslesesystem zurückzugreifen. Stattdessen wird durch die Positionierung des AFM-Cantilevers innerhalb des Sichtfelds der Kamera in der Brennebene des Objektivs eine Interferenz zwischen einem von der Rückseite des AFM-Cantilevers reflektierten Messlichtstrahl und einem vom Referenzspiegel des Mirau-Objektivs reflektierten Referenzstrahl erzeugt. Das erzeugte Interferenzmuster stellt die Topographie der Rückseite des AFM-Cantilevers dar. Während der AFM-Messungen wird die Auslenkung des AFM-Cantilevers, die durch die Wechselwirkungskräfte zwischen Spitze und Probe

https://doi.org/10.7795/110.20260421A

hervorgerufen wird, anhand der Änderungen des Interferenzmusters erfasst. Im Einzelnen stellt die Phasenverschiebung der Interferenzstreifen die z-Bewegung der AFM-Spitze dar, und die Verzerrung der Interferenzstreifen zeigt die Torsion des AFM-Cantilevers an. Auf diese Weise kann der AFM-Modus in einer kompakten, aber hochsynergetischen Bauweise realisiert werden. Das in dieser Studie entwickelte AFM-Sensorsystem weist eine laterale Messauflösung auf, die mit derjenigen kommerzieller AFM-Instrumente vergleichbar ist (bis zu 10 nm, abhängig von der verwendeten AFM-Spitze), und ein Rauschniveau von 0,04 nm, das in dieser Arbeit sowohl theoretisch vorhergesagt als auch experimentell bestätigt wurde. Die messtechnische Rückführbarkeit des HM wird durch Kalibrierungen mit nanoskaligen Normalen sichergestellt, die mit einem an der Physikalisch-Technischen Bundesanstalt (PTB) entwickelten metrologischen AFM kalibriert wurden.

Die in dieser Dissertation vorgestellten Anwendungsbeispiele zeigen ein hohes Anwendungspotenzial des entwickelten HM für die Referenzoberflächenmesstechnik. Eine der potenziell größten Anwendungen ist die Bereitstellung von Referenztopographiedaten für optische Messgeräte. Zur Demonstration dieser Anwendung wird eine Reihe von Probenoberflächen, die aus unterschiedlichen Materialien bestehen und mit verschiedenen Oberflächenbearbeitungsverfahren hergestellt wurden, mithilfe des AFM- und des IM-Modus des HM untersucht. Anschließend werden die AFM- und IM-Datensätze korreliert und miteinander verglichen. Die Ergebnisse zeigen, dass die Probenstrukturen durch AFM-Messungen nicht nur detailreicher aufgelöst werden können als durch IM-Messungen, sondern dass sich auch optische Artefakte in IM-Messungen unter Verwendung der AFM-Daten als Referenz leicht erkennen lassen. Dadurch lässt sich die Topographietreue optischer Messungen charakterisieren, woraus sich zugleich Ansatzpunkte zur Verbesserung optischer Messverfahren ableiten lassen.

https://doi.org/10.7795/110.20260421A

Contents

Acknowledgments I

Abstract III

Kurzfassung V

List of Tables X

List of Figures XI

List of Abbreviations XXIII

List of Symbols XXV

1. Introduction 1

2. State of the art of areal surface topography measurement 4

2.1. A short history of 3D nanometrology 5

2.2. Measurement principles and instrument realizations 6

2.2.1. Tactile measurement technology 7

2.2.2. Atomic force microscopy 9

2.2.3. Interferometrical measurement technology 14

2.2.4. Non-interferometrical optical measurement principles 28

2.2.5. Current hybrid measuring technology 31

3. Topography fidelity 35

3.1. State of the art issues in interferometric areal surface measuring microscope 36

3.2. Metrological characteristics 45

3.3. Instrument transfer function 49

3.4. Modelling methods 57

https://doi.org/10.7795/110.20260421A

3.5. Correlative reference metrology 62

4. Realization of the hybrid microscope...66

4.1. Design of the hybrid interference- and atomic force microscope 66

4.2. Realization of the IM-mode in the hybrid microscope......................................67

4.2.1. Optical and mechanical components of the IM-mode....................................68

4.2.2. Topography reconstruction algorithms and measurement noise 75

4.2.3. Calibration of bandwidth characteristics using the material measure CCS.....82

4.2.4. Repeatability of the IM-mode 90

4.3. Realization of the AFM-mode in the hybrid microscope 91

4.3.1. Working principle of the AFM-mode 91

4.3.2. AFM tip switching system 100

4.3.3. AFM measurement preparation 106

4.3.4. Measurement performance and calibration..112

5. Optimizations in the hybrid microscopes 120

5.1. Calibration of the effective wavelength...120

5.2. Noise reduction in the AFM-mode..123

5.3. Development of a one for all AFM tip switching system 132

5.4. Realization of the AFM-mode with 100x Mirau objectives 133

6. Applications of the hybrid microscope 137

6.1. *in-situ* AFM measurements 137

6.2. Roughness investigations with a 20x objective 141

6.3. Roughness investigations with a 100x objective 150

6.4. Investigation of optical artifacts using the hybrid microscope 156

https://doi.org/10.7795/110.20260421A

7. Conclusions and outlook 160

Appendix...163

https://doi.org/10.7795/110.20260421A

List of Tables

Table 1 Specifications of Mirau type objectives from Nikon [155] 68

Table 2 Calibrated lateral scaling factors using different objectives with the PSI mode (4+1 steps algorithm) in the hybrid microscope 85

Table 3 Repeatability of cantilever positions in three axes by using motorized AFM tip switching system Klappfix 104

Table 4 Repeatability of cantilever positions in three axes after AFM cantilever exchange 105

Table 5 Comparison of the result of lateral standards 2D 10000 measured by AFM-mode of the HM and the MAFM 117

Table 6 Evaluation of arithmetical mean height Sa from AFM repeat measurements acquired by the AFM-mode of the HM over three days 118

Table 7 Experimentally measured camera noises $Ncam$ in application of the new intensity intensive LED.. 127

Table 8 Comparison of the evaluated roughness parameters Sa and Sq based on IM and AFM measurements of five samples (measured by the HM equipped with a 20x objective).. 148

Table 9 Comparison of the evaluated roughness parameters Sa and Sq based on IM and AFM measurements of five samples (measured by the HM equipped with a 100x objective) 154

https://doi.org/10.7795/110.20260421A

List of Figures

Figure 1 Stedman diagram (diagram of wavelength vs. amplitude) for different surface measuring instruments, including SPM, SEM, optical, stylus and CMM techniques [35-38] 7

Figure 2 Curve of interaction force vs. tip-sample distance. Two regimes are highlighted for illustrating the different resultant forces used for realization of contact AFM and non-contact AFM, respectively [50] .. 10

Figure 3 Illustration of implementation of an optical-lever system into an AFM control loop. The QPD and PZT in the figure are abbreviations for quadrant photodiode and lead zirconate titanate (a kind of piezoelectric ceramic material), respectively. 13

Figure 4 Interference of two waves $\boldsymbol{E1}$ and $\boldsymbol{E2}$ with same amplitudes and propagating direction $\boldsymbol{z}$ at the moment of $\boldsymbol{t}=\boldsymbol{0}$ with phase offsets $\boldsymbol{\varphi 1}$ and $\boldsymbol{\varphi 2}$. (a) When the difference between phase offsets is equal to integral multiple of $\boldsymbol{2\pi}$, the two waves are in phase, and forming constructive interference pattern ($\boldsymbol{Er}$), whose amplitude is the sum of both amplitudes of the waves. (b) When the difference between phase offsets is equal to odd multiple of $\boldsymbol{\pi}$, the two waves are out of phase, and form destructive interference pattern, whose amplitude is the difference of both amplitudes of the waves. (c) When phase offsets do not fulfill the cases shown in (a) and (b), the amplitude of the interference pattern lies somewhere in between [59]. To be mentioned, for better illustration of the waves, $\boldsymbol{E1}$ in (a) and $\boldsymbol{Er}$ in (b) are plotted with offsets to distinguish them from $\boldsymbol{E2}$ in (a) and $\boldsymbol{z}$ axis. 14

Figure 5 Illustration of the basic principle of a Michelson interferometer. When the movable mirror is vertically displaced, the interference pattern observed at the detector changes accordingly, indicating a variation in phase and optical path length relative to the reference beam. The Moiré patterns visible in the interference image are not actual measurement data but artifacts resulting from a mismatch between the fine interference fringes and the limited resolution of the image. The red and blue colors used to represent the light beams serve only to distinguish the reference and measurement paths (reflected and transmitted beams) after the beam splitter; they do not correspond to the actual color of the light beam. 18

https://doi.org/10.7795/110.20260421A

Figure 6 Three types of areal surface interferometric instruments (a) Mirau type (b) Michelson type and (c) Linnik type 20

Figure 7 (a) 2D illustration of measurement and reference optical paths (marked in blue and orange respectively) in objective of a Mirau type interferometric instrument. (b) 3D illustration of the objective aperture and the solid-angle element of the aperture cone $\boldsymbol{sin\theta d\theta d\varphi}$ for estimating the total intensity $\boldsymbol{I}$ of the interference over a wide range of incident angle $\boldsymbol{\theta}$.. 20

Figure 8 Model and measuring principle of a Mirau type phase-shifting interferometer24

Figure 9 (a) Schematic illustration of the interference of light beams with different wavelengths in a WLI instrument. The resulting interference signal, referred to as a correlogram, reaches its maximum amplitude at zero OPD and exhibits a much shorter coherence length than in PSI. Consequently, the interference envelope is strongly localized and decreases rapidly along the vertical axis. (b) Measurement setup and principle of a WLI instrument, illustrated by a topography measurement of a sample with two different height levels, represented by points A and B. 26

Figure 10 The measuring principle of white-light phase-shifting 4+1 algorithm (WLPSI), for finding the corresponding height to the zero OPD, the height is determined as two components: (I) the modulation maximum $\boldsymbol{Modmax}$ corresponded height $\boldsymbol{H}'$ (II) 4+1 PSI algorithm determined phase corresponded height $\boldsymbol{H}''$. 28

Figure 11 Measuring principle of a confocal microscope and its typical axial response (red curve) during vertical scanning 29

Figure 12 Measuring principle of a focus variation microscope and its typical axial response (red curve) during vertical scanning. 31

Figure 13 Comparison of the different designs of hybrid instruments (a) high synergy design with example instrument: S-neox 3D optical profiler from Sensofar [83] (b) low synergy design with example instrument: multi-sensor measuring system from university of Kassel [84] (c) measurable ranges of two of measuring modules in high synergy design (d) measurable ranges of two of measuring modules in low synergy design 33

https://doi.org/10.7795/110.20260421A

Figure 14 Modules that enables AFM measurements using an optical metrological frame (a) LensAFM from Nanosurf [85] and (b) UltraObjective (the "objective" linked with yellow cable) from SIS [86]............................ 33

Figure 15 Profiles of simulated measurement error $\boldsymbol{\varepsilon H}$ along (a) slope orientation (x-axis) and (b) horizontal orientation (y-axis, orthogonal to the slope orientation). Random phase-shifting errors $\boldsymbol{\varepsilon i}$ are simulated as a gaussian distributed parameter with 1σ = 5°. 40

Figure 16 (a) the simulated interferogram (interference fringe) observed in camera when measuring over a tilted surface like (b), the wavelength of the light source applied in simulation is 530 nm. Fringe spacing represents that two fringes have a phase difference in 2π and a height different in $\boldsymbol{\lambda}$/2. (b) An inclined flat surface in size of 100 μm x 100 μm, perfectly aligned in y-axis (horizontal orientation) and 0.57° tilted in x-axis (slope orientation)... 42

Figure 17 Illustration of the metrological characteristics amplification coefficient and linearity of an actual response curve (2) comparing to the ideal response curve (1); the curve (3) is the linear fitted curve based on the curve (2) and it shares the same amplification coefficient as curve (2). The distance (4) is the maximum local difference between curve (2) and (3), known as linearity deviation 46

Figure 18 some examples of material measure available for ITF characterization (a) ITF test sample [121] (b) circular calibration standard (CCS) [12] and (c) binary pseudo-random array standards [13,124] ©IOP Publishing Ltd. All rights reserved. 51

Figure 19 Simulation of measurement and correction of designed (a) and binarized (c) radial profile of the CC pattern C13 of CCS (radius 30 μm and wavelength range is from 1 μm to 7.5 μm) using optical instrument whose ITF is characterized as k=1.0, m=1.5 and n=2.0. The (b) and (d) are the correspondent spectrum comparison respectively................. 55

Figure 20 The measured (a) and processed (b) topographies of a 1D chirped height pattern named as "BEAMETR" test pattern [131] (c) The horizontal cross-section of the measured and processed topographies. Reproduced from [13]. Red arrows are added to the original figure for showing the positions where they are overprocessed with the topography correction algorithm.. 57

https://doi.org/10.7795/110.20260421A

Figure 21 Process diagram illustrates the modelling concept for improving topography fidelity. Each step in the instrument, from wavefront propagation to the generation of measured topography $\boldsymbol{Hm}$, is shown. The comparison between measured topography $\boldsymbol{Hm}$ and the object topography $\boldsymbol{Ho}$ yields the measurement error, which is used to evaluate performance and is summarized in the good practice guide. 59

Figure 22 Illustration of the relationship of the two important components that applied in correlative reference metrology for topography fidelity enhancement (I) the optical measured AOI shown in blue and (II) AFM measured reference data in different sub-areas (red marked), which are locally correlated with the optical measurements. 65

Figure 23 Design details of the hybrid microscope. It enables two measurement modes, namely (I) the interference microscope (IM) mode and (II) the atomic force microscope (AFM) mode. From an instrumentation perspective, the two modes differ only in whether the AFM tip switching mechanism (component 12 in the figure) positions the AFM cantilever (12.3) within the optical path. 66

Figure 24 Computer-aided design (CAD) drawing of the hybrid microscope. Three key systems, the illumination system (colored with green), the imaging system (marked with dashed line) and positioning system are illustrated in detail, as well as some of the key components of the HM e.g. CMOS camera, light source and Mirau objective....................... 69

Figure 25 Illustration of the developed Köhler illumination system implemented in the hybrid microscope for evenly illuminating the sample surface. Six of its most important components are shown: light source (I), collector lens (II), field diaphragm (III), field lens (IV), aperture diaphragm (V) and condenser lens (VI)... 70

Figure 26 Spectral irradiance of the light sources applied in the HM: (a) “SL-162 590” for the amber light output measured at distance of 200 mm and (b) “SL-162 WHI” for the white-light output measured at distance of 285 mm 71

Figure 27 Illustration of the developed infinity-corrected imaging system implemented in the hybrid microscope. Three of its most important components are shown: CMOS detector (I), tube lens (II) and a Mirau objective (III). . 72

https://doi.org/10.7795/110.20260421A

Figure 28 Positioning system, illustrated with stage units (1) a lateral coarse motion stage- type M-545, (2) a vertical coarse motion stage type N-216, (3) a three axes piezo stage type P-545 and (4) a self-designed tilting stage 73

Figure 29 Relationship between phase shifts number N and additional phase shifts number M in N+M-step linear PSI algorithms, while the value of each phase shift is $2\pi N$ 76

Figure 30 Repeat measurements of a flat surface on CCS material measure for measurement noise characterization using 3 step PSI algorithm: (a) and (b) are repeated flat surface measurements and (c) is a topography difference, obtained by subtracting (a) measurements from (b) and processed with spatial high-pass filter (cut off wavelength 8 µm) for eliminating the impacts of the random form error. 79

Figure 31 Measurement noises theoretically and experimentally characterized by repeat measurements applying different PSI algorithms 79

Figure 32 Measurement noise vs total interferogram number Nt. Blue curve is the same simulated noise curve shown in Figure 31 while keep M=0 and the red dots are denoting the measurement noises evaluated by applying the linear PSI algorithm with N= 3, 5, 7 and 20 while M=0. These evaluated measurement noises are not processed with physical noise reduction techniques. The yellow dots denote the measurement noises of using 3 step linear PSI algorithm (N=3 and M=0) with applicating of corresponding noise reduction technique (topography and interferogram averaging technique)... 81

Figure 33 Calibration of the lateral scaling factors using the CCS material measure, demonstrated using the C33 pattern for 20x PSI measurements. (a) Horizontal diametrical profiles extracted from reference data measured with metrological AFM (blue) and horizontal diametrical profile extracted from calibration data measured with 4+1 step PSI algorithm (red). (b) An overview of CCS C33 pattern with pattern radius of 120 µm, the image is stitched with four PSI measurements. The position of the extracted diametrical profile is marked in white dashed line; (c) Profile comparison between reference data (blue) and calibration data (red) after correction with scaling factor (kx =0.9946)....................... 83

Figure 34 Data pre-processing of the ITF characterization using material measure CCS in example of C31 pattern. (a) Calibration data measured by 20x objective in PSI mode of hybrid microscope. (b) Reference data measured by a metrological AFM. (c) Comparison of the radial profiles extracted at the same angular position of the CCS circular pattern, as marked in (a) and (b), respectively. 87

Figure 35 Characterized ITFs at the angular direction 0°, evaluated based on PSI 20x measurements of CCS patterns C31-C33 (in colored lines) and Z01-Z05 (in colored dots). Smoothed ITF curve (black) fitted from evaluated ITF data (colored lines and dots). A –6 dB reference line, where the measured amplitude drop is cross 50% of its reference value, indicates a cross-over at 0.38 1/μm with the fitted ITF..................................... 89

Figure 36 Angular dependency of evaluated ITF based on 20x PSI measurements represented by the -6 dB contour of ITF vs structure size in μm. The lateral period limits at each angular directions are plotted in blue circles. They can be fitted with circle fitting algorithm into the red dashed circle with average lateral period limit of 2.55 μm. The roundness of the contour indicates good isotropy characteristic of the HM. 90

Figure 37 Repeat measurements of C33 pattern. (a) One of the 5 successively measured topographies captured using PSI 4+1-steps topography reconstruction algorithm. (b) Rest of four repeat measurements (c) Profiles comparison of the repeat measurements, which are extracted from a randomly selected horizonal position marked in (a)............... 90

Figure 38 Schematic illustration of the working principle of the AFM-mode developed in the HM. (a) A tilted AFM cantilever with tilting angle α is demonstrated in the figure. The black-and-white fringes on its backside are used to illustrate how the tilted topography is transformed into a phase map. In practice, they can only be observed under the camera with application of interferometric objective, since the interference is generated between the cantilever-reflected beam and the reference beam from reflected the reference mirror. They cannot be observed directly from the backside of cantilever (in contrast to fringe projection). A small region marked in yellow is the location where profile of AFM intensity curve is extracted from the whole interference pattern. Two pixels, $P0$ and Pn are arbitrarily selected from the profile. They

https://doi.org/10.7795/110.20260421A

correspond to different height $\boldsymbol{Hi}$ at z-axis. (b) Real FOV image of 20x Mirau objective when AFM-mode is activated. The tilted AFM cantilever is in the middle of the FOV. The cantilever is adjusted well so that the focal plane of the objective is located near its tip region. (c) Horizontal intensity profiles extracted at the position marked in (b), recorded under three conditions: (I) when the cantilever is aligned with the focal plane before tip-sample engagement, with no bending force (black curve); (II) after the first tip-sample engagement, with a small bending force (blue curve); and (III) after further bending by 50 nm following the first tip-sample engagement, with a larger bending force (red curve). Due to the tilt of the AFM cantilever, the relative height of each pixel is linearly related to its x-position. Therefore, the corresponding relative height is also indicated in (c) in red. 92

Figure 39 Simulated and experimentally determined sensitivity curves for the reference tip displacement $\Delta\boldsymbol{Dr}$ and calculated tip displacement $\Delta\boldsymbol{Dc}$, based on the newly calibrated effective wavelength $\boldsymbol{\lambda eff}$ and fringe phase shifts ∅ 98

Figure 40 CCS profiles measured in different measuring speed of 0.5 µm/s, 1 µm/s, 2 µm/s and 5 µm/s using the AFM-mode of the HM. 99

Figure 41 Prototype of the developed AFM tip switching system for enabling measurement modes switching of the hybrid microscope demonstrated in (a) the AFM-mode and (b) the IM-mode. The focal plane of the objective (Nikon 20x Mirau type) is marked with a red dashed line in both images to illustrate that, when the IM-mode is activated and the system is focused on the sample surface, the AFM tip is lifted by the tip switching system on the side at a safe position, avoiding any risk of touching the sample and/or damaging the AFM probe. Travel path of the AFM tip is also marked in (b) for demonstrating the switching process. The lowest point of the path is even lower than the focal plane. To address this, z-motion stage will lift the microscope by about 6 mm before the mode switching to ensure the AFM probe safety. . 101

Figure 42 Realization details of the Klappfix. Two different perspectives of Klappfix as mounted on a dummy objective (IV): (a) side view and (b) oblique view (45°). The Klappfix consists of three main parts (I) AFM tip holder, (II) objective adapter and (III) a rotation mechanism. (c) top view of the objective adapter (II) attached with rotation mechanism (III); (d) side

https://doi.org/10.7795/110.20260421A

view of AFM tip holder, equipped with three adjustments screws for fine adjusting the position of the AFM cantilever. Red rectangle marked is the end of the AFM tip holder, where the AFM probe is fixed. Zoomed figures (e) and (f) illustrate this part with and without an AFM probe mounted, respectively. For ensuring the position-repeatability of the AFM probe by AFM probe changing, an alignment chip [168] (g) with positioning groove is fixed on the end of AFM tip holder. 101

Figure 43 FOV images acquired after repeatedly active/inactive the tip switching system for switching the measurement mode from the AFM-mode to the IM-mode then back to the AFM-mode in different time 104

Figure 44 FOV images acquired each time after changing AFM probes in the HM system 105

Figure 45 Illustration of the vertical position of samples in AFM-mode and IM-mode, WD is short for working distance, its value depends on applied objective (e.g. 4.7 mm for Nikon 20x Mirau objective). TL is short for tolerance length, which is an additional vertical retraction distance of the Z motion stage, introduced for protecting the AFM tip from unwanted collision with the surface after mode switching, normally in a length of 50 μm. 109

Figure 46 Illustration of the control loop of the AFM-mode in the HM implemented using PID control technique.. 110

Figure 47 AFM signals acquired for noise analysis, which is measured (a) without contact established between tip and sample and (b) after tip approached the sample and making contact (c) illustrated the noise variations during the approaching process. It remains almost constant before tip-sample engagement and increases significantly after the tip contacting with the sample surface. 113

Figure 48 Spectrum analysis of the AFM signals acquired (a) when AFM tip hanging freely over the sample surface (no contact established between tip and sample) and (b) after tip sample contact established. Some of the major noise contributions from the piezo stage can be observed around 120 Hz and 200 Hz. 114

Figure 49 Height signal sampled at approximately 800 Hz for instrument noise analysis (a) the signal measured in closed-loop operated AFM-mode without tip scanning for 12s and (b) the spectrum of the acquired signal 115

https://doi.org/10.7795/110.20260421A

Figure 50 SPM lateral standards 2D 10000 (a) the SPM lateral standard set from 2D 100 to 10000; (b) over look of the 2D 10000 pitch standard whose up right corner is marked with red rectangle and (3) topographical details of the area marked in (2) measured by PSI mode of HM with 20x objective. Squares designed in 2D with pitch distance of 10000 nm can be observed. 116

Figure 51 Calibration measurement of the SPM lateral standards 2D 10000 acquired by the AFM-mode of the HM (a) measured topography in size of 40 x 20 µm² and (b) profile along x-axis (fast scan axis) extracted at a randomly selected position marked with white dashed line in (a). The green circles mark the centers of two structures of the 2D 10000 standard and are used only to illustrate the pitch distance. They do not represent the actual measured structures. 117

Figure 52 Repeated measurements of roughness standard ARS from company SiMETRICS [182] (a) seven AFM measurements named after R1 to R7 in the size of 2x20 µm² over a same sample position, acquired over three days; (b) comparison of seven vertical profiles extracted respectively from the seven AFM measurements (a) processed with operations: (I) lateral drift correction and (II) line-wise leveling. 119

Figure 53 Illustration of the incident and reflected light beams behavior when a sample is placed with a tilting angle $\boldsymbol{\alpha}$ 120

Figure 54 Simulated and measured effective wavelength $\boldsymbol{\lambda eff}$ as a function of the tilting angle $\boldsymbol{\alpha}$ using the HM, which is equipped with a Nikon 20x Mirau objective (NA 0.4) and a monochromatic LED light source (with a center wavelength is calibrated to 595 nm). Simulation models (Equ. 5.1) considering different levels of apodization are plotted in the diagram: (I) n=0 means no apodization effect occurs in the illumination system; (II) n=15 indicates the theoretically calculated apodization effect based on the specifications of the applied light source and (III) n= ∞ indicates the strongest apodization effect that the system allows only light beams parallel to the optical axis to illuminate the surface, while light beams with other incident angle are blend out. 121

Figure 55 Interference fringe profiles captured at different optical output of new and old light sources. Black curve is measured with fully powered amber LED light source and the other 5 are measured with new red LED light source with given different output voltage. The black curve is

https://doi.org/10.7795/110.20260421A

demonstrated with an offset of -20 digits for having a clear comparison between the other curves. 126

Figure 56 Measurement noise $NAFM$ determined by simulation and experimentally vs. light source output voltage. The simulation is based on the model (Equ. 4.31) with consideration of the camera noise $Ncam$. 127

Figure 57 Interference fringe profiles captured at different camera exposure time while keeping the output voltage of the new light sources at 500 mV. 128

Figure 58 (a) Cantilever backside captured by 20x objective (zoomed). The fringes are not perfectly aligned vertically, indicating that the cantilever backside is tilted not only in the intended horizontal direction but also undesirably in the vertical direction. A red rectangular area in the middle of the cantilever marks the capture position of the eight adjacent fringe profiles $W1-8$ (b) The first and the last fringe profiles $W1$ and $W8$ captured are marked with color blue and red respectively. Due to the undesired tilting angle in vertical direction, they have different phases, which can be observed in the diagram as lateral phase shifts between two profiles.. 131

Figure 59 Application of the new low-cost version of AFM tip switching system mounted on the (a) Nikon 20x Mirau objective, (b) Nikon 100x Mirau objective and (c) Nikon 10x Mirau objective with help of adapter ring when it is needed. FOV images of the AFM cantilever backside acquired using different objectives are also presented. They are arranged below the images of the corresponding objectives. 132

Figure 60 Interference fringe profiles captured at different optical output of new and old light sources while equipped with 100x Nikon Mirau objective......... 134

Figure 61 (a) AFM measurements over the same area (20µm x 2 µm) of a Cu roughness sample performed by the AFM-mode using a 100x Nikon Mirau objectives (b) a comparison of profiles extracted at the same position from the repeat measurements R1-R4 in (a)...................... 134

Figure 62 Measurement results of roughness standard ARS [182] from the company SiMETRICS (a) The IM-mode measurement results in size of 248 µm x 186 µm (b) Cropped IM measurement in size of 16 µm x 20 µm (c) 16 µm x 20 µm AFM measurement, which measured at the same position as (b). (d) Cross-section profiles comparison between IM and AFM measurements. Black rectangular marked in (a) indicates the location

https://doi.org/10.7795/110.20260421A

of cropped image (b). Dash circles marked in (b) and (c) are local valley structures. Based on highly overlapped circle positions between (b) and (c), it can be verified that IM and AFM are measured at the same topography of the sample surface. Vertical dashed white lines in (b) and (c) are marked as the position of profile shown in (d).......... 138

Figure 63 Measurement results of a N1 pattern of a CCS sample (a) The IM-mode measurement results in size of 248 μm x 186 μm (b) Cropped IM measurement in 16 μm x 20 μm (c) 16 μm x 20 μm AFM measurement, which measured at the same position as (b). (d) Cross-section profiles comparison between IM and AFM measurements. Red rectangular marked in (a) indicates the location of cropped image (b). This location is also where the AFM measurement (c) is taken placed. Horizontal red lines in (b) and (c) represent the same position on the sample. They are indicating where the profiles shown in (d) are extracted from both measurement results. 140

Figure 64 A collection of samples whose surfaces are made by different material and processed by different surface finishing methods (a) an old roughness sample made of bronze (b) an aluminum cylinder manufactured by turning (c) gold coated chip sample (d) chrome coated roughness sample and (e) thickness gauge block made of steel 142

Figure 65 Correlative topographical measurement results using both AFM- and IM-modes of the HM equipped with a 20x objective over samples: (a) an old roughness sample made of bronze (b) an aluminum cylinder manufactured by turning machine (c) gold coated ship sample (d) chrome coated roughness sample and (e) thickness gauge block made of steel 143

Figure 66 Correlative measurement results using both AFM- and IM-modes of the HM equipped with a 20x objective demonstrated as comparison of vertical profiles extracted at the same randomly selected position over samples: (a) an old roughness sample made of bronze (b) an aluminum cylinder manufactured by turning machine (c) gold coated ship sample (d) chrome coated roughness sample and (e) thickness gauge block made of steel 145

Figure 67 Spectrums of correlative profiles demonstrated in Figure 66 measured by the AFM- and IM-modes of the HM equipped with a 20x objective over (a) an old roughness sample made of bronze (b) an aluminum cylinder

https://doi.org/10.7795/110.20260421A

manufactured by turning machine (c) gold coated ship sample (d) chrome coated roughness sample and (e) thickness gauge block made of steel 146

Figure 68 Correlative topographical measurement results using both AFM- and IM-modes of the HM equipped with a 100x objective over samples: (a) an old roughness sample made of bronze (b) an aluminum cylinder manufactured by turning machine (c) gold coated ship sample (d) chrome coated roughness sample and (e) thickness gauge block made of steel 151

Figure 69 Correlative measurement results using both AFM- and IM-modes of the HM equipped with a 100x objective demonstrated as comparison of vertical profiles extracted at the same randomly selected position over samples: (a) an old roughness sample made of bronze (b) an aluminum cylinder manufactured by turning machine (c) gold coated ship sample (d) chrome coated roughness sample and (e) thickness gauge block made of steel 152

Figure 70 Spectrums of correlative profiles demonstrated in Figure 69 measured by the AFM and IM-modes of the HM equipped with a 100x objective over (a) an old roughness sample made of bronze (b) an aluminum cylinder manufactured by turning machine (c) gold coated ship sample (d) chrome coated roughness sample and (e) thickness gauge block made of steel 153

Figure 71 Overview of the Cu roughness sample. Surface pictured with digital camera in a size of 351 µm x 264 µm. 157

Figure 72 (a) PSI measurements using the IM-mode of the HM over the same sample position acquired at different dates. (b) Profile comparison over the same position extracted from the topographies shown in (a)........... 158

Figure 73 Comparison of the profiles measured by different instruments on the same location of the Cu sample.. 158

https://doi.org/10.7795/110.20260421A

List of Abbreviations

1D,2D,3D	*one-dimensional, two-dimensional, three-dimensional*
AFM	*atomic force microscope*
AI	*artificial intelligence*
AOI	*area of interest*
ASF	*amplitude point spread function*
BEM	*boundary element method*
BPRA	*binary pseudo-random array test standard*
CAD	*computer-aided design*
CC	*circular chirp*
CCD	*charge-coupled device*
CCS	*circular calibration standard*
CD	*critical dimension*
CFM	*confocal microscopy*
CMM	*coordinate measuring machines*
CMOS	*complementary metal-oxide semiconductor*
CoG	*center of gravity*
ContDLC	*contact mode AFM probe with diamond-like-carbon tip coating*
CSI	*coherence scanning interferometry*
CT	*computed tomography*
DFT	*discrete Fourier transform*
DOF	*depth of field*
EFO	*elementary Fourier optics model*
EMPIR	*european metrology programme for innovation and research*
FDTD	*finite difference time domain method*
FEM	*finite element method*
FFT	*fast Fourier transform*
FOV	*field of view*
fps	*frames per second*
FVM	*focus variation microscopes*
FWHM	*full width at half maximum*
GPG	*good practice guides*
GPS	*geometrical product specifications*
GUI	*graphical user interface*
GUM	*guide to the expression of uncertainty in measurement*
HM	*hybrid microscope*
IM	*interference microscope*
ISO	*international organization for standardization*
ITF	*instrument transfer function*
LED	*light-emitting diode*
MSMS	*multi-sensor measuring system*
MTF	*modulation transfer function*
NA	*numerical aperture*
NMM	*Nanomessmaschine (German)*
RMS	*root mean square*

https://doi.org/10.7795/110.20260421A

OM	*optical microscopy*
OPD	*optical path difference*
OTF	*optical transfer function*
PD	*position sensitive detector*
PID	*proportional-integral-derivative*
PSD	*power spectral density*
PSF	*point spread function*
PSI	*phase-shifting interferometry*
PTB	*Physikalisch-Technische Bundesanstalt (German)*
PZT	*lead zirconate titanate*
QPD	*quadrant photodiode*
RCWA	*rigorous coupled wave analysis*
SEM	*scanning electron microscope*
SFM	*scanning force microscopy*
SIM	*structured illumination microscopy*
SNR	*signal-to-noise ratio*
SP	*setpoint*
SPM	*scanning probe microscopy*
STD	*standard deviation*
STM	*scanning tunneling microscope*
TTF	*topographical transfer function*
UFO	*universal Fourier optics model*
VSI	*vertical scanning interferometry*
WD	*working distance*
WLI	*white-light interferometry*
WLPSI	*white-light phase-shifting interferometry*

https://doi.org/10.7795/110.20260421A

List of Symbols

Symbol	Description
$\vec{E}$	*electric field of the light*
t	*time*
$\vec{r}$	*spatial position*
$\vec{A}, A$	*amplitude vector, amplitude*
$\vec{k}, k$	*wave vector, wavenumber*
λ, λ_{eff}	*wavelength, effective wavelength*
ω	*angular frequency*
φ	*phase of the light*
c	*vacuum speed of the light*
I	*intensity of the light*
θ, θ_{max}	*incident angle, maximum incident angle*
f	*focal length of objective*
L	*length of optical path*
n_r, n_{air}	*refractive index, refractive index in air*
n_{apo}	*apodization factor*
P	*pupil function*
Θ	*phase difference between measured and reference beams*
Φ	*known phase shifts in PSI algorithm*
H	*surface topography*
z	*scan position in vertical axis*
C	*envelope function of the WLI correlogram*
v, v_z	*frequency, spatial frequency along the z-direction*
J	*Bessel function*
ε	*errors*
α_i	*amplification coefficients*
l_i	*linearity deviations*
N_M	*measurement noise*
D_{LIM}	*lateral period limit*
$\tilde{\theta}$	*angular orientation of CCS pattern*
P_{out}, P_{in}	*output and input power spectral density*
ρ	*cross-correlation coefficient*
$\tilde{E}$	*Young's modulus*
ΔD	*cantilever displacement*
S_{AFM}	*AFM signal*
S_x, S_y, S_z	*position of the piezo stage*

https://doi.org/10.7795/110.20260421A

https://doi.org/10.7795/110.20260421A

1. Introduction

Micro- and nano- three-dimensional (3D) metrology plays a fundamental role in numerous industries and research fields, particularly, for advanced manufacturing-, nanoelectronics-, optics- and semiconductor industry. Manufacturing developments in these fields pose increasing challenges in measuring structures with ever smaller size, more complex 3D shapes, and finer surface quality. Currently in micro- and nanometrology, a wide range of instruments are developed and applied to meet these challenges. These instruments are generally cataloged according to their different measuring principles as tactile instruments such as atomic force microscope (AFM), and optical instruments such as phase-shifting interference (PSI) microscope and white-light interference (WLI) microscope.

Optical instruments are known for their advantages of high measuring speed and non-contact measuring principle, which will less likely damage sample surfaces during measurements. However, its lateral resolution is fundamentally constrained by the diffraction limit. Tactile instruments, especially AFMs, provide excellent precision and accuracy in all three axes with high spatial resolution. However, such instruments are typically slower compared to optical instruments. For comparable measurement areas, AFM measurements can require more than two orders of magnitude more measurement time than optical techniques such as PSI.

Furthermore, significant discrepancies in measurement results of different optical and tactile instruments are frequently reported [1-4]. These discrepancies between optically measured data and tactile measured data originate from differences in their raw topographical measurements and are subsequently propagated into the estimation of surface characteristics and topography specifications. To better characterize these discrepancies, the concept of topography fidelity has been introduced in surface metrology. According to the international organization for standardization (ISO) [5], topography fidelity is defined as the "closeness of agreement between a measured surface profile or measured topography and one whose uncertainties are insignificant by comparison." This definition provides a new aspect to quantitatively evaluate the reliability and accuracy of surface measurements across different measurement techniques.

Compared with measurement results obtained using AFM, optical results typically exhibit lower topography fidelity due to the complex interactions between light and sample surfaces during measurements. Currently, many studies have been conducted to explore the possibility to enhance the topography fidelity of optical instruments from three different perspectives:

https://doi.org/10.7795/110.20260421A

(I) Calibrations of geometrical parameters of areal surface topography measuring instruments in terms of magnification, linearity, squareness, flatness, and noise etc. [6-8].

(II) Theoretical studies and modeling to simulate the optical areal surface topography measuring instruments, especially the interaction between light and surfaces [9-11].

(III) Characterizations of bandwidth characteristics of areal surface topography measuring instruments, for instance, via the instrument transfer function (ITF) [12-14].

One of the primary factors contributing to the poor topography fidelity of optical instruments is their limited spatial resolution, particularly in the lateral directions. Lateral resolution refers to an instrument's ability to distinguish between two closely spaced surface features. In the context of optical areal surface measuring instruments, lateral resolution is widely described using diffraction limit, which is determined by the wavelength of the applied light source and the numerical aperture (NA) of the applied optical objective. For instance, a representative lateral resolution for a commercial optical instrument is approximately 900 nm, calculated based on the Rayleigh criterion using a 20x interference objective with a NA of 0.4 and a light source with wavelength of 590 nm.

However, in practical applications, the achievable lateral resolution of conventional optical instruments may be largely reduced compared to the theoretical value calculated by the Rayleigh criterion. This reduction results in a lateral resolution in the range of several micrometers. As demonstrated in our previous study on the ITF [12], which characterizes the instrument response as a function of the spatial frequency of the sample surface, a surface feature must be at least 2550 nm wide (about three times larger than the value estimated using Rayleigh criterion) for 50% of its amplitude to be accurately measured. This evaluation is experimentally conducted using the same measurement setups as mentioned in previous text (20x interferometric objective with a NA of 0.4 and a light source with wavelength of 590 nm). Therefore, resolving surface structures with nanometric dimensions using such optical instruments is very difficult, if not impossible. This limitation leads to measurement discrepancies between the optically acquired topography and its reference topography, ultimately resulting in reduced topography fidelity of optical measurement.

To overcome this limitation, super-resolution optical imaging techniques like structured illumination microscopy (SIM) and stimulated emission depletion (STED) microscopy have been developed. SIM [15] enhances resolution by illuminating the sample with structured light and observing Moiré fringes formed by the interference between the structured light and the sample. This technique enables a resolution improvement of up to a factor of two. STED

https://doi.org/10.7795/110.20260421A

microscopy [16] employs an additional beam of light to inhibit the point spread function of fluorescence, which is excited by the laser. With this method, the lateral resolution limit can be reduced to a few tens of nanometers, thereby breaking the diffraction resolution limit. However, the implementation of these emerging techniques in surface measurement instruments suitable for general industrial applications remains under active development, and the associated costs are currently prohibitively high.

Scanning probe microscopy (SPM), particularly AFM, is widely used for high-resolution 3D metrology. Compared to optical methods, SPM offers superior resolution. AFM achieves lateral resolutions of just a few nanometers by scanning surfaces with a sharp tip (typically with a radius ranging from several tens of nanometers to just a few nanometers). However, as mentioned previously, its scanning nature makes it relatively slow.

A concept of hybrid microscope (HM), which integrates an AFM-mode within an interference microscopic (IM) mode with high synergy, can combine the advantages of both techniques: using the AFM-mode for high-resolution measurements when and where it is needed, and the IM-mode for fast, large-range measurements.

Another advantage of this concept is that the calibrated AFM-mode of the HM provides *in-situ* reference areal surface metrology for the IM-mode. IM measuring principle, due to its complex interaction between the optical light and surface, often results in measurement errors in their measured topographies, such as outliers, missing data points, and other measurement artifacts. These errors also lead to unsatisfying topography fidelity, especially in measurements requiring precise metrology over complex surfaces. In the concept of the HM, accurate and traceable measurements on the same area of interest (AOI) can be easily re-measured by the AFM-mode and serve as *in-situ* reference data for IM measurements. By doing this, the effort for sample transportation between different instruments and relocating the AOI are saved. The measurement error attributed to sample re-mounting and positioning will be tremendously reduced.

To achieve this concept, this doctoral work focuses on the development of a prototype of the HM and the demonstration of its applications. The dissertation is structured as follows: chapter 2 introduces the state of the art of the techniques applied in areal surface metrology; chapter 3 presents approaches for enhancement of the topography fidelity of the optical measurements; the development of the HM as well as its performance will be introduced in chapter 4; some of the optimizations and improvement of the HM are discussed in chapter 5; and in chapter 6 potential application scenarios and examples are demonstrated.

https://doi.org/10.7795/110.20260421A

2. State of the art of areal surface topography measurement

In recent decades, technological progress in metrology has made it possible to conduct 3D surface measurements at the micro- and nanometer scale. Instruments applied for such measurements can be broadly classified into three categories based on their underlying measurement principles. Optical instruments use light beams, such as incoherent or coherent lights, as non-contact probes to measure surface topography. Tactile instruments employ physical probes, such as styluses or AFM tips, to make direct contact with the surface and mechanically scan across surfaces to measure their topographical features. Hybrid instruments integrate two or more different types of measurement principles within a single system, allowing for complementary measurements and enhanced flexibility in surface characterization.

The measurement principles employed in 3D surface metrology determine surface topography by utilizing various physical interactions between the probe (sensor) and the sample. It is widely acknowledged that the probe–sample interactions in optical measurement instruments are more complex than those in tactile instruments, particularly when measuring surfaces with complex features such as steep slopes or V-shaped grooves [17]. As a result, comparisons of measurement results obtained from different optical areal surface measuring instruments, as well as between optical and tactile systems, often reveal significant discrepancies. For example, as discussed in the work of R. Leach [18], evaluated roughness results may vary considerably depending on the instrument used. More importantly, such discrepancies can occur even when the same measurement principle is applied. For instance, the stylus method, which is a commonly used tactile technique for surface roughness measurements, may produce different results by different instruments. To address these inconsistencies, a fundamental question must first be considered: when using any of these instruments for areal surface measurements, “are we getting the right answer?” [17].

To answer this question, obviously the question “How did these instruments measure?” must be answered in advance. Meaning that, with well understanding of current measuring principles and their measuring abilities, there will be a chance to distinguish the right answer from wrong ones. In this chapter, state of the art measuring principles applied in 3D nanometrology, including optical methods (PSI and WLI etc.) and tactile methods (stylus profilometry and AFM technique etc.) will be introduced in following sections.

https://doi.org/10.7795/110.20260421A

2.1. A short history of 3D nanometrology

3D nanometrology refers to the science of measurement, focusing on the precise quantitative determination of dimensions and geometrical properties of complex nanostructures [19]. These traditionally include measurements of thin films, surface roughness, form, position, volume of ideal shaped features etc. The dimensional range related to these measurements is at the nanoscale, to be more specific, the size ranges from 100 nm, the top end of precision engineering, to 0.1 nm, which refers to the bottom end of atomic physics and chemistry [20].

In the early 1980s, G. Binnig and H. Rohrer, invented the first scanning tunneling microscope (STM) and won the Nobel prize by it [21], making the first real-space measurement of surfaces at atomic resolution possible. This instrument is considered the ancestor of all types of SPMs, which refers to a branch of instruments that utilize a scanning tip to raster-scan samples physically and collect local information from the surface [22-24]. However, the STM technique can only be applied to the measurement of conducting samples, as it relies on tunneling current as the measured quantity. To overcome this limitation, AFM, invented by G. Binnig as well [25], was developed to measure the surfaces of insulating samples. With a very sharp tip, typically a few microns long and with a tip diameter of only a few nanometers, the atomic force between the tip and sample can be detected and subsequently used to image surface topography [23]. Therefore, as AFM first became commercially available in the year 1989 [26], it immediately became one of the foremost instruments for nanoscale measuring and one of the key members of the SPM family.

At the same time, research on the application of optical principles for 3D topography measurement advanced significantly. Since the invention of the first confocal microscope (CFM) by M. Minsky in 1955 [27], continuous innovation in optical measurement techniques has led to remarkable progress in surface metrology. In particular, during the 1980s, substantial developments in illumination systems and digital signal processing enabled the first practical applications of optical methods for nanoscale topography mapping, most notably through the introduction of PSI [28,29]. In the 1990s, coherence scanning interferometry (CSI), also known as vertical scanning interferometry (VSI) or WLI, was introduced as an alternative or complementary technique to PSI, addressing its limitations in measuring rough or discontinuous surfaces. Concurrently, modern confocal microscopy began integrating offline algorithms for 3D surface reconstruction, further enhancing its capability to resolve nanoscale features with high precision. At present, confocal and interferometric areal surface measuring microscopes remain the dominant optical instruments used in the field of 3D surface metrology [30,31].

https://doi.org/10.7795/110.20260421A

Since R. Feynman's influential lecture in the 1960s, in which he proclaimed, “There is plenty of room at the bottom” [32], more than six decades of dedicated research in 3D nanometrology have led to remarkable advancements. Instruments for nano-dimensional measurement are now based on a wide range of measurement methods. Furthermore, the measurable dimensional range has been significantly extended, reaching below 100 pm. Advanced techniques such as STM and non-contact AFM have pushed resolution limits even further, enabling height measurements at the sub-picometer scale and atomic resolution respectively [33,34]. As our understanding of physics, particularly quantum physics, continues to progress, previously established limitations are being systematically overcome, turning long held theoretical possibilities into practical measurement capabilities.

2.2. Measurement principles and instrument realizations

In the field of 3D micro- and nanometrology, a wide range of instruments has been developed to measure small-scale structures with dimensions ranging from the microscale and nanoscale down to the atomic scale. These instruments operate based on diverse measurement principles that determine how the probe interacts with the sample, including physical contact, optical interference, electron tunneling, and capacitive coupling. Based on the underlying measurement techniques, these instruments can be broadly classified into two main categories: tactile and contactless instruments.

Tactile instruments acquire measurement data through physical contact with the surface using a material probe. The measurement accuracy and resolution of these instruments can vary depending on the type and size of the probe used. Consequently, the achievable measurement range differs considerably, from hundreds of millimeters in large-scale wafer form measurements to the micrometer scale in high-precision surface roughness characterization.

Common tactile instruments based on their data acquiring technique can be further cataloged in classical tactile instruments, which measure point-wisely, and scanning instruments, which measure surface by scanning over structures. Typical tactile instruments, such as coordinate measuring machines (CMMs) and AFMs are well-established in the industry and play a vital role in dimensional metrology for industrial applications.

Contactless instruments, most commonly, employ optical principles to perform 3D measurements. This approach enables the use of non-material probes, allowing surface characterization without direct physical contact. However, as vibrating cantilever techniques have matured, certain measurement systems such as non-contact AFM are also capable of performing non-contact measurements, even though they rely on a material probe. Importantly,

https://doi.org/10.7795/110.20260421A

in both types of implementations, the measuring instruments do not establish physical contact with the sample. As a result, contactless instruments offer faster measurement speeds while minimizing the risk of damage to both the sample and the probe. Because of these significant advantages, contactless instruments such as PSI, WLI, CFM, computed tomography (CT), optical CMM, scanning electron microscope (SEM) hold an essential place in both industrial applications and scientific research within the field of dimensional metrology.

The aforementioned instruments differ significantly in their measurement principles and measuring capabilities, which makes direct comparison between them challenging. M. Stedman [35] addressed this problem using an amplitude-wavelength diagram, which is also known as the Stedman diagram. By modeling the response of an instrument to a sinusoidal input signal, which varies its wavelength and amplitude, the effective working range of the instrument can be plotted in the diagram with a closed area. In reference to literatures [35-38], a modern revisited Stedman diagram is shown in Figure 1.

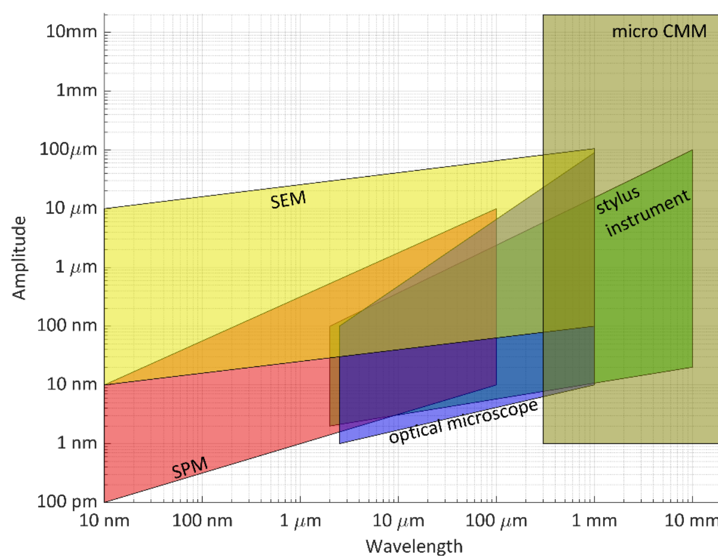

Figure 1 Stedman diagram (diagram of wavelength vs. amplitude) for different surface measuring instruments, including SPM, SEM, optical, stylus and CMM techniques [35-38]

2.2.1. Tactile measurement technology

Coordinate measuring machine in micro- and nanometrology

CMM is regarded as one of the most essential 3D measurement instruments in modern industry, particularly in fields that require precision machining and advanced manufacturing processes. It offers high flexibility and accuracy in measuring spatial coordinates, making it especially effective for evaluating complex geometric features [39,40]. A CMM is typically

equipped with a measuring head that houses one or more physical probes operating on the principle of tactile measurement. These probes are commonly designed with spherical tips composed of sapphire or ruby, with diameters ranging from several millimeters to a few hundred micrometers, depending on the specific application. For example, for high-precision measurements of microscale structures, tip diameters of approximately 500 µm or smaller are often employed.

Before a CMM measurement begins, the probe is initially positioned at a safe distance from the sample. During the measurement, the probe moves toward the sample until contact is detected. At the moment of contact, the CMM records the position of the probe center rather than the exact surface coordinate of the sample. Consequently, reconstruction of the actual sample topography requires geometric compensation based on the probe shape, typically by taking the probe radius into account when a spherical probe is used. Once a sufficient number of corrected measurement points has been acquired, a detailed 3D representation of the sample can be generated.

Traditionally, CMMs have featured large measurement volumes with very impressive measurement uncertainty levels [41]. For example, [42] reports a measurement uncertainty of 3.4 µm, with a coverage factor of 1.98 corresponding to an approximately 95% confidence level, within a measurement range of 400 mm for a tactile CMM. However, with the advancement of micro-fabrication technologies in recent decades, especially the increased application of precision micro-features with high aspect ratios in the semiconductor industry, demand for more precise dimensional measurements using CMMs has surged [43]. This demand has driven the development of micro-CMMs.

Micro-CMMs operate on the same fundamental principles as conventional CMMs but utilize significantly smaller probes (e.g., with diameters as small as 70 µm [44]) and are typically integrated with ultra-precise positioning stages. A notable example of such a stage is the NMM-1 device developed at TU Ilmenau [45,46], which achieves spatial resolutions below 0.1 nm along all three axes within a measurement volume of 25 mm x 25 mm x 5 mm (x, y, z). Additionally, H. Spaan demonstrated in his work [44] that the Isara 400 ultra-precision CMM can achieve high precision measurement with measurement uncertainties below 50 nm within a substantially larger measurement volume of 400 mm x 400 mm x 100 mm (x, y, z).

Stylus profilometry

Profilometry is a technique used to acquire detailed topographical information from a sample surface. It is commonly applied in measurement tasks such as evaluating step heights, characterizing surface waviness and roughness, and mapping the overall surface contour.

https://doi.org/10.7795/110.20260421A

Among the two primary types of profilometry, namely stylus profilometry and optical profilometry, stylus profilometry operates based on a tactile measurement principle. In this method, a topography sensor, consisting of a physical stylus, scans a surface while its vertical displacements are recorded and amplified to represent the surface profile or topography. Similar to the probe of a CMM, a stylus profilometer is typically equipped with a stylus that features a microscopic spherical tip with a radius of a few micrometers. This tip is generally made from wear-resistant materials such as diamond or sapphire to ensure high durability and measurement precision.

The topography sensor is a critical component integrated into the stylus profilometer. One of its primary functions is to precisely measure the vertical displacements of the stylus, which are essential for reconstructing the surface topography and ensuring accurate measurement results. Various sensing principles can be used to implement topography sensors in stylus profilometers, including inductive principles such as the linear variable differential transducer (LVDT), capacitive principles such as the linear variable differential capacitor (LVDC), as well as piezoelectric and optical principles, for example optical-lever detection or laser interferometry [47–49].

The vertical measuring range of modern stylus profilometers spans from a few micrometers to several millimeters. Depending on the type of topography sensor employed, the vertical resolution can range from several tens of nanometers down to sub-nanometer levels. However, achieving high lateral resolution and high measurement speed remains a challenge for stylus profilometry. Typically, the lateral resolution is more than ten times lower than the vertical resolution. For example, the Talysurf profilometer by Taylor Hobson [49] offers a vertical resolution of 15 nm, while its lateral resolution is limited to 250 nm. This limitation is primarily associated with the geometry of the stylus tip, particularly its diameter. Unlike optical systems, the measurement speed of stylus profilometers cannot be significantly increased, as the tactile nature of the method introduces a substantial risk of damaging the sample surface in high-speed measurements. Additionally, geometrical deviations and wear in the stylus shape can further compromise measurement accuracy. Therefore, careful consideration of the influence of stylus geometry and scanning parameters on the measurement results is essential to ensure measurement reliability of the stylus instruments.

2.2.2. Atomic force microscopy

AFM, also known as scanning force microscopy (SFM), is one of the earliest and most widely used techniques within the family of SPM. Similar to the previously introduced CMM and stylus profilometer, AFM also employs a physical probe to measure the surface topography of a

sample. However, unlike those techniques, interaction forces between the sensor and the sample surface are at the atomic scale. To enable force detection at such small scales, the AFM sensor is constructed as a flexible cantilever. It is typically several hundred micrometers in length and several tens of micrometers in width. An ultra-sharp tip, usually a few nanometers in diameter, is mounted at the free end of the cantilever. During AFM measurements, this tip is brought into close proximity with the sample and scanned across the sample surface, enabling the detection of surface features through the resulting cantilever deflections.

Atomic forces that work on the AFM tip can mainly be cataloged as attractive forces (e.g. van der Waal force) and repulsive forces (e.g. electrostatic and Pauli repulsion). Depending on the distance between sample and tip, different forces dominate. Such dependency (shown in Figure 2) describes the basic features of the tip-sample interaction. To be more specific: the resultant force is attractive in large tip-sample distances at the first place. Then, as the distance reduces, repulsive forces become stronger. After reaching an interaction balance point, at short tip-sample distances the repulsive interaction takes over and the resultant force starts to be repulsive.

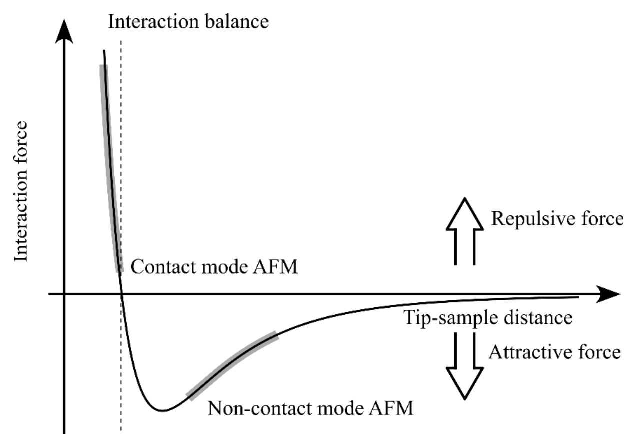

Figure 2 Curve of interaction force vs. tip-sample distance. Two regimes are highlighted for illustrating the different resultant forces used for realization of contact AFM and non-contact AFM, respectively [50]

As illustrated in Figure 2, two distinct regimes can be identified: (I) the contact regime and (II) the non-contact regime. AFM measurements can be performed based on either attractive or repulsive resultant forces. The fundamental distinction lies in the nature of the force utilized, attractive forces are employed in non-contact AFM, whereas repulsive forces are characteristic of contact AFM.

Non-contact AFM involves positioning the cantilever above the sample, with the tip oscillating at or near its resonance frequency with a small amplitude, typically ranging from sub-nanometer to approximately 10 nm. The lowest point of the oscillation remains several nanometers above the sample surface; consequently, the tip does not make physical contact

https://doi.org/10.7795/110.20260421A

with the surface. To clarify further, throughout the entire oscillation cycle of non-contact AFM, the tip operates exclusively within the regime of attractive forces. Over limited oscillation ranges, the resultant attractive force may exhibit quasi-linear behavior with respect to the tip–sample distance, though the interaction is fundamentally nonlinear.

During a measurement, the AFM tip scans across the sample surface. Variations in surface topography lead to changes in the tip–sample distance, which in turn alter the magnitude of the attractive forces acting on the tip. These force variations cause measurable deviations in both the amplitude and frequency of the oscillated AFM cantilever. Such deviations are detected using a readout system, typically an optical-lever system. The detected deviations will send to a feedback control system, which maintains a constant oscillation amplitude and/or frequency by adjusting the tip–sample distance through vertical movement of either the sample stage or the tip itself. By recording the vertical position of the stage and tip at each different lateral scan position, the surface topography of the sample can be reconstructed.

A variation of the non-contact AFM mode, known as tapping mode AFM, also exists. Similar to the non-contact mode, the tip oscillates near its resonance frequency during measurement. However, in tapping mode, the AFM tip briefly contacts the sample surface at the lowest point of each oscillation cycle. As a result, the tip momentarily enters the regime of repulsive forces during each contact event. This intermittent contact enables higher measurement sensitivity and typically leads to improved spatial resolution compared to non-contact AFM. However, due to the repeated contact between the tip and the sample, the scanning speed in tapping mode is generally reduced in order to preserve the sharp geometry of the AFM tip and minimize the tip breakage and sample damage. A more comprehensive discussion of the measurement principles of non-contact AFM as well as tapping mode AFM is beyond the scope of this work and is therefore omitted. Relevant details can be found in references [50–53].

Contact mode is another main operational mode of AFM, which is widely employed in both research and industrial applications, including topographical characterization, biosciences, materials science, machined surface analysis, as well as in the semiconductor and optics industries. This mode operates based on repulsive atomic forces, which also exhibit a nonlinear relationship with the tip–sample distance within the contact regime (as illustrated in Figure 2). Similar to non-contact AFM, contact mode utilizes a cantilever to probe the sample surface. However, the key distinction lies in the significantly smaller tip–sample distance and the substantially greater interaction forces involved. In this mode, external excitation of the cantilever is unnecessary, as the repulsive forces alone are sufficient to induce mechanical deformation, such as bending or torsion, to the AFM cantilever. These deformations are directly captured by the readout system and used to generate the measurement data.

https://doi.org/10.7795/110.20260421A

The AFM probes used in contact and non-contact AFM differ in three key aspects: (I) cantilever stiffness; (II) tip wear protection and (III) resonance frequencies (due to different vibration requirements). Compared to non-contact probes, contact probes are typically softer, with a lower spring constant (usually around 0.2 N/m), and offer greater resistance to tip wear. Low-stiffness cantilevers are designed to bend when the tip pushes against the sample, preventing the tip from indenting the surface or deforming the sample's structure. Normally, a sharp tip with less than 10 nm as radius can be found at the end of the cantilever. With such a probe, contact AFM can reach nanometer resolution in all three directions. In some cases, by using the sharpest commercially available tip (radius as small as 0.5 nm) [52], even an atomic-scale image of a periodic lattice can be generated.

Detecting cantilever deformation is a critical aspect of both types of AFM measurement. To achieve nanometer-level accuracy in detecting such fine deformations, various readout systems have been developed based on different techniques, such as piezoresistive methods [54], interferometric methods [40,55], and the classic optical-lever technique. These systems are integrated into the AFM to convert cantilever deformation into quantitative positional data, which, in combination with stage position information, forms the final measurement results.

Among different readout systems of AFM, the optical-lever system is the most widely used system due to its advantages: high sensitivity to small deformations, fast response time, and ease of implementation. An optical-lever system integrated into the AFM control loop is illustrated in Figure 3. It typically consists of three main components in general: a laser (signal transmitter), a cantilever with a reflective surface (acting as a mirror for signal reflection), and a position-sensitive detector (PD), such as a quadrant photodiode (QPD), which serves as the signal receiver.

In this setup, laser beams are directed onto the backside of the cantilever, which is typically coated with gold or other high-reflectivity materials to minimize signal intensity losses. The cantilever reflects the laser beams onto a PD. By optimizing the optical path length between the cantilever and the PD, even fine deflections of the cantilever can be significantly amplified, allowing for precise position displacement detection. For example, when the cantilever bends by as little as 5 nm in response to surface topography variations, the angle of the reflected laser beam changes, resulting in a measurable displacement of approximately 10 μm in the laser spot position on the PD, assuming a typical cantilever-to-detector distance of 10 cm. This corresponds to an optical amplification factor of 2000 [56]. Such a displacement is well within the detection capabilities of standard PDs. Therefore, the implementation of the optical-lever system enables highly sensitive and accurate detection of AFM cantilever deflection.

https://doi.org/10.7795/110.20260421A

Another essential component of the AFM is the control loop, i.e. the feedback electronics, as marked in color blue in Figure 3. It plays an important role in AFM measurements as well. Its primary function is to maintain a constant interaction force between the tip and sample by regulating their relative distance. The feedback electronics process the output signal from the PD to determine the current tip–sample distance and compares it to a predefined target value. Based on this comparison, a control signal is generated to adjust the relative position between the cantilever tip and the sample surface via piezoelectric actuators, such as the lead zirconate titanate (PZT) stage illustrated in Figure 3. As the measurement proceeds, the cantilever's position changes in response to surface topography, and the feedback electronics continuously correct these deviations. Together with the readout system, the feedback loop ensures stable interaction forces and enables high-precision AFM measurements.

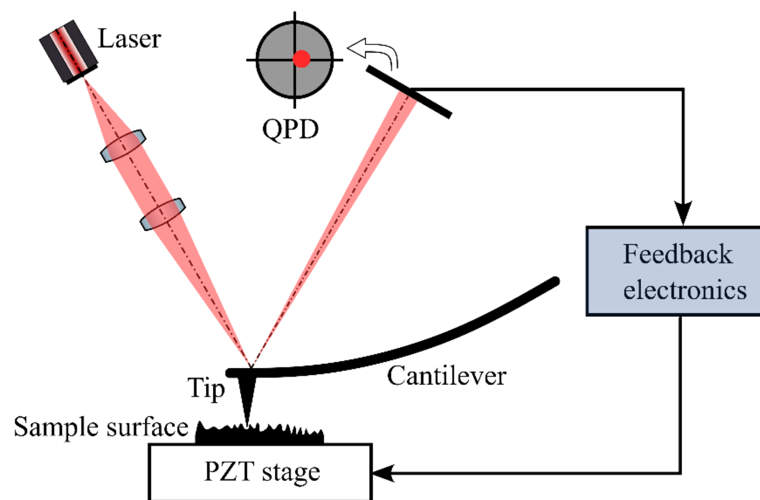

Figure 3 Illustration of implementation of an optical-lever system into an AFM control loop. The QPD and PZT in the figure are abbreviations for quadrant photodiode and lead zirconate titanate (a kind of piezoelectric ceramic material), respectively.

Modern AFM technology enables traceable, high-speed measurements across relatively large scan ranges. For example, G. Dai reported in [57] that a metrological AFM was developed at PTB using a precision motion stage (NMM), providing a measurement range of approximately 25 mm x 25 mm x 5 mm in the x-, y-, and z-directions, respectively, and a measuring speed of up to 1 mm/s. It also offers exceptional resolution, with lateral resolution governed by the tip radius (as small as 5 nm or less) and vertical resolution reaching the sub-nanometer to picometer scale. Owing to these capabilities, such AFM has found widespread applications in surface topography metrology, biological research, semiconductor industry, and other advanced fields, where it serves as an indispensable nanometrology tool.

https://doi.org/10.7795/110.20260421A

2.2.3. Interferometrical measurement technology

Interference of the light

In physics, interference refers to the phenomenon that occurs when two or more coherent waves overlap to form a new wave, whose amplitude and phase are determined by the superposition of the individual wave components. Waves are considered coherent if their phase difference remains constant over the duration of observation. Since the early 19th century, when T. Young proposed that visible light exhibits wave-like behavior and demonstrated this through his famous double-slit experiment [58], it has been recognized that optical interference can serve as a powerful technique for dimensional measurements.

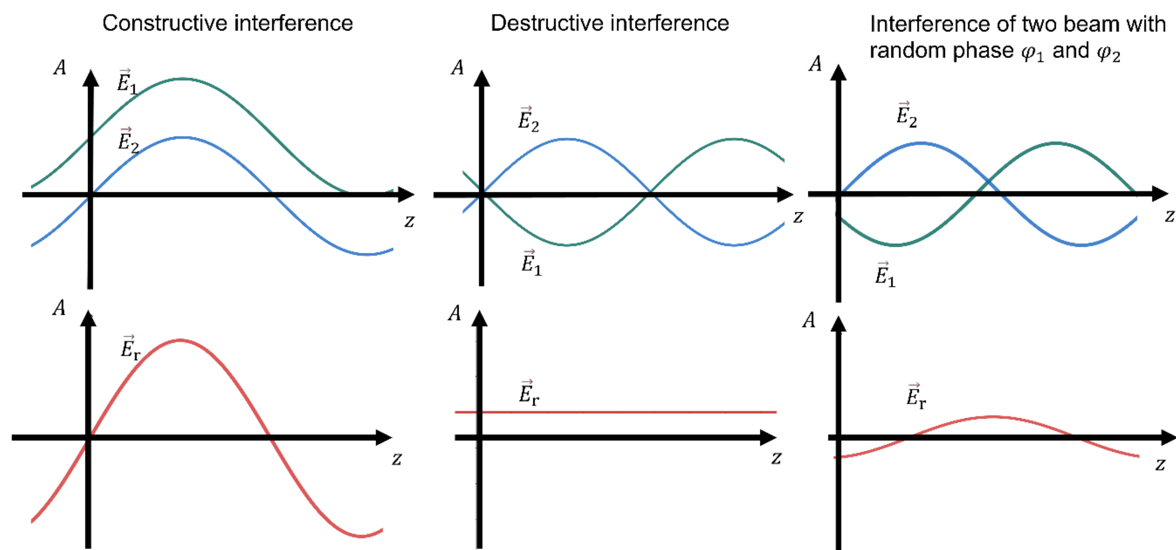

Figure 4 Interference of two waves $\vec{E}_1$ and $\vec{E}_2$ with same amplitudes and propagating direction z at the moment of $t = 0$ with phase offsets φ_1 and φ_2. (a) When the difference between phase offsets is equal to integral multiple of 2π, the two waves are in phase, and forming constructive interference pattern ($\vec{E}_r$), whose amplitude is the sum of both amplitudes of the waves. (b) When the difference between phase offsets is equal to odd multiple of π, the two waves are out of phase, and form destructive interference pattern, whose amplitude is the difference of both amplitudes of the waves. (c) When phase offsets do not fulfill the cases shown in (a) and (b), the amplitude of the interference pattern lies somewhere in between [59]. To be mentioned, for better illustration of the waves, $\vec{E}_1$ in (a) and $\vec{E}_r$ in (b) are plotted with offsets to distinguish them from $\vec{E}_2$ in (a) and z axis.

Light is an electromagnetic wave composed of both electric and magnetic field components. When considering only the electric field, the electric field vector $\vec{E}(\vec{r}, t)$, can be described by a wave function that depends on time t and spatial position $\vec{r}$ [60]:

$$\vec{E}(\vec{r}, t) = Re\left\{\vec{A}e^{i(\vec{k}\cdot\vec{r}-\omega t+\varphi_0)}\right\}. \qquad \text{(Equ. 2.1)}$$

https://doi.org/10.7795/110.20260421A

Where φ_0 indicates a phase offset, $\vec{A}$ is the complex amplitude vector of the electric field. $\vec{k}$ is the wave vector. Its magnitude, also known as wave number k, is related to the wavelength of the light λ by:

$$|\vec{k}| = k = \frac{2\pi}{\lambda}, \qquad \text{(Equ. 2.2)}$$

and ω is the angular frequency, related to the frequency ν by:

$$\omega = 2\pi\nu. \qquad \text{(Equ. 2.3)}$$

Optical interference occurs when n plane waves (where $n \geq 2$) overlap at the same spatial location. Consider a simple case of $n = 2$ as an example, when two plane waves with identical amplitude; the same polarization direction, and the same wavelength overlap at a point in space while propagating in the same direction, the resulting system is linear and can be described by the principle of superposition. The resulting electrical field $\vec{E}_r$ at that point can be expressed as:

$$\vec{E}_r(\vec{r}, t) = \sum_{i=1}^{2} \vec{E}_i(\vec{r}, t). \qquad \text{(Equ. 2.4)}$$

Incorporating the previous Equ. 2.1, the Equ. 2.4 can be written as [60]:

$$\vec{E}_r(\vec{r}, t) = Re\left\{\overrightarrow{A_1} e^{i(\vec{k}\cdot\vec{r}-\omega t+\varphi_1)} + \overrightarrow{A_2} e^{i(\vec{k}\cdot\vec{r}-\omega t+\varphi_2)}\right\}. \qquad \text{(Equ. 2.5)}$$

The Equ. 2.5 can be rewritten as:

$$\vec{E}_r(\vec{r}, t) = \frac{1}{2}\left[\overrightarrow{A_1} e^{i(\vec{k}\cdot\vec{r}-\omega t+\varphi_1)} + \overrightarrow{A_1}^* e^{-i(\vec{k}\cdot\vec{r}-\omega t+\varphi_1)} + \overrightarrow{A_2} e^{i(\vec{k}\cdot\vec{r}-\omega t+\varphi_2)} + \overrightarrow{A_2}^* e^{-i(\vec{k}\cdot\vec{r}-\omega t+\varphi_2)}\right]. \qquad \text{(Equ. 2.6)}$$

Here the $*$ is the symbol for the complex conjugate.

Assume that the two beams that propagate in the positive z-direction are identical in all properties except for a phase offset. This means that the two waves have identical wave vector $\vec{k}$, angular frequency ω, and amplitude $\vec{A}$. Since the propagation occurs purely along the z-direction, all components in the other directions vanish. Therefore, the z-component is equal to the magnitude of the vector, i.e., $\vec{r} = (0,0,z)$, $\vec{k} = (0,0,k)$ and $\vec{A} = (0,0,A)$. Consequently, Equ. 2.6 can be further simplified as:

$$\vec{E}_r(\vec{r}, t) = 2A\cos\left(\frac{\varphi_1-\varphi_2}{2}\right)\cos\left(\frac{\varphi_1+\varphi_2}{2} + kz - \omega t\right), \qquad \text{(Equ. 2.7)}$$

https://doi.org/10.7795/110.20260421A

where the wavenumber k is also given by the angular frequency ω divided by the speed of light in vacuum c.

The term $\cos\left(\frac{\varphi_1-\varphi_2}{2}\right)$ in Equ. 2.7 modulates the value of resulted field $\vec{E}_r$. Depending on the different value of $\varphi_1 - \varphi_2$, cases of interference are shown in Figure 4 (at the moment of $t = 0$):

(I) Constructive interference occurs when φ_1 and φ_2 satisfy the condition $\varphi_1 - \varphi_2 = n * 2\pi$,meaning that two waves $\vec{E}_1$ and $\vec{E}_2$ are in phase. In this case, the term $\cos\left(\frac{\varphi_1-\varphi_2}{2}\right)$ reaches its maximum value of 1. As a result, the amplitude of the resulting wave $\vec{E}_r$ becomes $2A$, which is twice that of each original wave (A). The resulting wave $\vec{E}_r$ has the same phase as the two original waves, and its zero crossings occur at the same positions as those of the original waves.

(II) Destructive interference occurs when φ_1 and φ_2 satisfy the condition $\varphi_1 - \varphi_2 = (2n + 1) * \pi$, i.e. when the two waves $\vec{E}_1$ and $\vec{E}_2$ are out of phase by π. Under this condition, the term $\cos\left(\frac{\varphi_1-\varphi_2}{2}\right)$ becomes zero. Consequently, the resulting wave $\vec{E}_r$ has zero amplitude at all points along the z axis and no resultant wave is observed.

(III) For all other phase differences, i.e. when neither condition (I) nor condition (II) is fulfilled, the amplitude of resulting wave $\vec{E}_r$ is given by $2A\cos\left(\frac{\varphi_1-\varphi_2}{2}\right)$. The resulting wave has the same frequency as the original waves, s, while its phase offset is determined by the average of φ_1 and φ_2.

In practice, however, light interference is not typically characterized by the direct overlap of electric fields, as the electric field itself is not directly observable. Instead, it is more intuitive and experimentally relevant to describe interference in terms $\langle\vec{E}^2\rangle$, which corresponds to the intensity I of the resulting light [60]:

$$I = \langle\vec{E}^2\rangle = \langle\left(\vec{E}_1 + \vec{E}_2\right)^2\rangle = \langle\vec{E}_1{}^2\rangle + \langle\vec{E}_2{}^2\rangle + 2\langle\vec{E}_1\,\vec{E}_2\rangle. \quad \text{(Equ. 2.8)}$$

Where, I_i are the intensities of each wave $\vec{E}_i$,

$$I_i = \langle\vec{E}_i{}^2\rangle = \frac{1}{2}\vec{A}_i \cdot \vec{A}_i{}^\star, \quad \text{(Equ. 2.9)}$$

and the interference term is given by:

$$2\langle\vec{E}_1\,\vec{E}_2\rangle = \frac{1}{2}(\vec{A}_1 \cdot \vec{A}_2{}^\star + \vec{A}_2 \cdot \vec{A}_1{}^\star). \quad \text{(Equ. 2.10)}$$

https://doi.org/10.7795/110.20260421A

With the consideration that both waves propagate in direction of the z-axis and are linearly polarized in the same direction (e.g. in x-direction), interference intensity in Equ. 2.8 can be calculated as follows [60]:

$$I = I_1 + I_2 + 2\sqrt{I_1 I_2}\cos(\varphi_1 - \varphi_2). \qquad \text{(Equ. 2.11)}$$

Equ. 2.11 shows that as the phase difference $\varphi_1 - \varphi_2$ varies, the value of the term in the interference expression, $\cos(\varphi_1 - \varphi_2)$, changes between -1 and +1. This leads to periodic variations in the interference intensity I ranging from its minimum value $(I_1 + I_2 - 2\sqrt{I_1 I_2})$ to maximum value $(I_1 + I_2 + 2\sqrt{I_1 I_2})$. A complete cycle of intensity variation, from minimum to maximum and back to minimum, corresponds to a phase difference of 2π between the two beams, which is equivalent to an optical path difference (OPD) of one wavelength λ between the two beams. This fundamental relationship forms the basis for dimensional measurements using the principle of optical interference:

$$OPD = \lambda \frac{(\varphi_1 - \varphi_2)}{2\pi}. \qquad \text{(Equ. 2.12)}$$

Interferometric instrument configuration

Following the discovery of the interference, this phenomenon was rapidly applied to the development of one of the most well-known instruments in dimensional metrology: the two-beam interferometer. A notable example of such an instrument is the Michelson interferometer (Figure 5), named after the American physicist A. Michelson. The Michelson interferometer quickly became one of the most widely adopted configurations in optical interferometry. Around the same period, other types of interferometers were also developed, including the Fizeau and Arago interferometers. To this day, several of these classical designs remain among the leading choices for high-precision displacement and surface property measurements.

The application of interferometric techniques to areal surface measurement began relatively late. However, advances in illumination systems and digital signal processing throughout the 20th century facilitated the development of modern surface-measuring interference microscopes, such as PSI and WLI. For example, these techniques now integrate high-resolution camera systems for capturing images of interference patterns. The measured images are then processed using advanced computer algorithms that enable accurate phase extraction and 3D surface reconstruction, significantly enhancing both measurement accuracy and efficiency. Owing to their non-contact nature, ease of use, high accuracy, and suitability for automation, modern interference microscopes have become widely adopted in industrial settings and have established an important role in topographical surface measurements [61,62].

https://doi.org/10.7795/110.20260421A

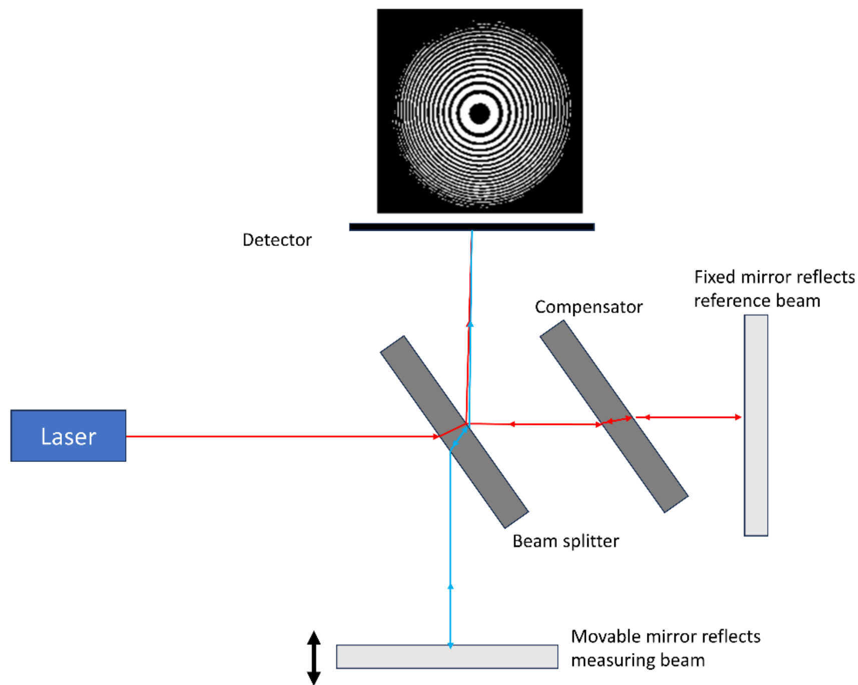

Figure 5 Illustration of the basic principle of a Michelson interferometer. When the movable mirror is vertically displaced, the interference pattern observed at the detector changes accordingly, indicating a variation in phase and optical path length relative to the reference beam. The Moiré patterns visible in the interference image are not actual measurement data but artifacts resulting from a mismatch between the fine interference fringes and the limited resolution of the image. The red and blue colors used to represent the light beams serve only to distinguish the reference and measurement paths (reflected and transmitted beams) after the beam splitter; they do not correspond to the actual color of the light beam.

Both classical interferometers and modern areal surface measurement interferometers require at least two coherent light beams during operation, commonly referred to as the reference beam and the measurement beam. Taking the Michelson interferometer (illustrated in Figure 5) as an example, light emitted from a coherent source (e.g., a laser) is directed into a 50/50 beam splitter, where it is divided into two beams of equal intensity. One of these beams, designated as the reference beam (indicated in red in Figure 5), passes through the beam splitter and is reflected off a stationary reference mirror before reaching the detector. Since the position of the reference mirror remains fixed during measurement, the optical path length of this beam remains constant.

The second beam, referred to as the measurement beam (indicated in blue in Figure 5), is reflected by the beam splitter toward sample (represented in Figure 5 as a movable mirror) and then directed back to the detector. The interference between the reference and measurement beams results in the formation of a fringe pattern consisting of alternating bright and dark fringes. Depending on the mirror alignment, the pattern typically appears as either concentric circles (when the beam is perpendicular to the mirror) or straight fringes (when the mirror slightly tilted). An example of concentric circular fringes recorded by the detector is

https://doi.org/10.7795/110.20260421A

shown in Figure 5. The resulting interference pattern, described by Equ. 2.11, varies with the vertical displacement of the movable mirror due to the corresponding change in phase difference, as given in Equ. 2.12. By analyzing these phase changes, the displacement of the movable mirror can be determined with high precision.

It is also important to note that in the Michelson interferometer, a compensator plate is inserted into the reference arm. Made of the same material and thickness as the beam splitter, this plate compensates for the optical path difference between the reference and measurement beams caused by transmission and reflection at the beam splitter.

Modern areal surface interferometric instruments are based on the same fundamental principles and employ similar optical configurations. In contrast to classical interferometers, they commonly integrate compact and cost-effective light-emitting diode (LED) illumination with suitable coherence properties and complementary metal-oxide semiconductor (CMOS) or charge-coupled device (CCD) cameras for areal image acquisition. To enable high lateral resolution, these systems are typically equipped with objectives of high NA. With respect to the design of the interferometric objective, modern interferometric microscopes are commonly classified into three configurations: Mirau, Michelson, and Linnik, as illustrated in Figure 6a to Figure 6c, respectively.

The defining feature of the Mirau configuration is the use of a specialized Mirau objective, which is typically designed for high magnifications (e.g., 20x to 100x) and short working distances (WDs). As shown in Figure 6a, the Mirau interference objective has a compact coaxial design in which both the beam splitter and the reference mirror are integrated into the objective assembly. The reference mirror is located on the optical axis near the center of the Mirau structure, while the partially reflective beam splitter is positioned between the objective lens and the sample surface. This arrangement is designed such that the optical path lengths of the reference and measurement beams are closely matched when the sample surface is near focus, thereby enabling interference. Neglecting additional phase shifts introduced by reflection and coating effects, the optical path difference approaches zero at focus, and well-defined interference fringes with high contrast can be recorded by the camera.

The Michelson configuration is typically employed with low magnification objectives, such as 2.5x and 5x. Its design (Figure 6b) is relatively simple and closely resembles that of the classical Michelson interferometer, incorporating a 50/50 beam splitter in the interferometric optical path. Unlike the Mirau objective, the Michelson design separates the reference and measurement beams into orthogonal paths while maintaining zero OPD at the focal plane. This arrangement is required because the larger reference surfaces used in low magnification objectives cannot be placed on the same optical axis as the measurement beam without

https://doi.org/10.7795/110.20260421A

causing significant obscuration. Despite this, the Michelson configuration supports longer working distances and offers a wide FOV together with a substantial DOF [63–64].

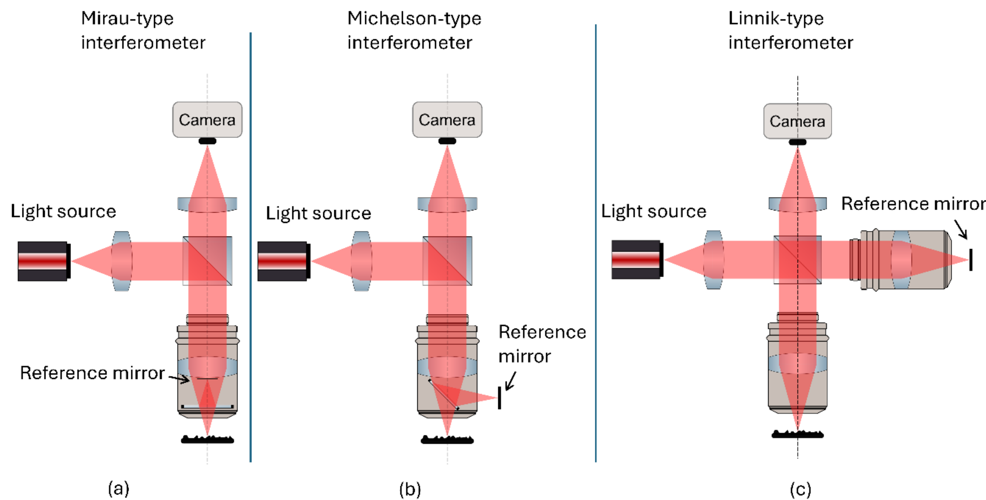

Figure 6 Three types of areal surface interferometric instruments (a) Mirau type (b) Michelson type and (c) Linnik type

The third type is named after its developer V.P. Linnik as Linnik configuration, who shares the most similarity to the Michelson system but is built with two identical microscope objectives in each of the reference and the measurement optical paths respectively [63]. Compared to the other two types, Linnik system has smaller intensity losses as only one beam splitter is used in this setup, and flexible objective choice. However, since the system requires optical setup of reference and measuring path to be identical, complex and precise alignments of the two microscope objectives in each optical path are necessary.

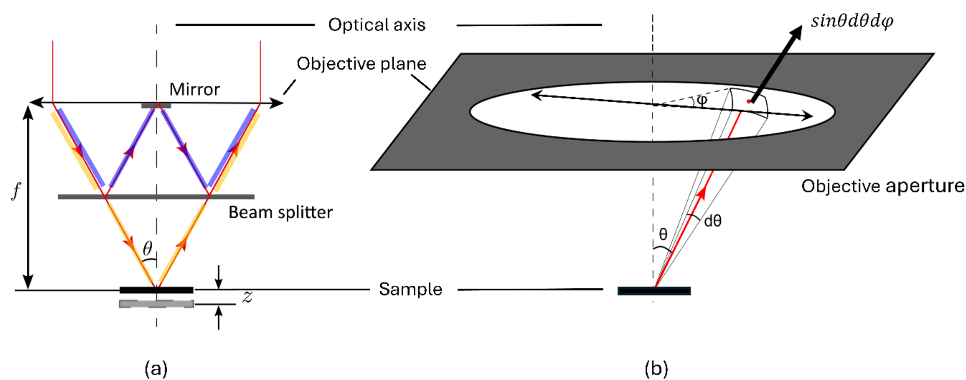

Figure 7 (a) 2D illustration of measurement and reference optical paths (marked in blue and orange respectively) in objective of a Mirau type interferometric instrument. (b) 3D illustration of the objective aperture and the solid-angle element of the aperture cone $sin\theta d\theta d\varphi$ for estimating the total intensity I of the interference over a wide range of incident angle θ.

When a high-NA objective is introduced into the optical path, the interference model cannot be fully described by the model introduced in Equ. 2.11. This is because the incident light no

https://doi.org/10.7795/110.20260421A

longer consists of parallel beams with identical optical paths, but instead forms optical cones, where the optical path length of each sub-beam depends on its incident angle θ. Figure 7 illustrates the optical paths within a Mirau-type configuration as an example. Theoretically, this model is also applicable to the other two configurations.

In a Mirau type configuration, optical paths are identical for all the light beams before being directed onto the beam splitter. These parts are not relevant for the measurement since there is no OPD between the reference and measurement beams. Therefore, only the optical paths contributing to the OPD are illustrated in Figure 7, namely after the reference and measurement beams are separated. As shown in Figure 7a, light beams with incident angle θ are presented by red lines with arrows. For distinguishing the reference light beam and the measurement beam, the corresponding beams are marked with blue and orange color respectively. The objective has a focal length of f. The length L, referred to as the optical path length, which the beam travels from being emitted out of the objective to being collected back into it at an incident angle θ, can be calculated as:

$$L = 2\frac{f}{cos\theta}, \quad \text{(Equ. 2.13)}$$

when the sample is located exactly at the focal plane of the objective.

Similar to the model used to describe interference fringes generated by a plane parallel plate, which is a classic case of thin film interference [60], a vertical displacement of the sample by a distance z leads to a change in the optical path length. The corresponding OPD is given by [60]:

$$OPD = 2n_{air}zcos\theta. \quad \text{(Equ. 2.14)}$$

Where n_{air} denotes the refractive index of air, which is approximately equal to 1. In this case, the intensity of the interference pattern corresponding to a beam with an incident angle θ can be described as:

$$I_\theta = I_r + I_m + 2\sqrt{I_r I_m}\cos(2kzcos\theta). \quad \text{(Equ. 2.15)}$$

When a 50/50 beam splitter is used, $I_r = I_m$. Therefore, Equ. 2.15 can be further simplifed as:

$$I_\theta = 2I_r[1 + \cos(2kzcos\theta)]. \quad \text{(Equ. 2.16)}$$

The total intensity I of the interference pattern can be estimated by integrating the contributions of all incident beams arriving at different angles, which pass through the circular

https://doi.org/10.7795/110.20260421A

aperture of the objective and fall within the acceptance range defined by its NA, as illustrated in Figure 7b [65]:

$$I = 2I_r \int_0^{2\pi} \int_0^{\theta_{max}} [1 + \cos(2kz\cos\theta)] \cdot P(\theta, \xi, \eta) \cdot sin\theta d\theta d\varphi. \qquad \text{(Equ. 2.17)}$$

Here, the $sin\theta d\theta d\varphi$ is the solid-angle element of the aperture cone, as it shown in Figure 7b. And the $P(\theta, \xi, \eta)$ denotes the pupil function, which characterizes how a light is modified as it passes through the aperture of an optical system. A typical circular pupil function can be expressed as:

$$P(\theta, \xi, \eta) = \begin{cases} cos^{n_{apo}}\theta & inside\ of\ the\ circle\ \xi^2 + \eta^2 \leq r^2 \\ 0 & otherwise. \end{cases} \qquad \text{(Equ. 2.18)}$$

Where n_{apo} denotes a factor describing the apodization effect [66].

Phase-shifting interferometry

Phase-shifting interferometry (PSI) is a widely used technique for interpreting interference patterns in areal surface measurement instruments. It enables rapid acquisition of 3D topographical data with high accuracy and repeatability. In particular, for height measurements, both the measurement error and associated uncertainty are typically evaluated to be below 1 nm [61,67]. Owing to these advantages, PSI is well-suited for tasks such as surface roughness measurements.

A model of Mirau-type PSI instrument is illustrated in Figure 8 to clarify its design and working principle. Typically, a PSI instrument comprises the following key components: a monochromatic light source, a vertical scanner, an interference objective, and a camera. During measurement, the vertical scanner introduces a sequence of precisely controlled vertical displacements between the sample and the objective to generate phase shifts. After each phase shift, the resulting interference pattern is captured by the camera. The acquired images, also known as interferograms, are used to reconstruct the 3D surface topography through the application of a PSI algorithm.

In this algorithm, surface topography H at the pixel with lateral coordinates (i, j) is interpreted as a function of the phase difference $\Theta\ (i, j)$:

$$H(i, j) = \frac{\lambda_{eff}}{2} \cdot \frac{\Theta(i, j)}{2\pi}. \qquad \text{(Equ. 2.19)}$$

Here, $\Theta\ (i, j)$ denotes the phase difference $\varphi_1 - \varphi_2$ between reference and measurement beams, and the effective wavelength λ_{eff} describes the distance of two maxima on the

https://doi.org/10.7795/110.20260421A

interference fringe. This parameter can be approximated as the wavelength λ of the light source with low NA objectives.

The primary task of a PSI algorithm is the estimation of the phase difference $\Theta\ (i,j)$, as the other parameters in Equ. 2.19 are either constant or can be calibrated prior to measurement. To evaluate Θ, PSI algorithms are developed based on the optical model introduced in Equ. 2.11. However, the intensity expression in Equ. 2.11 still depends on additional unknowns, such as the intensity values of the reference and measurement beams. To simplify this, I_{bias} is introduced to represent the intensity offset, defined as the sum of the reference and measurement beam intensities. Similarly, I_{mod} denotes the modulation term of the interference fringe and corresponds to $2\sqrt{I_1 I_2}$. With these parameters, the intensity I at pixel (i,j) can be rewritten as:

$$I(i,j)\ = I_{bias} + I_{mod} \cdot \cos[\Theta(i,j)]. \qquad \text{(Equ. 2.20)}$$

To solve an equation such as Equ. 2.20, which contains three unknown parameters, a system of at least three equations involving the same unknowns must be established. This is exactly the principle behind the linear PSI algorithm: by introducing N phase shifts ($N > 3$), multiple intensity values I_n are measured at phase shifts Φ_n, which are equally spaced over a full 2π cycle. Each of these intensity values can then be expressed as:

$$I_n(i,j)\ = I_{bias} + I_{mod} \cdot \cos[\Theta(i,j) + \Phi_n],\ n = 1, 2, 3\ldots N \qquad \text{(Equ. 2.21)}$$

Therefore, the unknown $\Theta(i,j)$ can be determined. By applying a least-squares fitting algorithm [68], and under the conditions: $\sum_{n=1}^{N} sin(\Phi_n) = 0$, $\sum_{n=1}^{N} cos(\Phi_n) = 0$, $\sum_{n=1}^{N} sin(2\Phi_n) = 0$, and $\sum_{n=1}^{N} cos(2\Phi_n) = 0$, $\Theta(i,j)$ can be solved as:

$$\Theta(i,j) = arctan\left\{\frac{-\sum_{n=1}^{N}[I_n(i,j) \cdot \sin(\Phi_n)]}{\sum_{n=1}^{N}[I_n(i,j) \cdot \cos(\Phi_n)]}\right\}. \qquad \text{(Equ. 2.22)}$$

Here, N denotes the total number of phase shifts required by the applied PSI algorithm.

As a representative example, the commonly used four-step linear PSI algorithm is considered [69]. This method uses four discrete phase shifts and requires the acquisition of four interferograms, $I_{1\ldots4}$, for reconstructing the surface topography. These interferograms are recorded at four equidistant phase steps, with phase shifts of $\Phi_{1\ldots4}$=0, $\pi/2$, π, and $3\pi/2$, respectively. The corresponding intensity values $I_{1\ldots4}$ at each phase-shifting step can be expressed as:

$$I_1\ = I_{bias} + I_{mod} \cdot \cos(\Theta), \qquad \text{(Equ. 2.23a)}$$

$$I_2 = I_{bias} + I_{mod} \cdot \cos\left(\Theta + \frac{\pi}{2}\right), \quad \text{(Equ. 2.23b)}$$

$$I_3 = I_{bias} + I_{mod} \cdot \cos(\Theta + \pi), \quad \text{(Equ. 2.23c)}$$

$$I_4 = I_{bias} + I_{mod} \cdot \cos\left(\Theta + \frac{3\pi}{2}\right). \quad \text{(Equ. 2.23d)}$$

According to the Equ. 2.22, the phase difference Θ between reference and measurement beams can be calculated as:

$$\Theta = arctan(\frac{I_4 - I_2}{I_1 - I_3}) \quad \text{(Equ. 2.24)}$$

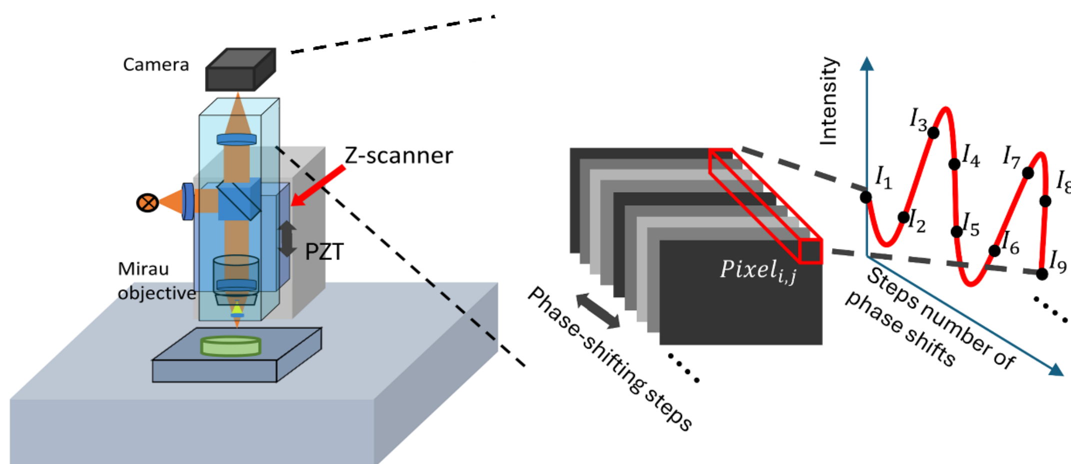

Figure 8 Model and measuring principle of a Mirau type phase-shifting interferometer

However, in practice, mechanical vibrations from the environment, positioning stages, and scanners may introduce inaccuracies in the applied phase shifts, leading to non-negligible measurement errors [70]. To mitigate such errors, linear PSI algorithms have been extended to incorporate additional interferograms into the final 3D topography reconstruction. One approach is to acquire extra M steps of linear phase shifts, resulting in a total of $N + M$ interferograms. These additional phase steps are indexed from $N + 1$ to $N + M$. Under the assumption of sufficiently high temporal coherence, the intensity values at phase steps n and $N + n$ should be identical, as they correspond to the same phase position offset by a full 2π. An example of this vibration-insensitive PSI algorithm is illustrated in Figure 8, where a four-step PSI algorithm ($N = 4$) is extended by five additional steps ($M = 5$). The interferograms I_2 and I_6 correspond to phase positions separated by a full 2π and therefore share the same theoretical intensity. The phase difference Θ obtained using this vibration-insensitive method can be expressed as [71]:

$$\Theta = arctan\left\{\frac{-[\sum_{n=1}^{M} I_n \cdot \sin(\Phi_n) + 2\sum_{n=M+1}^{N} I_n \cdot \sin(\Phi_n) + \sum_{n=N+1}^{N+M} I_n \cdot \sin(\Phi_n)]}{\sum_{n=1}^{M} I_n \cdot \cos(\Phi_n) + 2\sum_{n=M+1}^{N} I_n \cdot \cos(\Phi_n) + \sum_{n=N+1}^{N+M} I_n \cdot \cos(\Phi_n)}\right\} \quad \text{(Equ. 2.25)}$$

https://doi.org/10.7795/110.20260421A

A famous example of this type of PSI algorithm is the Schwider-Hariharan five-step algorithm [72,73]. It is also known as 4+1 step PSI algorithm. Taken the N value as four and M value as one, the corresponded phase shifts are $\Phi_{1...5}$=0, $\pi/2$, π, $3\pi/2$ and 2π. With these values, the Schwider-Hariharan five-step algorithm can be derived from Equ. 2.25 as:

$$\Theta = arctan\left[\frac{2I_4 - 2I_2}{I_1 - 2I_3 + I_5}\right]. \quad \text{(Equ. 2.26)}$$

Indeed, these algorithms are widely applied in PSI instruments, as they have a high performance in suppressing measurement noise and error caused by mechanical vibrations and thermal drifts [72,73].

Even with accurate estimation of the phase differences Θ using the PSI algorithm, a fundamental issue must still be addressed before substituting these values into Equ. 2.19 for topography reconstruction. Specifically, the calculated phase values Θ are inherently limited to the range $-\pi$ to π, due to the use of the arctangent function in Equ. 2.22 and Equ. 2.25, whose output is mathematically constrained within this interval. When measuring surfaces with large height variations, this limitation introduces ambiguity into the results, which can be expressed as an unknown integer multiple of half the effective wavelength, $\lambda_{eff}/2$ [67]. This phenomenon is referred to as the phase wrapping effect, and the process used to correct it is known as phase unwrapping.

Indeed, the development of phase unwrapping methods remains a critical topic in the field of surface topography measurement. Although a comprehensive review of these methods is beyond the scope of this dissertation, selected algorithms, such as Itoh's method for 1D data and quality-guided path-following techniques for 2D phase maps, have been developed to address the challenges associated with phase wrapping [74]. These algorithms are employed in this dissertation to effectively resolve the phase wrapping problem.

White-light interferometry

WLI is also a widely used technique in surface topography measurement, offering high vertical resolution. Similar to the configuration of the previously discussed PSI instruments (Figure 8), WLI systems share many of the same optical and mechanical components (Figure 9b), with the primary distinction being the type of light source employed. While PSI relies on a monochromatic light source, WLI utilizes a broadband white-light source with a short coherence length. The resulting interference signal is formed by the superposition of numerous spectral components with different wavelengths and amplitudes.

https://doi.org/10.7795/110.20260421A

Figure 9a provides a simplified illustration of this principle using three representative wavelength components, shown in red, green, and blue as λ_1 , λ_2 and λ_3, respectively. In a real white-light interferometer, however, the interference signal is generated by a much broader spectrum. Owing to this broadband nature, the interference envelope is confined to a narrow region along the z-axis, typically on the order of a few micrometers, as schematically indicated at the bottom of Figure 9a.

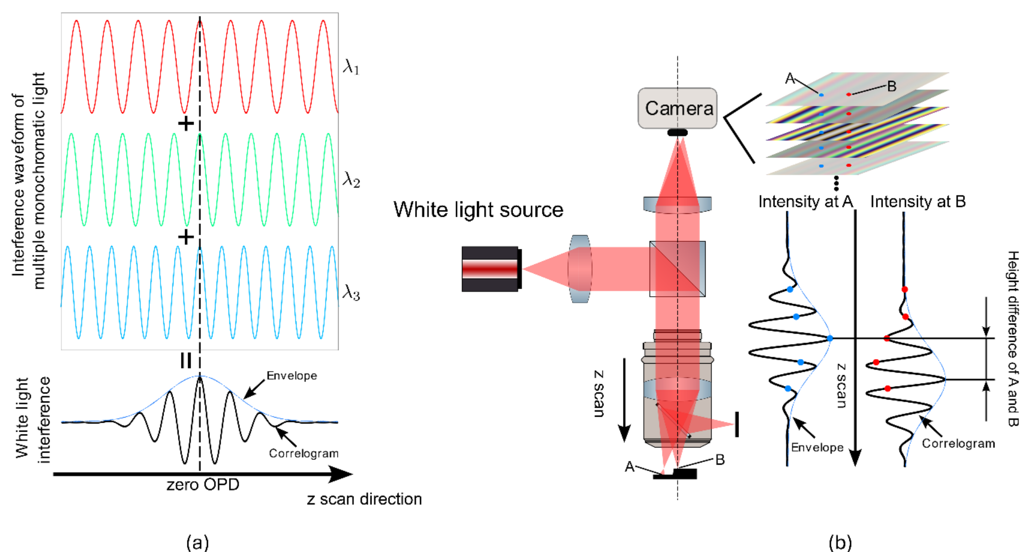

Figure 9 (a) Schematic illustration of the interference of light beams with different wavelengths in a WLI instrument. The resulting interference signal, referred to as a correlogram, reaches its maximum amplitude at zero OPD and exhibits a much shorter coherence length than in PSI. Consequently, the interference envelope is strongly localized and decreases rapidly along the vertical axis. (b) Measurement setup and principle of a WLI instrument, illustrated by a topography measurement of a sample with two different height levels, represented by points A and B.

From the WLI signal, it can be observed that the intensity curve reaches its maximum only at the zero-order fringe. This fringe corresponds to the vertical position where zero OPD occurs, meaning that at this vertical position the reference and measurement beams have identical length of optical paths. As the OPD increases, the phase differences between the various wavelength components grow, leading to partially coherent interference and eventually to complete incoherence.

To describe this behavior, the interference signal I at a single pixel can be expressed in a one-dimensional form along the scanning direction. In this representation, the interference term is modulated by an envelope function C , which depends on the optical path difference represented by $z - 2H$ [75]:

$$I(z) = I_{bias} + I_{mod} \cdot C(z - 2H) \cdot \cos(2\pi v_z z - \alpha) \qquad \text{(Equ. 2.27)}$$

https://doi.org/10.7795/110.20260421A

Such an axial intensity signal along the vertical scanning direction is also referred to as a correlogram in WLI measurements. To simplify the calculation, the form of the envelope function C is usually described by a Gaussian function or a cosine-shaped function [62,75]. The parameter v_z denotes the spatial frequency of the interference pattern and is related to the mean wavelength of the white-light source. The α denotes the phase change of reflection due to the complex reflectance of the surface.

WLI measurement algorithms primarily determine the vertical position corresponding to the maximum of the interference envelope. An example of such an interference envelope is shown in Figure 9b. During measurement, a z-scanner with a travel range of up to several tens of micrometers generates relative motion along the vertical axis between the sample surface and the objective, thereby introducing an OPD between the reference and measurement beams. The resulting correlogram at each pixel is recorded by the camera and subsequently used for surface topography reconstruction. The vertical coordinate at pixel (i, j) is then determined by locating the z-position at which the envelope reaches its maximum. Compared with PSI, the basic principle of WLI does not require explicit phase evaluation during topography reconstruction and therefore avoids ambiguity in the measured height values. However, conventional WLI algorithms face two primary limitations:

(I) A greater number of interferograms are required to accurately detect the peak positions in correlograms, as opposed to PSI, which typically results in longer measurement times,

(II) The technique is sensitive to various error sources, including optical aberrations, environmental vibrations, and measurement noise.

To address these issues, a modern algorithm known as white-light phase-shifting interferometry (WLPSI) [75] has been developed. This method combines two techniques in a single topographical measurement: envelope peak detection for coarse localization of the zero OPD position, and phase detection for fine measurement of the surface topography.

To reduce measurement time, WLPSI avoids continuous acquisition of interferograms along vertical axis. Instead, a correlogram (illustrated in red in Figure 10) is sampled in n discrete steps, each separated by a constant phase shift Φ. As an example, Larkin proposed a WLPSI algorithm [75], in which the phase shift Φ between two successive interferograms is $\pi/2$ (Figure 10 marked with circles). In this approach, the envelope function is represented by discrete modulation points Mod_i (Figure 10 marked with triangles). The modulation value Mod_n at n-th phase-shifting step is estimated using the five nearest captured interferograms, from I_{n-2} to I_{n+2}:

$$Mod_n = \frac{1}{4}\sqrt{4(I_{n-1} - I_{n+1})^2 + (-I_{n-2} + 2I_n - I_{n+2})^2} \quad \text{(Equ. 2.28)}$$

By doing so, the topography measured by WLPSI consists of two components, H' and H'':

$$H = H' + H'' \quad \text{(Equ. 2.29)}$$

The component H' corresponds to the vertical position of Mod_{max}, the maximum of the discrete modulation points estimated using Equ. 2.28. It is defined as the product of an integer N_{WLPSI} and the phase shift Φ:

$$H' = z(Mod_{max}) = N_{WLPSI} \cdot \Phi \cdot \frac{\lambda_{eff}}{2} \cdot \frac{1}{2\pi} \quad \text{(Equ. 2.30)}$$

Here, N_{WLPSI} is determined by step number n, at which step the maximum modulation value is observed.

The second component, H'', represents the phase-related topography, obtained through the application of the 4+1 PSI technique as described in Equ. 2.26:

$$H'' = \frac{\lambda_{eff}}{2} \cdot \frac{\Theta}{2\pi} \quad \text{(Equ. 2.31)}$$

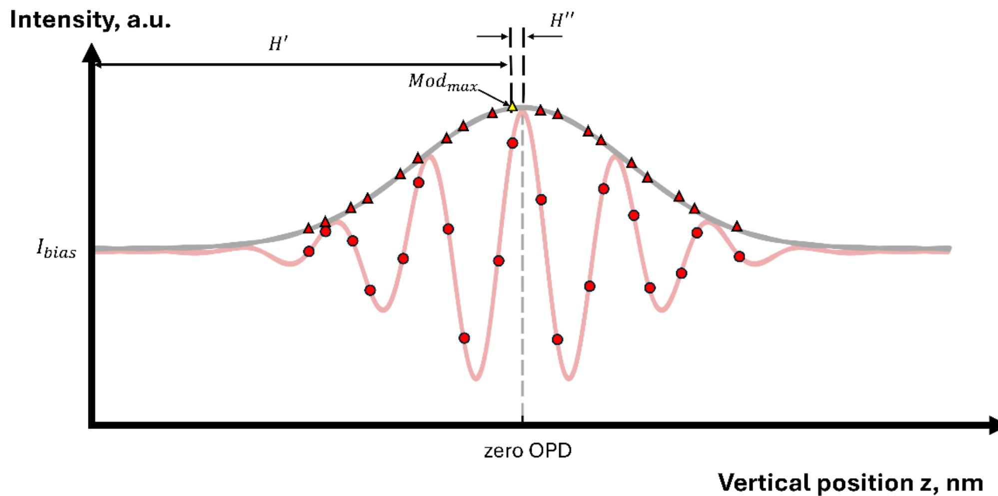

Figure 10 The measuring principle of white-light phase-shifting 4+1 algorithm (WLPSI), for finding the corresponding height to the zero OPD, the height is determined as two components: (I) the modulation maximum Mod_{max} corresponded height H' (II) 4+1 PSI algorithm determined phase corresponded height H''.

2.2.4. Non-interferometrical optical measurement principles

Optical areal surface measuring instruments can also be developed based on non-interferometric principles, such as confocal microscopy (CFM) and focus variation

https://doi.org/10.7795/110.20260421A

microscopy (FVM). Unlike interferometric methods, which rely on the analysis of interference signals, these techniques determine surface topography by evaluating intensity variations within a defined vertical scanning range. Compared with IM, instruments based on CFM and FVM typically employ objectives with high NA, which provide enhanced lateral resolution and improved capability for measuring structures with steep local slopes and sharp edges. The operating principles of CFM and FVM are briefly introduced in the following sections.

Confocal microscopy

CFM is a widely adopted imaging technique with broad applications across various research fields, including biology, chemistry, and materials science. Its ability to meet diverse research requirements has driven the development of numerous instrument types based on its fundamental principles. In dimensional metrology, such instruments are commonly referred to as confocal imaging microscopes and include various configurations such as disc-scanning, microdisplay-scanning, and laser-scanning confocal microscopes [30,76–78].

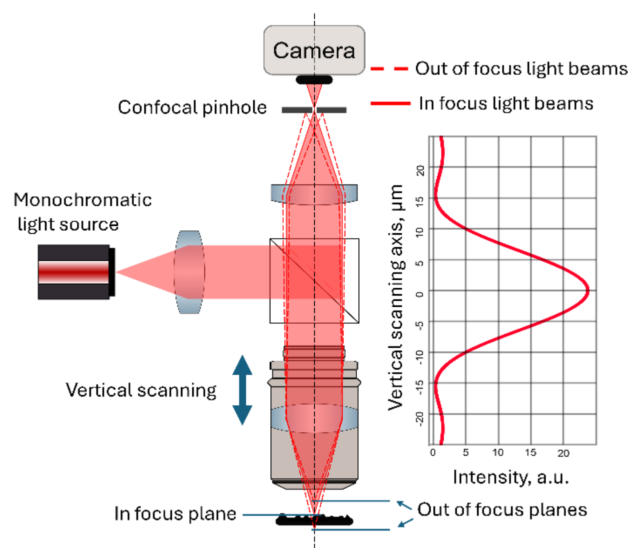

Figure 11 Measuring principle of a confocal microscope and its typical axial response (red curve) during vertical scanning

From an instrumentation perspective, implementing the fundamental principles of a CFM is relatively straightforward. Unlike IM, the design of a CFM does not require an additional reference beam, which facilitates the integration of objectives with high magnification and high NA. A classical CFM is typically built upon a basic reflectance microscope system, as illustrated in Figure 11. It incorporates two essential components: (I) a confocal pinhole, also referred to as the detection pinhole, and (II) a vertical scanning system. The pinhole is positioned in front of the detector at the optical conjugate plane of the focal plane. It spatially filters the light by blocking out-of-focus light beams (shown as dashed lines in Figure 11), allowing only in-focus light beams (solid lines) to reach the detector. In some advanced designs

of CFM, a second pinhole, called the illumination pinhole, can be also placed after the light source to restrict the illumination to a narrow axial region. Together, the illumination and detection pinholes improve signal quality and enhance measurement performance. The vertical scanning system is used to precisely control the relative movement between the objective and the sample along the optical axis. This enables layer-by-layer acquisition within DOF, allowing for 3D reconstruction of the surface topography.

During a confocal measurement, as the scanning system moves the sample (or objective) along the vertical axis, structures located within the focal plane appear bright, while out-of-focus regions are effectively suppressed by the detection pinhole. For each pixel (i, j) , the detector records an intensity curve (illustrated in red curve in the diagram of Figure 11), which reflects the intensity variation as a function of the scan position. By identifying the vertical position corresponding to the peak of this intensity curve, the surface topography can be precisely reconstructed. These intensity curves are commonly referred to as the axial response in the literature [30,79,80]. To ensure high accuracy in locating such peak position, fitting algorithms (e.g. paraboloid fitting) are frequently employed to analyze the discretely sampled intensity data.

Focus variation microscopy

FVM is a relatively recent advancement in areal surface metrology. Like the previously discussed CFM technique, FVM acquires topographical data through vertical scanning, taking advantage of the limited DOF of the optical system. The overall instrument setup of FVM closely resembles that of CFM, with the key distinction being its optical configuration: FVM does not require additional apertures such as confocal pinholes. However, to enhance measurement performance, particularly when measuring highly reflective surfaces or structures with steep flank angles, some FVM systems may incorporate components such as polarizers, analyzers, and ring lighting [81].

The fundamental principle of FVM is to use the vertical position of the focal plane as a reference for reconstructing surface topography. In this regard, FVM is conceptually similar to CFM. However, unlike CFM, which relies on detecting the maximum signal intensity to determine the focus position, FVM evaluates the degree of focus to identify the best-focused plane. During an FVM measurement, light reflected from the sample is imaged onto the detector with varying levels of sharpness. A vertical scanner moves the objective relative to the sample across a defined range, starting from a front-defocus plane, passing through the focal plane, and ending at a rear-defocus position. As the scan progresses, the degree of focus varies from low to high and then decreases. This variation can be described as a function of vertical scan position. By determining the vertical position where the degree of focus reaches

https://doi.org/10.7795/110.20260421A

its maximum, the surface height at the corresponding lateral coordinate (i, j) can be accurately determined.

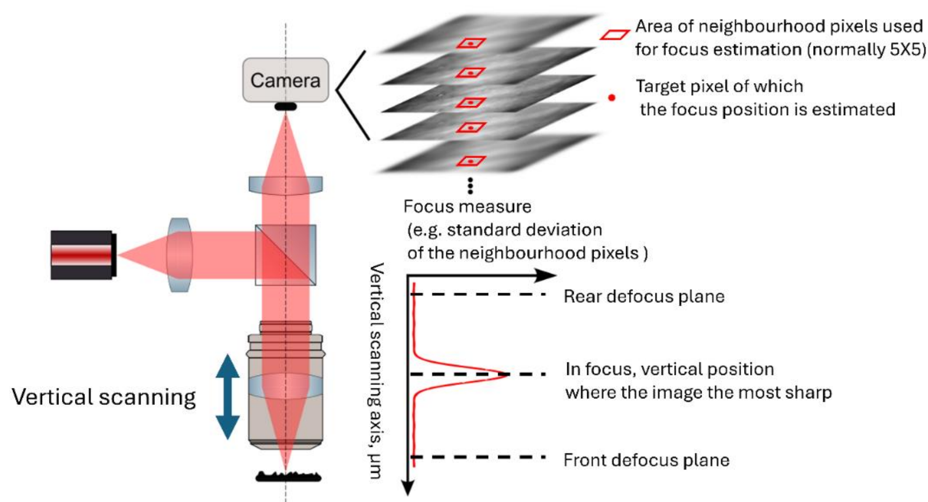

Figure 12 Measuring principle of a focus variation microscope and its typical axial response (red curve) during vertical scanning.

A commonly used algorithm [81] for evaluating the degree of focus at a target pixel involves calculating the standard deviation (STD) of intensities within a small neighborhood surrounding that pixel. An example of this algorithm is illustrated in Figure 12. The target pixel is indicated by a red point, and a square region of 5 x 5 pixels used for STD evaluation is outlined by a red parallelogram. At vertical positions corresponding to front and rear defocus, the intensity values within this range tend to be nearly uniform, resulting in a low degree of focus and a correspondingly low STD. As the sample approaches the focal plane, surface structures become increasingly distinguishable in the image, causing greater intensity variation and a corresponding increase in the STD value. As a result, the STD curve, expressed as a function of vertical scan position, serves as an effective quantity for quantifying the degree of focus and provides a reliable signal for 3D surface reconstruction.

2.2.5. Current hybrid measuring technology

In recent years, surface geometries encountered in industrial and scientific applications have become increasingly complex. Consequently, reliance on a single measurement principle is often inadequate for acquiring complete and reliable topographical data, since no single method is capable of meeting all measurement requirements simultaneously. In response to these limitations, hybrid surface measuring instruments have been developed, which integrate multiple measurement principles within a single instrumental framework. These hybrid instruments are designed to leverage the respective advantages and compensate for the

inherent shortcomings of individual measurement techniques. Notable examples of such instruments include the NX-Hybrid WLI from Park Systems, the multi-sensor measuring system (MSMS) from the University of Kassel, and the S-neox system by Sensofar [82–84].

A widely adopted design strategy for hybrid instruments involves expanding the instrument with additional measurement modules to facilitate the application of diverse measurement principles to a single sample. Representative implementations of this design include the NX-Hybrid WLI and MSMS (Figure 13b). In such instruments, the measurement modules are mounted onto a shared metrology bridge, while the sample is placed on a high-precision motorized stage with an extended travel range. This configuration permits sequential positioning of the sample beneath each module, thereby enabling comprehensive and multi-modal areal surface measurements. The measurement process follows a workflow analogous to an industrial pipeline. In such systems, the automated modules operate independently and sequentially as the sample is transferred from one module to another. For example, NX-Hybrid WLI enables fully automated measurements of wafers with diameters of up to 300 mm while maintaining high measurement speed and accuracy [84]. However, such hybrid instruments require substantial space, as each measurement module operates independently. This results in a relatively low level of integration between modules within the system.

Moreover, the lack of a unified coordinate system among the measurement modules introduces additional limitations. Since each module possesses its own measurement range, it is challenging to align these ranges to be fully matched. Even when nominal alignment is achieved, spatial discrepancies can arise as the sample transitions between modules, leading to partially non-overlapping measurement areas. An illustrative example of this limitation is presented in Figure 13d. Measurable ranges between module 1 (denoted by the red hatched region) and module 2 (denoted by the black hatched region) are not fully aligned, resulting in a significantly reduced overlapping area accessible to both measurement modules.

To address this problem, another design of the hybrid instrument focuses itself on a high-level synergetic approach. As an example, the S-neox instrument [83] is shown in Figure 13a. In this design, various optical techniques, such as CFM, PSI, WLI and FVM, are integrated into a single instrument. These techniques share most of the critical hardware components, including scanning stages, illumination optics, correction lenses, and a detection camera. Through this approach, the instrument achieves enhanced operational efficiency and a high degree of synergy. At the same time, the use of shared components reduces equipment redundancy and lowers overall instrumentation costs.

With a design concept of this kind, samples are no longer required to travel between measurement modules for module switching. During measurements, the sample can be

https://doi.org/10.7795/110.20260421A

analyzed using various techniques without repositioning, ensuring consistent measurable ranges across different modules, as illustrated in Figure 13c. Module switching is achieved through a mechanical or motorized revolver that selects the corresponding objective, while the appropriate illumination source is activated for the selected measurement module.

Measurements conducted across different optical modules can achieve excellent height resolution, typically within the sub-nanometer range. They are also capable of measuring sample surfaces over relatively large areas. A key limitation of this hybrid configuration is that all integrated measurement modules are based on optical principles, and thus the lateral resolution is fundamentally restricted by the diffraction limit of optical systems.

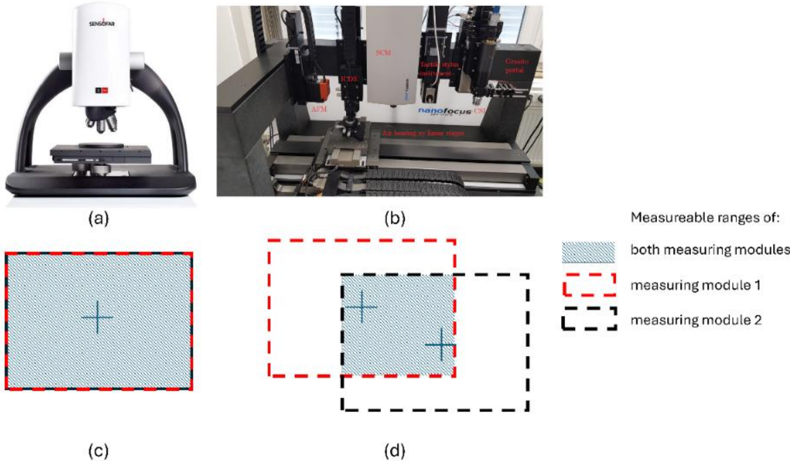

Figure 13 Comparison of the different designs of hybrid instruments (a) high synergy design with example instrument: S-neox 3D optical profiler from Sensofar [83] (b) low synergy design with example instrument: multi-sensor measuring system from university of Kassel [84] (c) measurable ranges of two of measuring modules in high synergy design (d) measurable ranges of two of measuring modules in low synergy design

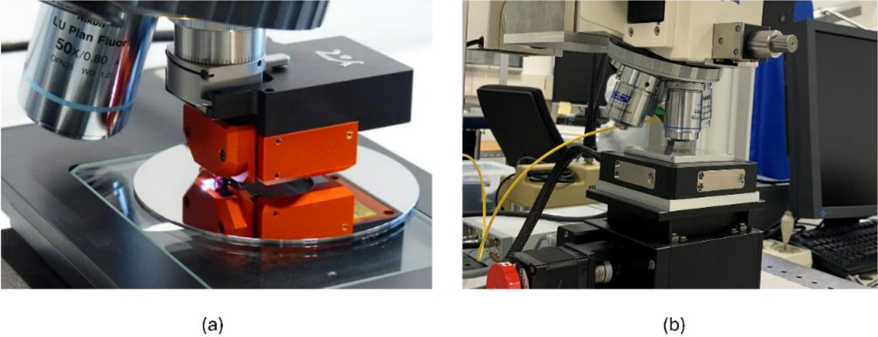

Figure 14 Modules that enables AFM measurements using an optical metrological frame (a) LensAFM from Nanosurf [85] and (b) UltraObjective (the "objective" linked with yellow cable) from SIS [86]

The LensAFM from Nanosurf (Figure 14a) and UltraObjective from SIS (Figure 14b) [85,86] address the challenge by designing the AFM module to be extremely compact, approximately the size of a standard optical objective. These modules can be integrated into optical metrological systems, allowing high-resolution AFM measurements to be performed at nearly the same position where the optical measurement has been conducted. However, both modules do not achieve a truly synergistic hybrid design, as each contains a complete and independent AFM setup, including a laser source, a readout system, and control electronics. Indeed, to the best of our knowledge, no commercially available hybrid instrument currently combines optical and alternative measurement principles, such as AFM, in a manner that achieves both high resolution and a high level of synergy.

https://doi.org/10.7795/110.20260421A

3. Topography fidelity

Over the past decade, industries such as advanced manufacturing, optics, and semiconductors have increasingly demanded highly accurate measurements of complex surface topographies with progressively smaller features. Optical instruments are often preferred for these tasks due to their rapid measurement speed and high vertical resolution. However, the topography fidelity of such instruments is not always satisfactory. According to ISO 25178-600:2017 [5], topography fidelity refers to the degree of agreement between a measured surface and its corresponding reference. Within this concept, a broad range of measurement errors is considered, all of which may affect the accuracy of surface topography measurements. These errors may originate from the applied optical principle or evaluation algorithm, from the sample and its surface characteristics, or from the instrument itself. They cannot be fully compensated for by calibrating the other metrological characteristics defined in the ISO standard [88].

One of the primary reasons for the limited topography fidelity of optical measurements is the complex interaction between the optical probe and the sample surface when challenging surface features are measured. Features such as deep grooves, steep edges, and diffusely reflecting regions can give rise to optical effects such as multiple reflections and scattering, which may distort the detected signal and thereby degrade the accuracy of the reconstructed surface topography. As a result, the reconstructed measurement data may contain various errors and artifacts, including outliers, missing data points, and incorrectly reconstructed features, such as the so-called batwing artifacts commonly observed in WLI measurements.

Generally, three main challenges must be considered when addressing the issue of topography fidelity in optical measurements. These include: (I) classical geometrical factors, such as magnification, linearity, squareness, flatness, and noise [87,88]; (II) the complex interaction between optical probe (light) and surface structures [12]; and (III) the bandwidth characteristics of the optical instrument [89].

There are various approaches to improving the topography fidelity of optical measurements by addressing the challenges mentioned above. These include: (I) the classical method of using physical standards to calibrate the optical instrument, followed by correction based on reference values [12,88,90,91]; (II) theoretical approaches that aim to reconstruct surface topography by simulating the interaction between the surface structure and the optical probe [9–11]; and (III) both theoretical and experimental methods for characterizing the bandwidth characteristics of an optical system in terms of its ITF and applying this knowledge to correct measurement results [12,92,93,119].

In this chapter, the factors related to optical instruments that contribute to limited topography fidelity will first be introduced, followed by a discussion of current approaches for improving topography fidelity. Finally, the potential for enhancing topography fidelity in the context of reference metrology will be discussed, with a focus on the capabilities of the developed HM. It is worth noting that, for the sake of clarity, the topography fidelity issue in this work is examined using PSI measurement examples, with the expectation that the findings will also be applicable to other types of optical measurements, especially to the WLI measurements.

3.1. State of the art issues in interferometric areal surface measuring microscope

Modern optical instruments that apply IM measurement principles, such as PSI and WLI, achieve excellent height resolution at high measuring speeds, without causing damage to the sample. However, several limitations remain that significantly impact the topography fidelity of such instruments. These include restricted lateral resolution, global measurement errors, and local measurement errors. The global errors can be further classified according to spatial frequency, such as form errors occurring at low spatial frequencies and measurement noise at high spatial frequencies. Local errors include artifacts such as outliers, overshooting signals, and missing data points [3,70,94,95].

Lateral resolution limitation

In optical surface metrology, lateral resolution refers to the ability of an optical instrument to distinguish two closely spaced objects as distinct features. This resolution is fundamentally constrained by the diffraction of light. As light propagates through a finite aperture, which is typically circular in shape and mathematically described by a pupil function, it cannot be perfectly focused to a single point. Instead, it produces a characteristic diffraction pattern known as an Airy disk, which represents the best achievable focus in an aberration-free system. When the system operates under coherent illumination, its response to a point source is described by the ideal amplitude point spread function (ASF) [96-99]:

$$ASF(x,y) = \frac{A_I}{\lambda z_i} \iint_{-\infty}^{\infty} P(\xi,\eta) \cdot e^{-j\frac{2\pi}{\lambda z_i}(x\xi + y\eta)} d\xi d\eta. \quad \text{(Equ. 3.1)}$$

Here, A_I is an intensity amplitude; z_i denotes the distance of the objective aperture (pupil plane) to the image plane. Normally, the pupil shape S_p is defined by the circ-function with radius r as:

https://doi.org/10.7795/110.20260421A

$$S_p = \mathrm{circ}\left(\frac{\sqrt{\xi^2+\eta^2}}{r}\right), \tag{Equ. 3.2}$$

and the corresponding pupil function $P(\xi,\eta)$ is given by:

$$P(\xi,\eta) = \begin{cases} 1, & inside\ S_p \\ 0, & otherwise \end{cases}. \tag{Equ. 3.3}$$

Therefore, by considering the circular shape of the objective aperture, Equ. 3.1 can be further simplified as [97]:

$$ASF(x,y) = \frac{A_I{}'}{\lambda z_i}\frac{J_1(2\pi\frac{r}{\lambda z_i}\sqrt{x^2+y^2})}{\sqrt{x^2+y^2}}. \tag{Equ. 3.4}$$

Here J_1 denotes the first-order Bessel function and $A_I{}'$ represents a constant intensity amplitude.

The response of the system when operating under incoherent illumination is then described as [97]:

$$PSF(x,y) = \left|\frac{A\prime}{\lambda z_i}\frac{J_1(2\pi\frac{r}{\lambda z_i}\sqrt{x^2+y^2})}{\sqrt{x^2+y^2}}\right|^2. \tag{Equ. 3.5}$$

This equation is known as the point spread function (PSF) and indicates the intensity distribution in the image plane. Since both functions (Equ. 3.4 and Equ.3.5) include a term involving the first-order Bessel function J_1 , and this function reaches its first zero at approximately 3.83, therefore the ASF and PSF will also reach their first null when the following condition is satisfied:

$$2\pi\frac{r}{\lambda z_i}\sqrt{x^2+y^2} = 3.83. \tag{Equ. 3.6}$$

By substituting $\sqrt{x^2+y^2}$ with variable d, which denotes the distance between two structures in the image plane and rewriting $\frac{r}{z_i}$ as $tan\ \theta$, Equ. 3.6 can be further simplified. Using the small-angle approximation, $tan\ \theta \approx sin\theta$, together with the definition of the numerical aperture $NA = sin\ \theta \cdot n_r,$ where $n_r \approx 1$ for air, Equ. 3.6 becomes:

$$d = 0.61\frac{\lambda}{NA}. \tag{Equ. 3.7}$$

Equ. 3.7 is also known as the Rayleigh criterion, one of the most widely accepted definitions in microscopy for determining the lateral resolution limit imposed by diffraction. For example, consider an optical instrument equipped with a monochromatic light source of wavelength

https://doi.org/10.7795/110.20260421A

λ =530 nm and objective with NA as 0.4. Based on these parameters, the resulting diffraction-limited lateral resolution is approximately 808 nm. This means that two laterally separated structures can only be resolved by this instrument if the distance between them exceeds 808 nm.

Other criteria such as total resolution:

$$d_t = 1.22\frac{\lambda}{NA}; \quad \text{(Equ. 3.8)}$$

Abbe resolution/limit:

$$d_a = 0.5\frac{\lambda}{NA}; \quad \text{(Equ. 3.9)}$$

and Sparrow resolution:

$$d_t = 0.47\frac{\lambda}{NA}, \quad \text{(Equ. 3.10)}$$

are also adopted in different areas (e.g. astronomy) for describing the resolve ability of an optical measuring instrument.

Vertical positioning error

In measurements using interferometric areal surface measuring instruments, it has been observed that random positioning errors of the vertical scanner, which is typically used for phase shifting, introduce a random form error related to the surface topography in the measured data [70,72,100,101]. Consequently, the topography fidelity of the optical measurement is affected.

To demonstrate such errors, a typical PSI measurement using the four-step PSI algorithm (Equ. 2.23 and Equ.2.24) is taken as an example. It is assumed that random vertical positioning errors during each phase shift introduce phase errors, denoted as $\varepsilon_{1\ldots4}$. According to Equ. 2.23, the four interferograms $I'_{1\ldots4}$, measured in the presence of phase shift errors $\varepsilon_{1\ldots4}$ can be mathematically described as:

$$I'_1 = I_{bias} + I_{mod} \cdot \cos(\Theta + \varepsilon_1), \quad \text{(Equ. 3.11a)}$$

$$I'_2 = I_{bias} + I_{mod} \cdot \cos(\Theta + \frac{\pi}{2} + \varepsilon_2) \cdot \quad \text{(Equ. 3.11b)}$$

$$I'_3 = I_{bias} + I_{mod} \cdot \cos(\Theta + \pi + \varepsilon_3) \quad \text{(Equ. 3.11c)}$$

$$I'_4 = I_{bias} + I_{mod} \cdot \cos(\Theta + \frac{3\pi}{2} + \varepsilon_4) \cdot \quad \text{(Equ. 3.11d)}$$

https://doi.org/10.7795/110.20260421A

By substituting $I'_{1\ldots4}$ into Equ. 2.24, the measured topography can be finally expressed as:

$$H' = \frac{\lambda_{eff}}{4\pi} \cdot \arctan\left[\frac{\sin(\Theta+\varepsilon_4)+\sin(\Theta+\varepsilon_2)}{\cos(\Theta+\varepsilon_1)+\cos(\Theta+\varepsilon_3)}\right] \qquad \text{(Equ. 3.12)}$$

If we denote the Equ. 3.12 as a function P:

$$\mathrm{P}(\Theta, \varepsilon_1, \varepsilon_2, \varepsilon_3, \varepsilon_4) = \frac{\lambda_{eff}}{4\pi} \cdot \arctan\left[\frac{\sin(\Theta+\varepsilon_4)+\sin(\Theta+\varepsilon_2)}{\cos(\Theta+\varepsilon_1)+\cos(\Theta+\varepsilon_3)}\right], \qquad \text{(Equ. 3.13)}$$

then the error free topography H can be represented as:

$$H = \mathrm{P}(\Theta, 0, 0, 0, 0). \qquad \text{(Equ. 3.14)}$$

In the presence of $\varepsilon_{1\ldots4}$, the measured topography H' will deviate from the error-free topography H. The measurement error ε_H can be expressed as the difference between these two topographies:

$$\varepsilon_H = H' - H = \mathrm{P}(\Theta, \varepsilon_1, \varepsilon_2, \varepsilon_3, \varepsilon_4) - \mathrm{P}(\Theta, 0, 0, 0, 0). \qquad \text{(Equ. 3.15)}$$

Since the value of $\varepsilon_{1\ldots4}$ are very small, Equ. 3.15 can be further approximated using Equation E.1 from the “Guide to the Expression of Uncertainty in Measurement” (GUM) [102], as follows:

$$\varepsilon_H \approx \sum_{n=1}^{4} \frac{\partial \mathrm{P}}{\partial \varepsilon_n} \cdot \varepsilon_n, \qquad \text{(Equ. 3.16)}$$

where, $\frac{\partial \mathrm{P}}{\partial \varepsilon_n}$, n =1…4 are sensitivity coefficients. They can be calculated as:

$$\frac{\partial \mathrm{P}}{\partial \varepsilon_1} = \frac{\partial \mathrm{P}}{\partial \varepsilon_3} = \frac{\lambda}{4\pi} \cdot \frac{sin^2\Theta}{2}, \qquad \text{(Equ. 3.17a)}$$

and

$$\frac{\partial \mathrm{P}}{\partial \varepsilon_2} = \frac{\partial \mathrm{P}}{\partial \varepsilon_4} = \frac{\lambda}{4\pi} \cdot \frac{cos^2\Theta}{2}. \qquad \text{(Equ. 3.17b)}$$

respectively.

Substituting the value of each sensitivity coefficient into Equ. 3.16:

$$\varepsilon_H = \frac{\lambda}{16\pi} \cdot (A' \cdot cos2\Theta + O') \qquad \text{(Equ. 3.18)}$$

where,

$$A' = \sum_{n=1}^{4} (-1)^n \varepsilon_n \qquad \text{(Equ. 3.19a)}$$

and

$$O' = \sum_{n=1}^{4} \varepsilon_n. \quad \text{(Equ. 3.19b)}$$

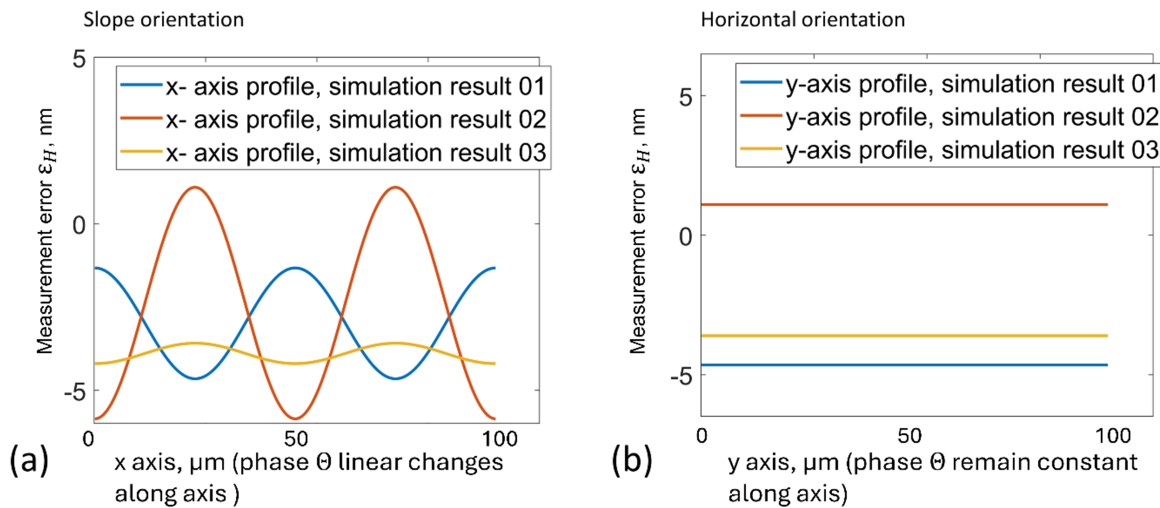

Figure 15 Profiles of simulated measurement error ε_H along (a) slope orientation (x-axis) and (b) horizontal orientation (y-axis, orthogonal to the slope orientation). Random phase-shifting errors ε_i are simulated as a gaussian distributed parameter with 1σ = 5°.

Equ. 3.18 indicates that the measurement error ε_H has two components: a topography-dependent term, $A' \cdot cos2\Theta$, and a topography-independent offset component O'. The term $A' \cdot cos2\Theta$ is referred to as a topography-dependent term, because it is a function of Θ. According to Equ. 2.19, Θ is directly related to the surface topography H. Therefore, any variation in the topography leads to corresponding changes in the error pattern, making this component inherently dependent on the measured surface.

Among these two components, the topography-dependent component is generally recognized as a random form error, which arises from the introduction of topography-related distortions due to phase-shifting errors. The random nature of this error originates from the variability of the coefficient A'. However, the shape of the error remains consistent across measurements, as its spatial frequency is defined by 2Θ. Therefore, as long as the range of Θ remains unchanged, repeated measurements will exhibit error waveforms with the same spatial pattern. The amplitude and offset of these errors will vary due to the random nature of A' and O', respectively.

To visualize the theoretical conclusion discussed above, simulated measurements are carried out. A set of three repeated measurements is performed over a flat sample with an area of 100 μm x 100 μm, which is intentionally mounted as a sloped surface (Figure 16b). The phase errors are intentionally introduced with 1σ = 5° for each random phase-shifting error ε_i . The surface is perfectly aligned along the y-axis (horizontal direction) and tilted by 0.57° along the

https://doi.org/10.7795/110.20260421A

x-axis (slope direction), meaning that the surface height and the corresponding Θ vary linearly along the x-axis, while remain constant along the y-axis. The simulation result of the measurement errors ε_H along both x- and y-axis are presented in Figure 15a and Figure 15b, respectively. These simulation results are consistent with the theoretical conclusion described earlier.

Effective wavelength issue

For measurements involving interference patterns, fringe spacing [103] is used as a fundamental unit of dimensional evaluation. Fringe spacing refers to the distance between two adjacent bright or dark fringes in an interference pattern, where the phase difference between these points is exactly 2π. This indicates that the OPD between the two points is equal to one full wavelength λ of the applied light source. In other words, the corresponding height difference between those points is $\frac{\lambda}{2}$ for a single return path interferometer configuration (see Figure 16a).

Generally, λ refers to the wavelength of a monochromatic light. If the light is not ideally monochromatic, the centroid wavelength λ_c will be used. Based on the power spectral density $p(\lambda)$ of the light source, the centroid wavelength λ_c can be evaluated as:

$$\lambda_c = \frac{1}{P_t} \int p(\lambda) \lambda d\lambda, \qquad \text{(Equ. 3.20)}$$

with P_t the total power of the light source:

$$P_t = \int p(\lambda) d\lambda \qquad \text{(Equ. 3.21)}$$

However, investigations [65,103-107] have shown that in systems using high-NA objectives, such as PSI instruments, the fringe spacing is not exactly equal to $\frac{\lambda}{2}$, as traditionally assumed. This deviation arises because high-NA objectives capture rays with large incident angles θ, which affect the optical path difference. As a result, if fringe spacing is incorrectly treated as $\frac{\lambda}{2}$, a systematic linear error will be introduced into the measured topography. To account for this, a correction factor f_{NA} must be applied to the wavelength λ in order to accurately estimate the fringe spacing. The product of f_{NA} and λ is referred to as the effective wavelength, denoted as λ_{eff}:

$$\lambda_{eff} = f_{NA} \cdot \lambda. \qquad \text{(Equ. 3.22)}$$

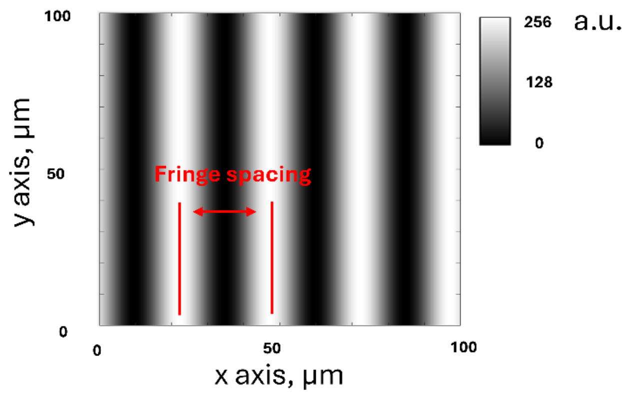

(a) Interference fringe observed in camera

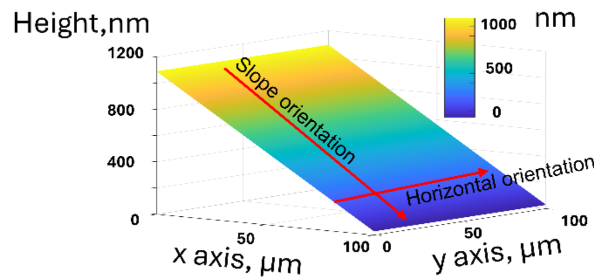

(b) An inclined flat surface

Figure 16 (a) the simulated interferogram (interference fringe) observed in camera when measuring over a tilted surface like (b), the wavelength of the light source applied in simulation is 530 nm. Fringe spacing represents that two fringes have a phase difference in 2π and a height different in λ/2. (b) An inclined flat surface in size of 100 µm x 100 µm, perfectly aligned in y-axis (horizontal orientation) and 0.57° tilted in x-axis (slope orientation).

According to Gate's theories [103] f_{NA} can be estimated as:

$$f_{NA} = \frac{\ln(\cos\theta_{max})}{\cos\theta_{max} - 1}. \qquad \text{(Equ. 3.23)}$$

In this analysis, it is assumed that in a perfect optical system with uniform surface illumination, the fringe spacing can be obtained by integrating all the light beam within maximal incident angle θ_{max} (i.e., over the entire circular aperture), each weighted by a factor related to its optical path length, which is a function of the corresponding incident angle θ.

In later research from G. Schulz [65], he mentioned that under the condition of uniform illumination, the integrated interference intensity I over the entire cone of light beams can be used for estimating the fringe spacing, therefore determining the correction factor f_{NA}. The intensity model he employed is identical to the one previously introduced in Equ. 2.17 and illustrated in Figure 7b.

$$I = I_0 \int_0^{2\pi} \int_0^{\theta_{max}} [1 + I_0 \cos(2kz\cos\theta)] P \cdot sin\theta d\theta d\varphi \qquad \text{(Equ. 3.24)}$$

https://doi.org/10.7795/110.20260421A

In the case of uniform illumination, the pupil function P over the integration area is equal to 1, simplifying the computation. Therefore, the corresponding correction factor can be determined based on the intensity model (Equ. 3.24) as:

$$f_{NA} = \frac{2}{\cos\theta_{max} + 1} \qquad \text{(Equ. 3.25)}$$

He also brings up in the same paper [65], in the case that illumination is not even distributed, pupil illumination function $P(\theta)$ must be considered into the intensity model:

$$P(\theta) = \begin{cases} \cos\theta & case\ I \\ \cos^2\theta & case\ II \\ \delta(\theta) & case\ III \end{cases}, \qquad \text{(Equ. 3.26)}$$

where cases I and II describe different levels of non-uniform illumination, primarily caused by reflection losses in the outer zones of the aperture cone. This phenomenon is commonly referred to as the apodization effect [66], and its magnitude can be quantitatively modeled using the exponent n_{apo} in the cosine function, as defined in Equ. 2.18. Case III represents an idealized scenario with an extremely small NA, in which only light rays incident at 90° to the surface are reflected back into the camera and contribute to the detected signal. In this limiting case, the exponent n_{apo} approaches infinity, and the pupil function effectively becomes a Dirac function δ. As a result, any deviation from uniform illumination (i.e., cases involving the apodization effect) will result in a correction factor f_{NA} greater than 1. As the illumination distribution becomes more uniform, leading to a reduction in f_{NA}. Ultimately, as the system approaches the ideal case III, the correction factor decreases toward 1.

J. Biegen [105] empirically observed that the correction factor f_{NA} is influenced not only by the NA but also by the type of objective used. For example, Mirau and Linnik objectives exhibit different values of f_{NA} even when they share the same value of NA. Later, C. Sheppard et al. [66] explained that this discrepancy arises from the reference mirror integrated within the Mirau objective, which obstructs part of the light beam at certain incident angles θ. This phenomenon, referred to as the central obscuration effect, results in an increased correction factor f_{NA} as the size of the obscuration grows. In addition, Sheppard pointed out that tilting of the sample surface also causes variation in the correction factor, further influencing the measurement accuracy.

C. Sheppard et al. [66] further concluded that the variation in the correction factor f_{NA}, caused by the aforementioned issues, is in fact a result of changes in the effective size of the aperture cone. This change alters the integration range of the interference intensity in Equ. 3.24. To account for this, Sheppard introduced the term “effective NA”, referring to the modified NA

https://doi.org/10.7795/110.20260421A

resulting from factors such as partial beam obstruction or surface tilting. He collectively described these influences as the effect of numerical aperture (NA effect).

In addition, an effect of the structure height in dependency of the correction factor when using high-NA objectives (starting from NA = 0.6) was reported by G. Schulz in his work [65]. He further investigated that this dependency is not the same, even when using the same instrument, but applying different topography reconstruction algorithms, such as the 4+1 step PSI method [72] and the Carré algorithm [108].

Various optical artifacts

Unlike the effects described above, which have a global impact on the measurement and lead to systematic and/or random errors, optical artifacts in this section are defined as local errors that compromise the topography fidelity of the measured topography. Examples include outliers, batwings, overshooting signals, and missing points.

Among these artifacts, some have been thoroughly investigated from a theoretical perspective, along with their influencing factors, such as the batwing effect in WLI [97] and overshooting signals in CFM [109] observed in step and edge measurements. However, certain artifacts (e.g. outliers) cannot be effectively modeled due to the complexity of the local surface structures where they appear. The intricate nature of these surfaces makes them challenging to model and simulate, especially when the model must also account for the interaction between light and the surface, including scattering and diffraction effects.

Regardless of the specific type of artifact, they all share a common characteristic: their occurrence is closely related to the properties of the local surface, such as geometrical structures and material features. This implies that, without prior knowledge of the local surface properties, it is difficult to distinguish these artifacts from reliable measurement results. It becomes even more difficult to investigate their causes or to develop correction methods aimed at improving topography fidelity in optical measurements.

Nevertheless, there remains significant potential for enhancing topography fidelity. In cases where the surface topography or material properties are known, measurement errors, including artifacts, may be partially corrected. The corresponding correction strategies will be detailed in the following sections. However, when measuring surfaces that are completely unknown or only partially known, it becomes often questionable to (blindly) apply correction approaches. In such scenarios, achieving high topography fidelity requires prior knowledge of the measured surface, typically obtained through reference metrology. This concept will also be discussed in detail in the final section of this chapter.

https://doi.org/10.7795/110.20260421A

3.2. Metrological characteristics

A classical approach to improving topography fidelity involves instrument calibration using material measures, guided by metrological characteristics. According to ISO 25178-600:2017 [5], metrological characteristics are defined as “characteristics of measuring equipment that can influence the results of measurement.” These characteristics encompass a range of parameters that quantitatively describe the instrument’s measurement capabilities, thereby providing a structured framework for assessing and enhancing its performance in surface topography measurements.

An instrument calibration ensures the measuring accuracy and reliability of an instrument. In such calibration, metrological characteristics such as amplification coefficient, linearity deviation, flatness deviation, measurement noise, topographic spatial resolution, and ITF can be evaluated based on its measurement results of material measures [110]. A material measure typically refers to a sample or standard for which at least one of the metrological characteristics to be measured is well defined and reproducible. More details about existing material measures specifically designed for the characterization of ITF, flatness, and vertical scaling factors can be found in [12,91,111,112].

Amplification coefficient and linearity deviation

Amplification coefficients α_i and linearity deviations l_i are among the most fundamental metrological characteristics used to evaluate how accurately an instrument responds to actual input quantities. According to ISO 25178-600:2017 [5], the amplification coefficient is defined as “the slope of the linear regression curve obtained from the response curve,” while the linearity deviation is defined as “the maximum local difference between the line, from which the amplification coefficient is derived, and the response curve.”

An illustrative figure demonstrating the amplification coefficient and linearity deviation is provided in Figure 17 [5]. The ideal instrument response, which maps actual input quantities on the horizontal axis to measured values on the vertical axis, is represented by curve (1). This curve exhibits perfect linearity and an ideal amplification coefficient α'_i. In practice, however, the response of an actual instrument may deviate from this ideal behavior due to non-linearity and scaling effects. Consequently, the actual response more closely resembles curve (2). The linear regression of curve (2), depicted as curve (3), has a slope α_i, which corresponds to the instrument's amplification coefficient. The point where the maximum difference between curves (2) and (3) occurs, indicated as point (4), represents the linearity deviation. In the case of a 3D measuring instrument, it is common to use α_x, α_y, α_z to denote the amplification

coefficients along the x-, y-, and z-axis, respectively. The corresponding linearity deviations are expressed as l_x, l_y and l_z.

Generally, the axes of a measurement system are independent of each other, which demands separate calibration and adjustment for each axis. The lateral axes, namely the x- and y- axis, can be calibrated using 2D cross-grating standards, while the vertical axis, or z-axis, is typically calibrated using a step height standard for short-range calibration or more step height standards in combination for long-range calibration [7]. In addition, PTB has introduced a simple approach for long-range calibration [113], which employs a single material measure containing multiple grooves with calibrated depths. This method eliminates the need for multiple standards or complex positioning procedures, making it well suited for practical industrial applications.

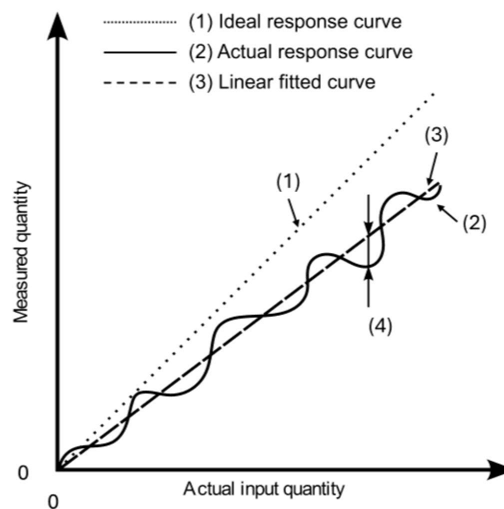

Figure 17 Illustration of the metrological characteristics amplification coefficient and linearity of an actual response curve (2) comparing to the ideal response curve (1); the curve (3) is the linear fitted curve based on the curve (2) and it shares the same amplification coefficient as curve (2). The distance (4) is the maximum local difference between curve (2) and (3), known as linearity deviation

Once the calibration is completed, the obtained amplification coefficients can be used to correct scaling effects in the measured data. For this purpose, two types of amplification coefficients are distinguished. The reference amplification coefficient α'_i denotes the ideal coefficient defined by the reference calibration input, whereas the measured calibration amplification coefficient a_i denotes the coefficient obtained experimentally from the instrument under calibration, typically determined as the slope of the measured response with respect to the reference input. Based on these two quantities, a correction constant c_i is defined as the ratio of the reference amplification coefficient to the measured amplification coefficient. This correction constant is then applied to compensate for the scaling deviation of each of the three measuring axes:

https://doi.org/10.7795/110.20260421A

$$c_i = \frac{\alpha'_i}{a_i} \text{ for } i = x, y, z \qquad \text{(Equ. 3.27)}$$

By applying the corresponding correction factor, the scaling error in the measured topography can be reduced, thereby improving topography fidelity.

Measurement noise

Noise is another important specification of areal surface measuring instruments, representing a specific type of measurement error observed in the measurement results. Unlike systematic errors, noise occurs in a random manner and does not depend on time. The sources of noise within an instrument can be diverse and are typically classified into two main categories. External sources include ground and acoustic vibrations, thermal dynamic noise and disturbances of ambient lights. Internal sources involve factors such as electronic shot noise in detectors and vertical scanning position instabilities [5,114,115]. The noise that appears under optimal measuring conditions, without influence from any external sources, is referred to as instrument noise [5]. This defines the lowest noise level achievable by the instrument and thus reflects its fundamental performance limit.

Typically, the metrological characteristic measurement noise $\mathrm{N_M}$ is commonly used to represent the total contribution of noise to measurement uncertainty [110]. According to ISO 25178-600:2017 [5], it is defined as "the noise added to the output signal occurring during the normal use of the instrument." In practice, $\mathrm{N_M}$ is commonly evaluated as the standard deviation of repeated measurements performed over a flat surface. It should be noted that, before performing such an evaluation, it is standard procedure to remove surface tilt and offset by applying a least-squares plane fitting algorithm to the measured topography [110].

Two methods for noise characterization are recommended in ISO [110], referred to averaging method and subtraction method. The averaging method calculates an average topography $\overline{H}(i,j)$ from n ($n \geq 2$) successive repeat measurements $H_1(i,j) \ldots H_n(i,j)$ to approximate a noise-free topography. The measurement noise N_M is then estimated as:

$$N_M = \sqrt{\frac{\sum_{k=1}^{n} \frac{1}{XY} \sum_{i=1}^{X} \sum_{j=1}^{Y} \delta H_k(i,j)^2}{n-1}}, \qquad \text{(Equ. 3.28)}$$

with

$$\delta H_k(i,j) = H_k(i,j) - \overline{H}(i,j). \qquad \text{(Equ. 3.29)}$$

Here, X and Y represent the total measured pixel number in x- and y-axis, respectively; Indices (i, j) are used for denoting the lateral coordinates of a pixel.

In the subtraction method, only two successively measured topographies H' and H'' are required. These are subtracted from each other to obtain a difference topography ΔH, and the root mean square (RMS) value of ΔH is used to characterize the measurement noise N_M [110]:

$$N_M = \frac{1}{\sqrt{2}} \sqrt{\frac{1}{XY} \sum_{i=1}^{X} \sum_{j=1}^{Y} \Delta H(i,j)^2}, \quad \text{(Equ. 3.30)}$$

with

$$\Delta H(i,j) = H'(i,j) - H''(i,j). \quad \text{(Equ. 3.31)}$$

The key idea in both methods is that, through the subtraction process (Equ. 3.29 and Equ. 3.31), the actual surface topography is effectively eliminated from the noise evaluation. As a result, the resulting differential topography can be regarded as entirely attributed to the measurement noise N_M.

Reducing measurement noise across the instrument's spectral range enhances both measuring capability and topography fidelity, particularly in regions with high spatial frequencies. This improvement is especially important for measurement tasks involving ultra-smooth surfaces or surfaces with very weak topographical signals [116–118]. In such cases, measurement noise fundamentally determines the lowest limit of the instrument's measurement capability. Further discussion on algorithms for noise reduction will be presented in the next chapter.

Other characteristics

For the sake of clarity, it is not feasible to introduce all metrological characteristics in detail. Nevertheless, two characteristics are highlighted here due to their particular relevance in this dissertation:

(I) ITF. Defined by ISO [5] as "a curve describing an instrument's height response as a function of the spatial frequency of the surface topography," the ITF is a key metrological characteristic for improving topography fidelity. The approach introduced in [13] demonstrates the potential of using a calibrated ITF to enhance the accuracy of topographical measurements. Further details about this approach are presented in the following section.

(II) Topography fidelity. Topography fidelity itself is also defined as a metrological characteristic in ISO [5]. However, due to the complexity of surface topographies, no material measure has yet been developed that can comprehensively capture all relevant topographical variations. As a result, the quantification of topography

https://doi.org/10.7795/110.20260421A

fidelity using a standardized material measure remains unresolved [90]. Consequently, the classical calibration approach for topography fidelity is currently not applicable.

3.3. Instrument transfer function

Using a calibrated ITF curve to improve the measurement result is one of the current approaches for enhancing topography fidelity [13]. In this approach, a simple and direct two-step roadmap is followed. Firstly, the ITF of the instrument is characterized using an ITF material measure. Secondly, the measured data are processed based on the ITF obtained in the first step, aiming to improve the topography fidelity.

ITF calibration

The lateral resolving ability of an areal surface measuring instrument can be effectively described by the ITF. In contrast to classical single-value parameters such as the Rayleigh criterion, the ITF offers more detailed information by expressing lateral resolving ability as a function of the measured spatial signal amplitude. Analogous to optical transfer function (OTF) used in conventional microscopy [99], the ITF follows a similar conceptual foundation. However, instead of describing the intensity response in the spatial frequency domain, the ITF focuses on the height response. The mathematical expression of the ITF, denoted as $ITF(\upsilon)$, can be written as:

$$ITF(\upsilon) = H'(\upsilon)/H(\upsilon) \qquad \text{(Equ. 3.32).}$$

Here, $H'(\upsilon)$ and $H(\upsilon)$ represent the measured and the true surface topography, respectively, both expressed in the spatial frequency domain. The variable υ denotes the spatial frequencies of the surface. Based on the ITF curve, a quantity known as the lateral period limit D_{LIM} is used to describe the spatial resolution of an instrument and its capability to measure surface features at higher spatial frequencies. The lateral period limit is defined as the spatial period at which the height response of the ITF drops to 50%.

The characterization of ITF is an essential task, not only as a necessary step for ITF-based topography fidelity enhancement, but also because it offers one of the most insightful means of understanding the measurement capabilities of an instrument [89]. To determine the frequency response of an instrument, various methods for ITF characterization have been developed. These methods can be broadly categorized into two types: theoretical approaches based on instrument modelling and experimental approaches based on the measurement of material measures.

Theoretical modeling methods for ITF characterization are introduced in [89,119]. To apply such methods, a series of numerically simulated test patterns, each containing spatial frequencies within the range of interest, must be generated [119,120]. These test patterns are typically created using sinusoidal functions defined by their spatial frequencies. Each pattern, characterized by a simulation amplitude a_{in} and a given spatial frequency υ, is treated as an input signal and processed through an appropriate instrument model, such as a classical Fourier optics imaging model [120]. The corresponding output topography, representing the instrument's response, is then simulated. The amplitude a_{out} of such simulated (virtual measured) topography at the same frequency υ , along with the known input amplitude a_{in}, is subsequently used to estimate the ITF:

$$ITF(\upsilon) = a_{out}(\upsilon)/a_{in}(\upsilon). \quad \text{(Equ. 3.33)}$$

ITF estimated by theoretical methods takes into account both geometric and spectral effects in the modeling of the measuring instrument. However, the accuracy of such results depends heavily on the selection of an appropriate instrument model, which in turn requires a deep understanding of the instrument's internal structure and behavior. As a result, this method may not be universally and/or reliably applicable, particularly for users of commercial instruments, where their instrument can often be regarded as a "black box." To address this limitation, G. Dai points out in his work [12] that, due to its lower application complexity, experimentally measuring the instrument response using suitable material measures offers a more straightforward and practical approach to ITF characterization. In the same work [12], he also mentioned that, for a more precise quantitative description of the ITF, three fitting parameters k, m and n can be used to describe the vertical scaling factor, the bandwidth, and the attenuation of the ITF, respectively:

$$ITF(\upsilon) = \frac{k}{[1+(m \cdot \upsilon)^n]}. \quad \text{(Equ. 3.34)}$$

Since ITF is introduced into the ISO framework as one of the key metrological characteristics, various experimental approaches have been widely developed and adopted for its characterization [12,13,90,119,121]. One of the main differences among these approaches lies in the shape of the features designed on the applied ITF material measures used for characterizing the transfer function. To date, no standardized material measure has been universally recommended for ITF characterization.

Step features, due to their ease of fabrication, are the first structure used in the production of ITF material measures [121], as illustrated in Figure 18a. In this approach, the derivative of the measured height response at the step edge is interpreted as containing the system's response across all spatial frequency components within the range of interest. This method closely

https://doi.org/10.7795/110.20260421A

resembles the traditional knife-edge technique used for modulation transfer function (MTF) calibration, as introduced in [122], particularly when the step height is small [123].

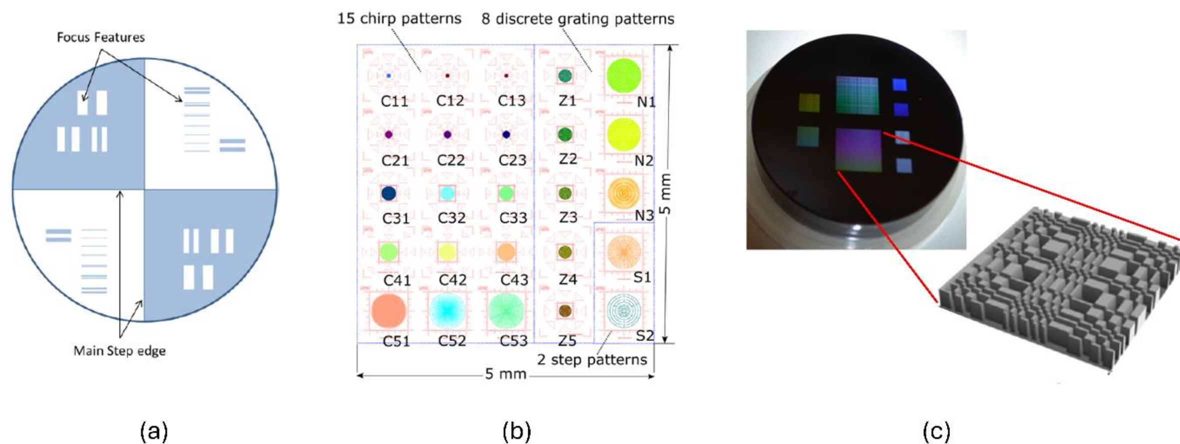

Figure 18 some examples of material measure available for ITF characterization (a) ITF test sample [121] (b) circular calibration standard (CCS) [12] and (c) binary pseudo-random array standards [13,124] ©IOP Publishing Ltd. All rights reserved.

Another type of material measure is designed based on a sinusoidal chirp signal [125], which provides a constant-amplitude, frequency-chirped pattern as a function of lateral position. By calculating the ratio of the measured amplitude to the manufactured amplitude at different spatial frequencies along the lateral direction, the ITF can be evaluated.

Approaches based on such material measures require prior knowledge for ITF estimation, including the manufactured amplitude and the local spatial frequencies as a function of lateral position. A common way to obtain this information is to use high-precision metrological instruments, such as metrological AFM [57], to calibrate the topography of the material measure. The resulting calibrated topography can then serve as reference data for ITF evaluation.

In practice, sets of material measures based on periodic rectangular (binary) chirp signals have been developed [12,126] to avoid the manufacturing challenges associated with producing perfect sinusoidal chirp patterns. As a manufacturing compromise, the bijective relationship between local spatial frequency and lateral position is no longer preserved. This results in increased complexity in the spatial frequency content, as the binarization introduces contribution of higher harmonics into the local topography signal.

Another common characteristic of both types of material measures is their circular design, which enables observation of angular-dependent anisotropy in the aspect of ITF. For example, using the circular calibration standard (CCS) developed at PTB [12], as illustrated in Figure 18 b, the ITF can be calibrated as:

$$ITF(\tilde{\theta}, \upsilon) = \frac{F_m(\tilde{\theta}, \upsilon)}{F_r(\tilde{\theta}, \upsilon)}. \quad \text{(Equ. 3.35)}$$

Here, $\tilde{\theta}$ denotes the angular orientation regards to the measured CCS pattern. F_m and F_r represent the Fourier transformations of the radial profiles obtained from the measured topography and the reference calibration data, respectively.

The third type of material measure, shown in Figure 18c is the binary pseudo-random array standard (BPRAS) [13]. The basic idea of using BPRAS for ITF evaluation is that the ITF can be determined by comparing the power spectral density (PSD) distribution of the measured topography P_{out} to the PSD of the reference topography P_{in} [119,127]:

$$ITF = \sqrt{\frac{P_{out}(\upsilon)}{P_{in}(\upsilon)}}. \quad \text{(Equ. 3.36)}$$

According to ISO 10110 [128], PSD is defined as the squared magnitude of the Fourier transform of the surface height profile along one dimension, following the removal of low-order surface form.

For the same reason as with the CCS material measure, the features on BPRAS are also manufactured as rectangular-shaped grooves. These features are pseudo-randomly distributed across the sample surface, and the design ensures that the PSD spectrum along the lateral axis exhibits a white-noise-like behavior. In other words, the PSD maintains a constant amplitude and is independent of spatial frequency. Consequently, any deviation of the measured PSD spectrum from the ideal white-noise-like distribution reflects the influence of the ITF [127].

ITF for measurement correction

K. Munechika points out in his work [13] that, if the ITF can be precisely characterized, it becomes possible to apply data deconvolution techniques to (partially) compensate for the attenuation of measured topographical signals, thereby enhancing the topography fidelity of the measurement. To illustrate this concept in a simplified form, a 2D example profile $H(x)$, extracted along the x-axis from the full topography H, is considered. According to Fourier transform theory, such a topographical profile can be represented as a sum of all its spatial frequency components. The profile $H(x)$ can thus be expressed as:

$$H(x) = \frac{1}{2\pi} \int_{-\infty}^{\infty} \overline{H}(\upsilon) \cdot e^{i\upsilon x} d\upsilon. \quad \text{(Equ. 3.37)}$$

Where the $\overline{H}(\upsilon)$ is the Fourier transform of the $H(x)$.In some literature [110], Equ. 3.37 is denoted as:

https://doi.org/10.7795/110.20260421A

$$H(x) = F^{-1}[\overline{H}(v)], \qquad \text{(Equ.3.38)}$$

Here F denotes the Fourier transformation operation, and F^{-1} denotes the inverse Fourier transformation.

Analog to the profile $H(x)$, a profile $H'(x)$ measured by an instrument over the same location without consideration of any types of measurement noise can be described as:

$$H'(x) = F^{-1}[\overline{H}'(v)]. \qquad \text{(Equ.3.39)}$$

Substituting the Equ.3.38 and Equ.3.39 into the ITF formular (Equ. 3.32), the relationship between of profile $\overline{H}(x)$ to the measured profile $\overline{H}'(x)$ can be given with known ITF $f_{ITF}(v)$ as:

$$H(x) = F^{-1}\frac{F[\overline{H}'(x)]}{ITF(v)}. \qquad \text{(Equ.3.40)}$$

Equ.3.40 indicates that, if ITF is known and a measured profile is available, the original topographical profile can be reconstructed. Similarly, the full 3D topography of the sample can be reconstructed from the measured 3D topography. By applying this approach, attenuated topographical information can be recovered, thereby enhancing the topography fidelity of the measurement.

A further investigation is carried out to evaluate the correction performance of this approach. To this end, radial profiles of a circular chirp (CC) pattern derived from the CCS sample are simulated and employed as test surface profiles. These simulated profiles include both the original designed form (without binarization) and the corresponding binarized version. In general, a designed radial profile R_p and its binarized form $R_p{}'$ can be mathematically expressed as functions of the radius r:

$$R_p(r) = h\sin\left[\theta_0 + 2\pi r\left(v_0 + \frac{\Delta v}{2R}r\right)\right], \qquad \text{(Equ.3.41a)}$$

and

$$R_p{}'(r) = \begin{cases} h, & \sin\left[\theta_0 + 2\pi r\left(v_0 + \frac{\Delta v}{2R}r\right)\right] > 0 \\ -h, & otherwise \end{cases}, \qquad \text{(Equ.3.41b)}$$

respectively. Here, h denotes the amplitude of the CC pattern structure and R represents the maximum radius of the CC pattern. The parameters v_0 and θ_0 are the initial spatial frequency and initial phase of the chirp signal, respectively. The frequency bandwidth Δv is defined by the minimum wavelength λ_{min} (reciprocal of v_0) and the maximum wavelength λ_{max} of the radial profile, and can be expressed as:

$$\Delta v = \frac{1}{\lambda_{min}} - \frac{1}{\lambda_{max}}. \quad \text{(Equ.3.42)}$$

Figure 19 illustrates a simulated example demonstrating the application of a calibrated ITF (characterized by parameters k=1.0, m=1.5 μm and n=2.0 as specified in Equ. 3.34) to enhance the measurement result. The simulated radial profile is taken from the topography of a CC pattern (C13), which has a pattern radius of 30 μm and the design wavelength from $\lambda_{min} = 1$ μm to λ_{max} = 7.5 μm.

The example is demonstrated in two different cases. In the first case, a sinusoidally chirped profile (represented by the blue curve in Figure 19a) is used to model a radial profile derived from the actual surface of the C13 pattern. This profile serves as the input data to the instrument. During a simulated measurement, the instrument processes this input according to its ITF characteristics. The resulting measured data, illustrated as the green curve Figure 19a, represents the output of the instrument.

A comparison between the input and output profiles reveals two key effects: (I) the amplitude of the output data is generally reduced compared to the input, and (II) the amplitude further diminishes with increasing spatial frequency. These effects become more apparent in the Fourier domain, as shown in Figure 19b. The spectrum of the input data (blue curve) exhibits a plateau within the frequency bandwidth Δv, whereas the spectrum of the output data (green dashed curve) deviates from this plateau and shows a progressive attenuation at higher frequencies. This attenuation behavior is accurately characterized by the ITF curve, depicted as the purple curve in Figure 19b.

The corrected topographies, derived according to Equ. 3.40, are illustrated in both figures and are highlighted in red. It should be emphasized that, in practical applications, such correction is only applicable to measurements having signals with a high signal-to-noise ratio (SNR), as demonstrated in this case. Applying the correction to low-SNR signals would also amplify the noise, potentially leading to substantial errors in the reconstructed topography. To mitigate this issue, a cutoff frequency is introduced, defined as the frequency at which the gain of the ITF falls to –6 dB. This threshold serves to distinguish high-SNR signals from those with low SNR during the correction process. A gain of –6 dB indicates that the height response of the ITF has decreased to 50% at this frequency. The corresponding spatial period of this frequency, also known as lateral period limit D_{LIM}, defines the lateral resolution limit of the instrument, representing the smallest high-frequency surface features that can be reliably resolved and measured [5].

https://doi.org/10.7795/110.20260421A

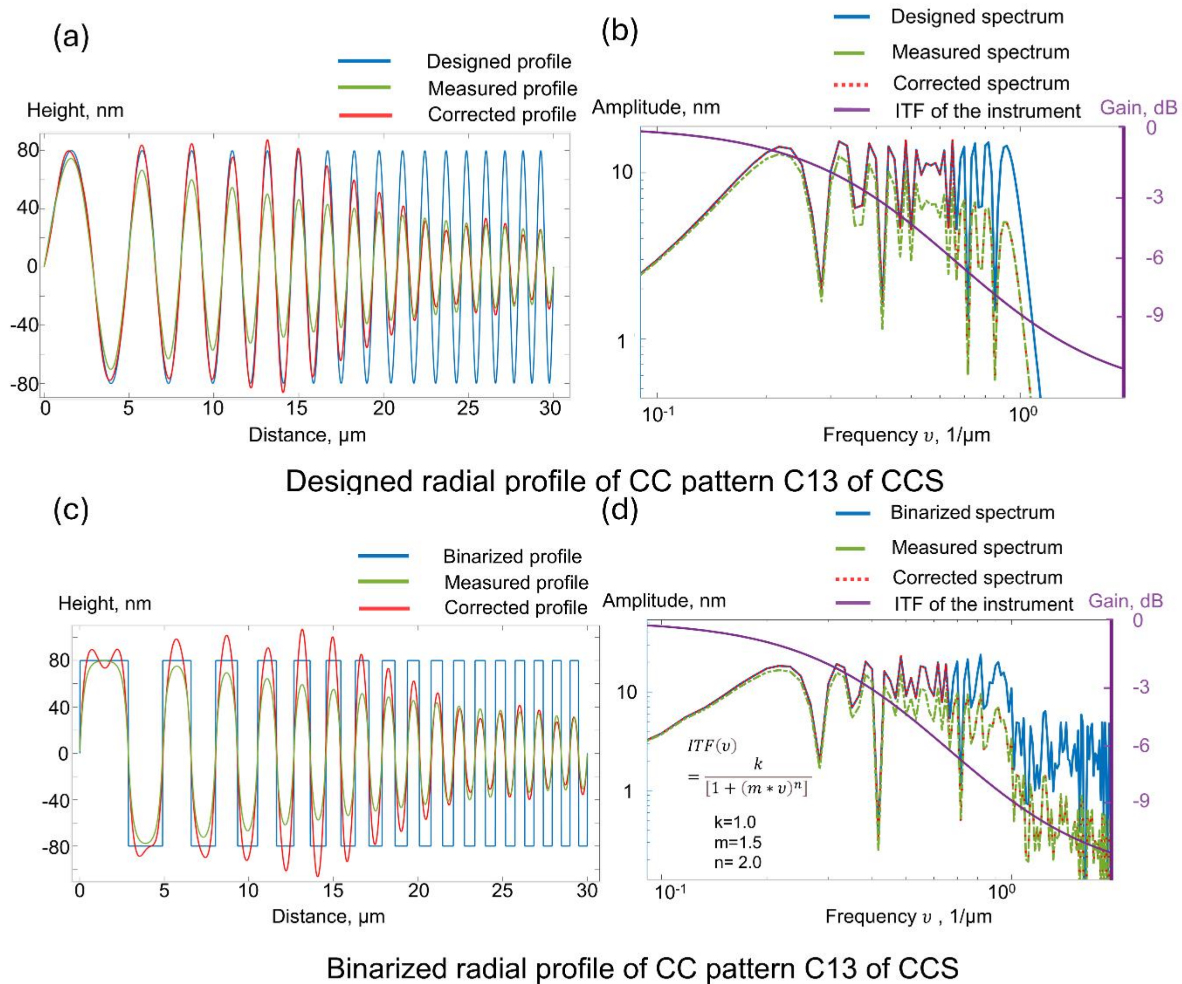

Figure 19 Simulation of measurement and correction of designed (a) and binarized (c) radial profile of the CC pattern C13 of CCS (radius 30 µm and wavelength range is from 1 µm to 7.5 µm) using optical instrument whose ITF is characterized as k=1.0, m=1.5 and n=2.0. The (b) and (d) are the correspondent spectrum comparison respectively.

As shown in Figure 19a, the effectiveness of the topography correction can be evaluated by comparing the corrected profile to the uncorrected one, thereby demonstrating the improvement in topography fidelity. For structures designed with low spatial frequencies, the correction can closely recover the original shape, achieving an almost 1:1 correspondence with the input data. However, further investigation, represented by the second case using a binarized radial profile (Figure 19c and Figure 19d) , reveals that the applicability of this correction method is strongly dependent on the topographical structure. When the radial profile is binarized, the correction becomes less effective and no longer meets expectations. Notably, overshootings, classified as measurement artifacts, are present in the corrected results, indicating that the correction algorithm, rather than eliminating existing errors, introduces further error into the reconstructed topography.

This observation above shows a fundamental limitation of the correction method, namely that its applicability is significantly restricted to specific types of topographical features. Whether

the input signal is a 1D profile or a 2D topography, improved correction performance can be achieved when the spectral content of the input is simple and primarily composed of low-frequency components. Input signals with a clearly defined relationship between lateral position and spatial frequency, such as a chirp signal illustrated in Figure 19a and the central region of Figure 20c, are more likely to be corrected accurately without introducing additional measurement errors during the correction process.

However, as the topographical features become more complex, especially when its local frequency components increase in complexity, the correction results become less convincing. In some cases, additional measurement errors are introduced into the corrected profile, as shown by the overshooting issue in Figure 19c. These errors are particularly problematic because they do not appear in the corresponding spectral representation. To be more clear, in the low-frequency range of Figure 19d, no visible difference can be observed between the red and blue curves, even though significant differences are present between the corresponding radial profiles shown in Figure 19c.

Similar issues have been reported in previously published studies [14,92]. As illustrated in Figure 20 and indicated by red arrows, a comparable problem is observed. Although some low-frequency components of the chirped signal are successfully corrected, new artifacts emerge in the form of oscillations over flat surface regions. From the perspective of frequency analysis, these regions are characterized by a mixture of low- and high-frequency components with similar amplitudes. However, after correction, despite being accurately measured in the original data, these regions are adversely affected.

One of the underlying reasons for this issue is that using ITF alone to correct the measured data implicitly assumes that the phase transformation (PT) across the entire spatial frequency spectrum remains constant and can therefore be neglected. However, this assumption does not hold in practice. In a recent publication by P. de Groot [129], it is emphasized that a more complete characterization of the instrument's response should involve the topographical transfer function (TTF).

The TTF provides a fully characterized linear system response by incorporating both the ITF and the effects of phase transformation, thereby offering a more accurate basis for topographical correction:

$$TTF(\theta, \upsilon) = ITF(\theta, \upsilon) e^{i\emptyset(\theta, \upsilon)} . \qquad \text{(Equ. 3.43).}$$

Theoretically, TTF can be applied to correct imperfections and irregularities in the frequency domain, where $\emptyset(\theta, \upsilon)$ is a function describing PT as a function of spatial frequency υ. However, key questions remain unresolved, including how to accurately calibrate $\emptyset$, and

https://doi.org/10.7795/110.20260421A

whether it is independent of the surface topography H ? These open questions currently hinder the practical implementation of TTF for improving the topography fidelity in optical measurements.

Another underlying reason for the observed measurement error may be the lack of consideration of boundary effects [130]. This phenomenon often manifests as artifacts near the edges of the measured area, such as unexpected signal overshootings and oscillations. In our simulation study, as demonstrated in Figure 19, this issue is mitigated by applying profile reflection at the boundary regions. Nevertheless, in Figure 20c, some of the artifacts marked with red arrows may still be attributed to residual boundary effects.

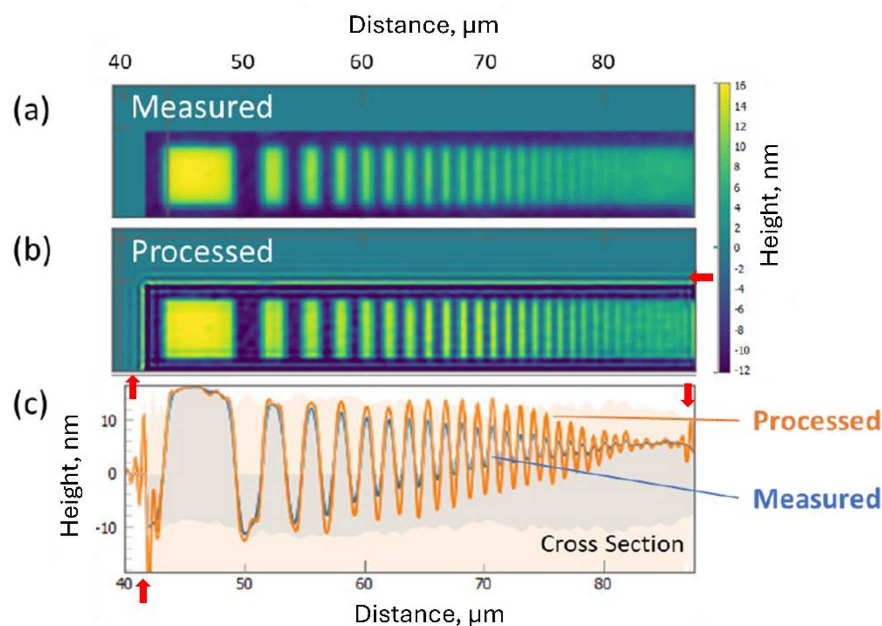

Figure 20 The measured (a) and processed (b) topographies of a 1D chirped height pattern named as "BEAMETR" test pattern [131] (c) The horizontal cross-section of the measured and processed topographies. Reproduced from [13]. Red arrows are added to the original figure for showing the positions where they are overprocessed with the topography correction algorithm.

3.4. Modelling methods

Over the past few decades, optical measuring instruments have been widely adopted in surface and coordinate metrology due to their high speed, excellent vertical resolution, and non-contact operation. However, the complex optical interactions between the sample surface and the measuring instrument introduce challenges in achieving high accuracy and traceability.

To better understand these interactions and evaluate the measurement capabilities of optical instruments, numerous studies have focused on system modelling [9–11,99,120,132–150] in

the field of optical areal surface metrology. These modelling approaches aim to simulate the behavior of wavefronts involved in optical microscopy (OM), with particular emphasis on IMs.

Measurement performance under varying measurement conditions and across different surface features can be thoroughly analyzed using such models, which also facilitate the identification and quantification of measurement errors. The knowledge obtained through these investigations has been summarized in the Good Practice Guides (GPG) published by the European Metrology Programme for Innovation and Research (EMPIR) project TracOptic 20IND07 [147]. By utilizing these GPG as a source of prior knowledge, users are enabled to make informed decisions when selecting appropriate instrumentation for specific measurement tasks. This informed selection contributes to the reduction of measurement errors and the enhancement of topography fidelity. The strategy of leveraging such modeling approaches for improving measurement outcomes is hereinafter referred to as the modeling concept.

Methods for modelling different instruments are not always the same. Indeed, even for the same instrument, various modelling approaches may be applied. Thus, in this work, for the sake of clarity, a conventional WLI instrument is used as an example to illustrate how an optical instrument can be modelled and how such a model can contribute to the improvement of topography fidelity. However, the application of this modelling method is not limited to WLI instruments. As reported in previous works [134,136,149], the approach can also be extended to other types of optical measuring instruments, such as PSI and FVMs.

Figure 21 illustrates a process diagram demonstrating the step-by-step application of the modeling concept to a WLI instrument. The procedure begins with the use of physical modeling techniques to describe the interaction between a monochromatic incident plane wavefront U_i and an object surface topography H_o.The reflected wavefront U_r is then expressed as a function of U_i and H_o, written as:

$$U_r = g(U_i, H_o). \tag{Equ. 3.44}$$

The reflected wavefront U_r then propagates through the optical imaging system of the WLI instrument (e.g., objective, BS, and tube lens), resulting in a modified wavefront U'_r before reaching the intensity-sensitive detector (e.g., a camera). This propagation process can be accurately described using the principles of Fourier optics [99] as:

$$F(U'_r) = F(U_r) \cdot TF. \tag{Equ. 3.45}$$

where TF denotes the transfer function of the WLI optical imaging system. The camera records the intensity I_m, which can be expressed as:

https://doi.org/10.7795/110.20260421A

$$I_m = Re(U'_r) \qquad \text{(Equ. 3.46)}$$

This process is repeated for each monochromatic wavefront. The results are then combined according to their spectral density. By superimposing the contributions from each wavelength component, a WLI interference image is generated as a result of using a light source with broad spectral bandwidth in the IM-mode.

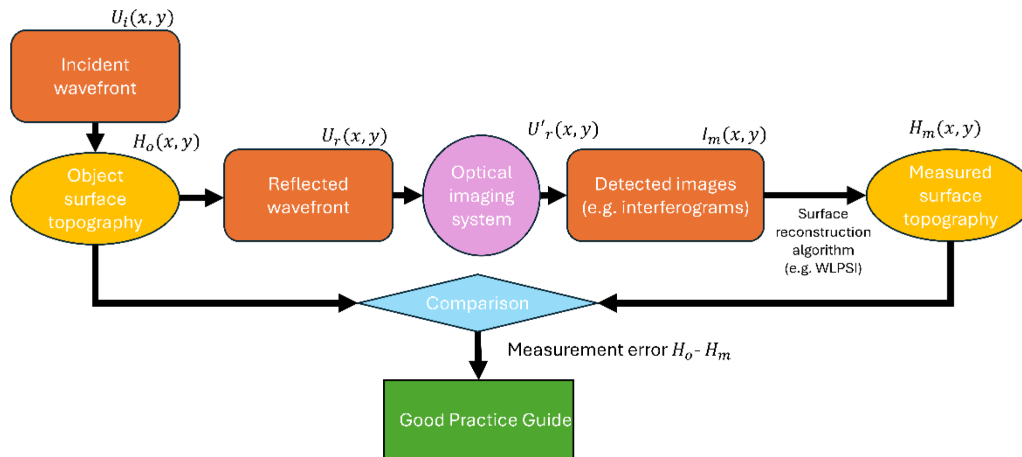

Figure 21 Process diagram illustrates the modelling concept for improving topography fidelity. Each step in the instrument, from wavefront propagation to the generation of measured topography H_m, is shown. The comparison between measured topography H_m and the object topography H_o yields the measurement error, which is used to evaluate performance and is summarized in the good practice guide.

After all interference images have been simulated, the correlogram $I_m(z)$ at each lateral coordinate (i, j) can be obtained as a function of intensity with respect to the vertical scanning position z. With the help of a WLI surface reconstruction algorithm, such as the WLPSI algorithm described in Equ. 2.28 to Equ. 2.31, the measured topography H_m can be determined. Measurement error can then be evaluated by comparing the measured topography H_m with the object topography H_o. This comparison enables an evaluation of the measurement performance of WLI in accurately reconstructing the object topography H_o. By defining H_o with various types of topographical features, including steps, slopes, spikes, and randomly rough surfaces, the corresponding instrument responses and measurement errors can be sequentially simulated. Based on the quantitative value of the measurement error, the measurement capability of the instrument can be evaluated. Finally, these simulation results will be documented as prior knowledge and summarized in GPG.

Therefore, in future practical applications, it is possible to select an instrument that is well suited to a specific measurement task with the support of GPG. This selection is informed by simulation results that theoretically predict the smallest possible measurement error. By adopting this approach, large measurement errors can be avoided, which improves the

accuracy of the measurement and, in turn, enhances the measurement fidelity of the optical measured results.

There are two most critical aspects in the application of modelling concept: the determination of the function g in Equ. 3.44 and the transfer function TF in Equ. 3.45. The key to determining the g function lies in selecting an appropriate modelling approach to describe the wavefront interactions and using it to predict the reflected wavefront U_r, from which topographical information is derived [134].

Using the WLI instrument as an example, modelling methods can generally be categorized based on whether they rigorously solve Maxwell's equations. These include:

(I) Non-rigorous methods (approximate models), such as the Elementary Fourier Optics (EFO) model [120], the Universal Fourier Optics (UFO) model [11,137], and the Foil model [145];

(II) Rigorous methods, such as Rigorous Coupled-Wave Analysis (RCWA) [147], the Finite-Difference Time-Domain (FDTD) method [148], the Finite Element Method (FEM) [149], and the Boundary Element Method (BEM) [140].

Generally speaking, rigorous methods enable more accurate simulation of images captured over complex topographical features, such as sharp edges and grooves [149]. This is because such methods consider physical interactions including multiple scattering, polarization effects, and material-dependent wavefront behavior. However, achieving this level of accuracy typically requires substantial computational resources. For example, simulating a simple step structure within a volume of 20 μm x 10 μm x 20 μm using the FDTD method [150] may take several hours, even on high-performance workstations.

In contrast, non-rigorous methods employ physics-based simplifications to model the instrument with significantly lower computational cost [134]. Nonetheless, these efficiency gains come with limitations. In practice, non-rigorous methods are only valid under certain assumptions, and when these conditions are not satisfied, the resulting simulations can deviate notably from those produced by rigorous approaches.

Another reason for the deviation observed in simulation results when using non-rigorous methods is that such methods do not account for complex interactions between the object topography and the wavefront, such as multiple light reflections. For example, in the EFO method [10], the original topography is first converted into an equivalent thin phase map, which is then processed using transformation functions to predict the resulting interference images. Although this approach greatly reduces computational requirements, it cannot represent

https://doi.org/10.7795/110.20260421A

multiple reflections caused by local topographical variations, as the topography is simplified into a phase map in the very beginning of the modelling.

Some studies [9,134] have shown that differences in simulation results are not only evident between the application of rigorous and non-rigorous methods, but can also arise from the use of different rigorous modelling approaches, such as FEM and BEM. These discrepancies present significant challenges in practice when selecting the most appropriate model. However, for the sake of clarity, such discussions are not addressed in this work.

Another critical aspect of the modelling concept is the determination of the TF, which remains challenging. In general, the TF of an interference microscope operating under Köhler illumination takes the same form as the OTF of an imaging system illuminated by a fully incoherent light source [10]. According to W. Goodman [99], the OTF can be expressed as the autocorrelation of the pupil function. For example, for an instrument designed with a circular pupil function, the corresponding OTF can be written as [10]:

$$\mathrm{OTF} = \frac{2}{\pi}\left[cos^{-1}\left(\frac{|v|}{v_{max}}\right) - \frac{|v|}{v_{max}}\sqrt{1-(\frac{|v|}{v_{max}})^2}\right]\cdot rect(\frac{v}{2v_{max}}) \qquad \text{(Equ. 3.47)}$$

with v_{max} the maximum detectable lateral spatial frequency:

$$v_{max} = \frac{2NA}{\lambda}. \qquad \text{(Equ. 3.48)}$$

However, in practical applications, the actual TF is more complex than the idealized form as described by Equ. 3.47. First, focus errors and non-uniform illumination distributions, known as apodization effects, introduce aberrations into the OTF, and consequently into the TF. Second, even under optimal measurement conditions and with precise alignment, the real instrument includes additional optical components such as tube lenses. These components affect the propagation of the wavefront and introduce further deviations into the TF when compared to its ideal form as represented by Equ. 3.47.

As mentioned above, applying the modelling concept in practice poses significant challenges, particularly for instrument users who may not have detailed knowledge of the parameters required to select an appropriate modelling method or to estimate the transfer function. To address these challenges, the GPG [146] summarizes key findings from the simulation studies described earlier, together with practical measurement experiences. It offers clear recommendations for selecting suitable optical instruments and using them effectively, without requiring users to carry out complex modelling procedures themselves. However, in certain application scenarios described in the GPG, prior knowledge of the object surface topography is required.

Additional issues that require attention in the application of the modelling concept include ambiguity and nonlinearity. The ambiguity issue arises from the fact that, although modelling methods can compute simulated images or interferograms for a well-defined topography without ambiguity, interferograms obtained in practice may not represent the actual surface in a unique and unambiguous manner. For example, variations in measurement conditions, such as changes in the wavelength of the light source or tilting angles introduced during sample mounting, can lead to identical interferograms being interpreted as different topographies.

One possible way to resolve this ambiguity is to use the original topography as prior knowledge. However, in industrial settings, unlike in calibration procedures where the topography of a reference standard is known, the surface to be measured is typically unknown. In such cases, the most effective approach to access the original topography is through application of *in-situ* reference metrology. This involves measuring the surface using highly accurate and traceable instruments, such as metrological large range AFM [151].

The nonlinearity issue is related to the algorithms used for reconstructing topographies from interferograms, particularly those that involve phase detection. Errors within these algorithms can propagate through the topography reconstruction process, often appearing as periodic deviations with random amplitudes and phase offsets. These errors ultimately lead to form deviations in the final measurement results [70,72,100,152].

In conclusion, the modelling method is a valuable approach for gaining deeper insight into the behavior of optical instruments, which highlights its ongoing importance within the field of surface metrology. While it holds significant potential for enhancing topography fidelity, further investigation is required to resolve the challenges associated with its practical implementation before it can become an effective and widely adopted solution for this purpose.

3.5. Correlative reference metrology

Reference metrology refers to the process of characterizing and calibrating a measuring instrument using reference material measures in order to ensure its measurement performance. Traceable and accurate reference values, which are calibrated from these reference material measures, serve as essential components of reference metrology. These reference values can also be used for comparison and validation across different instruments.

In dimensional metrology, particularly in areal surface metrology at the micro- and nanoscale, the role of reference metrology is to provide accurately and traceably calibrated 3D topography data. This typically involves a standardized calibration procedure, the use of recommended

https://doi.org/10.7795/110.20260421A

types of reference material measures, and the specification of the associated metrological characteristics.

While essential, these metrological characteristics alone are not sufficient to fully characterize the measurement performance of an instrument, particularly with respect to the complex interactions between the probe and the sample. To address this limitation, the concept of topography fidelity has been introduced as a new metrological characteristic within the Geometrical Product Specifications (GPS) framework [5].

However, to the best of our knowledge, the classical methods used for instrument calibration cannot yet be applied to the calibration of topography fidelity. This is because a universally accepted calibration procedure and a corresponding reference material measure for topography fidelity are still under development. As a result, no formal agreement has been reached on how to characterize or standardize topography fidelity at present [90].

To address this problem, the concept of correlative reference metrology [1] has been proposed as a promising approach. It enables a quantitative assessment of optical measurement fidelity by using reference data obtained at the same spatial location. For example, such data can be provided by a metrological large-range AFM [151], offering a practical approach to improve topography fidelity. The concept is also applicable when using non-metrological AFMs to generate reference data [153], as long as the accuracy and uncertainty of the reference measurements are significantly better than those of the data to be calibrated, such as measurements obtained from optical instruments.

Unlike classical methods in reference metrology, this new concept does not focus on characterizing a predefined set of GPSs using specific reference material measures. Instead, it emphasizes the delivery of accurate and traceable 3D reference topography data. By correlating the reference data with the measured data, comparisons can be performed both in the spatial and frequency domains. As a result, the application of correlative reference metrology presents a promising approach for thoroughly characterizing the instrument. This includes, in particular, the evaluation of sample–probe interactions and the spectral properties of the system. Both aspects are considered as key contributors to topography fidelity.

The concept enables a direct comparison between reference data and measured data, which eliminates the reliance on physical material measures. In this way, it effectively resolves the challenge identified in [90], namely the unavailability of appropriate material measures for the calibration of topography fidelity.

G. Dai demonstrated this concept in his earlier work [1] by comparing AFM reference data with optical measurements on a PTB roughness standard. This approach not only allows for the

calibration of roughness-related parameters but also enables the determination of instrument response and the measurable lateral frequency range based on reference data. This, in turn, creates further possibilities for improving topography fidelity of the measurement.

However, implementing this concept requires considerable effort in transporting and relocating the measured area of interest between different instruments. This process may introduce additional measurement errors that could otherwise be avoided. One possible solution is the use of a multi-sensor areal measuring instrument to eliminate the need for sample transfer and repositioning. Nevertheless, current multi-sensor instruments face two major limitations: first, they are costly and therefore not accessible for general industrial or research applications; second, they exhibit a low level of synergy, as discussed in the previous chapter.

To address these challenges, a novel hybrid microscope [71] intended for the realization of *in-situ* correlative reference metrology has been developed at PTB and has shown promising results. This microscope combines an IM-mode with an AFM-mode in a high synergy level, offering a broad range of application potential, including improvements in measurement fidelity. The development and performance of this instrument will be presented in the following chapters.

Another important aspect not addressed in the concept [1] is the specific methodology for applying correlative reference metrology to enhance topography fidelity. At present, the details regarding this part of the approach remain insufficiently developed.

One possible approach to achieving topography fidelity enhancement involves the use of artificial intelligence (AI) technology. In this approach, an optical measurement is first carried out over a large measurement area, shown as the blue marked region in Figure 22. Subsequently, several AOIs, marked as red rectangles in the same figure, are selected for successive measurement using the AFM technique in order to generate a reference data set. It must be mentioned that the selected surface features within these AOIs should be representative of the remaining optically measured region. By correlating the AFM data with the optical data at the same locations, data pairs can be established. These data pairs may serve as prior knowledge for analyzing the instrument response at representative surface features. Based on this analysis, it becomes possible to predict and even correct the instrument response over the rest of the optical measurement area, which is not measured by the AFM technique.

The use of AI techniques can accelerate the analysis process and improve topography fidelity, as this concept offers two major potential advantages:

1. Reduction of the needs of AFM reference data.

https://doi.org/10.7795/110.20260421A

Assuming that the instrument maintains stable conditions over a given period of time, the accumulation of reference data measured by AFM increases as the instrument is used more frequently. As a result, the instrument responses associated with various surface features are progressively collected. Over time, as the reference database becomes sufficiently comprehensive with respect to the different types of surface structures, the number of AOIs requiring additional AFM reference measurements may gradually decrease. Eventually, it may become possible to perform reliable topography correction and improvement without the need for further AFM measurements

2. Preparing/training the AI algorithm with simulated reference data.

The AI model can be trained using both simulated and experimental reference data, which implies that the initial training phase does not necessarily need to fully depend on real instrument usage. By employing simulated data generated through the modeling approach described in the previous section, the AI model can be partially trained in advance, thereby reducing the overall training effort required during practical application

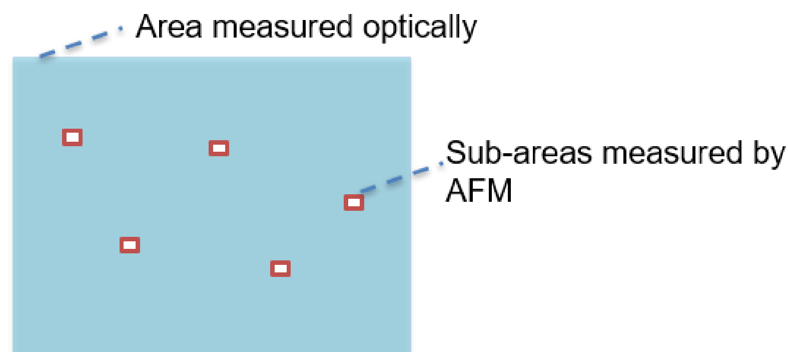

Figure 22 Illustration of the relationship of the two important components that applied in correlative reference metrology for topography fidelity enhancement (I) the optical measured AOI shown in blue and (II) AFM measured reference data in different sub-areas (red marked), which are locally correlated with the optical measurements.

https://doi.org/10.7795/110.20260421A

4. Realization of the hybrid microscope

4.1. Design of the hybrid interference- and atomic force microscope

The design of the hybrid interference-atomic force microscope (HM) is based on a main frame of an optical microscope. An IM-mode and an AFM-mode are then integrated into the main frame of the HM for realizing the corresponding measuring mode respectively. This main frame is shown in the Figure 23.

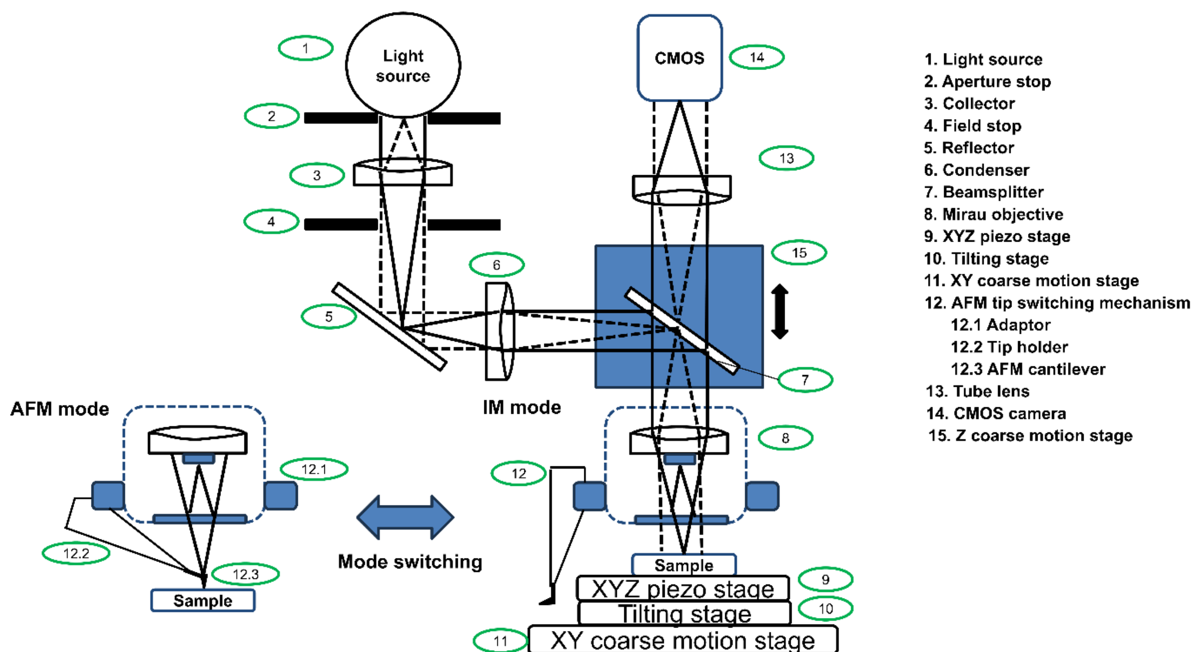

Figure 23 Design details of the hybrid microscope. It enables two measurement modes, namely (I) the interference microscope (IM) mode and (II) the atomic force microscope (AFM) mode. From an instrumentation perspective, the two modes differ only in whether the AFM tip switching mechanism (component 12 in the figure) positions the AFM cantilever (12.3) within the optical path.

One of the primary focuses of the HM design is to achieve a highly synergistic integration of the IM-mode and the AFM-mode. To realize this, both modes are designed to share as many components as possible while minimizing compromises in their respective measurement performances. For example, the stage system is implemented through the coordinated operation of four stage components: the XYZ fine piezo stage (component 9 in Figure 23), the tilting stage (component 10 in Figure 23), the XY coarse motion stage (component 11 in Figure 23), and the Z coarse motion stage (component 15 in Figure 23). These stage components are embedded within the HM and serve both measuring modes, enabling each to perform its specific tasks effectively.

https://doi.org/10.7795/110.20260421A

Other systems shared by the IM-mode and the AFM-mode include the image-forming system and the illumination system. These systems comprise optical components such as the light source, beam splitter, objective, camera, and related elements. More details about these optical components are provided in the following sections.

Regarding the configuration, the AFM-mode differs from the IM-mode only by the introduction of an AFM tip into the optical path during measurement. This introduction is achieved through a key feature of the HM, a motorized AFM tip switching mechanism named Klappfix (component 12 in Figure 23). It positions the AFM tip either outside or within the optical path to enable mode switching. When the AFM tip is positioned outside the light path, the microscope operates in the IM-mode, allowing for fast, non-contact optical surface measurements. In contrast, when the AFM tip is introduced into the light path, the AFM-mode is activated. The back side of the AFM cantilever is brought into focus within the FOV while the AFM tip is brought into contact with the sample surface. By doing this, the tip-sample interactions induce bending and torsion forces acting on the AFM cantilever. These forces cause deformation of the cantilever, which can be detected by a CMOS camera through analysis of the variations in the interference fringes. The detailed principle of using the camera to detect the AFM tip-sample interaction will be described in later sections.

One notable advantage of this highly synergistic HM design is that, in the AFM-mode, the IM principle is employed to detect tip-sample interactions. This eliminates the need for an additional signal readout system typically required in conventional AFMs, such as an optical-lever readout system, which generally consists of a laser source, a detector, and the associated tip- and signal-adjustment mechanisms. As a result, the HM approach not only reduces instrumentation costs by employing the existing IM-mode as its built-in AFM signal readout system but also simplifies the AFM signal adjustment process by eliminating the need for an additional readout system.

4.2. Realization of the IM-mode in the hybrid microscope

The IM-mode of the HM was independently developed by our research group, AG 5.23 at PTB [154]. It integrates both the PSI principle, based on a monochromatic light source, and the WLPSI principle, based on a broadband light source. The realization of this measurement mode required comprehensive development efforts, including the design and implementation of the hardware and software components of the optical microscope main frame, the development of control and communication protocols between hardware elements, the investigation and implementation of PSI and WLPSI algorithms, and the creation of measurement data post-processing functions together with a user-friendly graphical user

interface (GUI). To assess the performance of the developed IM-mode, its bandwidth and functional specifications were characterized using material measures available at PTB. The following sections present the development process and the corresponding characterization results in detail.

As noted in the preceding chapter, the PSI and WLPSI measuring principles share fundamental similarities in their optical, mechanical, and algorithmic designs. From a hardware perspective, their primary difference lies in the type of light source used, with PSI employing a coherent light source and WLPSI using an incoherent one. Therefore, to avoid redundancy, the explanation of the IM-mode development will be primarily focused on PSI as an illustrative example.

Another point that must be clarified is that the HM is compatible with several commercially available Mirau objectives (see Table 1). For the sake of clarity, this chapter will focus on a Mirau-type objective with 20x magnification and a NA of 0.4 to demonstrate the working principles of both AFM- and IM-modes in the HM and to evaluate their measurement performance.

Table 1 Specifications of Mirau type objectives from Nikon [155]

Magnification	Working distance, mm	Numerical aperture
10x	7.4	0.30
20x	4.7	0.40
50x	3.4	0.55
100x	2.2	0.70

4.2.1. Optical and mechanical components of the IM-mode

The HM is developed based on the classical design of an optical microscope. Three key systems of a classical optical microscope, namely the illumination system, imaging system, and positioning system (shown in Figure 24), are carefully integrated into the HM and optimized in this work. These systems will be described separately in detail in the following sections.

The illumination system and the imaging system together form the fundamental optical structure of the HM. They are mounted on the main frame of the HM, referred to as the

https://doi.org/10.7795/110.20260421A

horizontal bridge, and are held in their vertical position by a linear actuator N-216 NEXLINE [156]. This actuator functions as the Z-coarse motion stage in the HM and provides a holding force of up to 800 N.

The illumination system is a critical component in the development of any optical principle-based measurement system. For the HM, a 4f Köhler illumination system [157] has been implemented. Compared to the design of other illumination systems (e.g. diffusion illumination and critical illumination system), this design offers significant advantages, including high efficiency, uniform illumination distribution, and the minimization of glare and optical artifacts that could distort the image formation.

To illustrate the working principle of the implemented illumination system of the HM (system colored in green in Figure 24), a detailed 4f Köhler illumination configuration is shown in Figure 25 . This system consists of six main components: a light source (I), a collector lens (II), a field diaphragm (III), a field lens (IV), an aperture diaphragm (V), and a condenser lens (VI). Additionally, a prism mirror is included to improve system compactness by redirecting the light propagation path.

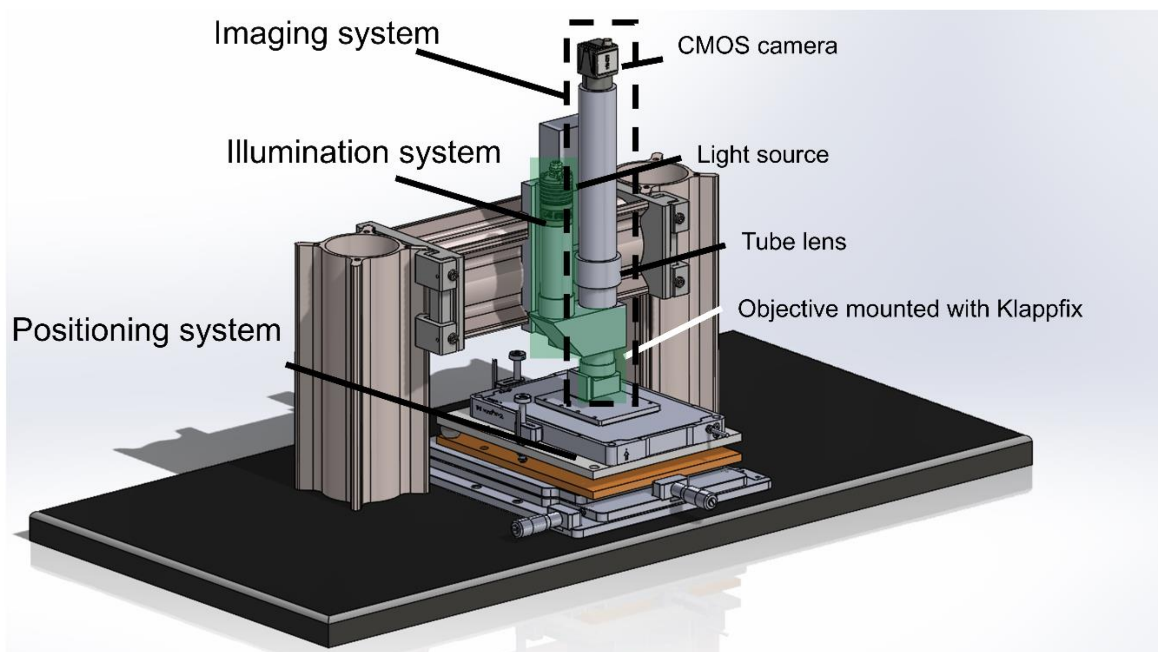

Figure 24 Computer-aided design (CAD) drawing of the hybrid microscope. Three key systems, the illumination system (colored with green), the imaging system (marked with dashed line) and positioning system are illustrated in detail, as well as some of the key components of the HM e.g. CMOS camera, light source and Mirau objective.

Overall, the light source (I in Figure 25) is a critical component of the illumination system and plays an essential role in the development of other systems within the HM, as its coherence length and nominal wavelength directly affect the measurement performance of both the IM-mode and the AFM-mode. The light sources used in the HM are high-intensity spot LEDs

manufactured by Advanced Illumination [158], namely the models SL162-WHI and SL162-590, which provide white light with a nominal wavelength of 550 nm and amber light with a nominal wavelength of 590 nm, respectively. These outputs are used for WLI and PSI measurements of the IM-mode, respectively. To ensure the accuracy of the wavelengths for measurement purposes, the spectral irradiance distributions of both light outputs are calibrated using a spectrometer, with support from the PTB working group 4.11 „Spectroradiometry" [159]. The calibration results are presented in Figure 26.

As shown in the calibration results presented in Figure 26a, the light source used for the PSI mode is a quasi-monochromatic spotlight with a centroid wavelength λ_c of 594.2 nm. The calibration was performed at full input power and at a distance of 200 mm. The spectral distribution exhibits a full width at half maximum (FWHM) of approximately 20 nm, demonstrating good coherence performance of this light source. Typically, the centroid wavelength λ_c is not sensitive to the calibration distance, but it can be significantly influenced by the input power and the light source operating temperature. For example, when the same light source is calibrated at the same distance and temperature but with the input power reduced to 50% of its full power, the centroid wavelength λ_c shifts to 589.2 nm. The calibration of the light source used for the WLI measurement is performed in the same manner as illustrated in Figure 26b. In this case, the centroid wavelength λ_c is 551.8 nm (at full power supply).

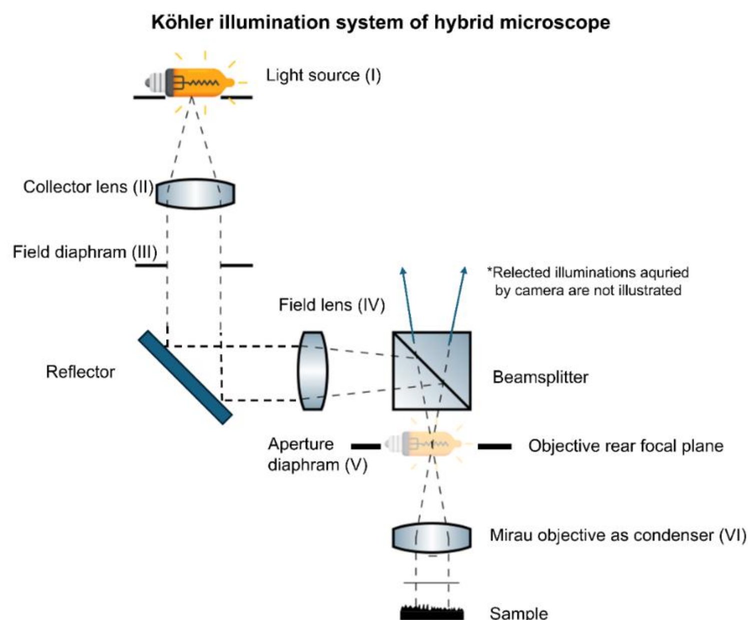

Figure 25 Illustration of the developed Köhler illumination system implemented in the hybrid microscope for evenly illuminating the sample surface. Six of its most important components are shown: light source (I), collector lens (II), field diaphragm (III), field lens (IV), aperture diaphragm (V) and condenser lens (VI).

https://doi.org/10.7795/110.20260421A

As shown in Figure 25, light beams are first emitted from the light source (I) and then pass through the collector lens (II), which is positioned at a focal length f_c in front of the light source. This lens gathers and collimates the light beams. The collimated beams are subsequently reflected by a reflector and directed toward the field lens (IV). A field diaphragm (III) is placed at the back focal plane of the field lens, corresponding to the rear focal length f_f, and is used to control the size, glare, and contrast of the illuminated area. The field lens (IV) focuses the light beams onto a plane located at its front focal length f_f, thereby forming a magnified image of the light source at that plane. An aperture diaphragm (V) is also positioned at this location. By adjusting the size of the aperture, the effective size of the light source can be modified, which in turn controls the divergence angle of the light beams contributing to the illumination field. The light beams then pass through the objective lens (VI), which functions as a condenser lens. This lens transforms the beams into a uniformly distributed illumination field at its back focal plane, which coincides with the sample position. As a result, the sample is uniformly illuminated and is not affected by either the image of the light source or its intensity distribution as detected by an intensity-sensitive detector, such as a CMOS camera.

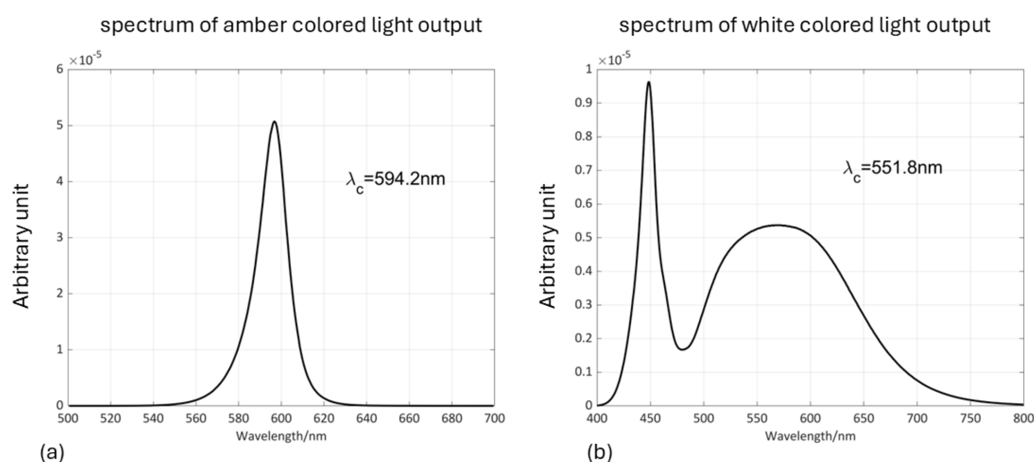

Figure 26 Spectral irradiance of the light sources applied in the HM: (a) “SL-162 590” for the amber light output measured at distance of 200 mm and (b) “SL-162 WHI” for the white-light output measured at distance of 285 mm

Another critical system is the imaging system, which is also referred to as the image forming system. To avoid issues such as spherical aberration, focus corrections, and other optical alignment challenges, an infinity corrected imaging system is preferred over a finite corrected configuration in the design of the HM. As shown in Figure 27 the imaging system implemented in the HM primarily consists of three essential components: an intensity sensitive detector (I), a tube lens (II), and an infinity corrected objective (III). A 50/50 beam splitter is placed between the objective (III) and the tube lens (II) to enable the implementation of the HM in a compact reflected light microscopy configuration. Since the sample is already illuminated by the illumination system described in Figure 25, and the image of the light source does not interfere

with the sample image, the following explanation will focus on how the image of the illuminated sample surface propagates through the optical system and is ultimately detected by the detector (I).

In the infinity corrected imaging system, the illuminated surface is located at the rear focal plane of the objective. Light beams reflected from this surface pass through the objective lens (III) and are converted into parallel beams. At this moment, no image of the surface is formed yet. These parallel beams then enter the tube lens (II), which focuses them to form an image at its back focal plane. The intensity sensitive detector (I) is positioned at this plane to capture the image and transmit the data to a computer for further measurement related processing.

The design of the infinity corrected imaging system enables additional optical components, such as a beam splitter, to be inserted between the objective lens (III) and the tube lens (II) without affecting the focus location or quality of the final image.

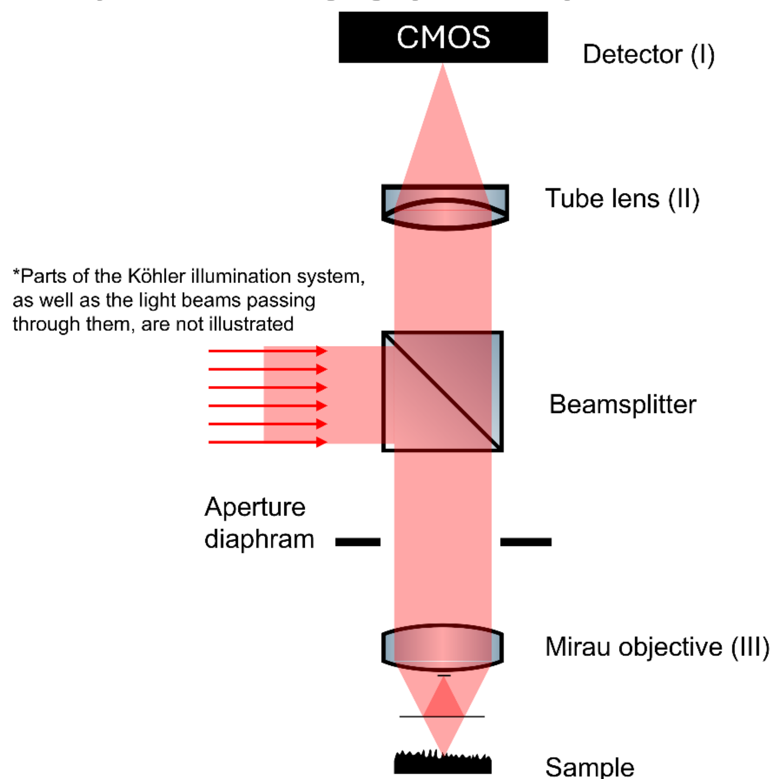

Figure 27 Illustration of the developed infinity-corrected imaging system implemented in the hybrid microscope. Three of its most important components are shown: CMOS detector (I), tube lens (II) and a Mirau objective (III).

The detector (I) used in the HM is a CMOS camera (model UI 3040CP M GL Rev.2) manufactured by the company IDS [160]. This monochromatic camera features a global shutter and operates in progressive scan mode. It achieves a frame rate of up to 243 frames

https://doi.org/10.7795/110.20260421A

per second (fps) at a resolution of 1.57 megapixels (1448 x 1086 pixels), with a pixel size of 3.45 µm by 3.45 µm. The camera allows users to define the size of the AOI and supports multi AOIs operation. Since the camera operates based on a line scan principle, reducing the width of the AOI, that is, the number of scanned lines, enables an increase in the frame rate of up to 3000 fps (measured by number of scanned lines of 8). This facilitates rapid monitoring of the interferogram.

The third system, the positioning system, also plays a critical role in the HM. Its responsibilities extend beyond the precise control of sample movement along all three spatial axes in both IM-mode and AFM-mode. It is also essential for executing sample pre-setting tasks, such as locating the measurement AOIs, adjusting the focal plane of the objective, and performing tilting operations to compensate for sample mounting errors.

To fulfill these diverse tasks, a positioning system composed of multiple integrated stages has been developed and implemented in the HM. This system is realized through the coordinated operation of four stage units: (1) a lateral coarse motion stage, type M-545 from Physik Instrumente (PI) [161]; (2) a vertical coarse motion stage, type N-216 from PI [156]; (3) a three axes piezo stage, type P-545 from PI [162]; and (4) a self-designed tilting stage.

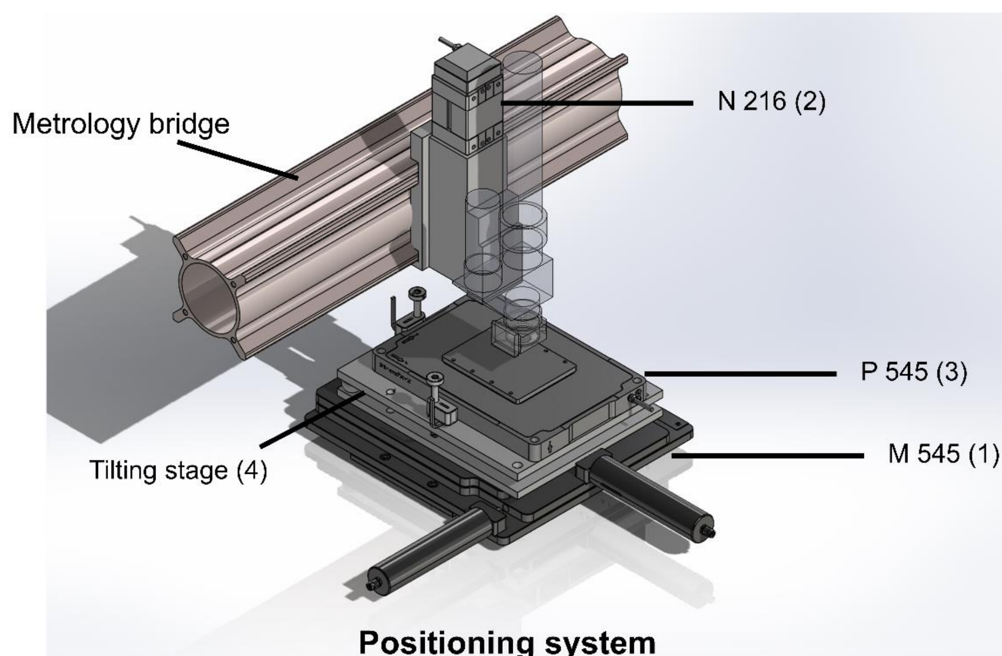

Figure 28 Positioning system, illustrated with stage units (1) a lateral coarse motion stage- type M-545, (2) a vertical coarse motion stage type N-216, (3) a three axes piezo stage type P-545 and (4) a self-designed tilting stage

As shown in Figure 28, the vertical coarse motion stage (2) is connected to the horizontal bridge of the HM and supports the fundamental structure from the side. The remaining stage units (1), (3), and (4) are arranged beneath the fundamental structure. The fast piezo stage (3) is positioned on top of the tilting stage (4), which is firmly mounted on the lateral coarse motion

stage (1). This arrangement is designed to maximize the dynamic performance of the piezo stage by minimizing unnecessary mechanical loads and external disturbances.

The movements of the lateral coarse motion stage, M-545, are driven by two linear actuators from PI. These actuators are equipped with stepper motors and allow for a minimum incremental motion of 1 µm. They independently control linear movement along the x- and y-axes, providing a travel range of 25 mm by 25 mm. This wide lateral travel capability enables efficient and precise positioning of the AOIs on the sample.

The vertical coarse motion stage, N-216, operates based on the PiezoWalk principle developed by the company PI [163], providing exceptional positioning accuracy with a resolution below 1 nm in open loop operation over a long travel range of 20 mm. With a holding force of up to 800 N, the stage ensures mechanical stability and is capable of supporting the fundamental structure of the HM from the side without any risk of instability. This stage enables precise vertical displacement between the objective and the sample, making it essential for focusing the sample at the objective's focal plane during IM-mode operation, and for performing coarse distance alignment of the tip and sample before initiating AFM measurement in the AFM-mode.

The three-axis piezo stage, P-545, is a high speed XYZ stage designed for high dynamic performance in microscopy applications. It is equipped with piezo actuators, flexure hinge structures, and piezoresistive displacement sensors. The stage can operate in both open loop and closed loop modes, providing a travel range of 70 µm in x-direction, 70 µm in y-direction, and 50 µm in z-direction.

In the IM-mode, the high positioning accuracy of the piezo stage, with a resolution of less than 1 nm, enables precise vertical displacements required for vertical scanning in WLI measurements and phase-shifting in PSI measurements. In AFM-mode, its fast response time of less than 5 ms allows for efficient raster scanning in the lateral plane, while simultaneously performing adjustments in z-direction to maintain constant tip-sample interaction.

A self-developed tilting stage is also integrated into the positioning system. It incorporates two vertically mounted actuators, specifically Picomotors from the company Newport Corporation [164], to provide or compensate for tilting angles around the x- and y-directions. These piezo linear actuators offer a travel range of 25 mm and support both manual and motorized adjustment. With the assistance of these actuators, the tilting stage enables precise control of the tilting angle within a range of ±18 degrees around each lateral direction. The stage is also spring preloaded to eliminate backlash during adjustments.

https://doi.org/10.7795/110.20260421A

The tilting angles of this stage are used to investigate the relationship between angular alignment and the measurement performance of the IM-mode, as discussed in later sections. More frequently, the stage functions as a tilting compensation mechanism, for correcting sample mounting errors during measurements conducted in both IM-mode and AFM-mode. By doing so, form errors caused by surface tilting can be significantly reduced in optical measurements. Additionally, the risk of collision between non-AFM tip components and the sample surface, caused by large tilting angles, can be avoided during AFM measurements.

4.2.2. Topography reconstruction algorithms and measurement noise

Although this dissertation does not focus on developing or optimizing interference topography reconstruction algorithms, such as the PSI and WLPSI algorithms introduced in Section 2.2.3, several primary investigations are conducted and efforts are made to enhance the measurement performance of the IM-mode developed in the HM.

Firstly, the IM-mode provides access to multiple topography reconstruction algorithms, offering users greater flexibility. These include, among others, the 3-step algorithm, the inverted T-3-step algorithm, the 4-step algorithm, the 5-step algorithm, and the symmetrical 4-step algorithm (also referred to as the 3+1-step algorithm) [69]. Depending on the measurement objective and the geometry of the measurand, users can select a suitable reconstruction algorithm or modify one to meet their specific requirements. These integrated algorithms are generally formulated as linear PSI algorithms, as described by Equ. 2.25. The main characteristic of such algorithms is that each employs a constant phase shift value to acquire its set of interferometric data. Although they differ in the number and magnitude of phase shifts, the shift value remains fixed within each algorithm [165].

One of the most direct effects of selecting different PSI algorithms for topography reconstruction is the reduction of measurement noise. Intuitively, this can be understood by considering that algorithms using a greater number of interferograms contribute more data to the topography estimation. As a result, measurement noise, particularly the contribution from camera shot noise, can be reduced. This qualitative observation can be quantitatively verified using the analysis method described in GUM [102].

Assuming that the camera shot noise follows a Poisson distribution, its STD can be denoted as σ_I. An interferogram I'_n measured by the camera at n-th phase shifts, can then be expressed as:

$$I'_n = I_{bias} + I_{mod} \cdot \cos[\Theta + \Phi_n] + \varepsilon_{I,n},\ n = 1, 2, 3\ldots n \quad \text{(Equ. 4.1)}$$

Where $\varepsilon_{I,n}$ denotes the shot noise ε_I at n-th phase shifts.

According to the Equ. 2.25, the phase difference Θ can now be estimated by taking the shot noise into account as follows:

$$\Theta(\varepsilon_{I,n}) = -arctan\left\{\frac{\sum_{n=1}^{M}[I'_n(\varepsilon_{I,n})\cdot\sin(\Phi_n)] + 2\sum_{n=M+1}^{N}[I'_n(\varepsilon_{I,n})\cdot\sin(\Phi_n)] + \sum_{n=N+1}^{N+M}[I'_n(\varepsilon_{I,n})\cdot\sin(\Phi_n)]}{\sum_{n=1}^{M}[I'_n(\varepsilon_{I,n})\cdot\cos(\Phi_n)] + 2\sum_{n=M+1}^{N}[I'_n(\varepsilon_{I,n})\cdot\cos(\Phi_n)] + \sum_{n=N+1}^{N+M}[I'_n(\varepsilon_{I,n})\cdot\cos(\Phi_n)]}\right\}$$

(Equ. 4.2)

It is emphasized that in the Equ. 4.2, N represents the number of phase shifts within a complete period of 2π, while M denotes the number of additional phase shifts measured beyond the first period in order to reduce measurement error. The relationship between N and M is illustrated in Figure 29.

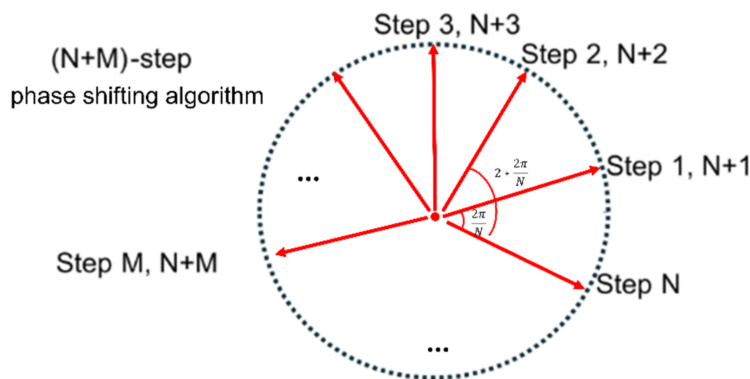

Figure 29 Relationship between phase shifts number N and additional phase shifts number M in N+M-step linear PSI algorithms, while the value of each phase shift is $\frac{2\pi}{N}$.

The propagation of the shot noise ε_I into the estimated phase Θ can be determined using analysis method introduced in GUM as follows:

$$\sigma_\Theta = \sqrt{\sum_{n=1}^{N+M} c_n{}^2\, \sigma_I^2}, \quad \text{(Equ. 4.3)}$$

where the sensitivity coefficient c_n can be estimated as follows:

$$c_n = \frac{\partial\Theta\,(\varepsilon_{I,n})}{\partial\varepsilon_{I,n}} = \begin{cases} \frac{-1}{N\cdot I_{mod}}\cdot sin(\Phi_n + \Theta); & 0 < n \le M \\ \frac{2}{N\cdot I_{mod}}\cdot sin(\Phi_n + \Theta); & M < n \le N \\ \frac{1}{N\cdot I_{mod}}\cdot sin(\Phi_n + \Theta); & N < n \le N+M \end{cases}. \quad \text{(Equ. 4.4)}$$

The σ_Θ can be expressed as a function of N and M:

https://doi.org/10.7795/110.20260421A

$$\sigma_{\Theta} = \frac{\sigma_I}{I_{mod}} \sqrt{\frac{2N - M + \sum_{n=1}^{M} \cos(2\Phi_n + 2\Theta)}{N^2}}. \qquad \text{(Equ. 4.5)}$$

Therefore, the STD of the measured surface σ_Z, which directly represents the measurement noise caused by shot noise, can also be expressed as a function of N and M:

$$\sigma_Z = \frac{\lambda \sigma_I}{4\pi \cdot I_{mod}} \sqrt{\frac{2N - M + \sum_{n=1}^{M} \cos(2\Phi_n + 2\Theta)}{N^2}}. \qquad \text{(Equ. 4.6)}$$

During a measurement, the light source and the camera operate under stable conditions; therefore, the parameter λ , I_{mod} and σ_I in Equ.4.6 can be treated as constants. Consequently, the measurement noise can be considered directly proportional to the term inside the square root:

$$\sigma_Z \propto \sqrt{\frac{2N - M + \sum_{n=1}^{M} \cos(2\Phi_n + 2\Theta)}{N^2}}. \qquad \text{(Equ. 4.7)}$$

By applying a PSI algorithm in which no additional phase shifts are taken beyond the first period $(M = 0)$ the relationship can be simplified as follows:

$$\sigma_Z \propto \frac{1}{\sqrt{N}}. \qquad \text{(Equ. 4.8)}$$

This analytical conclusion is consistent with the research of P. de Groot [114], which shows that measurement noise can be expressed as a constant noise density η_M multiplied by the square root of the measurement bandwidth:

$$\sigma_Z = \eta_M \sqrt{\frac{P_A}{t}}, \qquad \text{(Equ. 4.9)}$$

where the measurement bandwidth is represented by the ratio of the corresponding array size P_A to the data acquisition time t.

In this context, the array size P_A remains equal to the pixel number of the CMOS camera used in the IM-mode measurement of the HM. Since no additional lateral filtering is applied during post-processing, value of P_A is held constant. Consequently, the measurement noise can be considered as dependent only on the data acquisition time t. The variable t can, in turn, be expressed as the product of the unit data acquisition time t_0 and the total number of acquired interferograms N. Therefore, Equ. 4.9 can be rewritten as a function of the interferogram number N:

$$\sigma_Z = \eta_M \sqrt{\frac{P_A}{t_0}} \cdot \sqrt{\frac{1}{N}}. \qquad \text{(Equ. 4.10)}$$

When using an $N+M$-step linear PSI algorithm with $M \neq 0$, the situation becomes more complex. As indicated by Equ. 4.7, the measurement noise σ_Z can be further reduced by incorporating additional M steps into the algorithm. However, two important considerations must be taken into account:

(I) Adding M steps interferogram acquired outside the first period does not have the same effect as increasing the number of sampling points within the first period. A weighting factor must be introduced into the evaluation of measurement noise to account for these M additional acquisitions.

(II) if M is not an integer multiple of half the value of N, the summation $\sum_{n=1}^{M}\cos(2\Phi_n + 2\Theta)$ will not cancel out to zero. As a result, the measurement noise will exhibit a dependency on the phase Θ.

Another approach to further improving measurement performance by reducing measurement noise involves the integration of several commonly used physical noise reduction techniques into the development of the IM-mode. One such technique is interferogram averaging. In contrast to the conventional approach, in which only one interferogram is acquired at each phase-shift position, interferogram averaging involves recording N_I interferograms at each phase step and averaging them prior to phase evaluation:

$$I'_n = \frac{\sum_{i=1}^{N_I} I'_{n,i}(\varepsilon_{n,i})}{N_I}, \qquad \text{(Equ. 4.11)}$$

where the N_I denotes the number of acquired interferogram images at the n-th phase shifts, and $\varepsilon_{n,i}$ is the noise added to the measured interferogram $I'_{n,i}$. Due to the random nature of noise, averaging process like Equ. 4.11 can greatly suppress the negative impacts of the noise on the measurement results.

Another common noise reduction technique applied is topography averaging, which produces a low-noise topography by averaging repeated measurements of the same surface:

$$H = \frac{\sum_{i=1}^{N_H} H_i}{N_H} \qquad \text{(Equ. 4.12)}$$

Where the N_H denotes the number of repeat measurements H_i.

To verify the effectiveness of the two aforementioned approaches for improving measurement performance, measurement noise is characterized over a flat region of the CCS sample, which exhibits a low, well-characterized surface roughness (approximately $S\text{q}$=0.3 nm [12]). The

https://doi.org/10.7795/110.20260421A

evaluation follows the subtraction method recommended by ISO [5], as described in Equ. 3.30 and Equ.3.31.

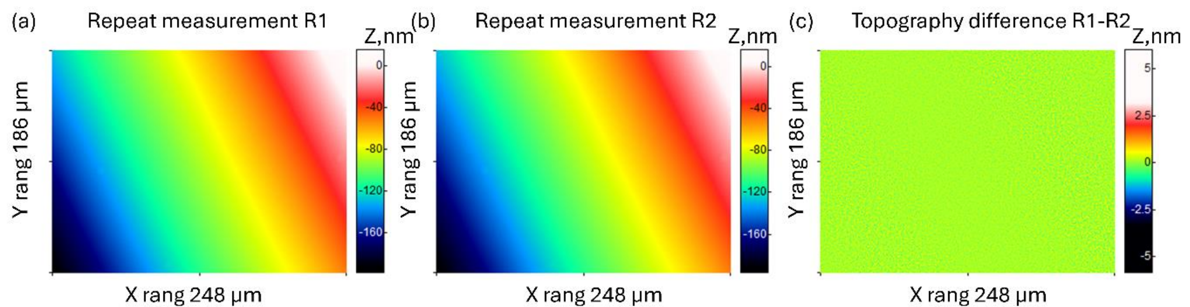

Figure 30 Repeat measurements of a flat surface on CCS material measure for measurement noise characterization using 3 step PSI algorithm: (a) and (b) are repeated flat surface measurements and (c) is a topography difference, obtained by subtracting (a) measurements from (b) and processed with spatial high-pass filter (cut off wavelength 8 µm) for eliminating the impacts of the random form error.

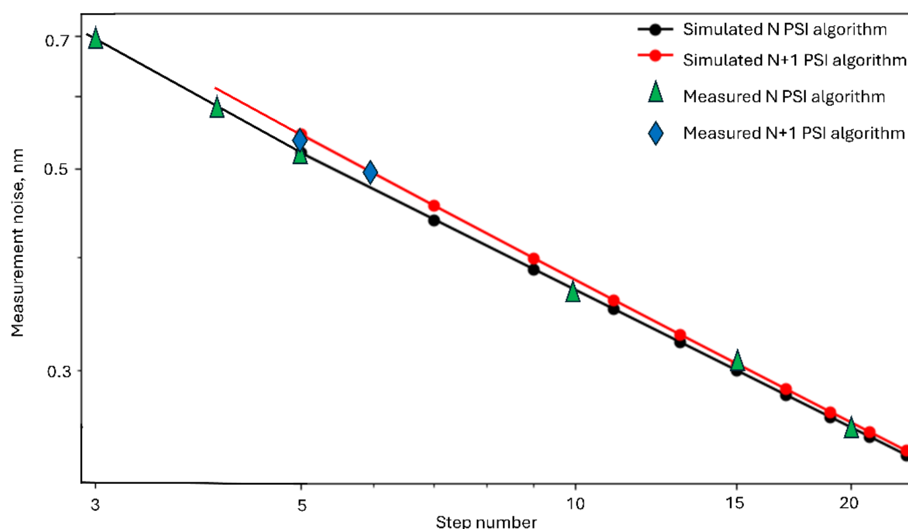

Figure 31 Measurement noises theoretically and experimentally characterized by repeat measurements applying different PSI algorithms

As an example, two repeated PSI measurements are performed over an area of 248 µm x 186 µm using a 20x Mirau objective with a NA of 0.4. The measurements are shown in Figure 30a and Figure 30b respectively. A 3-step PSI algorithm is applied for topography reconstruction (N=3 and M=0). The resulting topography difference ΔH is calculated according to the Equ.3.31 and subsequently processed using a spatial high pass filter (L-filter) with a cutoff wavelength of 8 µm). The filtered topography is illustrated in Figure 30c. This topography difference is then used to evaluate the measurement noise based on Equ. 3.30. The resulting noise level is approximately 0.69 nm.

Furthermore, the dependence of measurement noise on the applied PSI algorithm is investigated. Both commonly used N-steps algorithm (such as the standard linear 3-, 4-, and

5-step algorithms) and N+M-step linear PSI algorithms (such as the Schwider–Hariharan 5-step algorithm and the symmetrical 6-step algorithm) [69] are theoretically and experimentally evaluated through repeated measurements on a flat region of the CCS sample for noise characterization. The theoretical estimation is conducted using a Monte Carlo method [102], based on the simulation model described in Equ. 4.1. The characterization results are presented in Figure 31.

As shown in Figure 31, the simulated noise curves exhibit good agreement with the experimentally measured noise levels. Both sets of data indicate that different PSI algorithms exhibit varying sensitivities to measurement noise. In general, PSI algorithms that involve a greater number of phase steps tend to yield lower noise levels. This is attributed to the fact that algorithms with more steps incorporate a larger number of interferograms into the topography reconstruction process. As noise is inherently random, the increased number of data points enhances the averaging effect within the algorithm, thereby reducing the overall influence of noise on the final measurement result.

Another observation is that PSI algorithms with the same total number of steps tend to produce similar noise levels. However, the measurement noise level obtained using standard N-steps PSI algorithm (e.g. 5-steps algorithm with $N = 5$ and $M = 0$) is generally lower than that of N+1-steps algorithms (e.g. symmetrical 4+1 steps algorithm with $N = 4$ and $M = 1$). Moreover, when the value of M remains unchanged, but N value increases, the noise levels tend to decrease in a continuous way. This trend can be explained by Equ. 4.7, which shows that the measurement noise is primarily influenced by the value of N.

Indeed, the two physical noise reduction techniques introduced in Equ. 4.11 and Equ. 4.12 are both based on the same underlying principle for achieving noise suppression: increasing the number of interferograms used in topography reconstruction. To describe this more generally, a new parameter N_t is introduced, representing the total number of interferograms involved in the reconstruction process:

$$N_t = (N + kM) \cdot N_I \cdot N_H. \qquad \text{(Equ. 4.13)}$$

Here k is introduced as a weighting factor, since in Equ. 4.7 is already indicates that N and M do not contribute equally to the evaluation of measurement noise. The value of k lies between 0…1 and depends on the specific values of N and M in the applied PSI algorithm. An investigation is conducted to evaluate the relationship between measurement noise and the total number of interferograms N_t. The results are summarized in Figure 32.

https://doi.org/10.7795/110.20260421A

In this investigation, measurement noise is analyzed as a function of increasing N_t , achieved by increasing the total number of phase steps (i.e., sum of $N + kM$) in the PSI algorithm, with or without the application of one or both physical noise reduction techniques.

The calibrated measurement noise obtained using a 3-step PSI algorithm (N_t equals 3, calculated with $N = 3$, $M = 0$, $N_I = 1$ and N_H=1) is approximately 0.69 nm. This value is considered the worst possible noise level, denoted $N_{M,max}$, as it is determined using a PSI algorithm with the minimum number of interferograms applied in topography reconstruction. Noise measurements performed with increased total phase step numbers N_t, without applying any additional noise reduction techniques (N is equal to the total number of steps N_t), are indicated as red dots in Figure 32. Both the experimental and theoretical results indicate that measurement noise decreases when N is increased, while all other parameters in Equ. 4.13 are held constant. For example, measurement results show that increasing N from 3 to 20 reduces the noise level from 0.69 nm to 0.27 nm.

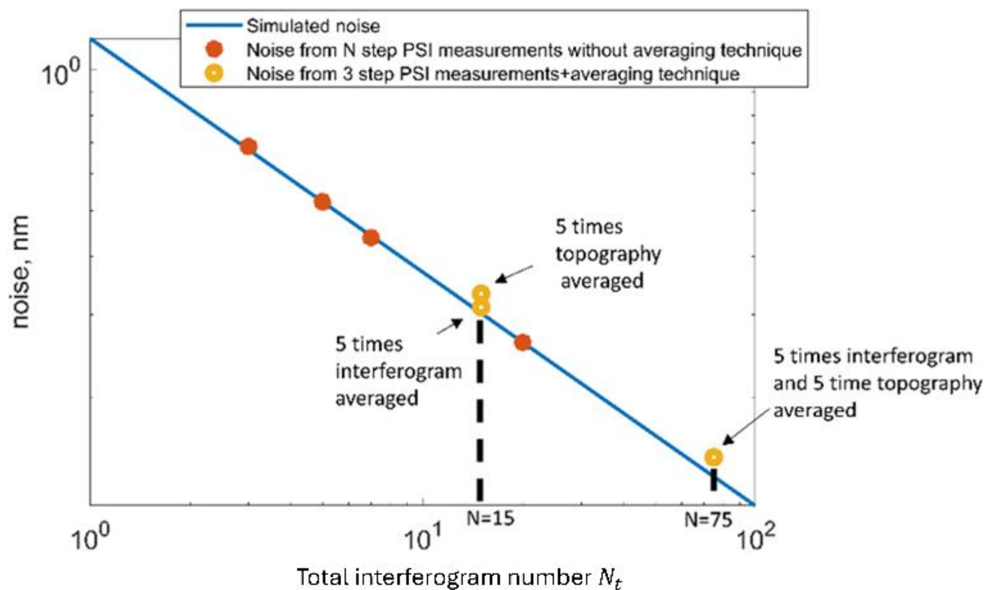

Figure 32 Measurement noise vs total interferogram number N_t. Blue curve is the same simulated noise curve shown in Figure 31 while keep M=0 and the red dots are denoting the measurement noises evaluated by applying the linear PSI algorithm with N= 3, 5, 7 and 20 while M=0. These evaluated measurement noises are not processed with physical noise reduction techniques. The yellow dots denote the measurement noises of using 3 step linear PSI algorithm (N=3 and M=0) with applicating of corresponding noise reduction technique (topography and interferogram averaging technique).

Measurements obtained using a 3-step PSI algorithm in combination with at least one noise reduction technique are represented by yellow dots. Compared to $N_{M,max}$, all noise values estimated with the application of noise reduction techniques are significantly lower. This clearly demonstrates the high effectiveness of these techniques in suppressing measurement noise.

https://doi.org/10.7795/110.20260421A

As shown in Figure 32, when $N_t = 15$, the measurement noise obtained using either the topography-averaging technique ($N = 3$, $M = 0$, $N_I = 1$ and $N_H = 5$) or interferogram-averaging technique ($N = 3$, $M = 0$, $N_I = 5$ and $N_H = 1$) is 0.31 nm and 0.33 nm, respectively. These values are slightly higher than the simulated noise level of 0.30 nm, which corresponds to the configuration ($N = 15$, $M = 0$, $N_I = 1$ and $N_H = 1$).

This observation indicates that, even when the total interferogram number N_t is fixed, increasing the number of interferograms within the first period ("oversampling" the vertical scanning range) is the most effective method for suppressing measurement noise compared to applying physical noise reduction techniques. On one hand, a larger number of phase steps N improves the accuracy of phase estimation in phase-shifting interferometry, resulting in better performance than configurations that rely on increased values of N_I and N_H for noise averaging. On the other hand, the use of averaging techniques may introduce additional noise sources. For instance, potential sources include short-term instability of the positioning stage during interferogram averaging and limited reproducibility of stage positioning during topography averaging.

4.2.3. Calibration of bandwidth characteristics using the material measure CCS

The material measure CCS enables a straightforward and efficient evaluation of the measurement performance of the IM-mode of the HM through characterizing the ITF from its measurement results, particularly for assessing its bandwidth characteristics. The patterns of the CCS [12] are designed in a range of sizes, with diameters varying from 60 µm to 600 µm. This design makes the CCS applicable to a wide range of objectives. Currently, the IM-mode of the HM supports measurements with all objectives listed in Table 1, ranging from 10x to 100x, using both implemented optical measurement modes (PSI and WLI). For clarity, however, PSI measurements obtained using the 20x Mirau objective, which provides a FOV of 248 µm x 186 µm, are selected to demonstrate this characterization process.

To ensure the accuracy of ITF characterization using the CCS, the lateral amplification coefficients, also referred to as lateral scaling factors, of IM measurements must be properly calibrated and corrected in advance. In general, the scaling factors of a 3D areal surface measuring instrument are calibrated independently along the x-, y-, and z-directions. The standard approach for this calibration involves performing reference and calibration measurements on a 2D grating standard to determine the scaling factors in the lateral (x and

https://doi.org/10.7795/110.20260421A

y) directions, and on one or more step height standards to determine the scaling factor in the vertical (z) direction.

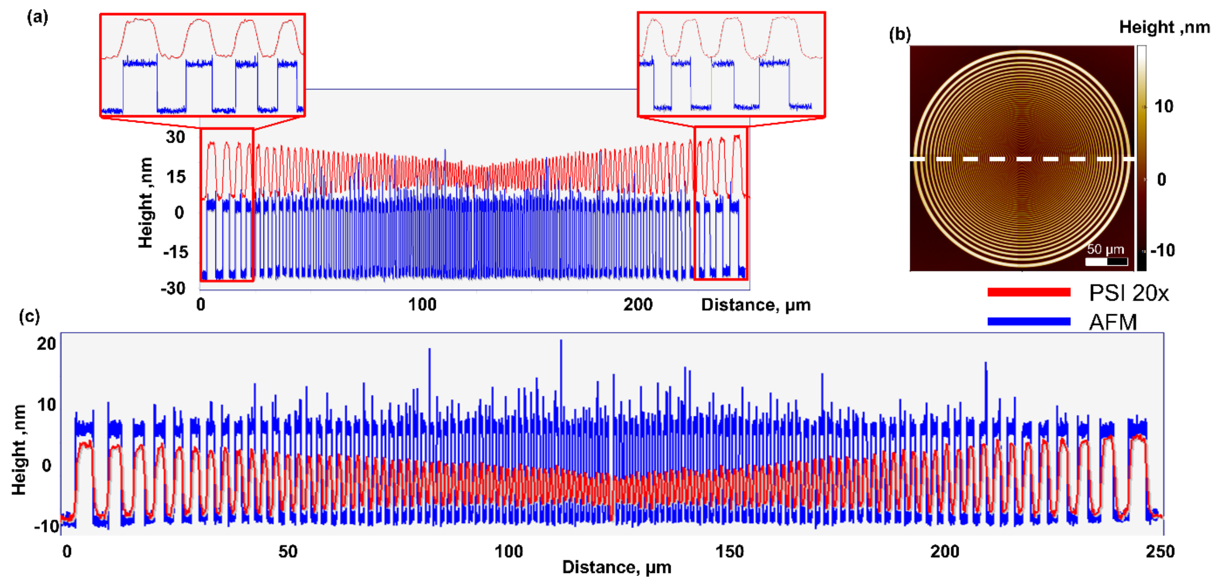

Figure 33 Calibration of the lateral scaling factors using the CCS material measure, demonstrated using the C33 pattern for 20x PSI measurements. (a) Horizontal diametrical profiles extracted from reference data measured with metrological AFM (blue) and horizontal diametrical profile extracted from calibration data measured with 4+1 step PSI algorithm (red). (b) An overview of CCS C33 pattern with pattern radius of 120 µm, the image is stitched with four PSI measurements. The position of the extracted diametrical profile is marked in white dashed line; (c) Profile comparison between reference data (blue) and calibration data (red) after correction with scaling factor (k_x =0.9946).

Calibrating the scaling factors using the CCS sample reduces the need for multiple standards and simplifies the process by eliminating additional reference measurements. A single reference measurement on the CCS sample is sufficient for both scaling factor determination and ITF characterization. Although the CCS is primarily designed for ITF characterization, its isotropic circular structure (see Figure 33b) also facilitates the determination of lateral scaling factors. While the scaling factor in the z-direction is one of the ITF parameters (denoted as k in ITF fitting function shown in Equ. 3.34), it can be characterized in parallel with the ITF curve. Therefore, this section focuses exclusively on the calibration of the lateral scaling factors.

The calibration of lateral scaling factors using the C33 pattern of the CCS sample is illustrated in detail in Figure 33. Diametrical profiles extracted from reference data, measured with a metrological AFM [14], and from calibration data, acquired using the 4+1-step algorithm of PSI mode of the HM, are employed for this purpose. For example, horizontal profiles extracted from the same radial position of the CCS pattern at a radial angle of zero (indicated by the white dashed line in Figure 33b) are used to calibrate the horizontal scaling factor k_x (in x-direction). Two such profiles, corresponding to the AFM reference (blue) and PSI calibration

(red) data, are shown in Figure 33a. Similarly, profiles extracted at a radial angle of 90 degrees are used to calibrate the scaling factor k_y.

It should be noted that the width of the FOV is approximately 186 µm when using the 20x objective, which is insufficient to capture the entire C33 pattern (with a radius of 120 µm) in a single measurement. Therefore, to calibrate the lateral scaling factor along the width (in y-direction), either the outer regions of the pattern are excluded if not captured, or a stitching technique is employed to reconstruct the full pattern from multiple PSI measurements, as illustrated in Figure 33b.

The presence of a scaling issue becomes evident when comparing the measured CCS structures between calibration and reference data. As shown in Figure 33a, two raw profiles are aligned at their left endpoints, but a noticeable deviation appears at the right end. This discrepancy is attributed to a mismatch in scaling. For clarity, the reference profile is vertically shifted by 30 nm in the plot to improve the visibility of such error. To correct this error, a horizontal scaling factor k_x is applied to the calibration profile so that both ends of the CCS structure align with the reference data. The correlation coefficient between the reference profile and the corrected calibration profile is used as a quantitative indicator of the accuracy of the correction.

Assuming a 2D analog profile along x-direction $H(x)$ serves as the input topographical signal for both the reference and calibration measurements. The output signals of these measurements, the resulting profiles, after acquisition with N sampling points, can be expressed as functions of the coordinate in the x-direction. These are denoted as H_r for the reference profile and H_c for the calibration profile, respectively:

$$H_r = [H_{r1}, H_{r2} \dots H_{rN}], \quad \text{(Equ. 4.14)}$$

and

$$H_c = [H_{c1}, H_{c2} \dots H_{cN}]. \quad \text{(Equ. 4.15)}$$

They are measured over the same x-axis:

$$x = [x_1, x_2 \dots x_N]. \quad \text{(Equ. 4.16)}$$

Then the cross-correlation coefficient ρ of these measured profiles is defined as:

$$\rho = \frac{1}{N-1} \sum_{n=1}^{N} \left(\frac{H_r(x_n) - \overline{H_r}}{\sigma_r} \right) \left(\frac{H_c(x_n) - \overline{H_c}}{\sigma_c} \right), \quad \text{(Equ. 4.17)}$$

https://doi.org/10.7795/110.20260421A

where the $\overline{H_r}$ and $\overline{H_c}$ are the mean values of the reference and calibration profiles, respectively, and σ_r and σ_c represent the STD of the reference and calibration profiles. This coefficient serves as a quantitative measure of similarity between the two profiles after applying the scaling correction.

Due to the scaling issue, although both discrete profiles have same N sampling points, the calibrated profiles H_c does not correctly representing the topography H. As a consequence, the cross-correlation coefficient ρ will deviate significantly from 1, indicating a lack of strong positive correlation between the reference and calibration profiles.

Therefore, a scaling factor k_x must be introduced to correct the scaling discrepancy. By selecting an appropriate value for k_x and without accounting for any amplitude attenuation in the calibration profile, the following condition is satisfied:

$$H_r(x) \approx H_c(k_x x). \qquad \text{(Equ. 4.18)}$$

Consequently, after applying the correction, both profiles represent the same topography H, and the cross-correlation coefficient ρ reaches its maximum value. In this case, the coefficient should be very close to, or even equal to, 1, indicating near-perfect agreement. By identifying the value of k_x that yields the maximum cross-correlation, the optimal scaling factor in x-direction can be determined. This method can be applied to determine the scaling factor k_y in y-direction in the same way. An example of the corrected profile comparison is shown in Figure 33c, where the optimal value of k_x is determined to be 0.995, resulting in excellent alignment of the structural features on both ends.

Table 2 Calibrated lateral scaling factors using different objectives with the PSI mode (4+1 steps algorithm) in the hybrid microscope

Objective magnification	Averaged $\boldsymbol{k_x}$	Averaged $\boldsymbol{k_y}$
10x	**0.997**	**0.997**
20x	**0.992**	**0.992**
100x	**0.990**	**0.990**

In practice, at least three successive measurements are performed on different CCS patterns of the same design size to calibrate the lateral scaling factors using the method described above. Performing multiple measurements allows for averaging of the evaluated scaling factors, thereby enhancing the accuracy and reliability of the calibration. The calibrated lateral

https://doi.org/10.7795/110.20260421A

scaling factors k_x and k_y, obtained from PSI measurements using three different objectives (10x, 20x, and 100x), are summarized in Table 2.

From the results presented in Table 2, two key observations can be made. First, there is a clear agreement between k_x and k_y for each applied objective. This indicates that no significant discrepancies exist between the lateral axes within the developed IM-mode, suggesting that the system exhibits geometrical isotropy in the lateral directions. Second, the lateral scaling factors vary depending on the objective used. This variation primarily arises from the optical characteristics of the different objectives and cannot be easily resolved through hardware modifications. However, the issue can be effectively corrected through software. By performing calibrations to determine the scaling factors specific to each objective, and by incorporating a corresponding scaling correction algorithm into the topography reconstruction process, the influence of this variation on the measurement results can be effectively eliminated.

Furthermore, the same calibration procedures for lateral scaling factors are applied to both the WLI mode and the PSI mode using alternative PSI algorithms. In both cases, measurements are conducted with the 20x objective. The results are consistent with the values presented in Table 2. This consistency arises because the scaling issue is fundamentally a geometrical problem, primarily determined by the optical configuration, such as the objectives and tube lens. As long as the interferograms are captured under the same optical configuration, the calibration results remain largely independent of the specific topography reconstruction algorithm applied, whether WLI or PSI algorithm.

After the lateral scale issue has been thoroughly corrected, characterization of ITF of the developed IM-mode can be performed using the available material measure CCS and its reference measurements [12]. Generally, ITF reveals the bandwidth property of an instrument. Since the HM incorporates different objectives corresponding to varying FOV sizes, different sizes of CCS patterns are applied for ITF characterization when using different objectives.

From the smallest to the largest objective magnification, the corresponding FOV sizes for 10x, 20x, and 100x objectives are 496 µm x 372 µm, 247 µm x 185 µm, and 49 µm x 37 µm, respectively. Therefore, the ITF characterization of each objective will be carried out with CCS patterns:

- Circular chirp patterns with a radius of 30 µm are used for the 100x objective, including C11 which consists spatial wavelength from 0.1 µm to 5.0 µm, C12 from 0.5 µm to 15.0 µm and C13 from 1.0 µm to 7.5 µm.

https://doi.org/10.7795/110.20260421A

- Circular chirp patterns with a radius of 120 µm are used for the 20x objective, including C31 which consists spatial wavelength from 0.4 µm to 20.0 µm, C32 from 0.8 µm to 20.0 µm and C33 from 1.2 µm to 8.6 µm.
- Circular chirp patterns with a radius of 150 µm are used for the 10x objective, including C41 which consists spatial wavelength from 0.8 µm to 10.3 µm, C42 from 2.4 µm to 20.0 µm and C43 from 4.8 µm to 10.2 µm.

Additionally, the CCS sample includes a set of circular discrete grating patterns (Z01 to Z05) with spatial wavelengths ranging from 0.8 µm to 12.0 µm and a radius of 120 µm, which are well-suited to the FOV of the HM when using the 20x objective. Therefore, the ITF of the IM-mode while equipping the 20x objective can be also effectively characterized using these patterns.

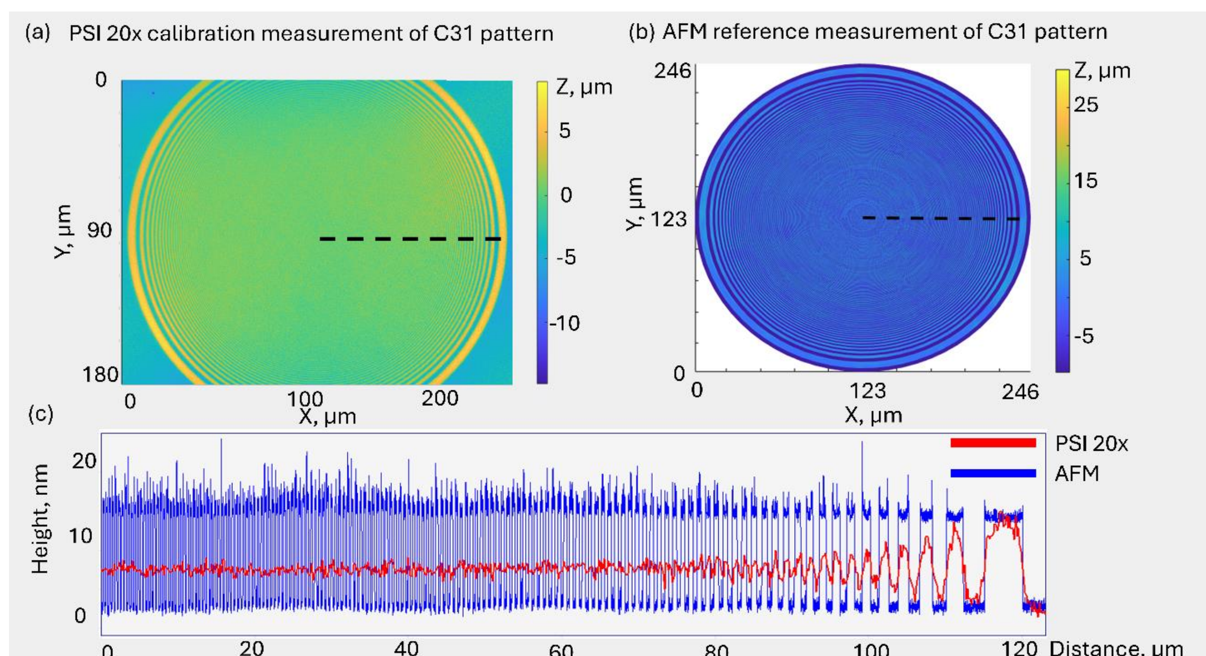

Figure 34 Data pre-processing of the ITF characterization using material measure CCS in example of C31 pattern. (a) Calibration data measured by 20x objective in PSI mode of hybrid microscope. (b) Reference data measured by a metrological AFM. (c) Comparison of the radial profiles extracted at the same angular position of the CCS circular pattern, as marked in (a) and (b), respectively.

The ITF calibration procedure applied in this work follows the method established in our previous study [12]. According to this procedure, both the calibration and reference measurements of the CCS pattern are first transformed into radial profiles as part of the data pre-processing. An example of this pre-processing is shown in Figure 34, using measurements of the circular chirp pattern C31 (radius of 120 µm, with a designed structure wavelength ranging from 0.4 µm to 20.0 µm). In general, it is recommended to perform ITF calibration measurements by aligning the geometrical center of the FOV with the center of the CCS

pattern, ensuring that the entire circular structure is fully captured within the FOV. However, for rectangular FOVs (as shown in Figure 34a), capturing the entire circular structure is not always feasible, which may complicate the subsequent evaluation of the isotropic properties of the ITF. Further details regarding this limitation will be provided in the following sections.

After the calibration data are acquired using the IM-mode of the HM, both calibration (Figure 34a) and reference data (Figure 34b) must be pre-processed before ITF evaluation. In this pre-processing step, the data are first prepared using cropping and leveling functions. These operations serve to localize the CCS pattern and to correct for sample mounting errors, respectively. The determination of the location of pattern center in both datasets is also performed during this step. Following this, radial profiles at identical angular positions are extracted from both the calibration and reference datasets. These profiles are then trimmed so that they all begin at the identified pattern center and extend to the outermost structure of the CCS pattern, as illustrated in Figure 34c.

The ITF characterization begins by processing the reference and calibration radial profiles at the same angular direction, as described in Equ. 3.35, using our self-developed ITF characterization software. The software then generates the raw ITF curve corresponding to this angular direction. By repeating this procedure with measurements of different CCS patterns, the resulting calibration bandwidth can be extended in a complementary manner, similar to assembling puzzle pieces, as each pattern contributes its own spatial frequency range. The ITF characterization concludes by smoothing the raw ITF curves using a fitting function (Equ. 3.34), which helps reduce ripple effects introduced by the binarized nature of the CCS structures. Examples of characterized and fitted ITFs are shown in Figure 35. For further details on the ITF characterization procedure, please refer to paper [12].

In the example shown in Figure 35, the characterized ITFs are evaluated based on 0° radial profiles obtained from PSI mode measurements using the 20x objective of the HM. The raw ITF curves plotted in blue, red, and yellow are evaluated based on measurements of circular chirp patterns, while the round markers in the corresponding colors represent discrete ITF values obtained from measurements of circular discrete grating patterns. A smoothed ITF curve, fitted using all raw ITF data, is plotted as a orange line and parameterized by $k{=}0.95, m{=}2.57\ \mu\mathrm{m}$ and $n{=}1.76$. Additionally, a green dashed line marks the -6 dB gain level to indicate the cut-off frequency of the ITF curve, corresponding to a 50% reduction in gain. In this case, the cut-off frequency is approximately 0.38 μm^{-1}, corresponding to a lateral period limit D_{LIM} of about 2.63 µm, where D_{LIM} is defined as the spatial period at which the ITF gain falls below -6 dB. This means that features with lateral periods smaller than 2.63 µm will experience at least a 50% reduction in measured amplitude. More conservatively, this

https://doi.org/10.7795/110.20260421A

suggests that features narrower than 2.63 µm may not be reliably captured by the PSI mode of the HM when using the 20x objective.

By comparing the D_{LIM} values across all angular directions, the angular dependence of the lateral resolution can be assessed. This enables straightforward identification of angular asymmetries in the performance of the measuring instrument. In this study, ITF measurements obtained in PSI mode with the 20x objective are used to demonstrate the anisotropic behavior of the HM. The results are summarized in Figure 36.

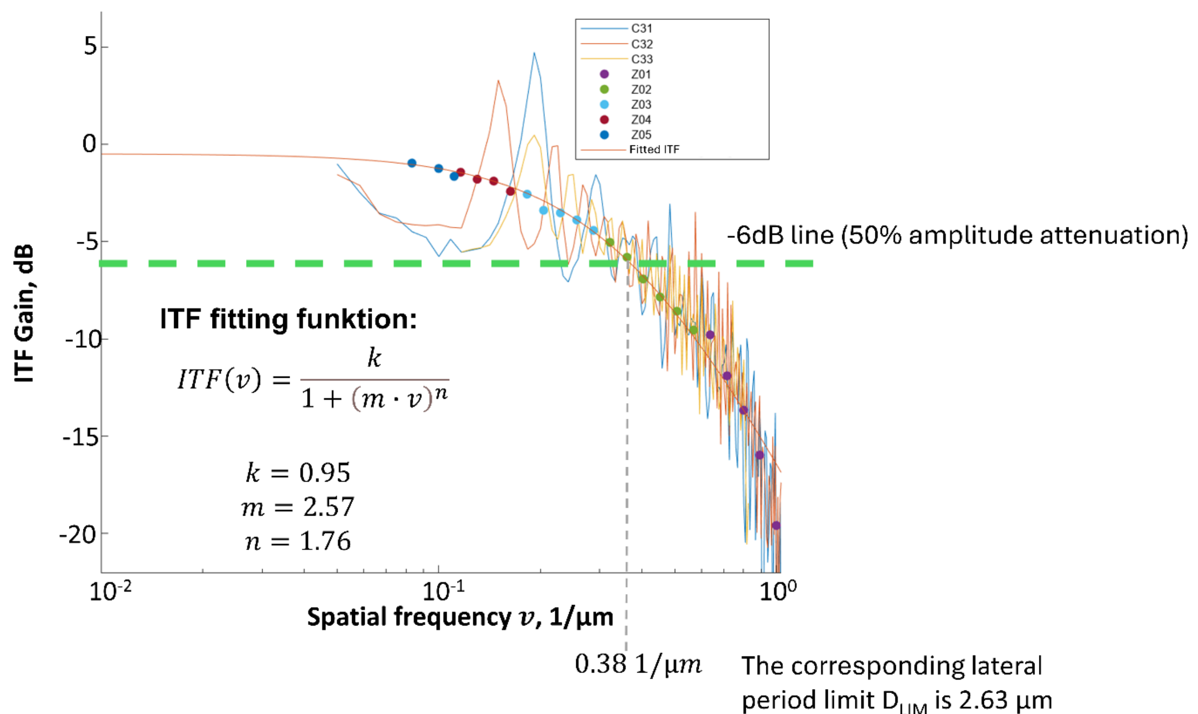

Figure 35 Characterized ITFs at the angular direction 0°, evaluated based on PSI 20x measurements of CCS patterns C31-C33 (in colored lines) and Z01-Z05 (in colored dots). Smoothed ITF curve (orange) fitted from evaluated ITF data (colored lines and dots). A –6 dB reference line, where the measured amplitude drop is cross 50% of its reference value, indicates a cross-over at 0.38 1/µm with the fitted ITF.

From the results shown in Figure 36, no strong anisotropic characteristics are observed. The contour shape exhibits relatively good roundness, indicating consistent lateral resolution along different angular directions. In contrast to the results obtained from a commercial instrument reported in our previous study [12], no symmetrical anisotropy is detected in our developed HM system. The global maximum and minimum of the lateral period limit are found at 192° and 275°, respectively, corresponding to an absolute difference of approximately 300 nm in resolvable structure size. Relative to the mean lateral period limit over all angular directions, this corresponds to an overall variation of about 12%, while the maximum deviation from the mean remains below 8%. These asymmetrical deviations may be attributed to imperfections in the optical components, such as the aspherical objective lens.

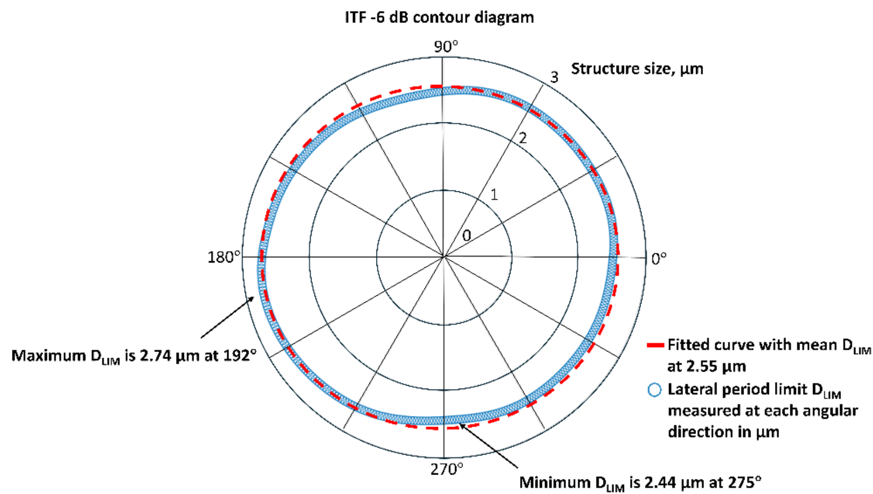

Figure 36 Angular dependency of evaluated ITF based on 20x PSI measurements represented by the -6 dB contour of ITF vs structure size in µm. The lateral period limits at each angular directions are plotted in blue circles. They can be fitted with circle fitting algorithm into the red dashed circle with average lateral period limit of 2.55 µm. The roundness of the contour indicates good isotropy characteristic of the HM.

4.2.4. Repeatability of the IM-mode

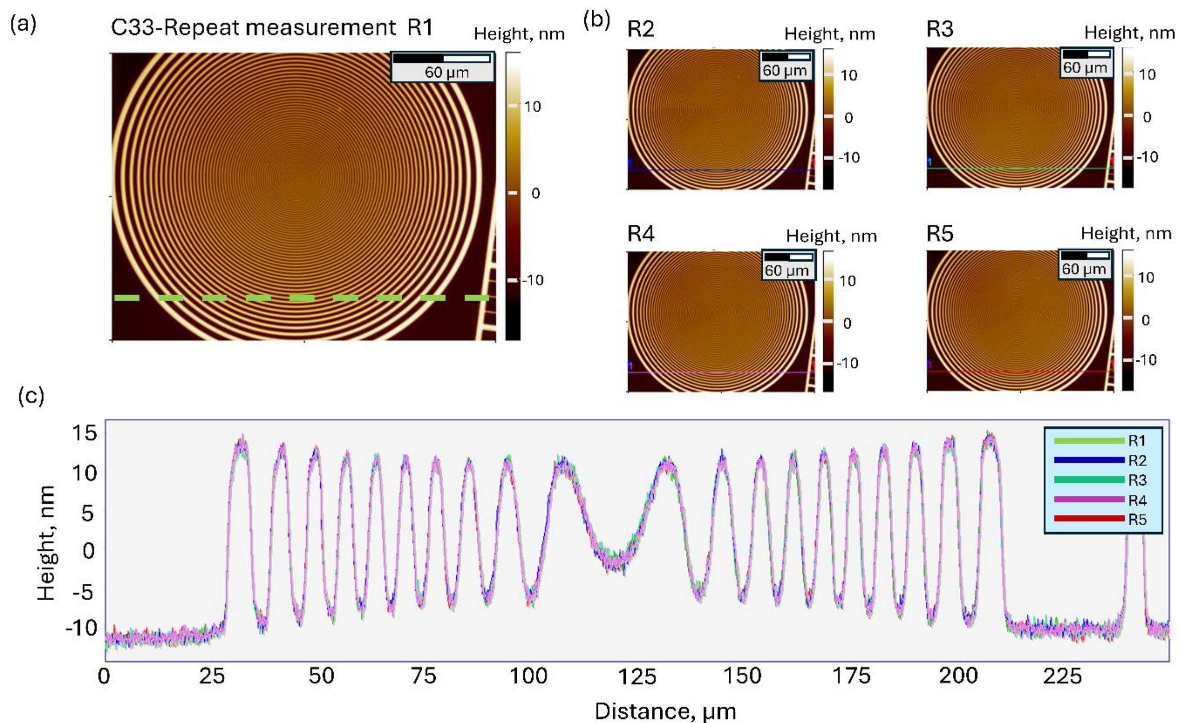

Figure 37 Repeat measurements of C33 pattern. (a) One of the 5 successively measured topographies captured using PSI 4+1-steps topography reconstruction algorithm. (b) Rest of four repeat measurements (c) Profiles comparison of the repeat measurements, which are extracted from a randomly selected horizonal position marked in (a).

https://doi.org/10.7795/110.20260421A

Repeatability is also one of the essential performance-related characteristics of an areal surface measuring instrument. It indicates the instrument's ability to produce consistent measurement results under the same measurement condition. In our investigation, repeated measurements were performed on various samples with different material compositions and surface structures to evaluate the repeatability of the developed IM-mode of the HM. For clarity, this section focuses on a representative practical case, illustrated in Figure 37 to demonstrate the repeatability of the IM-mode. In this case, five successive PSI measurements were acquired using the 20x objective within a short measurement window of three minutes. This short measurement window was selected to minimize variations in environmental conditions, such as temperature, air pressure, and humidity, thereby allowing the analysis to focus on the short-term repeatability of the IM-mode.

The high similarity between the measured topographies and the good overlap of the extracted profiles indicates the excellent repeatability of the developed IM-mode of the HM. The largest STD observed over the measured topographies is 2.0 nm, demonstrating good short-term repeatability. The primary source of this variation is lateral vibration of the sample, which causes the underlying surface structure to influence the repeatability evaluation. When a flat surface is been measured instead, this effect is minimized, and the evaluated STD decreases significantly to approximately 0.5 nm. This reduced value aligns closely with the measurement noise level discussed in the previous section.

4.3. Realization of the AFM-mode in the hybrid microscope

This section presents one of the main focuses of this dissertation: the development of the AFM-mode in the HM. It addresses two key aspects. First, the working principle and system design of the implemented AFM-mode, which, in contrast to conventional AFM design, employs a novel readout system based on an interferometric principle to enable AFM measurements. Second, the performance evaluation of the developed AFM-mode, including measurement accuracy, traceability calibration, noise characterization, and other measurement performance related aspects.

4.3.1. Working principle of the AFM-mode

The AFM-mode of HM is innovatively developed. To the best of our knowledge, no AFM shares the same working principle as our own developed AFM-mode. Compared to a classical type of AFM instrument, which typically incorporates an optical-lever system to read out the cantilever deformations caused by sample-tip interactions, the AFM-mode employs an

https://doi.org/10.7795/110.20260421A

interferometric readout system to detect these deformations. At the same time, it maintains high synergistic compatibility with the developed IM-mode, meaning that no additional optical or electrical components are necessary for the realization of the AFM-mode, such as QPD or laser source.

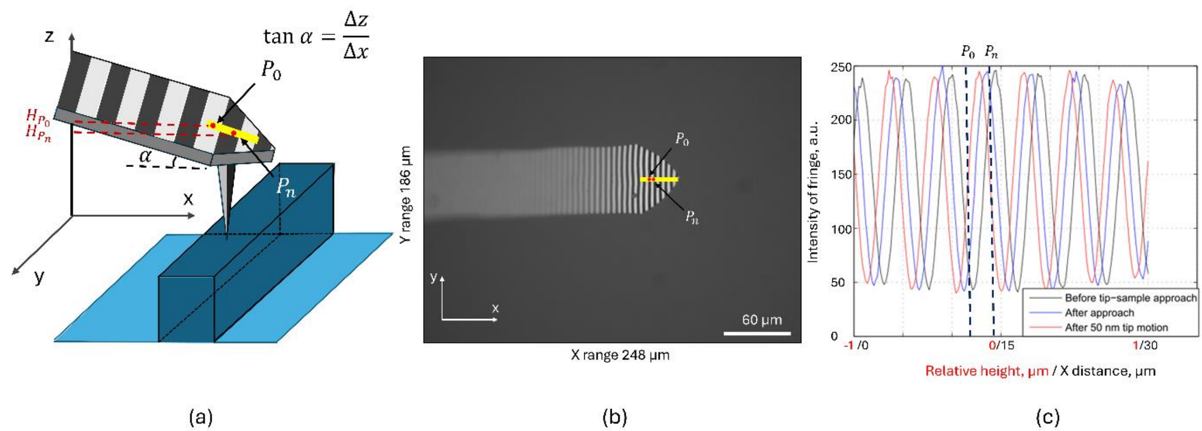

Figure 38 Schematic illustration of the working principle of the AFM-mode developed in the HM. (a) A tilted AFM cantilever with tilting angle α is demonstrated in the figure. The black-and-white fringes on its backside are used to illustrate how the tilted topography is transformed into a phase map. In practice, they can only be observed under the camera with application of interferometric objective, since the interference is generated between the cantilever-reflected beam and the reference beam from reflected the reference mirror. They cannot be observed directly from the backside of cantilever (in contrast to fringe projection). A small region marked in yellow is the location where profile of AFM intensity curve is extracted from the whole interference pattern. Two pixels, P_0 and P_n are arbitrarily selected from the profile. They correspond to different height H_i at z-axis. (b) Real FOV image of 20x Mirau objective when AFM-mode is activated. The tilted AFM cantilever is in the middle of the FOV. The cantilever is adjusted well so that the focal plane of the objective is located near its tip region. (c) Horizontal intensity profiles extracted at the position marked in (b), recorded under three conditions: (I) when the cantilever is aligned with the focal plane before tip-sample engagement, with no bending force (black curve); (II) after the first tip-sample engagement, with a small bending force (blue curve); and (III) after further bending by 50 nm following the first tip-sample engagement, with a larger bending force (red curve). Due to the tilt of the AFM cantilever, the relative height of each pixel is linearly related to its x-position. Therefore, the corresponding relative height is also indicated in (c) in red.

The key innovation of the AFM-mode is the readout system based on the interference principle. This principle is applied to achieve high resolution detection of tip-sample interactions, specifically the detection of bending and torsion of the AFM cantilever. However, in the following discussion, the focus is placed on how the readout system acquires bending signals rather than torsion signals. This constraint is not inherent to the readout system itself, but results from the use of conventional 1D AFM probes. During the development phase of the AFM-mode, contact-mode diamond like carbon (ContDLC) AFM probes from the company BudgetSensors are mainly used for the measurements [166]. Based on their geometric design, these probes exhibit strong anisotropic stiffness, which results in low sensitivity for detecting

https://doi.org/10.7795/110.20260421A

cantilever torsion signals rather than bending signals. As a consequence, the use of such probes allows only maximum 2.5D measurements, rather than full 3D topography measurements [167]. Indeed, theoretically, the developed readout system is capable of measuring the torsion of the AFM cantilever when the HM is equipped with a true 3D AFM tip [167], thereby enabling critical dimension (CD) measurements and full 3D topography acquisition. Investigations into this capability are ongoing and represent a potential direction for future development, which will be outlined in the outlook chapter of this work.

The readout system employs the same optical and mechanical components used for acquiring interferograms in the IM-mode, as described in previous sections. The only difference lies in the optical configuration: instead of illuminating the sample surface, the AFM-mode directs the measurement beam onto the backside of the AFM cantilever, which is positioned within the optical path at the focal plane and functions as a reflective surface. The measurement beam reflected from the cantilever interferes with the reference beam reflected from the reference mirror, and the resulting interference pattern is recorded by a CMOS camera. For this purpose, as shown in Figure 38, a tilted AFM cantilever is introduced into the FOV of the 20x Mirau objective (248 µm x 186 µm).

The working principle of the readout system is based on the analysis of the interference pattern acquired by the camera. As illustrated in Figure 38b, a pixel $P_0(i,j)$ within the camera image captures a small region on the backside of the monitored cantilever. The corresponding intensity at pixel P_0 denoted as I_{P_0} can be described as:

$$I_{P_0}(i,j) = I_{bias} + I_{mod} \cdot \cos\left[\Theta_{P_0}(i,j)\right] \qquad \text{(Equ. 4.19)}$$

The phase $\Theta_{P_0}(i,j)$ encodes the relative vertical position $H_{P_0}(i,j)$ of the localized area on the cantilever surface. The relationship between these two quantities is governed by the following equation:

$$H_{P_0}(i,j) = \lambda_{eff} \cdot \frac{\Theta_{P_0}(i,j)}{4\pi} \qquad \text{(Equ. 4.20)}$$

A neighboring pixel $P_n(i+n,j)$, whose intensity $I_{P_n}(i+n,j)$ is governed by the same principle, exhibits a different value because its phase Θ_{P_1} differs from that of Θ_{P_0}. This phase difference arises from the height variations induced by the intentional vertical tilt of the cantilever.

A horizonal profile of measured intensities over the back side of the cantilever is illustrated in Figure 38c in black sinusoidal curve, which is extracted at the yellow marked position shown in Figure 38b, where the coordinated j remain constant. This curve represents the variation of intensity along the x-axis at each horizontally arranged pixel P_n with n is an integer ($n \in Z$). In

https://doi.org/10.7795/110.20260421A

this work, such profiles are referred to as AFM intensity curves. Since the cantilever is tilted along the x-axis, each pixel P_n aligned along this direction corresponds to a linearly varying height H_{P_n} as described in Equ.4.20. Accordingly, the horizontal axis of Figure 38c can also be represented in terms of the corresponding height of each pixel, marked in red.

It is important to note that this curve is recorded without the AFM tip approaching the sample surface. At this point, the height of the AFM cantilever remains aligned with the focal plane of the objective, and the cantilever is not yet affected by tip-sample interaction forces. Therefore, the corresponding pixel height H_{P_n} can be hereafter referred to as the focal plane height, and the associated pixel phase Θ_{P_n} as the reference phase. Accordingly, this intensity curve is referred to as the reference curve.

During AFM measurements, the cantilever bends as the tip approaches the sample. Thus, resulting in a variation in the height of AFM cantilever backside. The new height position can be denoted as $H'_{P_n}$for the neighboring pixel P_n. The vertical displacement ΔD resulted from bending can be expressed as:

$$\Delta D_{P_n} = H_{P_n} - H'_{P_n} = \lambda_{eff} \cdot \frac{\Theta_{P_n} - \Theta'_{P_n}}{4\pi}. \qquad \text{(Equ. 4.21)}$$

For improved clarity in describing the phase difference between the phase Θ'_{P_n} , which corresponds to the bent height H'_{P_n}, and the reference phase Θ_{P_n} at the focal plane height H_{P_n}, the term $\Theta_{P_n} - \Theta'_{P_n}$ is replaced by $\emptyset_{P_n}$. Accordingly, the vertical displacement ΔD_{P_n} can be expressed as:

$$\Delta D_{P_n} = \lambda_{eff} \cdot \frac{\emptyset_{P_n}}{4\pi} \qquad \text{(Equ. 4.22)}$$

In the small region selected for evaluation, the local deformation of the cantilever can be ignored, making ΔD independent of coordinate. This implies that the vertical displacement ΔD can be considered independent of the lateral coordinate within this region. As a result, the phase difference $\emptyset_{P_n}$ at P_n is equal to the phase difference $\emptyset_{P_0}$ at P_0 , i.e. $\Delta D_{P_n} = \Delta D_{P_0}$ (Equ.4.22). Thus, within this region, the phase difference can be regarded as a constant ($\emptyset_{P_0} = \emptyset_{P_n} = \emptyset$). The corresponding intensity at point P_n after being affected by the bending-induced phase shift, is given by:

$$I'_{P_n}(i,j) = I_{bias} + I_{mod} \cdot \cos\left[\Theta_{P_n}(i,j) + \emptyset\right] \qquad \text{(Equ. 4.23)}$$

Here, $\emptyset$ denotes a phase offset resulting from the displacement ΔD at this small region. Since each pixel in the AFM intensity curve follows the same interference equation (Equ.4.23) and

https://doi.org/10.7795/110.20260421A

exhibits sinusoidal intensity variation due to the addition of the same phase value $\emptyset$, the entire AFM intensity curve affected by the bending-induced displacement ΔD is shifted uniformly by $\emptyset$ along the x-axis when compared to the reference curve. This behavior is illustrated in Figure 38c with two AFM intensity profiles, shown in blue and red. They are used for demonstrating how the AFM intensity curve responds to bending of the cantilever. The blue curve corresponds to a small bending force, recorded at the moment when the AFM tip first engages with the sample. The red curve represents AFM intensity curve encountering with a larger bending force. It is measured after the cantilever is further deflected by 50 nm following the first engagement.

According to Equ. 4.22, evaluating the phase shifts $\emptyset$ along the x-axis is essential for determining the vertical displacement ΔD, which quantitatively describes how far the AFM cantilever is displaced from the focal plane. This displacement reflects the magnitude of the atomic bending force currently acting between the tip and the sample surface. By maintaining this force at a constant level through the AFM's control loop, while simultaneously recording the tip and stage positions, the operational principle of contact mode AFM under constant force conditions is realized.

The evaluation of the phase shifts $\emptyset$ is performed using a classical phase detection algorithm, such as the fast Fourier Transform (FFT), which offers high sensitivity and computational efficiency. A reference AFM intensity curve $I_{AFM,r}$ acquired near the focal plane (as shown in Figure 38b) can be expressed as:

$$I_{AFM,r}(x) = \sum_{n=-\infty}^{\infty} c_n e^{jnvx} \qquad \text{(Equ. 4.24)}$$

By using a monochromatic LED with good coherence properties, the equation can be rewritten as the sum of a dominant signal component and a less significant residual term R:

$$I_{AFM,r}(x) = c_d e^{jv_d x} + R \qquad \text{(Equ. 4.25)}$$

Here, c_d denotes the complex Fourier coefficient of the dominant signal, and its corresponding frequency v_d is depends on the tilting angle α of the cantilever:

$$v_d = \frac{4\pi \tan\alpha}{\lambda_{eff}}. \qquad \text{(Equ. 4.26)}$$

Neglecting R, Equ. 4.25 can be further simplified as:

$$I_{AFM,r}(x) = c_d \cdot [\mathrm{j}\sin(v_d x) + \cos(v_d x)]. \qquad \text{(Equ. 4.27)}$$

The reference phase $\emptyset_r$ of this dominant signal is evaluated as:

$$\emptyset_r = \arg[I_{AFM,r}] = \tan^{-1}\left[\frac{\Im(I_{AFM,r})}{\Re(I_{AFM,r})}\right] = \tan^{-1}\left[\frac{c_d \cdot \sin(v_d x)}{c_d \cdot \cos(v_d x)}\right]. \qquad \text{(Equ. 4.28)}$$

Where the $\Im\left(I_{AFM,r}\right)$ and $\Re\left(I_{AFM,r}\right)$ denote the imaginary and real parts of $I_{AFM,r}$.

Due to the displacement ΔD, phase shifts $\emptyset$ will be introduced into the dominant signal as explained in Equ. 4.23, therefore any AFM intensity curve I_{AFM} under influences of bending forces can be expressed as:

$$I_{AFM}(x) = c_d \cdot [\mathrm{j}\sin(v_d x + \emptyset) + \cos(v_d x + \emptyset)]. \qquad \text{(Equ. 4.29)}$$

The resulting phase $\emptyset_{AFM}$ is evaluated using the same procedure as in Equ. 4.28 and is given by:

$$\emptyset_{AFM} = \emptyset_r + \emptyset \qquad \text{(Equ. 4.30)}$$

The phase shift $\emptyset$ is determined from the difference between the phase $\emptyset_{AFM}$ of AFM intensity curve I_{AFM} and the reference phase $\emptyset_r$. Furthermore, based on Equ. 4.22, the displacement ΔD can be accurately determined with the resolution in height axis reaching sub-nanometer levels.

A simulation is conducted to investigate the sensitivity between the calculated tip displacement ΔD_c and the reference tip displacement ΔD_r. The calculated tip displacement ΔD_c is evaluated based on Equ. 4.22, where the phase shift $\emptyset$ is simulated using the model described in Equ. 4.23 to 4.30. In addition, the simulation takes into account the attenuation along the z-axis caused by the limited temporal coherence of the applied light source:

$$I_{P_0}(i,j,\Delta D_r) = I_{bias} + I_{mod} \cdot \cos[\Theta_{P_0}(i,j)] \cdot g(\Delta D_r). \qquad \text{(Equ. 4.31)}$$

Here $g(\Delta D_r)$ is the function that is applied for describing the intensity attenuation [97]:

$$g(\Delta D_r) = \mathrm{sinc}\left[\frac{2\pi \Delta D_r}{\lambda_{eff}} \cdot (1 - \cos\theta_{max})\right]. \qquad \text{(Equ. 4.32)}$$

The reference tip displacement ΔD_r represents the vertical position of the cantilever tip and varies linearly with the applied vertical atomic force F, which causes bending of the cantilever beam. According to classical beam bending theory, the reference tip displacement ΔD_r is given by:

$$\Delta D_r(x) = F \cdot x^2 \cdot \frac{3L - x}{6\tilde{E}\tilde{I}}. \qquad \text{(Equ. 4.33)}$$

https://doi.org/10.7795/110.20260421A

Here, $\tilde{E}$ denotes Young's modulus, $\tilde{I}$ is area moment of inertia (can be calculated with cantilever width=50 µm and thickness= 2 µm) and L the length of the cantilever beam (450 µm). Since the reference tip displacement ΔD_r is measured near the free end ($x = L$), the equation simplifies to:

$$\Delta D_r = F \cdot \frac{L^3}{3\tilde{E}\tilde{I}} \ . \qquad \text{(Equ. 4.34)}$$

Three experimental determinations of the sensitivity between ΔD_r and ΔD_c are also conducted. In these experiments, tip-sample contact is established in the first place. After that, ΔD_c is directly calculated as the product of the phase shift $\emptyset$, caused by fringe displacement on the backside of the cantilever, and the effective wavelength λ_{eff} according to Equ. 4.22. And ΔD_r is derived from the z-axis stage displacement, which varies in a controlled, monotonic stepwise manner. A linear relationship with a slope of 1 is expected, indicating that a 1 nm displacement in the stage (representing by the reference tip displacement ΔD_r) should correspond to a 1 nm displacement calculated from the phase shift variation (representing by calculated tip displacement ΔD_c). If the expected linear relationship with a slope of 1 is not observed, sensitivity calibration is recommended to restore the slope to unity by updating the effective wavelength λ_{eff} in the Equ. 4.22. Such sensitivity calibration between ΔD_r and ΔD_c is required each time a new AFM probe is installed in the system, ensuring accurate displacement readout under varying probe tilting angles. The influence of the tilting angle on the effective wavelength will be discussed in detail in chapter 5.

Figure 39 presents three experimentally determined sensitivity curves, each obtained using a newly calibrated effective wavelength λ_{eff} of 719.0 nm (blue curve), 707.5 nm (red curve) and 734.9 nm (yellow curve) respectively. For comparison, a simulated sensitivity curve (violet curve) generated based on the theoretical model described above is also included. Owing to the small displacement range considered here (0–50 nm), the differences in effective wavelength (the slope differences of the individual sensitivity curves), cannot be clearly distinguished in Figure 39. This observation indicates two important points. First, the noise present during the experimental determination of the sensitivity curves influences the calibrated effective wavelength. For the three experimentally obtained values, the mean effective wavelength is 720.5 nm and the corresponding standard deviation is 13.8 nm. Second, although this influence is noticeable in the calibrated λ_{eff}, its effect on the calculated displacement remains very small within the investigated range. Over a displacement interval of 50 nm, the variation introduced by this wavelength scatter is below 1 nm.

During an AFM measurement, the output signal of the readout system is the current displacement ΔD. It is transmitted to the CPU-based control loop at a sampling frequency of

up to 3000 Hz. This signal is referred to hereafter as the AFM signal S_{AFM}. Since the system operates in constant force mode, the displacement ΔD is to be maintained at a constant value. To achieve this, a classical proportional-integral-derivative (PID) controller is implemented within the AFM-mode control loop.

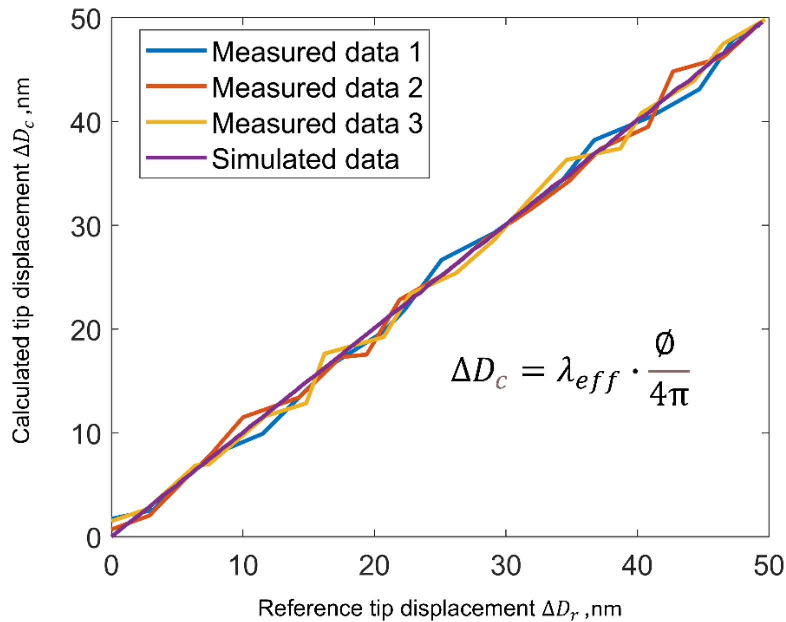

Figure 39 Simulated and experimentally determined sensitivity curves for the reference tip displacement ΔD_r and calculated tip displacement ΔD_c, based on the newly calibrated effective wavelength λ_{eff} and fringe phase shifts $\emptyset$

The controller is initialized with a target displacement ΔD_t, which corresponds to a bending force optimized for stable measurement conditions. This configuration offers two primary advantages. First, it ensures that the tip remains in contact with the sample throughout the measurement, thereby preventing the loss of tip-sample contact. Second, it prevents the application of excessive force that could alter the tip geometry and/or damage the sample surface.

The controller continuously receives the measured displacement ΔD, calculates the difference between the target displacement ΔD_t and the current displacement ΔD, and generates a motion command based on this deviation. This command is directly used to adjust the vertical position of the sample, thereby regulating the tip sample distance. A detailed explanation of this control loop and its implementation is provided in the following sections.

Finally, the measurement results h obtained in AFM-mode consist of two primary components: (I) the current AFM signal S_{AFM} and (II) the current position of the piezo stage, denoted by

https://doi.org/10.7795/110.20260421A

S_x, S_y and S_z along the respective Cartesian axes. The measurement result $h\,(S_x, S_y)$ at a given lateral stage position (S_x, S_y) is expressed as:

$$h\,(S_x, S_y) = -S_z(S_x, S_y) + S_{AFM}(S_x, S_y). \qquad \text{(Equ. 4.35)}$$

In this expression, $S_z\,(S_x, S_y)$ represents the vertical position of the stage, and the negative sign is introduced to correct for axis direction inconsistencies in the z-coordinate. The negative sign from S_z of the measured vertical position of the stage in Equ.4.35 is applied because the measurement is performed in the scanning sample principle.

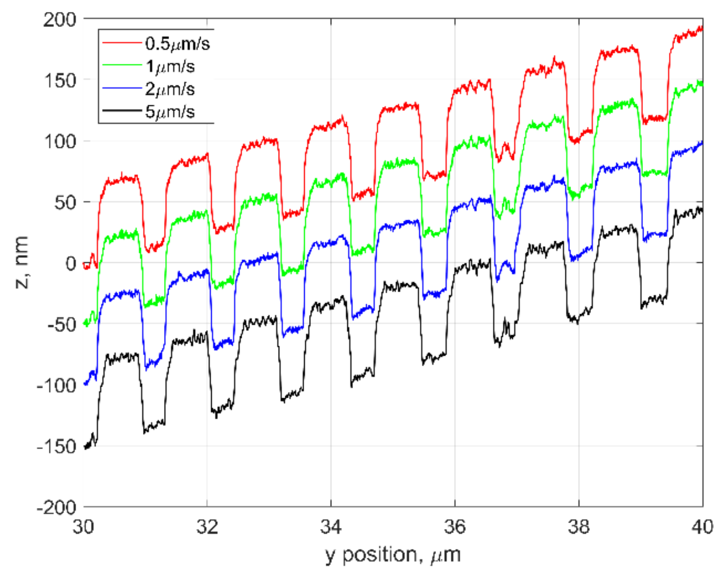

Figure 40 CCS profiles measured in different measuring speed of 0.5 µm/s, 1 µm/s, 2 µm/s and 5 µm/s using the AFM-mode of the HM.

A series of line repeat measurements is performed on a CCS pattern with a nominally structure height of 64 nm. These measurements are conducted using the developed AFM-mode of the HM system, following the measurement principle described in the preceding sections. The corresponding results are presented in Figure 40.

As illustrated in Figure 40, line measurements are repeatedly performed at the same position with different measurement speeds from 0.5 µm/s up to 5 µm/s. The results demonstrate excellent repeatability between measurements, confirming that the developed AFM-mode delivers reliable measurement performance. Although a scanning speed of 5 µm/s may not be sufficient to compete with commercial AFM systems in terms of throughput, it is important to emphasize that this limitation does not arise from the measurement principle itself. Instead, it is primarily due to the performance constraints of the integrated low-cost camera and the limited dynamic characteristics of the employed piezo stage. A substantial improvement in

measurement speed could be achieved by implementing a high-dynamic piezo stage and a high-speed camera. However, such enhancements would require a significantly higher cost.

Furthermore, the absence of real-time communication between the hardware and the CPU-based controller imposes an additional limitation on the measurement speed. This limitation arises primarily because the CPU does not function as a real-time system and, as a result, does not consistently prioritize measurement-related tasks during execution. Accordingly, hardware commands such as reading the current stage position (for example, S_z) from its controller, and acquiring the AFM output signal S_{AFM} are not executed synchronously. Consequently, the signal-processing in the AFM-mode suffers from variable, yet significant, delays between S_{AFM} and S_z. This means that the received output signal S_{AFM} from the readout system does not align temporally, and therefore also does not align spatially, with the stage position S_z, even though both sets of data are requested simultaneously at the programming level.

This latency issue becomes particularly critical when measuring structures with significant height variations. If the stage fails to respond in time to significant topographical changes, such as step edges, the risk of AFM tip breakage or sudden loss of tip-sample contact increases substantially. One possible solution to address this problem is to replace the existing CPU-based control system with a high-speed real-time control unit. Further details regarding the currently implemented control system will be provided in the following sections.

4.3.2.AFM tip switching system

An AFM tip switching system is developed for realization of the mode switching between the IM- and the AFM-mode of the HM. The original idea for designing this system is to achieve a simple but convenient mechanism for switching the AFM cantilever, e.g. motorized and without the need to dismount microscopic objectives.

One of the most straightforward implementations of this system involves mounting it directly onto the objective using an objective adapter, as previously illustrated in Figure 23. A prototype based on this design, referred to as the Klappfix, was developed by the PTB colleague Helmut Wolff and is shown in Figure 41.

Detailed images of the Klappfix are shown in Figure 42a, where it is mounted on a dummy objective. The system consists primarily of three components: (I) an objective adapter, (II) an AFM tip holder, and (III) a rotation mechanism driven by a DC stepper motor.

https://doi.org/10.7795/110.20260421A

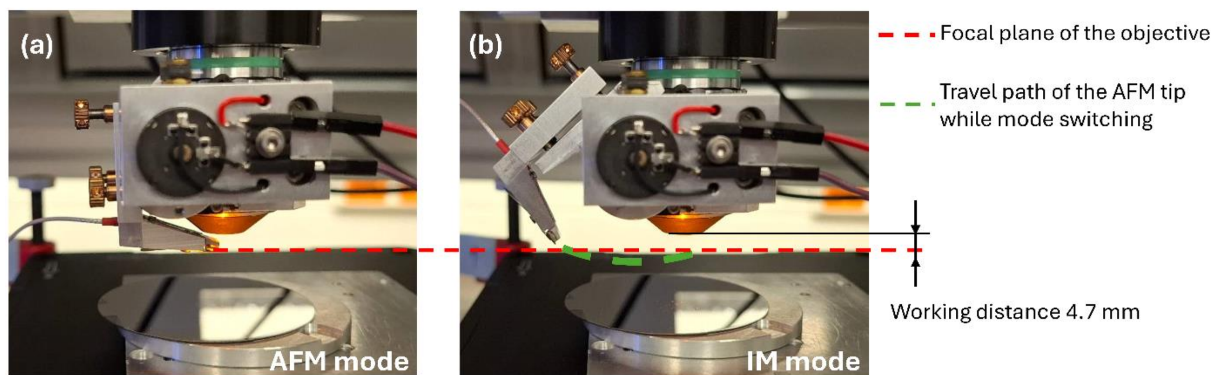

Figure 41 Prototype of the developed AFM tip switching system for enabling measurement modes switching of the hybrid microscope demonstrated in (a) the AFM-mode and (b) the IM-mode. The focal plane of the objective (Nikon 20x Mirau type) is marked with a red dashed line in both images to illustrate that, when the IM-mode is activated and the system is focused on the sample surface, the AFM tip is lifted by the tip switching system on the side at a safe position, avoiding any risk of touching the sample and/or damaging the AFM probe. Travel path of the AFM tip is also marked in (b) for demonstrating the switching process. The lowest point of the path is even lower than the focal plane. To address this, z-motion stage will lift the microscope by about 6 mm before the mode switching to ensure the AFM probe safety.

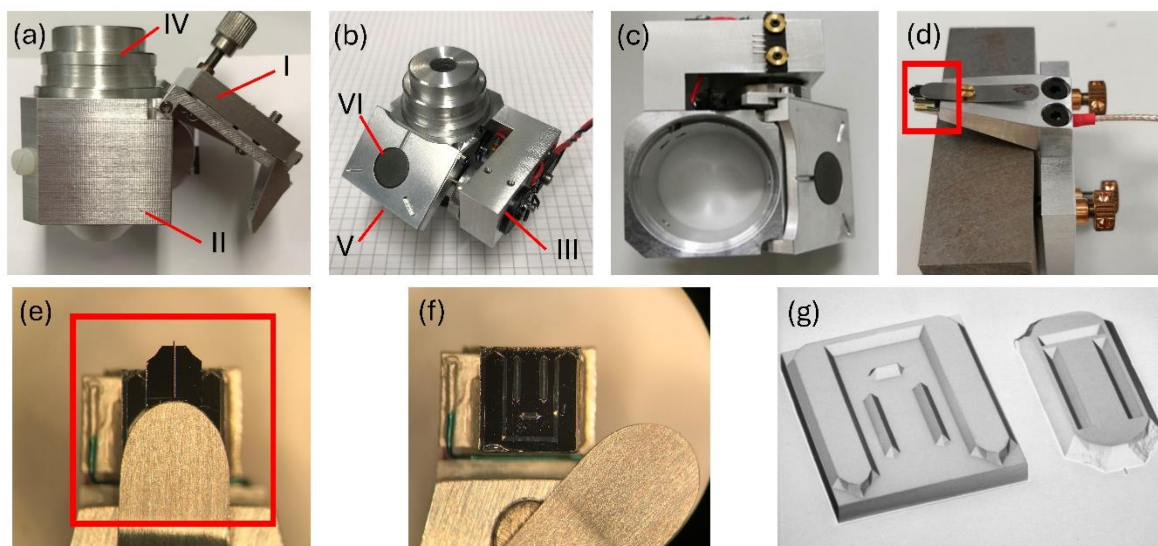

Figure 42 Realization details of the Klappfix. Two different perspectives of Klappfix as mounted on a dummy objective (IV): (a) side view and (b) oblique view (45°). The Klappfix consists of three main parts (I) AFM tip holder, (II) objective adapter and (III) a rotation mechanism. (c) top view of the objective adapter (II) attached with rotation mechanism (III); (d) side view of AFM tip holder, equipped with three adjustments screws for fine adjusting the position of the AFM cantilever. Red rectangle marked is the end of the AFM tip holder, where the AFM probe is fixed. Zoomed figures (e) and (f) illustrate this part with and without an AFM probe mounted, respectively. For ensuring the position-repeatability of the AFM probe by AFM probe changing, an alignment chip [168] (g) with positioning groove is fixed on the end of AFM tip holder.

The objective adapter (II) is designed in a cubic form with a hollow cylindrical cavity at its center, as shown in Figure 42c. This cavity is manufactured for a loose fit with the mounting diameter of the objective lens. Two plastic screws are applied on the side of the adapter body to fix its position relative to the objective. This design allows the AFM tip switching system to

accommodate objectives with varying WD, such as the Nikon 10x Mirau objective (WD = 7.4 mm) and the Nikon 20x Mirau objective (WD = 4.7 mm). The set screws enable fine adjustments of the relative position between the switching system and the objective, ensuring that the backside of the cantilever appears within the objective's FOV and is vertically aligned with its focal plane.

The rotation mechanism (III), which includes a rotatable clapper (V) with two working states, is mounted on one side of the objective adapter (II) and is driven by a DC stepper motor. Magnetic connection points (VI) are incorporated on both sides of the clapper to provide stable and repeatable connections between the objective adapter and the clapper, as well as between the clapper and the AFM tip holder.

During an IM measurement, as shown in Figure 41a, the clapper remains open, positioning the AFM tip holder outside the objective's FOV. When the AFM-mode is activated, the clapper closes and rotates the AFM tip holder into the optical path. As a result, the cantilever becomes visible in the FOV and is vertically aligned with the focal plane. To ensure precise and repeatable positioning of the cantilever during mode switching, an alignment mechanism is implemented, as illustrated in Figure 42b. This mechanism consists of alignment grooves and spheres arranged in a triangular configuration, providing mechanical stability and reproducibility in the clapper's positioning.

The AFM tip holder (I) is a key component of the AFM tip switching system. It is specifically designed to secure the AFM probe and to maintain the tip at the lowest position within the entire system during AFM measurements. The holder consists of two main parts: a base plate equipped with three adjustment screws and a probe-holding arm tilted at an angle of 8 degrees.

The base plate, which contains a built-in magnet at its center, facilitates the connection between the AFM tip holder and the objective adapter. Three adjustment screws are integrated into the plate: one at the top, which enables fine-tuning of the cantilever's vertical position by adjusting its tilting angle, and two at the bottom (left and right), which allow precise lateral alignment to ensure that the cantilever can be observed within the FOV.

One end of the tilted arm is securely fastened to the base plate using screws, while the other end, highlighted in Figure 42 with a red rectangle, holds the AFM probe supported by a sheet metal spring. An alignment chip, as shown in Figure 42f and further detailed in Figure 42g, is attached to the same end of the arm. This chip contains ridges that fit precisely into the corresponding alignment grooves on the AFM probes, ensuring stable and repeatable positioning of the cantilever within the FOV when a new AFM probe is mounted.

https://doi.org/10.7795/110.20260421A

A rotation mechanism, shown in Figure 42b, is driven by a DC stepper motor (III) from Faulhaber (type 1512 006SR) [169] and is used to motorize the switching between measurement modes by changing the clapper position. The motor is currently powered by an analog voltage output card (PCIE 1824 from Advantech [170]) installed in the control computer of the HM system. Depending on the polarity of the input DC voltage, the motor rotates clockwise to move the clapper from the open position to the closed position, or counterclockwise to return it from the closed position to the open position. This allows motorized switching between measurement modes by moving the AFM cantilever into or out of the optical path and the FOV.

The repeatability of the AFM cantilever position along all three spatial axes, using the mode switching system described above, is investigated through a series of tests involving repeated transitions between the AFM-mode and the IM-mode. In this investigation, FOV images are acquired each time the AFM-mode is reactivated. The lateral and vertical positions of the cantilever are then analyzed based on these images. As an example, five such FOV images, shown in Figure 43, are captured successively after repeatedly activating and deactivating the tip switching system to alternate the measurement mode from the AFM-mode to the IM-mode and back to the AFM-mode.

The similarity of the five images shown in Figure 43 demonstrates the high repeatability of the cantilever position after mode switching operations of the HM. The cantilever position along all three spatial axes is quantitatively evaluated based on the center of gravity (CoG) of each extracted cantilever contour and the phase of the imaged interference fringe. By performing this evaluation across all acquired FOV images, the positional repeatability can be determined. The results of this analysis are summarized in Table 3.

A similar investigation is conducted to evaluate the position repeatability not only during measurement mode switching but also following the exchanges of AFM cantilevers. Five FOV images are acquired, each after an old AFM cantilever is removed and a new cantilever is placed in the HM system, as shown in Figure 44. The quantitative estimations of the position repeatability are summarized in Table 4.

In comparison to the highly consistent AFM cantilever positions observed during repeated measurement mode switching (Table 3), significantly larger positional deviations are evident following AFM probe replacement. This outcome is expected, as it is inherently difficult to maintain the exact same cantilever position after exchanging the probe due to several factors: (I) AFM probes and cantilevers may vary slightly in geometry, (II) despite the use of an alignment chip, small deviations in mounting position can still occur, (III) the AFM tip holder must be manually dismounted and re-mounted during probe exchange, introducing positional

https://doi.org/10.7795/110.20260421A

variability, and (IV) localized thermal expansion may result from heat transfer during manual AFM probe exchange.

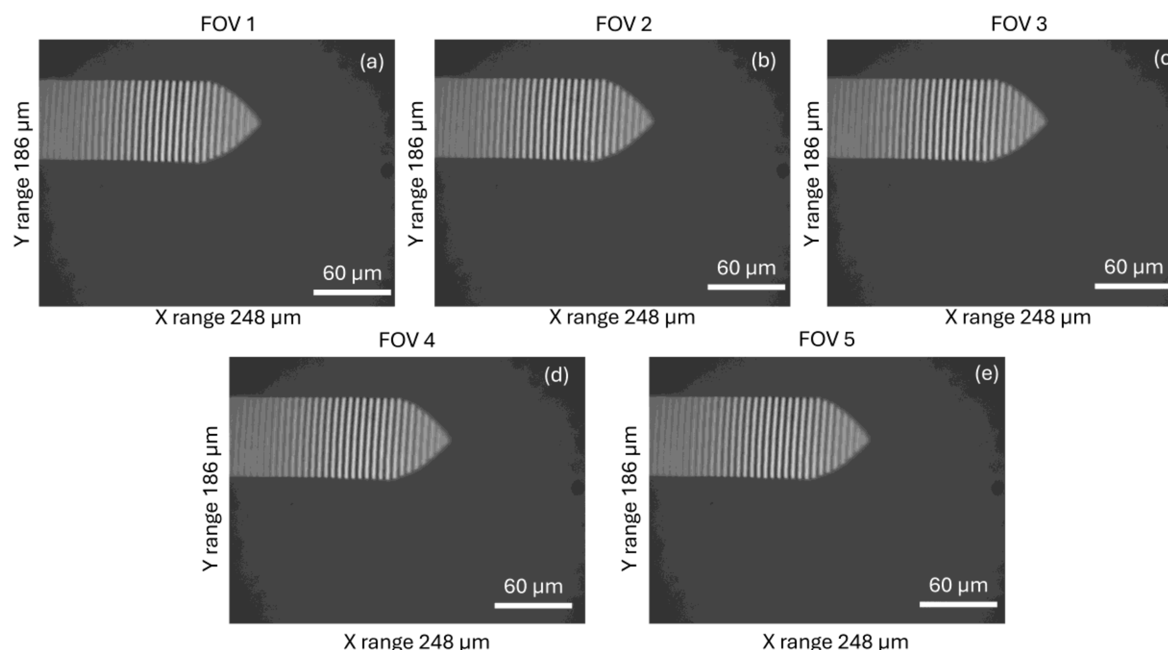

Figure 43 FOV images acquired after repeatedly active/inactive the tip switching system for switching the measurement mode from the AFM-mode to the IM-mode then back to the AFM-mode in different time

Table 3 Repeatability of cantilever positions in three axes by using motorized AFM tip switching system Klappfix

	FOV 1	FOV 2	FOV 3	FOV 4	FOV 5	Standard Deviation
Relative lateral position in x-axis, µm	56.79	57.19	57.13	57.51	57.71	0.35
Relative lateral position in y-axis, µm	125.53	125.58	125.70	126.25	126.19	0.35
Relative vertical position in z-axis, nm	-120.4	-97.6	-82.7	-108.2	-91.4	14.7

Nevertheless, as long as the newly mounted cantilever remains within the FOV, repositioning it to its optimal working location is a simple and straightforward process. Typically, it takes less than one minute to realign the cantilever using the three adjustment screws, allowing the objective to refocus on the back side of the cantilever near the tip end. The term “tip end” refers to the region of the AFM cantilever within the FOV where the AFM tip is located on the opposite side.

https://doi.org/10.7795/110.20260421A

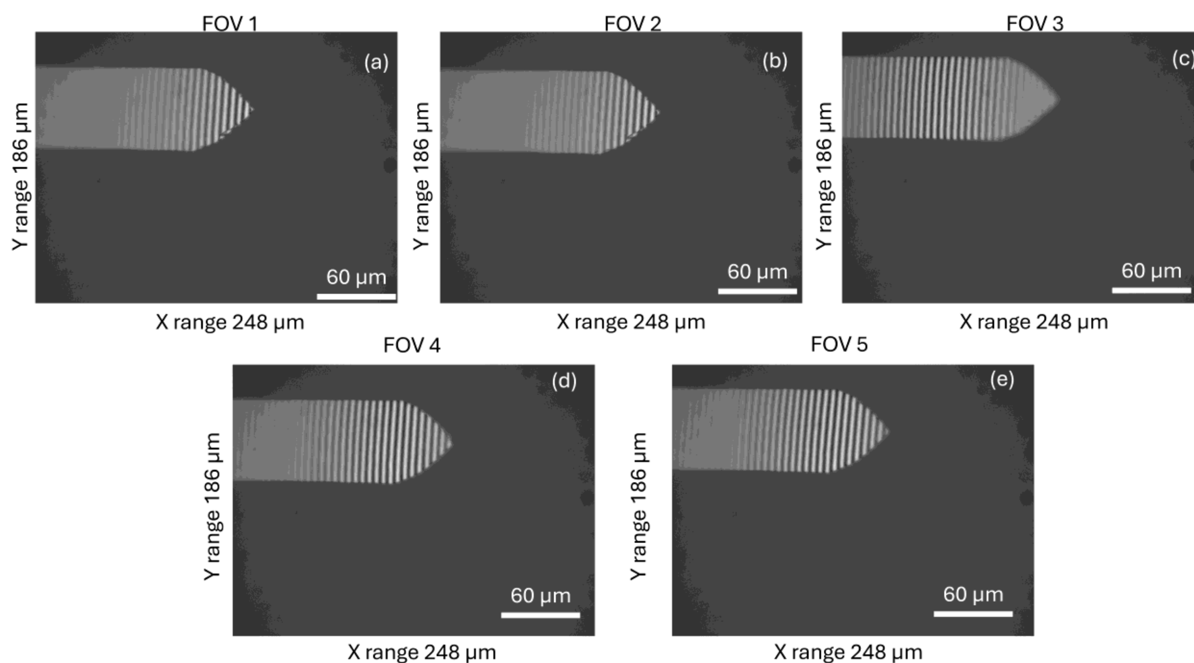

Figure 44 FOV images acquired each time after changing AFM probes in the HM system

Table 4 Repeatability of cantilever positions in three axes after AFM cantilever exchange

	FOV 1	FOV 2	FOV 3	FOV 4	FOV 5	Standard Deviation
Relative lateral position in x-axis, µm	55.73	53.64	45.81	53.52	46.50	4.55
Relative lateral position in y-axis, µm	122.33	121.17	123.21	124.25	120.89	1.40
Relative vertical position in z-axis, nm	-1891.3	-1860.7	2046.1	93.5	139.5	1644.7

It should be noted that, as demonstrated both in Figure 43 and Figure 44, the AFM tip itself is not visible within the FOV. Only the backside of the AFM cantilever can be observed. This leads to a minor practical issue when a brand-new AFM tip is mounted in the system for the first time, since the user may initially not know the lateral position of the AFM tip with respect to the camera imaging system. To address this problem, a test AFM measurement together with an optical measurement is recommended to be carried out on a rough surface. By correlating the two measurements over the full measured area, the lateral position of the AFM tip can be determined. Owing to the excellent position repeatability provided by the AFM tip switching system, such a large-area time consuming correlation procedure is not required thereafter. Instead, the lateral position of the AFM tip in the HM system can be registered as prior knowledge until the tip is replaced.

https://doi.org/10.7795/110.20260421A

4.3.3.AFM measurement preparation

In the HM system, activating the AFM-mode through the tip switching system does not indicate that the system is fully ready for AFM measurement. Several additional preparation steps are required to ensure optimal measurement performance. These steps include initializing the AFM signal, performing the tip approach, calibrating the sensitivity between the AFM signal and the stage signal, and adjusting the PID control parameters. Although these procedures are largely similar to those used in conventional AFM systems, they are not identical. For example, both systems require tip approach and cantilever sensitivity calibration before measurement, but the specific implementation details differ.

One of the most significant differences lies in the method used to set up the AFM signal. In contrast to conventional AFM systems, the AFM signal in the AFM-mode of the HM system can be easily configured by selecting a desired AOI within the FOV image in which interference fringes are observed. This capability is made possible by the highly integrated optical and mechanical design of the HM system.

Typically, the selected AOI has a width of 8 pixels, corresponding to 8 image lines, which is the minimum allowed to ensure compatibility with high-speed camera readout. Each line in the AOI contains approximately 300 pixels in length, corresponding to 300 pixel-columns. The interference fringe profiles in these 8 lines are individually processed using the FFT algorithm to extract the phase component associated with the spatial frequency of the fringes.

This phase value is then used to calculate the AFM signal S_{AFM}, as described in Equ. 4.21, by multiplying it with the effective wavelength λ_{eff}. In the absence of atomic force interactions, such as bending and/or torsional forces, the AFM signal S_{AFM} remains approximately constant. In this case, most fluctuations in the signal are caused by environmental disturbances, such as air turbulence.

In contrast, setting up the AFM signal in conventional systems typically requires manual alignment of the laser spot on the cantilever and of the reflected beam on the QPD, involving at least four separate adjustments to obtain an optimized AFM signal. The quasi-hand-free signal setup procedure in the HM system therefore greatly reduces the complexity and effort required for alignment and signal configuration.

After the AFM signal is properly set up and optimized, the AFM tip can be approached to the sample surface. In general, the tip approach process is realized by gradually reducing the gap between the tip and the sample. This continues until the tip reaches its working position defined by the selected AFM measurement mode. In contact mode AFM, this working position is

https://doi.org/10.7795/110.20260421A

typically located a few tens of nanometers beyond the point where the tip first makes contact with the sample surface. The method for identifying this first contact point will be discussed in detail in later sections.

This gradual reduction of the gap helps to avoid a hard AFM tip landing on surface, thus to avoid possible tip damage which happens often in the tip approaching processes in conventional AFM tools. As noted in the research of M. Xu [171], most cases of tip volume loss or breakage do not result from gradual wear during scanning but rather from improper or uncontrolled engagement between the tip and the surface.

The AFM tip approach process in the HM system is carried out through the coordinated movement of the vertical coarse motion stage and the piezo fine stage. At the beginning of the approach, the coarse stage, which holds the AFM tip, remains stationary. Meanwhile, the piezo stage incrementally moves the sample upward along the vertical axis toward the tip. By default, each upward step of the piezo stage is set to 5 nm. In the HM software design, this step size can be adjusted by the user, allowing the overall approach time to be optimized based on the properties of the mounted AFM tip and the sample surface. Although a larger step size can shorten the overall approach time, it also increases the risk of tip damage or breakage.

Throughout the approach process, the AFM signal S_{AFM} is continuously monitored and compared to a reference signal measured under conditions free from any type of tip-sample interactions, i.e. before tip engaged to surfaces. These signals will be used for the detection of the tip-sample contact, because once the contact happens, the AFM signal S_{AFM} will significantly deviate from the reference value under the impact of bending force.

The piezo stage performs incremental upward stepwise motions to search for the contact position. The search range is limited to 30 µm, which corresponds to approximately 60% of the stage's maximum travel distance. If contact is not detected within this range, the piezo stage first retracts by 30 µm and returned to its starting position. Subsequently, the coarse stage moves downward by 28 µm. After this, a new approach cycle begins with the piezo stage resuming its upward stepwise motion. This cycle runs until tip-sample contact is successfully detected.

It is important to note that the coarse stage is intentionally designed to move downward by 28 µm, which is slightly less than the 30 µm retraction of the piezo stage. This precaution helps to avoid unintended contact between the tip and the sample that could result from inaccurate motion of the coarse stage. As a result, the AFM tip is protected.

Approach efficiency can be improved by identifying an appropriate vertical starting point for the approach process, which shortens the search range. The preliminary IM measurement

https://doi.org/10.7795/110.20260421A

result of the sample surface using the IM-mode is applied before initiating the AFM approach. This preliminary step not only provides rough topographical information but also offers a reliable estimate of the vertical position at which the approach should begin.

The IM-mode provides a non-contact optical method that enables rapid and accurate determination of the objective's focal plane. By performing vertical adjustments through Z coarse stage, the system identifies the position $\hat{Z}$ at which interference fringes appear, indicating that the sample surface is aligned with the focal plane of the objective. This method significantly reduces the risk of damaging the sample or other components of the instrument. The identified focal position corresponds to the current distance between the objective and the sample surface, which is referred to as the working distance (WD) in Figure 41b.

With the help of the IM measurement, the previously determined vertical position $\hat{Z}$ can serve as a rough indicator for where the tip approach process should end. However, after switching from the IM-mode to the AFM-mode, the focal plane no longer aligns with the sample surface but instead with the backside of the cantilever. Therefore, the height of the AFM tip must be taken into account in the vertical positioning. Given that the AFM tip has a nominal height of 15-20 µm, a tolerance gap of 50 µm, labeled as TL in Figure 45, is reserved when switching from the IM-mode to AFM-mode at the vertical position $\hat{Z}$. Meaning that, when in IM-mode interference fringe is observed at vertical position $\hat{Z}$, the vertical position will be $\hat{Z}$+TL after AFM-mode is activated.

This reserved tolerance reduces the maximum tip-sample distance down to approximately 30 µm, as illustrated in the AFM-mode configuration shown in Figure 45. As a result, the approach process can be completed in less than two minutes, thus significantly improving the tip approaching efficiency by narrowing the search range. A detailed illustration comparing the vertical arrangement of system components in both measurement modes is presented in Figure 45. For clarity, certain components have been rescaled to better highlight key structural elements.

Beyond shortening the approach searching range, another advantage of performing an IM measurement is that the acquired topography typically covers a large measurement area. This topography serves as a 3D map for navigating AOIs for subsequent AFM measurements.

Once tip-sample contact is confirmed through the approach process, the AFM measurement preparation proceeds automatically based on the user's configuration. The system either initiates the sensitivity calibration procedure, if a calibration is desired, or transitions directly to the control process if a calibration is not desired.

https://doi.org/10.7795/110.20260421A

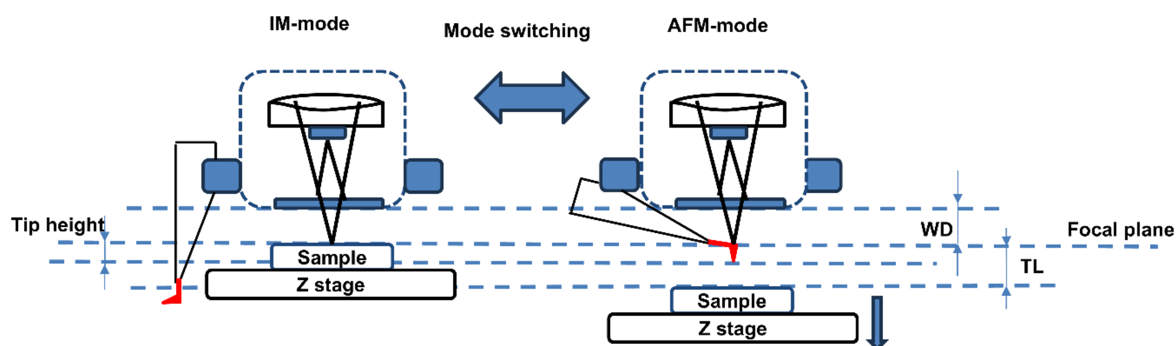

Figure 45 Illustration of the vertical position of samples in AFM-mode and IM-mode, WD is short for working distance, its value depends on applied objective (e.g. 4.7 mm for Nikon 20x Mirau objective). TL is short for tolerance length, which is an additional vertical retraction distance of the Z motion stage, introduced for protecting the AFM tip from unwanted collision with the surface after mode switching, normally in a length of 50 µm.

The sensitivity calibration process determines the sensor's response to cantilever displacement by monitoring changes in the AFM signal while the piezo stage is linearly moved around a predefined working position, as previously illustrated in Figure 39.

In conventional AFM systems, calibrating the sensor's detection sensitivity is a critical step in measurement preparation, as it ensures proper system functionality and measurement accuracy. This calibration is typically performed by comparing the output of QPD of the optical-lever readout system with the actual cantilever displacement. The displacement is induced by controlled vertical movements between the AFM probe and the sample after tip-sample contact has been established.

A key advantage of the interferometric principle used in the AFM-mode developed in the HM system is that it eliminates the need for an optical-lever readout system. Instead, the AFM signal is directly linked to the effective wavelength λ_{eff}, which is defined by the fringe spacing of the interference pattern observed on the back side of the cantilever.

Once λ_{eff} is determined through sensitivity calibration, it remains relatively stable during subsequent AFM measurements, unless the AFM probe is replaced. This stability is due to the fact that λ_{eff} primarily depends on the center wavelength of the light source λ and the cantilever tilting angle α, both of which remain constant across different measurements. Therefore, if no probe exchange occurs and the power of the light source remains stable, λ_{eff} also remain stable, and thus additional calibration is typically unnecessary. This inherent stability simplifies the measurement procedure by avoiding redundant calibration, helps preserve the geometry of the AFM tip, and reduces the risk of tip damage and/or breakage.

However, sensitivity calibration is still required in cases where recalibration of the effective wavelength λ_{eff} becomes necessary. This applies, for example, when (I) the light source is changed, (II) objectives with different numerical apertures are used, or (III) adjustments are made to the tilting angle α of the cantilever. A detailed investigation into the determination of λ_{eff} and the factors influencing its stability will be presented in the following chapter.

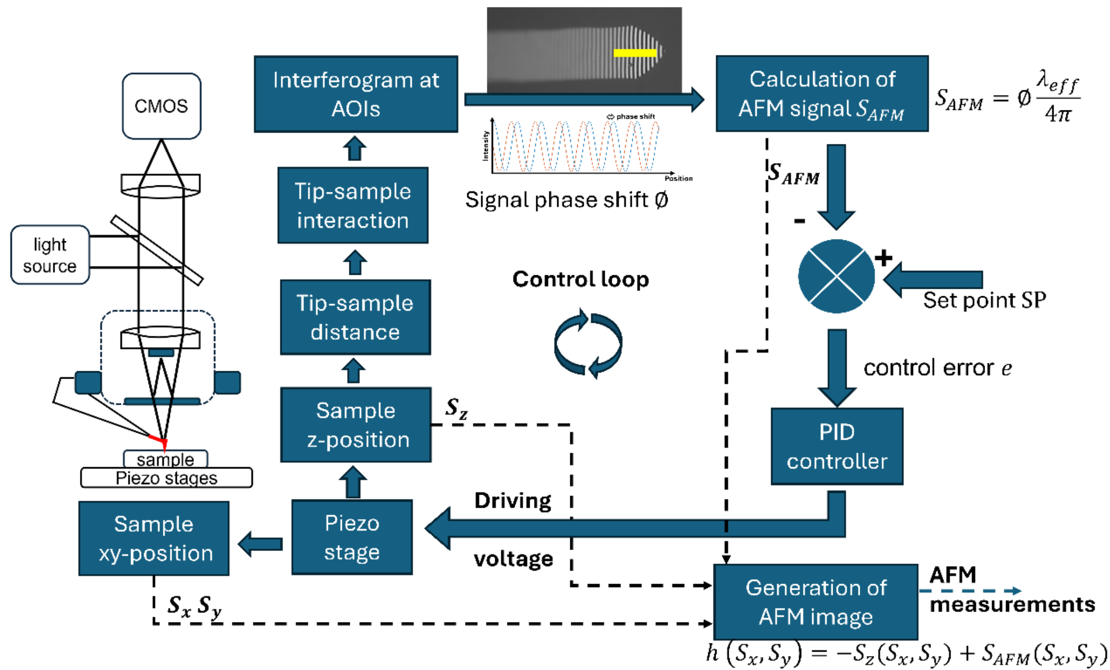

Figure 46 Illustration of the control loop of the AFM-mode in the HM implemented using PID control technique

Once the sensitivity curve has been properly calibrated and the AFM tip has reached its default working position, also known as the set point (SP) in control theory [172], the system transitions to the control phase. In this phase, a controller is applied to regulate the motion of the piezo stage based on the current AFM signal, ensuring that the tip-sample interaction remains constant. The system remains in this state while awaiting further operational commands, such as the start of line or area scanning.

The most widely used control approach to achieve this is the PID controller, which is preferred for its ease of implementation and reliable performance when the control parameters are properly tuned [173]. Its general control equation is expressed as follows:

$$d(t) = k_p e(t) + k_i \int_0^t e(t)dt + k_d \frac{de(t)}{dt}. \qquad \text{(Equ. 4.36)}$$

Here, the control variable d represents the relative vertical distance that the piezo stage is expected to move before the next control cycle begins. The control error e is defined as the

https://doi.org/10.7795/110.20260421A

difference between the AFM signal S_{AFM} and the SP. The parameters k_p, k_i and k_d represent the proportional, integral, and derivative gains, respectively.

The fully developed AFM control loop consists of four steps, as illustrated in Figure 46. In the first step, the AFM signal S_{AFM,t_0}, measured at time t_0, is used to estimate the control error e relative to the SP. In the second step, the error e is processed by the PID controller, which applies the specified controller parameters and using Equ. 4.36 to calculate the control variable d. In the third step, a movement command is sent to the closed-loop operated piezo stage to adjust its position. It ensures that the sample is moved vertically in order to maintain the desired tip-sample interaction at the set value. In control theory, this stage is referred to as a "plant" or "process" [173]. In the final step, a new interferogram is acquired by the camera at time t_1, the next sampling time following t_0. The corresponding AFM signal S_{AFM,t_1} is recalculated by analyzing the new interferogram. This completes the current control loop, and the system becomes ready to proceed with the next control cycle.

The three controller parameters k_p, k_i and k_d play a critical role in determining the control performance and can be optimized based on the RMS value of the control error e during AFM measurements. A lower RMS value indicates better control performance, while a higher RMS value suggests that the controller is struggling to maintain accurate tracking of the surface topography. Based on practical experience, default values of $k_p = 0.8$, $k_i = 0.01$ and $k_d = 0$ generally result in good control performance in the developed HM. However, these parameters may need to be adjusted depending on the geometrical and material characteristics of the sample, as well as the current instrumental and measurement conditions.

Another approach to achieving the control task, known as hybrid AI-PID control [174], has been studied in terms of its feasibility for implementing as a controller in the AFM-mode of the HM. This method integrates an AI based controller with a traditional PID controller to enhance control performance (having smaller RMS value during controlling). Simulation results [175] demonstrate that a hybrid AI-PID control could reduce RMS by a factor of up to four compared to the value obtained using a PID controller.

A prototype of the hybrid AI PID controller has been developed in Python and implemented in the control loop of the AFM-mode. Current research indicates that after 500 training iterations, each time trained with 10 μm long line measurements at a measuring speed of 5 μm/s, the RMS control deviation decreases from 5.51 nm (using the PID controller only) to 4.65 nm when applying the hybrid AI-PID controller in the first experiment. Similarly, in the second experiment, the deviation is reduced from 3.73 nm to 3.10 nm. This represents an approximate

https://doi.org/10.7795/110.20260421A

20% improvement in control performance, highlighting the significant potential of this approach for applications requiring high precision control.

4.3.4. Measurement performance and calibration

This section focuses on evaluating the measurement performance of the developed AFM-mode in the HM system to verify its suitability for accurate and reliable reference metrology. The discussion will address three key aspects: noise, traceability, and repeatability.

Noise

Noise, as a critical performance specification, defines the fundamental measurement capability of a sensor or instrument, particularly its ability to resolve weak topographical signals. In this study, the noise level N_s of the developed sensor has been investigated based on AFM signals acquired using a 20x magnification Mirau objective and a 595 nm amber LED light source [158]. Additionally, the overall measurement noise N_{AFM} of the complete AFM-mode has been characterized. The relationship between these two noise levels is described by the following equation:

$$h\left(S_x, S_y\right) + N_{AFM} = -S_z\left(S_x, S_y\right) - N_z + S_{AFM}\left(S_x, S_y\right) + N_s + N_e \qquad \text{(Equ. 4.37)}$$

where the N_e and N_z denotes the environmental and stage positioning noise respectively.

To ensure the best SNR, the light source is operated at full power during noise characterization. The reasoning for this choice, as well as a detailed analysis of the relationship between noise and light source power, will be presented in the next chapter.

The noise level N_s of the developed sensor is investigated under two scenarios:

(1) Minimum sensor noise N_s, measured with the tip freely hanging above the sample: This refers to the noise presented in the AFM signal when there is no interaction between the AFM tip and the sample surface. In this condition, external vibration sources, such as those introduced by the closed-loop operated piezo stage, contribute minimally. The noise level primarily depends on the signal quality captured by the camera.

(2) Sensor noise N_s acquired in the control phase with tip-sample contact established: This refers to the noise presented in the AFM signal when the tip reaches its working point, where it is in contact with the sample surface. In this scenario, the system operates in closed loop, with the PID controller continuously adjusting the vertical position of the piezo stage to maintain the AFM signal at the predefined SP. The noise level under this condition

https://doi.org/10.7795/110.20260421A

is expected to be higher than the minimum sensor noise, due to additional vibrations and mechanical disturbances introduced by the established tip-sample contact.

The sensor noises N_s in both scenarios are characterized based on continuously sampled AFM signals over a duration of 3s, with a sampling frequency of 3000 Hz. The results are depicted in Figure 47a and Figure 47b, respectively.

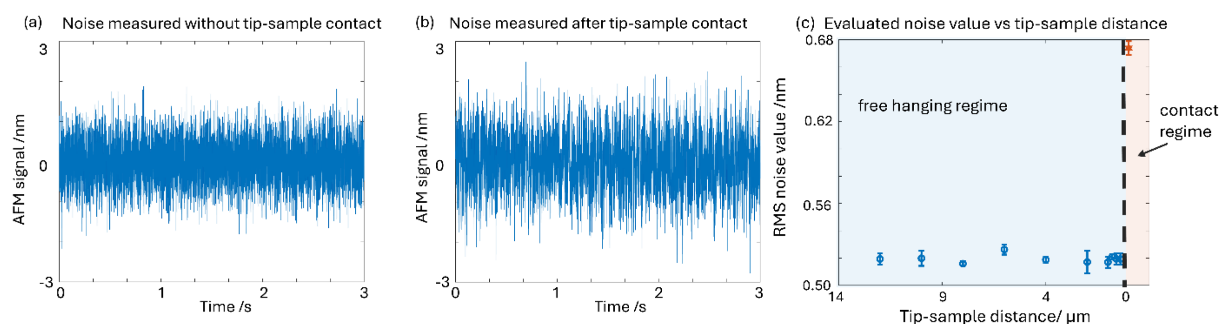

Figure 47 AFM signals acquired for noise analysis, which is measured (a) without contact established between tip and sample and (b) after tip approached the sample and making contact (c) illustrated the noise variations during the approaching process. It remains almost constant before tip-sample engagement and increases significantly after the tip contacting with the sample surface.

These signals shown in Figure 47a and Figure 47b exhibit RMS values of 0.52 nm for the sensor noise and 0.67 nm under tip-sample contact, respectively. The difference between the two values is due to the additional disturbances introduced by the closed-loop operated piezo stage once tip–sample contact is established. Furthermore, a series of noise measurements as a function of tip-sample distance are presented in Figure 47c. At each distance, the measurements are repeated at least three times, and the resulting STD are indicated as error bars in Figure 47c.

In this investigation, it is evident that as the tip approaches the sample, the noise level remains stable at approximately 0.52 nm in the freely hanging regime. However, once tip-sample contact is established, the measured noise increases immediately by about 0.16 nm. This difference is more clearly observed in the corresponding spectral diagrams, as illustrated in Figure 48.

Frequency analysis using FFT is applied to both AFM signals shown in Figure 47a and Figure 47b to identify their dominant noise components. The resulting spectra are illustrated in Figure 48 as blue and red curves, respectively. Overall, the two spectra show good agreement in the high-frequency range, whereas noticeable differences emerge in the low-frequency domain. Specifically, after tip-sample contact is established, the measured noise is generally higher in this domain compared to that in the freely hanging state. The additional peaks observed in the

red curve, particularly around 120 Hz and 200 Hz, represent noise contributions introduced by the piezo stage.

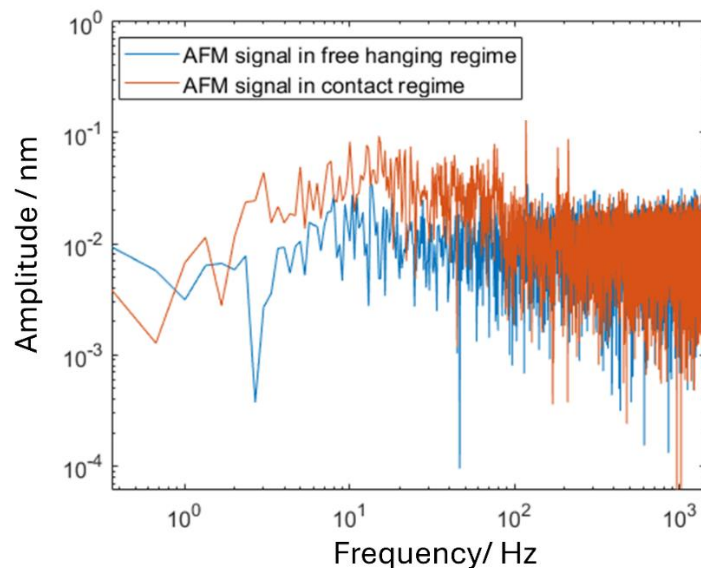

Figure 48 Spectrum analysis of the AFM signals acquired (a) when AFM tip hanging freely over the sample surface (no contact established between tip and sample) and (b) after tip sample contact established. Some of the major noise contributions from the piezo stage can be observed around 120 Hz and 200 Hz.

Following the investigation of sensor noise N_s, attention is now directed to the measurement noise N_{AFM}. In contrast to N_s, which reflects only the noise of the sensor, the N_{AFM} reflects the noise level observed during actual AFM measurements. Its minimum value, commonly referred to as instrument noise, is a key specification in instrument development, as it defines the lowest achievable noise level of the system. To determine the instrument noise of the developed AFM-mode, approximately 9000 sampling points of the height signal h are recorded at a fixed position over a duration of 12s, with the tip in contact with the sample and the whole system operating in closed-loop mode. A representative time-domain measurement, along with its corresponding frequency spectrum, is shown in Figure 49a and Figure 49b respectively.

The instrument noise is evaluated to be 0.84 nm, which is approximately 0.16 nm higher than the sensor noise N_s measured after establishing tip-sample contact, and about 0.32 nm higher than that measured in the free-hanging state. As shown in the spectrum in Figure 49b, distinct peaks appear also around 120 Hz and 200 Hz, which are primarily attributed to vibrations induced by the piezo stage. An additional strong peak occurs at approximately 80 Hz, which, based on an impulse test, corresponds to the eigenfrequency of the developed HM.

Additionally, the noise level in the low-frequency domain remains relatively high. This high noise level is primarily attributed to various environmental disturbances and the limited

https://doi.org/10.7795/110.20260421A

performance of the current vibration-isolation measures, including the air bearing stage and the noise reduction chamber, as discussed in [176]. Enhanced noise performance could potentially be achieved through the implementation of improved isolation strategies, such as a better vibration isolation table [177] and a more effective noise reduction chamber [178]. Further details regarding the noise reduction approaches employed in AFM-mode will be presented in the following chapter.

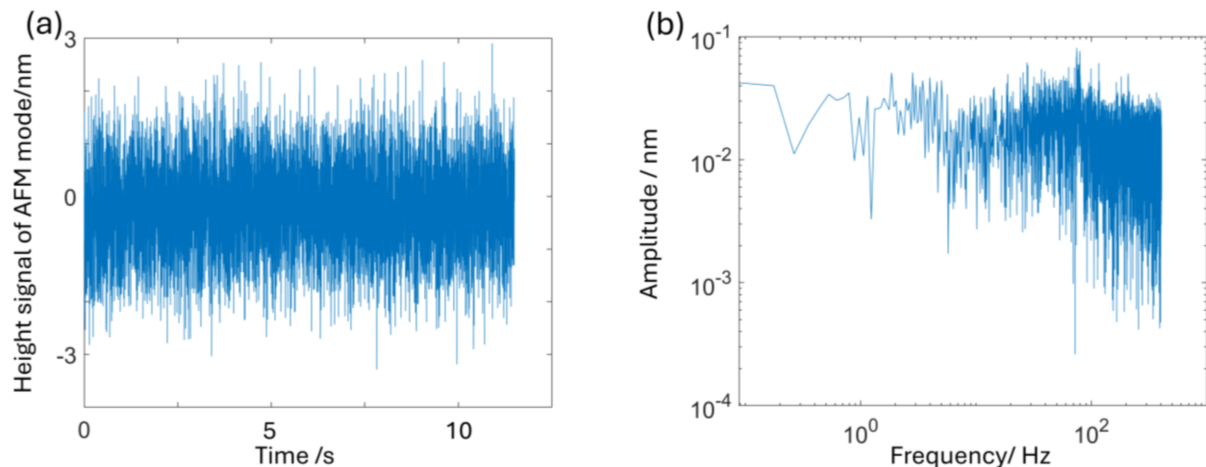

Figure 49 Height signal sampled at approximately 800 Hz for instrument noise analysis (a) the signal measured in closed-loop operated AFM-mode without tip scanning for 12s and (b) the spectrum of the acquired signal

Traceability

Traceability is another critical aspect in evaluating the performance of the AFM-mode of the HM, particularly when it is used for reference areal surface metrology. As the AFM measurements are mainly derived from the output signals of piezoresistive sensors embedded in the piezo stage, results of the AFM-mode must be traceably calibrated before application.

To establish the traceability chain between the AFM-mode of the HM and the SI unit of length (meter), one well-established approach is to perform traceable calibrations using step height and lateral standards. The measured values are then compared with reference values calibrated by metrological instruments, whose traceability is typically ensured through high-precision laser interferometry.

In this work, a lateral standard 2D 10000, manufactured with a nominal pitch of 10000 nm and a step height standard with structure height of 100 nm, are used for traceable calibration, as shown in Figure 50. A metrological AFM [179], whose traceability is linked to the optical wavelength of frequency stabilized laser [151], is employed to provide reference values,

including structure height and pitch. For comparison, the AFM-mode of the HM is applied to measure the same measurement area as measured in the reference measurements.

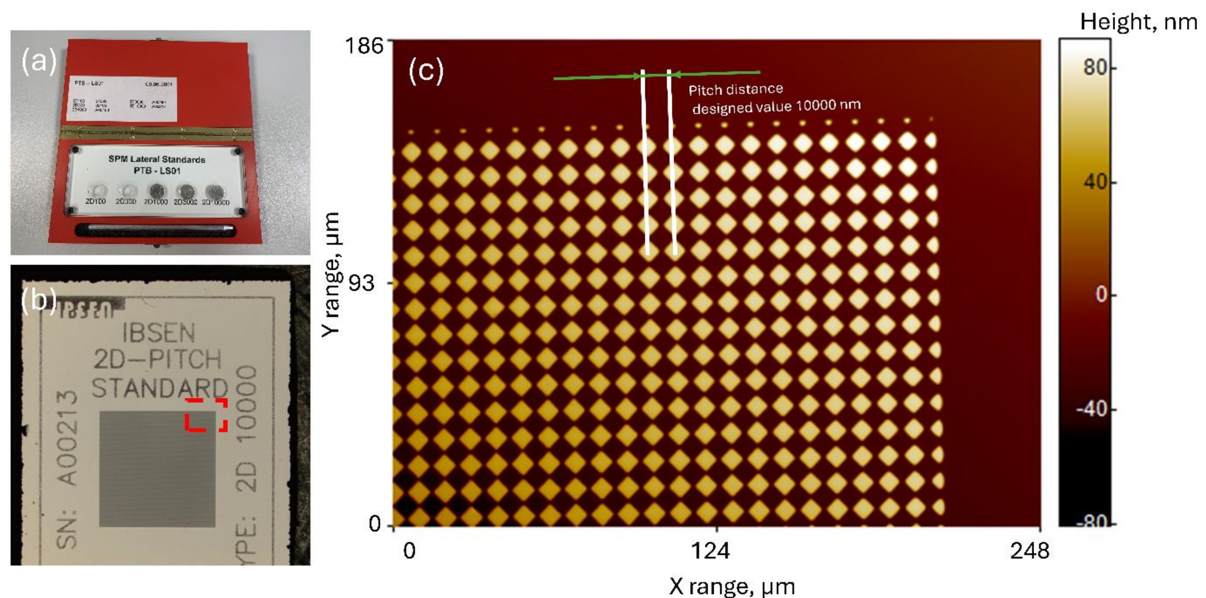

Figure 50 SPM lateral standards 2D 10000 (a) the SPM lateral standard set from 2D 100 to 10000; (b) over look of the 2D 10000 pitch standard whose up right corner is marked with red rectangle and (3) topographical details of the area marked in (2) measured by PSI mode of HM with 20x objective. Squares designed in 2D with pitch distance of 10000 nm can be observed.

Reference values, including the step height (100.9 nm ± 0.7 nm) and pitch distance (9999.5 nm ± 0.2 nm), are determined from measurements performed by the metrological AFM. These values are generally used to determine the scaling factors of the instrument along the three spatial axes [179]. Calibration measurements using the AFM-mode of the HM are performed across multiple AOIs, each measuring an area of 40µm x 20µm, with the fast scan direction set to either the x-or y-axis. The scan speed is set as 2 µm/s. An example of such a measurement is shown in Figure 51a. A representative profile along the fast scan axis (in this case, the x-axis) is randomly selected and presented in Figure 51b. All topography data are post-processed using a line-wise leveling technique to eliminate measurement drift and errors due to sample mounting.

The step height and lateral pitch distance are evaluated using the method recommended in ISO 5436 [180] and the PTB routine calibration procedure for 2D gratings [181], respectively. The evaluation results are summarized in Table 5. The scaling factors for the x-, y-, and z-axis of the AFM-mode of the HM are determined to be 0.9961, 0.9978, and 1.008, respectively. The deviations between the evaluated height and pitch values and their corresponding reference values are small, remaining below 1% in all three axes.

https://doi.org/10.7795/110.20260421A

Table 5 Comparison of the result of lateral standards 2D 10000 measured by the AFM-mode of the HM and the MAFM

	Step height, nm	Height STD, nm	Pitch value (x), nm	Pitch value (x) STD, nm	Pitch value (y), nm	Pitch value (y) STD, nm
AFM-mode HM	101.6	0.9	9960.5	70.2	9977.5	51.5
Metrological AFM	100.9	0.7	9999.5	0.2	9999.5	0.2

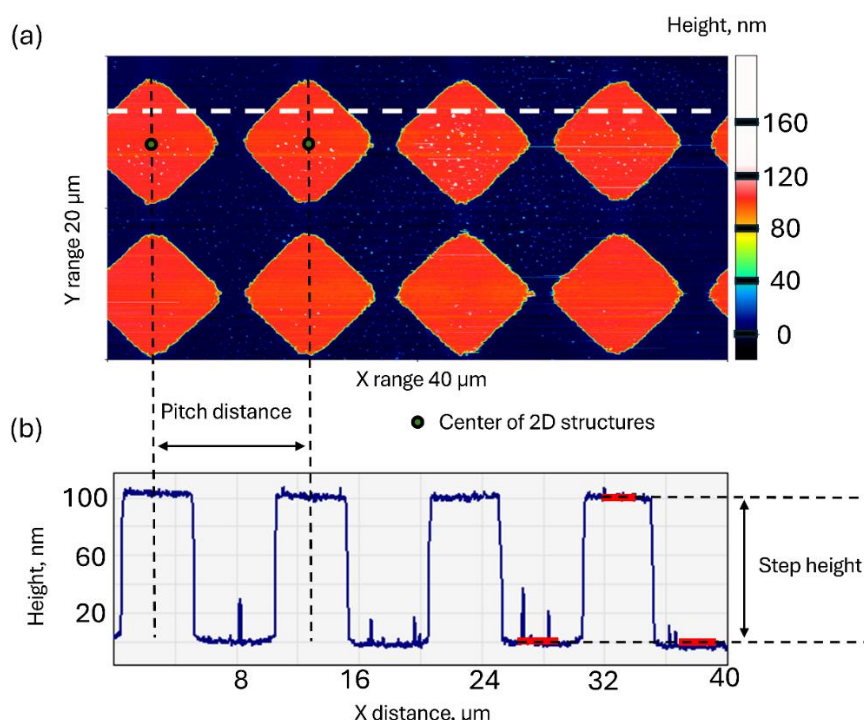

Figure 51 Calibration measurement of the SPM lateral standards 2D 10000 acquired by the AFM-mode of the HM (a) measured topography in size of 40 x 20 µm² and (b) profile along x-axis (fast scan axis) extracted at a randomly selected position marked with white dashed line in (a). The green circles mark the centers of two structures of the 2D 10000 standard and are used only to illustrate the pitch distance. They do not represent the actual measured structures.

The relatively large standard deviations observed in the pitch evaluation from the AFM-mode measurements along both lateral directions are likely due to inhomogeneities in the manufactured 2D grating structures. In contrast to the reference measurements, which are performed over large AOIs across the standard, the calibration measurements measure only a few 2D grating features. As a result, the manufacturing-induced variations strongly impact on the evaluation results.

Repeatability

The final part of the performance evaluation focuses on the repeatability of the developed AFM-mode. This investigation is conducted on a randomly selected area of a roughness standard (ARS f3 type ADT) provided by SiMETRICS [182]. Repeat measurements in a size of 2x20 µm² of the same AOI are taken successively in one hour as well as between days. The results are shown in Figure 52a. They appear consistent with each other. Profiles between repeated measurement extracted from a randomly selected position indicated by the red dashed line in Figure 52a, are shown in Figure 52b, exhibiting good agreement.

Repeat measurements, labeled R_1 through R_7, are acquired using the y-axis as the fast scan axis. A pixel distance of 20 nm and a scan speed of 2 µm/s are configured during the repeat measurements. To minimize the influence of drift and sample mounting imperfections, all measurements are post-processed using drift correction and line-wise leveling techniques.

Two parameters are applied for quantitatively describing the repeatability, (I) roughness parameter arithmetical mean height S_a:

$$S_a = \frac{1}{A_m} \iint |R(x, y)| \, dx \, dy \qquad \text{(Equ. 4.38)}$$

and (II) the average STD of n times repeat measurements R_i:

$$STD = \frac{1}{X \cdot Y} \sum_{y=1}^{Y} \sum_{x=1}^{X} \sqrt{\frac{\sum_{i=1}^{n} [R_i(x,y) - \mu(x,y)]^2}{n-1}} \qquad \text{(Equ. 4.39)}$$

With $\mu(x, y)$ indicates the mean value:

$$\mu = \frac{\sum_{i=1}^{n} R_i}{n} \qquad \text{(Equ. 4.40)}$$

Here, x and y denote the lateral positions, and A_m is the measurement area. The X and Y denote the total number of pixels along the x- and y-axes, respectively.

Table 6 Evaluation of arithmetical mean height S_a from AFM repeat measurements acquired by the AFM-mode of the HM over three days

	R1 (Day 1)	R2(Day 2)	R3(Day 2)	R4(Day 2)	R5(Day 3)	R6(Day 3)	R7(Day 3)
S_a	21.0 nm	21.2 nm	21.1 nm	21.0 nm	21.7 nm	21.5 nm	21.4 nm

https://doi.org/10.7795/110.20260421A

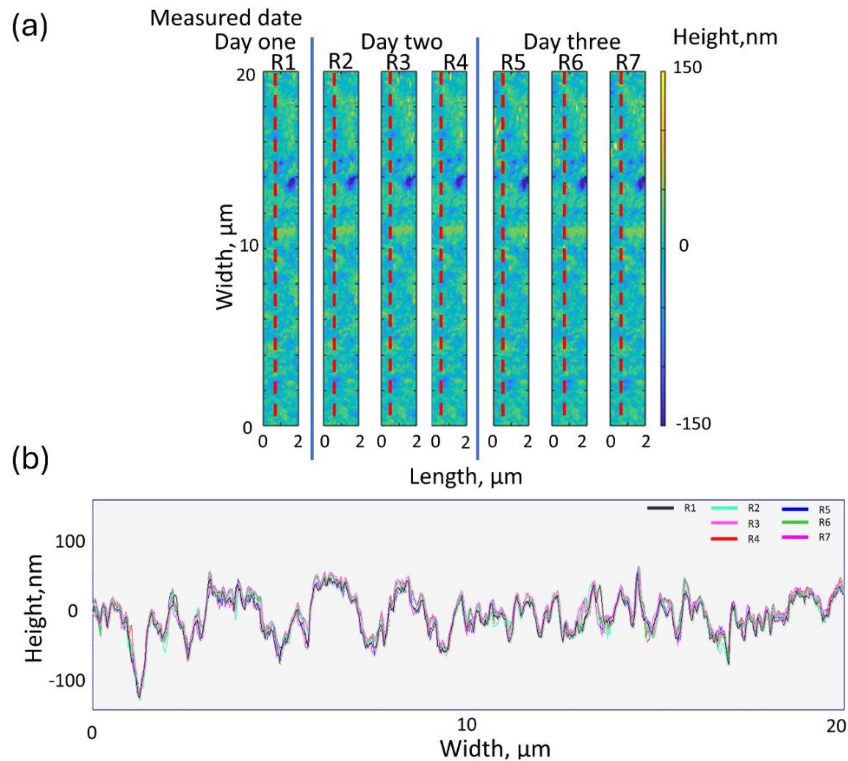

Figure 52 Repeated measurements of roughness standard ARS from company SiMETRICS [182] (a) seven AFM measurements named after R1 to R7 in the size of 2x20 µm² over a same sample position, acquired over three days; (b) comparison of seven vertical profiles extracted respectively from the seven AFM measurements (a) processed with operations: (I) lateral drift correction and (II) line-wise leveling.

The calculated S_a values for the repeat measurements are summarized in Table 6. The results, despite the fact that they are measured within a single day or across multiple days, demonstrate good repeatability. Minor variations in S_a observed across different days are attributed to lateral drift over the 24-hour period, resulting in slight positional shifts between measurements (e.g., R_2 and R_5).

On the other hand, the average STD value, used as an indicator of long-term repeatability, is calculated over the entire area (100 x 1000 pixels) across all seven measurements and gives a value of approximately 6.5 nm. However, this result is significantly influenced by lateral drifts. When considering only short-term repeatability, based on measurements acquired within the same day, from the example R_2 to R_4, which are recorded within one hour, the STD decreases by approximately 40%, reaching 3.7 nm. This value can be further reduced to 2.5 nm by excluding regions affected by non-systematic measurement artifacts or outliers, such as those caused by AFM tip pick-up effects. This is achieved by applying a histogram filter which filters out the top 10% topography data during the evaluation. A portion of the remaining variation can be attributed to instrument noise, approximately 0.8 nm as previously characterized, while the rest is likely due to system dynamic response characteristics, environmental vibrations, residual drift, and other measurement-related artifacts.

5. Optimizations in the hybrid microscopes

5.1. Calibration of the effective wavelength

The effective wavelength λ_{eff} plays a crucial role in both IM- and AFM-mode measurements. It may even be regarded as a foundational parameter underlying all measurements performed by the HM. As explained in Chapter 3, due to the enlarged NA value, λ_{eff} can no longer be considered the same as the nominal wavelength of the applied light source. Instead, it needs to be corrected by a NA-dependent factor f_{NA}.

Furthermore, this correction factor f_{NA} is also influenced by the tilting angle α of the sample, which is positioned on the piezo stage and serves as a reflective mirror during the measurement. The reasoning is intuitive: when the mirror is not aligned perpendicularly to the optical axis, the law of reflection implies that a portion of the incident light will not return along the same path. Instead, it is deflected outside of the aperture, thereby reducing the effective aperture, as illustrated in Figure 53.

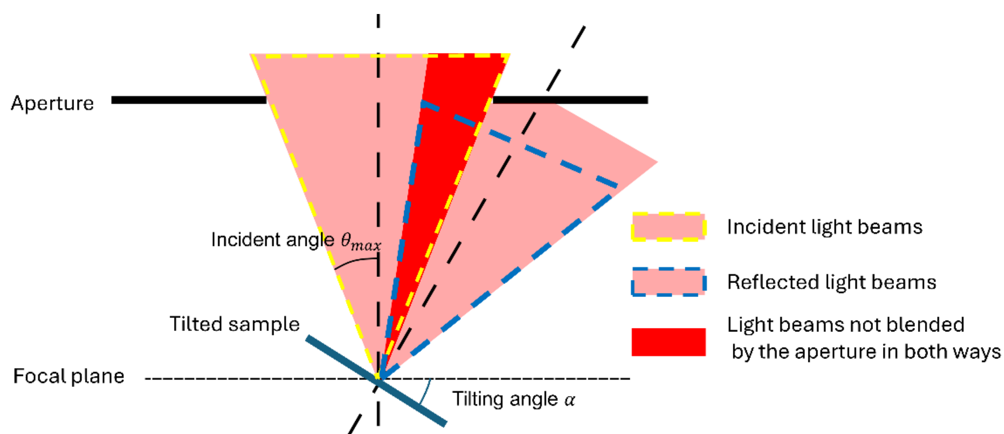

Figure 53 Illustration of the incident and reflected light beams behavior when a sample is placed with a tilting angle α

Determination of the effective wavelength λ_{eff}, used in the IM-mode of the HM is determined through both simulation and experiment. The simulation is based on the theoretical model introduced in Equ. 2.17, incorporating the pupil function defined as:

$$P(\theta) = circ\left(\frac{\theta}{\theta_{max}}\right) \cdot \cos^n \theta \cdot \cos\theta\,(1+\cos\theta)^2. \qquad \text{(Equ.5.1)}$$

In the experimental setup, a flat mirror is placed at the focal plane of the objective, and the effective wavelength λ_{eff} is estimated by analyzing the fringe spacing in the interference patterns captured by the camera. To investigate the dependence of λ_{eff} on the tilting angle α,

https://doi.org/10.7795/110.20260421A

the mirror is deliberately tilted within a range of −18° to 18°. The objective used in this study is a Nikon 20x Mirau-type objective with a NA of 0.4, which theoretically permits a maximum tilt range of approximately ±23°. To improve calibration accuracy, each measurement at a given tilt angle is repeated 4 times. The determined effective wavelengths with respect to the titling angle are summarized in Figure 54.

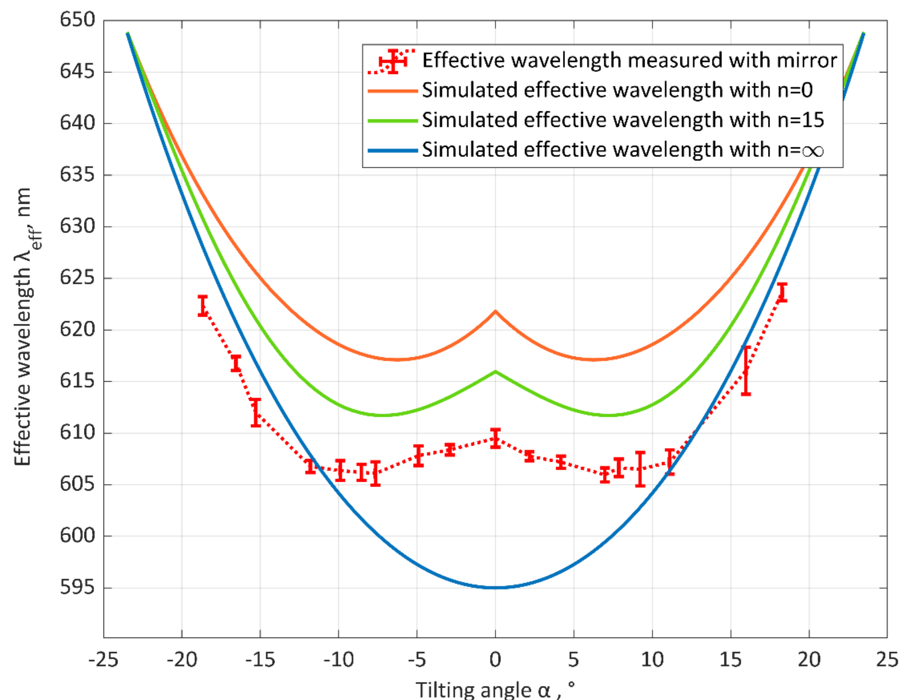

Figure 54 Simulated and measured effective wavelength λ_{eff} as a function of the tilting angle α using the HM, which is equipped with a Nikon 20x Mirau objective (NA 0.4) and a monochromatic LED light source (with a center wavelength is calibrated to 595 nm). Simulation models (Equ. 5.1) considering different levels of apodization are plotted in the diagram: (I) n=0 means no apodization effect occurs in the illumination system; (II) n=15 indicates the theoretically calculated apodization effect based on the specifications of the applied light source and (III) n=∞ indicates the strongest apodization effect that the system allows only light beams parallel to the optical axis to illuminate the surface, while light beams with other incident angle are blend out.

In the daily usage of the IM-mode, it is generally true that tilting angles resulting from mounting errors are compensated by adjusting the tilting stage before any interferometric measurements are performed. Therefore, attention is first directed to the effective wavelength λ_{eff} simulated or calibrated under the condition of zero tilting angle.

Based on the model described in Equ. 2.17, the simulated value of λ_{eff} is calculated as 616 nm at α=0, corresponding to a correction factor f_{NA} =1.035. Only minor deviations are observed when alternative models are applied, such as the one proposed by G. Schulz (Equ. 3.23, f_{NA}=1.044) or the model based on Gates' approach (Equ. 3.25, f_{NA}=1.048). However, the experimentally measured value of λ_{eff}=609.5 nm is notably lower than the smallest

https://doi.org/10.7795/110.20260421A

theoretically predicted value, corresponding to a correction factor of approximately f_{NA}=1.024. This discrepancy suggests that current models still exhibit limitations in accurately capturing the practical behavior. A possible explanation for this discrepancy is the underestimation of the apodization effect. This highlights the need for further investigation to improve the accuracy and completeness of the current modeling approach.

Figure 54 also shows that, despite a systematic offset between simulation and measurement, both the measured data (red curve) and the simulated data (green curve) exhibit a symmetric inverse-M-shaped dependence on the tilting angle α. As the tilting angle increases, the both experimentally and theoretically determined λ_{eff} first decreases and then increases sharply. This behavior carries two significant implications:

(I) A single, constant correction factor for determining λ_{eff} is not universally valid.

(II) Without compensating for tilting using an external tilting stage, measurement errors of up to 2.7% may be introduced. These errors depend on the tilting angle α and result from the application of an incorrect effective wavelength λ_{eff}.

This leads to an important question: what if the tilting angle is not caused by a mounting misalignment of the sample, but instead originates from local surface slopes within the measured structure? In such cases, the resulting measurement errors cannot be completely avoided in a single optical measurement, because the correct effective wavelength applicable to each local region is not known a priori. As a result, position-dependent measurement errors are introduced across the surface. Nevertheless, such errors may be corrected if the approximate topography of the measured surface is known in advance, for example from an additional WLI measurement. Based on such prior topographic information, the local tilting angle at different surface positions can be estimated, allowing a position-dependent calculation of the corresponding NA correction factor. This suggests a possible strategy for locally compensating slope-induced measurement errors. Related investigations on this approach are currently in progress.

Moreover, the observed dependence of λ_{eff} on the tilting angle α further confirms the necessity of the sensitivity calibration procedure described in the AFM-mode measurement protocol. Since the tilting angle of a newly installed AFM cantilever is not known in advance, performing a dedicated calibration to determine the effective wavelength is essential for achieving accurate AFM measurements.

https://doi.org/10.7795/110.20260421A

5.2. Noise reduction in the AFM-mode

The measurement noise N_{AFM} present in the AFM measurements of the HM originates from three primary sources. These include environmental disturbances, such as vibrations, electronic noise, for example, shot noise from electronic devices, and positioning noise of stages:

$$N_{AFM} = \sqrt{N_Z^2 + N_S^2 + N_e^2 + \ldots}. \quad \text{(Equ. 5.2)}$$

Here the components N_s , N_Z and N_e represent three major noise contributions to the final AFM measurement result, originating from the sensor, the stage, and the environment, respectively. In order to effectively reduce the overall measurement noise N_{AFM}, it is necessary to analyze and address each of these noise sources individually.

The stage-related noise contribution N_Z reflects the performance characteristics of the employed piezo stage in the developed HM system. Improving this aspect is challenging without access to detailed technical information from the stage manufacturer. The positioning noise of the currently used stage, operating in closed-loop mode, is characterized to be approximately 0.48 nm. Under the present conditions, the most cost-effective strategy for reducing N_z would be to replace the existing stage with a high-quality, low-noise alternative. However, since our analysis shows that positioning noise is not the dominant contributor to the measurement noise in the AFM measurements, this issue is not handled intensively in this study and is not considered as a primary concern.

The environmental contribution N_e arises from various external vibration sources, including ground vibrations, air turbulence, and acoustic disturbances. In the current setup, N_e is estimated to be approximately 0.08 nm, as the HM operates under standard laboratory conditions in a temperature-controlled environment and is mounted on an air-bearing vibration isolation stage. According to the investigation by J. Degenhardt [176], this value could be further reduced by effectively isolating environmental noise sources. For example, the use of advanced isolation techniques such as vibration isolators [177] and sound-absorbing materials has the potential to lower this noise component by at least 60%. However, since N_e represents one of the smallest contributions in the measurement noise, it is also not considered a primary focus of this study.

The final contributor to the overall measurement noise is the sensor noise N_s which is calibrated by analyzing the phase variation from the interference pattern captured by the camera. As discussed in the previous chapter, N_s is identified as the most dominant component of the measurement noise, with an estimated value of 0.68 nm when tip-sample

https://doi.org/10.7795/110.20260421A

contact is established. This is notably close to the total measured noise of 0.84 nm, highlighting the significant influence of the sensor noise on the system's overall performance.

Originally, this type of noise could arise from two main sources: (I) mechanical vibrations affecting the AFM cantilever and (II) noise originating from the employed CMOS camera. The mechanical vibrations are effectively suppressed by the Z coarse stage (NEXLINE), which features a stiff structural design and a high holding force. As a result, the camera noise is considered to be the primary contributor in this case.

The CMOS camera introduces various types of noise [183], including shot noise, dark current, and fixed pattern noise. Most of these noise components increase in magnitude with the intensity of the light captured by the camera. For instance, shot noise increases proportionally to the square root of the signal intensity, while fixed pattern noise scales linearly with the signal.

However, it is difficult for end users to estimate the individual contributions of each noise type originating from the CMOS camera. To better understand the influence of camera noise on the overall measurement noise, a normally distributed noise term N_{cam} is used to represent the combined effect. This noise level is experimentally calibrated under the typical AFM-mode operating conditions, with the camera running at 3000 fps and the light source operating at its full power output. Under these conditions, camera noise N_{cam} is determined to be 0.78 digits out of a maximum of 256 digits.

Assuming a discrete, noise free fringe pattern profile $P[n]$ of length N is affected by camera noise N_{cam}. The measured profile used for evaluating the AFM signal S_{AFM} can then be expressed as $P_m[n]$:

$$P_m[n] = P[n] + N_{cam}[n], n = 1 \dots N. \qquad \text{(Equ. 5.3)}$$

The propagation of camera noise N_{cam} through the Discrete Fourier Transform (DFT)-based phase detection algorithm, which is applied to evaluated S_{AFM}, can be mathematically described with following equations. First, determine the amplitude spectrum of $P_m[n]$:

$$F\{P_m[n]\} = \check{P}[c] + E[c] = \sum_{n=1}^{N}\{P[n] + N_{cam}[n]\}e^{\frac{-j2\pi cn}{N}}. \qquad \text{(Equ. 5.4)}$$

Here $F\{\ \}$ denotes the DFT operation. $E[c]$ is the discrete Fourier transform of the noise N_{cam}, c is the spatial frequency index. Then finding the index of dominated spatial frequency c_d and evaluating the phase corresponded to the dominate frequency $\vartheta[c_d]$ as:

$$\vartheta[c_d] = tan^{-1}\left(\frac{\Im(\check{P}[c_d]+E[c_d])}{\Re(\check{P}[c_d]+E[c_d])}\right). \qquad \text{(Equ. 5.5)}$$

https://doi.org/10.7795/110.20260421A

The $\Re$ and $\Im$ operators are used for extracting the real and imaginary part of the DFT respectively. Finally, the S_{AFM} signal suffering from the camera noise N_{cam} will be determined as:

$$S_{AFM} = \lambda_{eff} \cdot \frac{\vartheta[c_d]}{4\pi}. \quad \text{(Equ. 5.6)}$$

The model demonstrates that measurement noise can be reduced by increasing the SNR. The SNR value in this case is defined as the ratio between the dominant frequency component signal $\check{P}[c_d]$ to the noise $E[c_d]$. This improvement can be achieved by increasing the output intensity of the light source, which enhances the amplitude of the dominant frequency signal. This increase in intensity also leads to a rise in N_{cam}. However, since the dominant component of N_{cam} is shot noise, which increases only in proportion to the square root of the light intensity, the SNR continues to improve with increasing intensity. As a result, the overall measurement noise can be reduced.

For quantitative analysis of how N_{cam} propagates through the model introduced above, the GUM [102] provides two approaches: the classical GUM method and the Monte Carlo simulation method. The classical GUM method can be applied only when an explicit mathematical model of the noise propagation is available. In this approach, the influence of each noise source is quantified using sensitivity coefficients, which are obtained from the partial derivatives of the model with respect to the input quantities. However, due to the mathematical complexity of the model, as illustrated in Equ. 5.3 to Equ. 5.6, the application of the classical GUM method is highly challenging.

Therefore, in this study, the Monte Carlo method is applied to perform the analysis, serving as an alternative approach capable of handling complex mathematical models. The model described above is implemented in MATLAB and executed with more than 10^6 iterations to ensure statistically reliable results. The simulated and experimental values of N_{AFM} , evaluated using fringe profiles measured at different light source output levels (represented by varying amplitude values, as shown in Figure 55), are summarized in Figure 56.

As shown in Figure 56, both the experimental and simulated results exhibit the same decreasing trend, as expected. With increasing light source power, the measured noise decreases approximately in proportion to the inverse square root of the power. However, an offset is observed between the two curves. In particular, the simulated noise values are consistently higher than the experimental results. This discrepancy arises from the model simplification used in the simulation: to reduce computational effort, the STD of camera noise N_{cam} is fixed to the highest measured value, which is related to the pixel with the highest intensity. In practice, the fringe profile contains pixels with varying intensities, and pixels with

https://doi.org/10.7795/110.20260421A

lower intensities are associated with lower camera noise. As a result, this simplification leads to an overestimation of the camera noise in the simulation.

It should be noted that the previously mentioned amber LED light source (wavelength 595 nm) is not suitable for this investigation. This is due to two main reasons. First, its output is controlled via a rotary switch, and the corresponding output voltage is not precisely quantified. Second, although the maximum light output is sufficient for AFM signal evaluation, it results in a very low SNR ratio. For example, a interference fringe profile acquired from the backside of the AFM cantilever using the amber LED at its full power is shown in Figure 55, represented by the black curve labeled “Old LED”. The maximum intensity amplitude of this fringe is only about 9 digits. For a clear comparison, this curve is shifted by -20 digits in Figure 55.

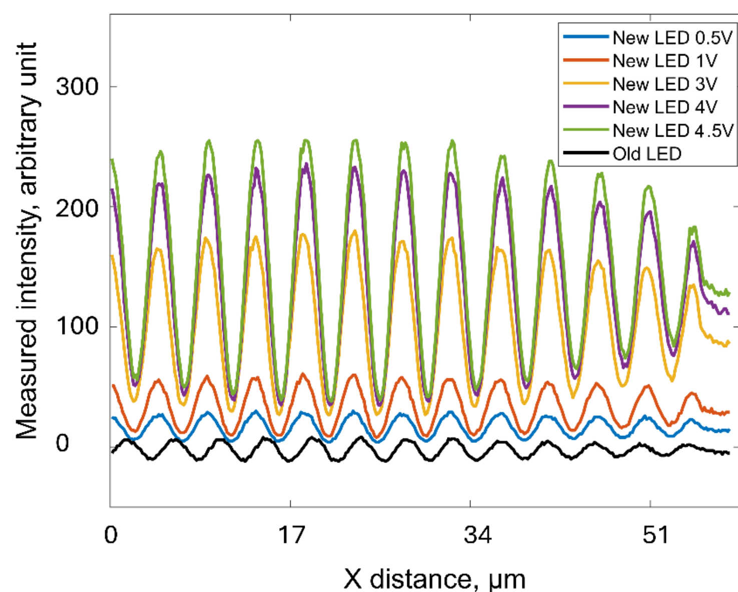

Figure 55 Interference fringe profiles captured at different optical output of new and old light sources. Black curve is measured with fully powered amber LED light source and the other 5 are measured with new red LED light source with given different output voltage. The black curve is demonstrated with an offset of -20 digits for having a clear comparison between the other curves.

To address this issue, a new monochromatic LED light source, the type SOLIS-620D from the company Thorlabs [184] with higher power, has been integrated into the HM system to replace the amber LED. The new LED is suitable for both measurement modes of the HM due to its appropriate coherence properties. It has a full width at half maximum (FWHM) bandwidth of 20 nm and a nominal wavelength of 620 nm, corresponding to red light emission. Its output intensity is numerically controlled via a dedicated LED controller based on a specified output voltage. Most notably, the maximum output intensity is approximately 20 times higher than that of the previous LED, offering significant potential for noise reduction. Several fringe profiles acquired at different output voltage levels are shown in Figure 55. The corresponding camera

https://doi.org/10.7795/110.20260421A

noise values N_{cam} associated with this new LED source have been experimentally determined and are summarized in Table 7.

Table 7 Experimentally measured camera noises N_{cam} in application of the new intensity intensive LED

Output voltage of the new LED light source, V	0.1	0.2	0.3	0.5	1.5	2.5	3.5	4.5
Amplitude of the fringe profile, digit	3	5	8	13	39	64	88	111
Camera noises N_{cam} , digit	0.41	0.57	0.69	0.86	1.47	1.87	2.19	2.48

The maximum output voltage of the new light source can be set up to 10 V. However, the camera approaches saturation when the output voltage is set to 4.5 V, with the corresponding fringe amplitude reaching 111 digits. Therefore, the experimental investigation of the relationship between measurement noise and light source intensity begins at 0.5 V, where the fringe amplitude (blue curve) is comparable to that obtained using the amber light source at its full power, and extends up to 4.5 V, just below the camera's saturation limit. As the output voltage increases, both the fringe amplitude and the associated camera noise increase accordingly. Notably, the fringe amplitude exhibits a linear growth, whereas the camera noise increases in proportion to the square root of the intensity. This behavior fits the increase pattern of the camera shot noise [183] and indicates that the shot noise is the dominate noise source of the camera.

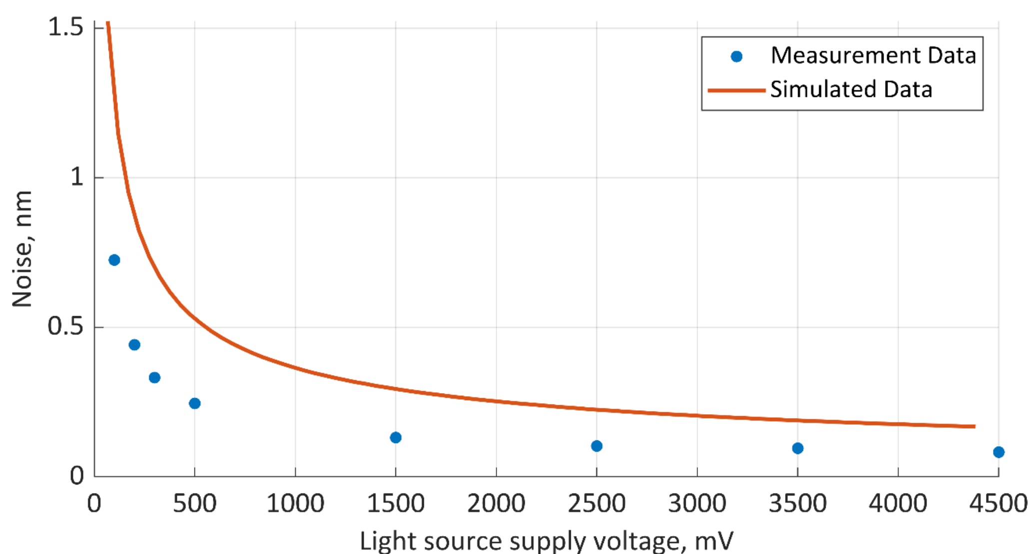

Figure 56 Measurement noise N_{AFM} determined by simulation and experimentally vs. light source output voltage. The simulation is based on the model (Equ. 4.31) with consideration of the camera noise N_{cam}.

https://doi.org/10.7795/110.20260421A

In the Figure 55, phase shifts (horizontal shifts) are observed in fringe profiles acquired either with the same light source at different output voltage or across different light sources. This observation indicates variations in the effective wavelength. For example, the black curve, recorded using a light source with a center wavelength of 595 nm, exhibits noticeable differences in fringe period compared to profiles obtained using sources centered at 620 nm. Interestingly, phase shifts are also present when using the same LED. This occurs because powering up the LED can lead to slight shifts in its center wavelength, due to the non-uniform gain across its spectral components.

Another method for enhancing the amplitude of the fringe profile, and thereby improving noise performance, is by increasing the camera exposure time. This effectively extends the integration time of the camera sensor, allowing it to accumulate more incoming light. As illustrated in Figure 57, five fringe profiles are captured from the backside of the same cantilever under the same light power (voltage of 500 mV), with exposure time as the only varying parameter. The results demonstrate that the amplitude of fringe profiles increases linearly with increasing exposure time.

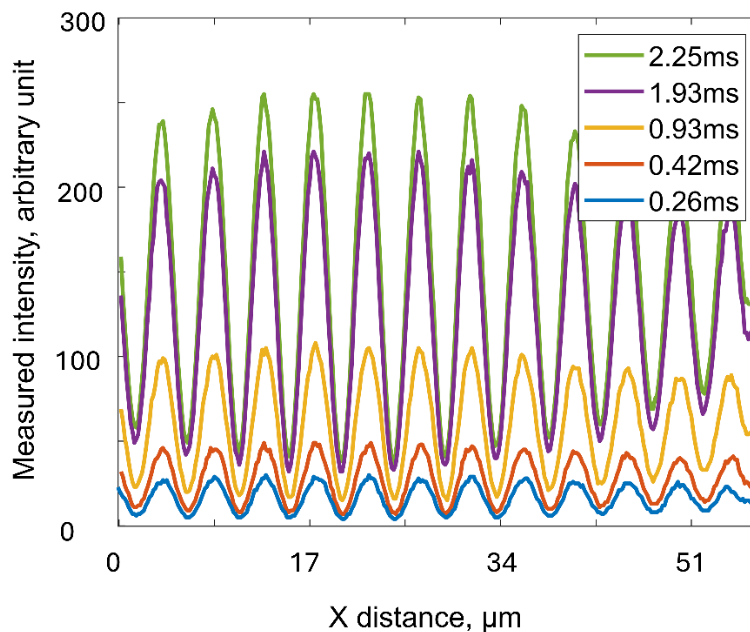

Figure 57 Interference fringe profiles captured at different camera exposure time while keeping the output voltage of the new light sources at 500 mV.

One key advantage of this approach is that the amplitude enhancement becomes independent of the power supplied to the light source. As a result, the central wavelength of the light remains constant even as the fringe amplitude increases. This stability is evident in Figure 57, where no phase shift is observed between fringe profiles recorded at different exposure times.

https://doi.org/10.7795/110.20260421A

However, this method comes with the trade-off of a reduced sampling rate, as longer exposure times extend the acquisition duration of each frame. Consequently, the overall measurement time increases, which introduces greater latency in the feedback loop. This latency can lead to slow measurement speed, loss of tip-sample contact or increased tip wear, ultimately compromising the performance and reliability of the developed AFM-mode.

The third approach for noise reduction is implemented without compromising the measurement performance of the AFM-mode. It is achieved through the application of an averaging technique during fringe profile data processing. In our earlier design, the AFM signal has been determined using the phase extracted from a single fringe profile. However, the camera has the ability to simultaneously capture up to eight fringe profiles without extending the measurement time, i.e. the image acquisition and image transferring time.

Therefore, ideally noise can be reduced by utilizing all captured profiles for phase calculation (AFM signal estimation) instead of relying on a single profile. Assuming there are 8 reference curves that are not affected by any type of tip-sample interaction, they can be denoted as W_i, with $i = 1 \dots 8$. Apart from the noise components, each of these profiles W_i contains the same underlying signal component defined by the dominant frequency v. Considering the presence of camera noise N_{cam}, one of these fringe profiles along the x-axis can be mathematically expressed as :

$$W_i = A\sin(vx + \vartheta) + N_{cam,i}(x) \quad \text{(Equ. 5.7)}$$

Here, A denotes the amplitude and ϑ the phase of the dominant frequency component, while x represents the spatial position along the x-axis of the fringe profile.

Once tip-sample contact is established, and in the absence of torsional forces, the phase variations $\Delta\vartheta$ observed across the 8 adjacent profiles $\widehat{W}_i$, caused by bending-induced deformations, are assumed to be identical. Under this assumption, the 8 fringe profiles can be regarded as 8 independent observations of the same underlying signal, differing only in their respective noise contributions:

$$\widehat{W}_i = A\sin(vx + \hat{\vartheta}) + N_{cam,i}(x), \quad \text{(Equ. 5.8)}$$

with

$$\hat{\vartheta} = \vartheta + \Delta\vartheta. \quad \text{(Equ. 5.9)}$$

The averaged profile $\overline{W}$ can be expressed as:

$$\overline{W} = \frac{\sum_{i=1}^{8} \widehat{W}_i}{8} = \frac{\sum_{i=1}^{8} N_{cam,i}(x)}{8} + A\sin\left(vx + \hat{\vartheta}\right). \quad \text{(Equ. 5.10)}$$

As evident from Equ.5.10, the AFM signal related phase shifts $\Delta\vartheta$ remain unchanged. The advantage of this averaging approach lies in noise reduction. Due to the random nature of the camera noise N_{cam}, which allows the noise contribution in the averaged profile to be reduced through averaging, with the standard deviation decreasing by a factor of $\sqrt{8}$.

In praxis, the phase offset ϑ may not be identical across all 8 profiles due to an undesired vertical tilting angle introduced during the mounting of the AFM probe. Within the FOV, this tilting angle causes the fringes to deviate from being perpendicular to the x-axis, resulting in diagonally oriented fringes, as illustrated in Figure 58a. Under such conditions, the 8 adjacent profiles W_i will be expressed as follows:

$$W_i = A\sin\left(vx + \vartheta + \breve{\vartheta}_i\right) + N_{cam,i}(x), \quad \text{(Equ. 5.11)}$$

Each profile has an individual phase offset $\breve{\vartheta}_i$.

With consideration of bending force caused phase shifts $\Delta\vartheta$, the profiles can be expressed as:

$$\widehat{W}_i = A\sin\left(vx + \vartheta + \breve{\vartheta}_i + \Delta\vartheta\right) + N_{cam,i}(x). \quad \text{(Equ. 5.12)}$$

As the vertical spacing between adjacent profiles is uniform and the vertical tilting angle across this region is assumed to be homogeneous, the individual phase offsets $\breve{\vartheta}_1$ to $\breve{\vartheta}_8$ can be described using an arithmetic sequence:

$$\breve{\vartheta}_i = \breve{\vartheta}_1 + d(i-1), i = 1 \dots 8, \quad \text{(Equ. 5.13)}$$

where d is the common phase difference between two profiles.

The averaged profile $\overline{W}$ can be then described as:

$$\overline{W} = \frac{A\sum_{i=1}^{8} \sin\left(vx + \vartheta + \breve{\vartheta}_i + \Delta\vartheta\right)}{8} + \frac{\sum_{i=1}^{8} N_{cam,i}(x)}{8}. \quad \text{(Equ. 5.14)}$$

With the help of sum-to-product formula of trigonometry:

$$\sin(a) + \sin(b) = 2\sin\left(\frac{a+b}{2}\right)\cos\left(\frac{a-b}{2}\right), \quad \text{(Equ. 5.15)}$$

the Equ. 5.14 can be further simplified as:

$$\overline{W} = K\sin\left(vx + \vartheta + \dot{\vartheta}_i + \Delta\vartheta + 3.5d\right) + \frac{\sum_{i=1}^{8} N_{cam,i}(x)}{8}, \quad \text{(Equ. 5.16)}$$

https://doi.org/10.7795/110.20260421A

with a constant K:

$$K = \frac{A\sum_{i=1}^{4}\cos\left[-0.5-(i-1)d\right]}{4}. \qquad \text{(Equ. 5.17)}$$

The Equ.5.14 indicates that the AFM signal related phase shifts $\Delta\vartheta$ remain still unchanged after application of averaging technique. The only effect is the introduction of a constant phase offset with a magnitude of $3.5d$ in the averaged profile, which occurs both before and after tip–sample contact. Since the evaluation of the AFM signal relies solely on phase variations rather than absolute phase values, this phase offset has no influence on the signal evaluation. Therefore, it can be concluded that the averaging technique enhances noise performance without compromising accuracy, even when the fringe profiles are not perfectly aligned due to an undesired tilting angle.

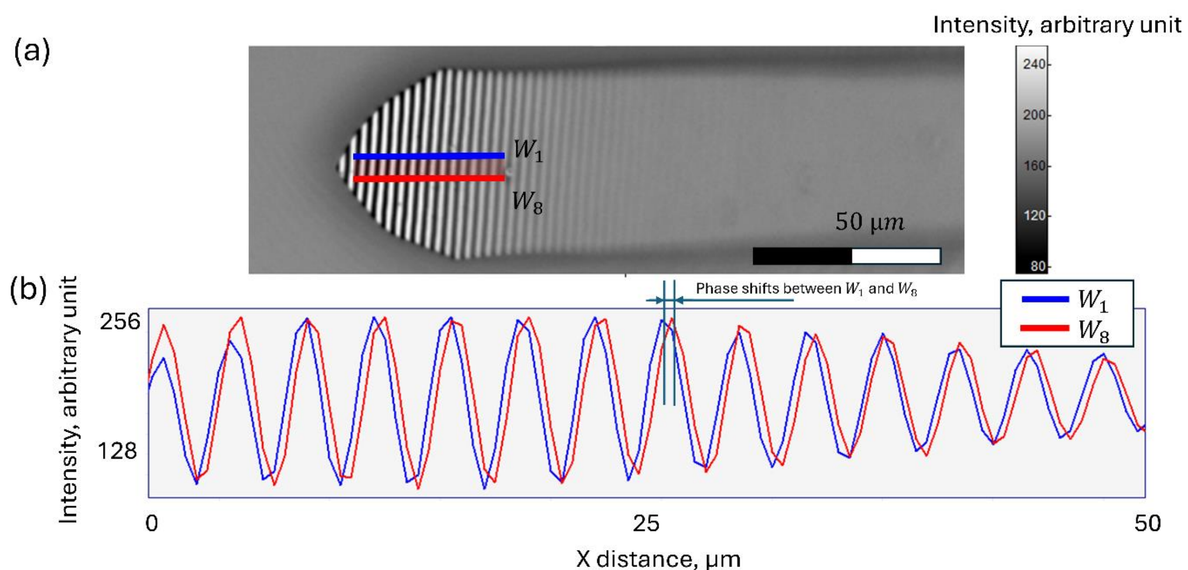

Figure 58 (a) Cantilever backside captured by 20x objective (zoomed). The fringes are not perfectly aligned vertically, indicating that the cantilever backside is tilted not only in the intended horizontal direction but also undesirably in the vertical direction. A red rectangular area in the middle of the cantilever marks the capture position of the eight adjacent fringe profiles W_{1-8} (b) The first and the last fringe profiles W_1 and W_8 captured are marked with color blue and red respectively. Due to the undesired tilting angle in vertical direction, they have different phases, which can be observed in the diagram as lateral phase shifts between two profiles.

By applying the aforementioned noise reduction techniques, the sensor noise is reduced from approximately 0.52 nm to 0.04 nm, as measured with the tip and sample not in contact. The measurement noise, measured when tip–sample contact is established, is also improved by 25%, decreasing from 0.84 nm to 0.63 nm. The remaining measurement noise is primarily attributed to vibrations from the piezo stage and external environmental sources. As discussed previously, further noise reduction may be achieved through the implementation of a low-noise, high-performance stage and the application of effective environmental isolation strategies.

5.3. Development of a one for all AFM tip switching system

The current AFM tip switching system is specifically designed for use with the Nikon 20x Mirau type objective. However, the developed measurement modes, including both the AFM-mode and the IM-mode, function reliably with objectives of different magnifications and from different manufacturers. To improve the adaptability of the HM system, a new version of the AFM tip switching mechanism has been developed to support a broader range of objective types. This updated design is shown in Figure 59a.

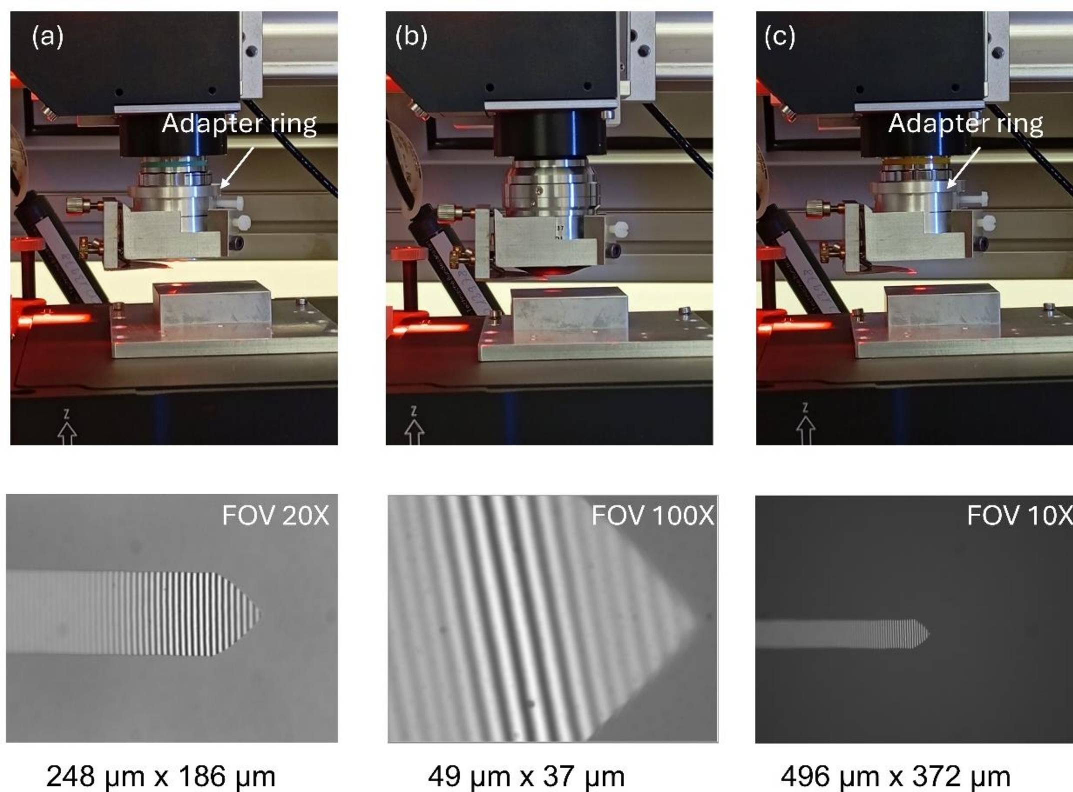

Figure 59 Application of the new low-cost version of AFM tip switching system mounted on the (a) Nikon 20x Mirau objective, (b) Nikon 100x Mirau objective and (c) Nikon 10x Mirau objective with help of adapter ring when it is needed. FOV images of the AFM cantilever backside acquired using different objectives are also presented. They are arranged below the images of the corresponding objectives.

This new design has two key features compared to the previous version:

(I) The new system eliminates the need for a DC motor and an analog voltage output card, thereby reducing overall design costs. However, tip switching must now be performed manually. Application testing results show no functionally significant differences between manual and motorized AFM tip switching. Specifically, the cantilever position STDs, evaluated based on FOV images acquired after successive mode switching, increased from 0.35 µm, 0.35 µm, and 0.01 µm when

https://doi.org/10.7795/110.20260421A

using the motorized system to 0.9 µm, 1.1 µm, and 0.05 µm when using the manual system in the x-, y-, and z-directions, respectively [185]. These variations are quite small and would not (significantly) impact on the daily usage of the HM. The primary distinction between the two versions lies in user convenience: the previous version allows hands-free operation, whereas the new design requires manual switching.

(II) In contrast to the earlier version, which was developed exclusively for objectives with an outer diameter of 26 mm such as the Nikon 20x Mirau objective, the new design offers improved adaptability. It supports objectives with different geometries through the use of an adapter ring. As shown in Figure 59a, b, and c, application tests are conducted with the new AFM tip switching system installed on Nikon Mirau objectives with magnifications of 20x 100x, and 10x, respectively.

In this new version, the hollow cylinder of the objective adapter is designed with an inner diameter of 31.5 mm to accommodate objectives with larger outer diameters, such as the Nikon 100x objective, which has an outer diameter of 31 mm. To adapt objectives with smaller outer diameters, such as the Nikon 10x and 20x Mirau objectives (both with an outer diameter of 26 mm), an adapter ring is inserted between the objective adapter and the objective, as shown in Figure 59a and c. This adapter ring ensures the perpendicular alignment of the AFM tip switching system relative to the sample, thereby maintaining the AFM tip as the lowest point during AFM measurements. It also preserves coaxial alignment between the tip switching mechanism and the objective. By supporting interchangeable objectives of various diameters, this design removes the need to manufacture a new AFM tip switching system for each objective size. Instead, only a different adapter ring is required.

5.4. Realization of the AFM-mode with 100x Mirau objectives

With the help of the new power intensive light source [184] and the new version of the AFM tip switching system (Figure 59), the HM measurement is no longer limited to using the 20x Mirau objective but is also compatible with other Mirau objectives currently available at PTB, including the Nikon 10x and 100x Mirau objectives. In fact, commonly available models of interference objectives, such as Mirau, Michelson, and Linnik types, are theoretically having the potential to be applied in the HM as well. Their integration requires only minimal reconstruction effort, which generally involves the fabrication of a compatible adapter ring.

As an example, a Nikon 100x Mirau objective is applied in the HM system to demonstrate its measurement performance in both the IM-mode and the AFM-mode. One of the biggest advantages of using the objective with a high magnification (100x) instead of a low

https://doi.org/10.7795/110.20260421A

magnification (20x) in optical measurement is that it offers better resolution as the NA value of the 100x objective is 0.7, greater than that of the 20x objective (NA=0.4).

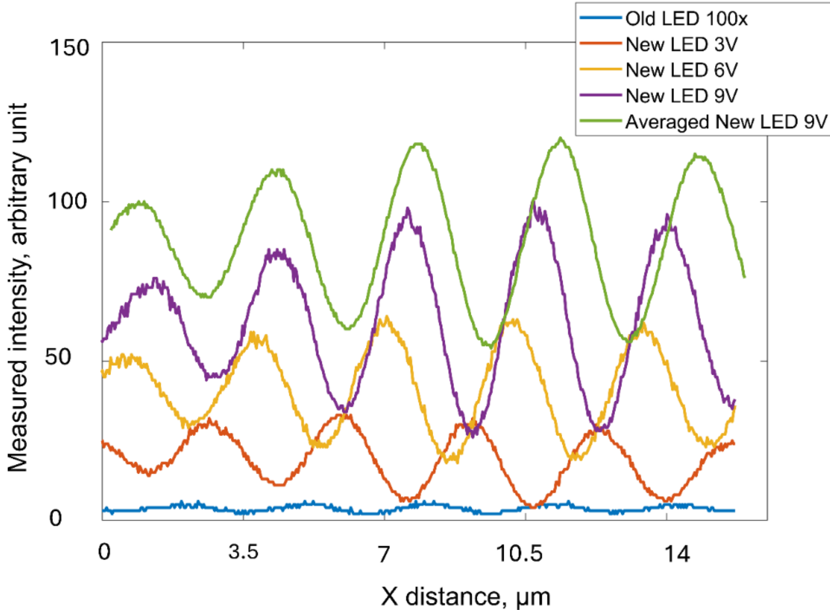

Figure 60 Interference fringe profiles captured at different optical output of new and old light sources while equipped with 100x Nikon Mirau objective.

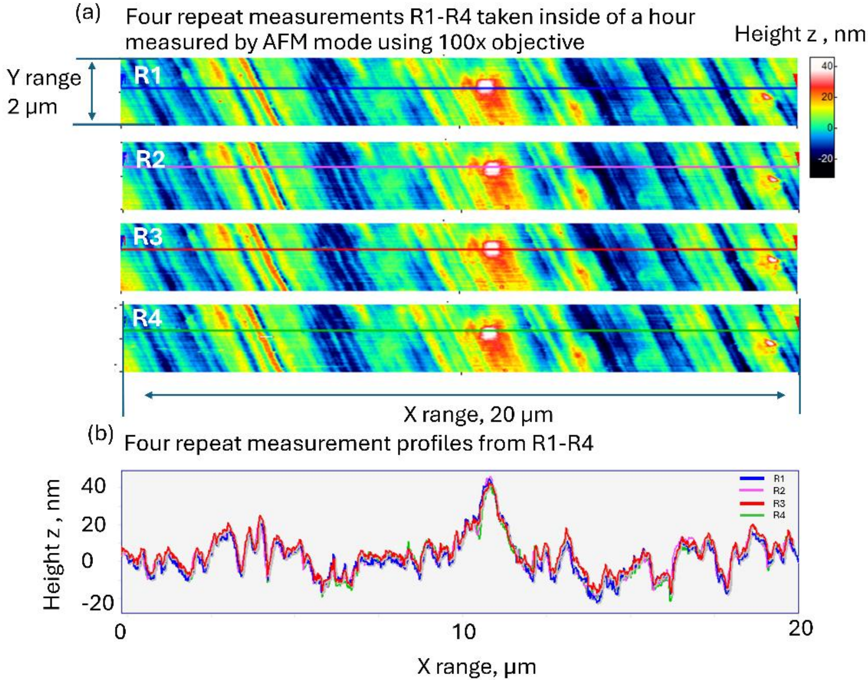

Figure 61 (a) AFM measurements over the same area (20µm x 2 µm) of a Cu roughness sample performed by the AFM-mode using a 100x Nikon Mirau objectives (b) a comparison of profiles extracted at the same position from the repeat measurements R1-R4 in (a)

https://doi.org/10.7795/110.20260421A

Comparing to the large size of FOV under equipping the 20x objective, the FOV under equipping the 100x objective has only a size of 49 µm x 37 µm area, as demonstrated in Figure 59b. Once an AFM probe must be exchanged, if the mounting position exhibits relatively large deviations along the three spatial axes, it can take considerable time, typically around 15 minutes, to relocate the AFM cantilever within the FOV and prepare it for the next measurement. The main reason for these deviations is the absence of an alignment chip in the new AFM tip switching system, which is due to the limited available space (appr. 2 mm) in the vertical direction. In the previous design, this chip was used to ensure repeatable positioning during probe replacement. Optimization efforts are currently underway to address this issue.

In addition, the measurement performance of the AFM-mode using different objectives is not identical, even when all other measurement conditions and instrumental setups are kept constant. This is because the quality of the observed interference fringe profiles varies fundamentally. Beyond the expected differences, such as variations in coherence length caused by the differing DOF range and NA values of the 20x and 100x objectives, one of the most noticeable distinctions is the reduction in interference fringe amplitude. Specifically, the amplitude observed with the 100x objective is significantly lower than that with the 20x objective, resulting in clearly increased measurement noise. This difference is primarily attributed to the optical design of the objectives: the rear aperture of the 20x objective is approximately 9 times larger than that of the 100x objective. Example fringe profiles acquired using the 100x objective at different light source output voltages are shown in Figure 60.From the Figure 60, several key observations can be made:

(I) The advantages of the new light source over the old one are evident. Even when operated at its maximum output voltage, the old light source fails to generate a satisfactory fringe pattern, as shown by the blue curve, which exhibits an amplitude of only 3 digits.

(II) As the output voltage of the new light source increases from 3 V to 9 V, the fringe amplitude also increases, as expected. However, noticeable phase shifts are observed when the voltages are increased, resulting from variations in the emitted wavelength. The reason remains the same as explained by investigations using 20x objective. However, these effects are significantly more noticeable in this scenario.

(III) Even with the new light source with its output power setting near to its maximum (9V out of 10V), the resulting fringe amplitude remains far from saturating the camera sensor. This indicates that, under the current system configuration, it is difficult to

achieve the same measurement performance with the 100x objective as with the 20x objective.

(IV) The averaging algorithm introduced earlier proves effective in smoothing the fringe profile (green curve) and reducing measurement noise, with the calibrated sensor noise reaching as low as 0.07 nm. However, the algorithm also causes a shift in the fundamental wavelength and slightly reduces the fringe amplitude.

Furthermore, four repeated AFM measurements (R1 to R4) are performed on the same surface area of a randomly selected copper sample using the AFM-mode with a 100x objective. These measurements are conducted successively and completed within one hour. The resulting topographies, corrected using line-wise leveling, are shown in Figure 61a. Corresponding profiles, representing the same topography after drift correction, are presented in Figure 61b. Good repeatability can be seen in the measured results.

https://doi.org/10.7795/110.20260421A

6. Applications of the hybrid microscope

The developed HM system demonstrates great potential for industrial applications, particularly in delivering both optical and reference measurements of engineered surfaces. It has been successfully employed in a range of topographical investigations involving sample surfaces composed of materials such as silicon, aluminum, gold, and copper. These investigations encompass a diverse set of surface finishing techniques, including turning, milling, polishing and etching.

During the investigation, both optical and AFM measurements are performed *in-situ*, without the need for remounting the sample. The sample is adjusted to remove unwanted tilting before measurement starts using the tilting stage. Optical measurements are performed using the 4+1-step PSI algorithm, without the application of additional noise-reduction techniques. AFM measurements are carried out using a kind of ContDLC AFM probe [166], with a pixel spacing of 20 nm and a scanning speed of 2 µm/s. The fast scan axis is oriented perpendicular to the cantilever, corresponding to the x-axis in the defined coordinate system of the HM system. Other instrumental parameters, such as camera exposure time and light source output voltage, are kept constant for all measurements to ensure comparability of the results.

Each AFM measurement is divided into several smaller areas, each with a limited scan range of 2 µm x 20 µm and a measurement time of 20 minutes. The approach of dividing a large scan area into multiple smaller areas is used to minimize the risk of losing tip–sample contact due to sudden, impulse-like environmental disturbance. This is particularly important as the HM operates under standard laboratory conditions, without the benefit of advanced environmental isolation. In this case, if the AFM tip loses contact with the sample surface, the measurement must be restarted. To avoid unnecessary time loss, AFM measurements with shorter measurement duration are advantageous.

Following measurement completion, the optical and AFM measurements are post-processed using a first-order plane correction algorithm and a line-wise leveling algorithm (also first order), respectively, to eliminate sample mounting- and drift-related error. Subsequently, the two measurements are spatially aligned using (I) the pre-calibrated AFM tip position and (II) a phase correlation algorithm (see Appendix) for correlating the results of both measurements.

6.1. *in-situ* AFM measurements

Two of the most important applications of the HM system are: (I) enabling *in-situ* AFM measurements to enhance the resolution of optical measurements, and (II) providing reference

measurements in areal surface metrology to ensure the fidelity of the optical data. To demonstrate these capabilities, both optical and AFM measurements are performed on a randomly selected surface area of a roughness standard (ARS f3 type ADT) from SiMETRICS [182]. An optical measurement covering an area of 248 µm x 186 µm with a resolution of 1448 x 1086 pixels is acquired using the IM-mode of the HM system equipped with a 20x objective (Figure 62a).

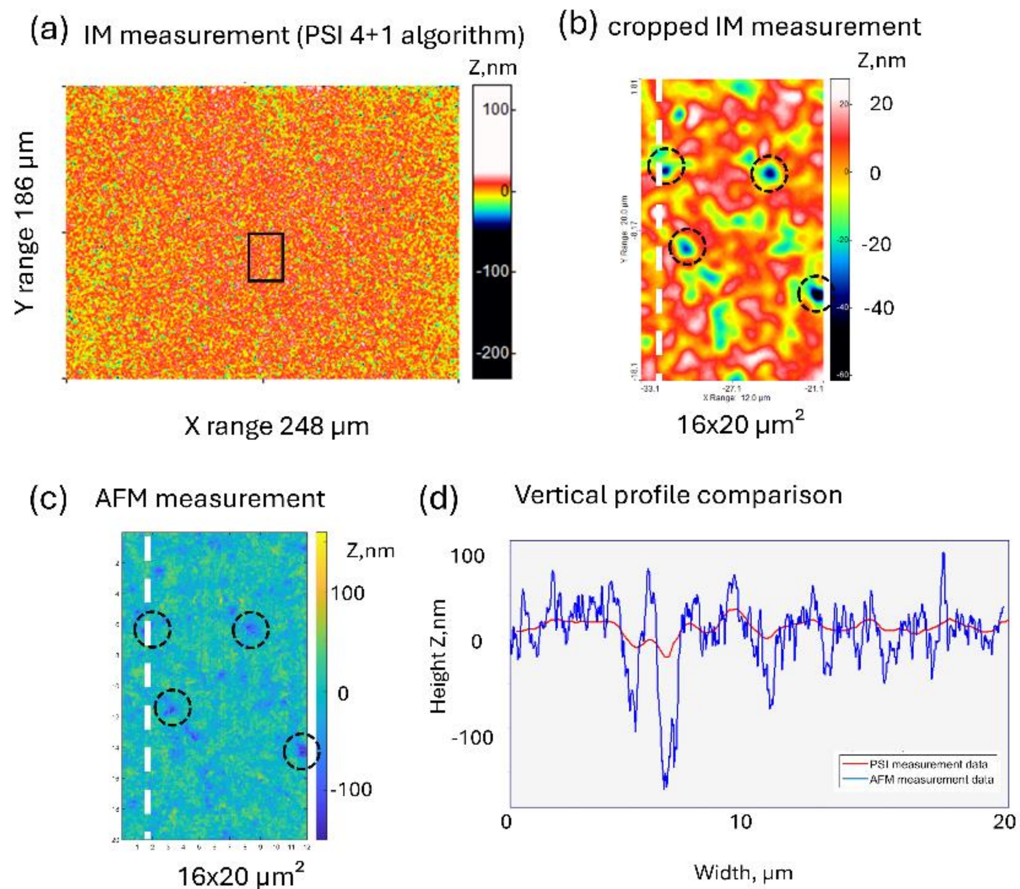

Figure 62 Measurement results of roughness standard ARS [182] from the company SiMETRICS (a) The IM-mode measurement results in size of 248 µm x 186 µm (b) Cropped IM measurement in size of 16 µm x 20 µm (c) 16 µm x 20 µm AFM measurement, which measured at the same position as (b). (d) Cross-section profiles comparison between IM and AFM measurements. Black rectangular marked in (a) indicates the location of cropped image (b). Dash circles marked in (b) and (c) are local valley structures. Based on highly overlapped circle positions between (b) and (c), it can be verified that IM and AFM are measured at the same topography of the sample surface. Vertical dashed white lines in (b) and (c) are marked as the position of profile shown in (d)

To resolve finer surface features and assess the fidelity of the optical measurement, an AFM measurement is conducted within the previously acquired optical measurement area. Due to the limited scan range of the AFM-mode, a small AOI, measuring 16 µm x 20 µm with a resolution of 600 x 1000 pixels, is selected. This AOI is constructed by stitching together eight

https://doi.org/10.7795/110.20260421A

smaller AFM images (each 2 µm x 20 µm) and is marked by a black rectangle in Figure 62a. The AFM result is presented in Figure 62c.

For a more direct comparison between the two measurement datasets, a cropped area from the optical measurement, matching the size and location of the AFM measurement, is extracted and enlarged, as shown in Figure 62b. Four dashed circles are highlighted in Figure 62b and Figure 62c, indicating local valley structures in the surface topography. The strong spatial agreement of these features in both measurements confirms the correlation between the optical and AFM measurements.

Furthermore, Figure 62d illustrates a comparison of the topography profiles obtained from both measurement datasets at the same lateral position, as indicated by the vertical dashed white lines in Figure 62b and Figure 62c. Several important observations can be made from this comparison:

(I) Low spatial frequency surface features are consistently and reliably captured by both measurement modes of the HM system.

(II) The AFM measurement reveals considerably finer details of the surface topography, particularly in the high spatial frequency domain, which are not resolved by the IM-mode.

(III) Optical measurements may exhibit inaccuracies under certain conditions and can fail to faithfully represent the actual surface topography. For example, local height deviations on the order of several hundred nanometers are observed between the optical and reference AFM profiles.

The topographical deviations noted in observations (II) and (III) primarily result from the lateral resolution limitations inherent to optical measurement techniques, which are fundamentally constrained by the diffraction limit. This limit is determined by the wavelength of the light source and the NA of the optical system, as discussed in Chapter 3 (Equ. 3.1– Equ. 3.10). In principle, surface measurements obtained using optical methods such as the IM-mode can be modeled as a convolution of the true surface with a PSF, whose effective radius is defined by the diffraction limit. As a result, the measured topography corresponds to a low-pass filtered representation of the true surface, in which fine details and the fidelity of surface features are inherently attenuated. This filtering effect leads to observable local deviations and measurement errors, particularly in areas with high spatial frequency content.

Another application example [71] involves the measurement of pitch structures on an N1 pattern from a selected CCS sample, with a nominal structure height of 32 nm. The optical

https://doi.org/10.7795/110.20260421A

measurement is acquired over a topography area of 248 µm x 186 µm, as shown in Figure 63a. The corresponding AFM measurement, shown in Figure 63c, is acquired at a resolution of 800 x 1000 pixels. An enlarged optical measured topography in the same size and at the same position as the AFM measurement is shown in Figure 63b. Both measurements clearly reveal the pitch structures etched into the surface of the CCS sample.

However, a comparison of the measured profiles obtained from the AFM- and IM-modes, as shown in Figure 63d, reveals clear differences in structural geometry, particularly in terms of height and edge sharpness. Specifically, the average structure height measured by the optical method is evaluated to be 10.2 nm, which is significantly smaller than the 27.9 nm measured by the AFM. Moreover, the sharp step edges of the pitch structures are not resolved in the optical profile. These discrepancies can be attributed to the lateral resolution limitations of the IM-mode, consistent with the effects discussed in the previous example.

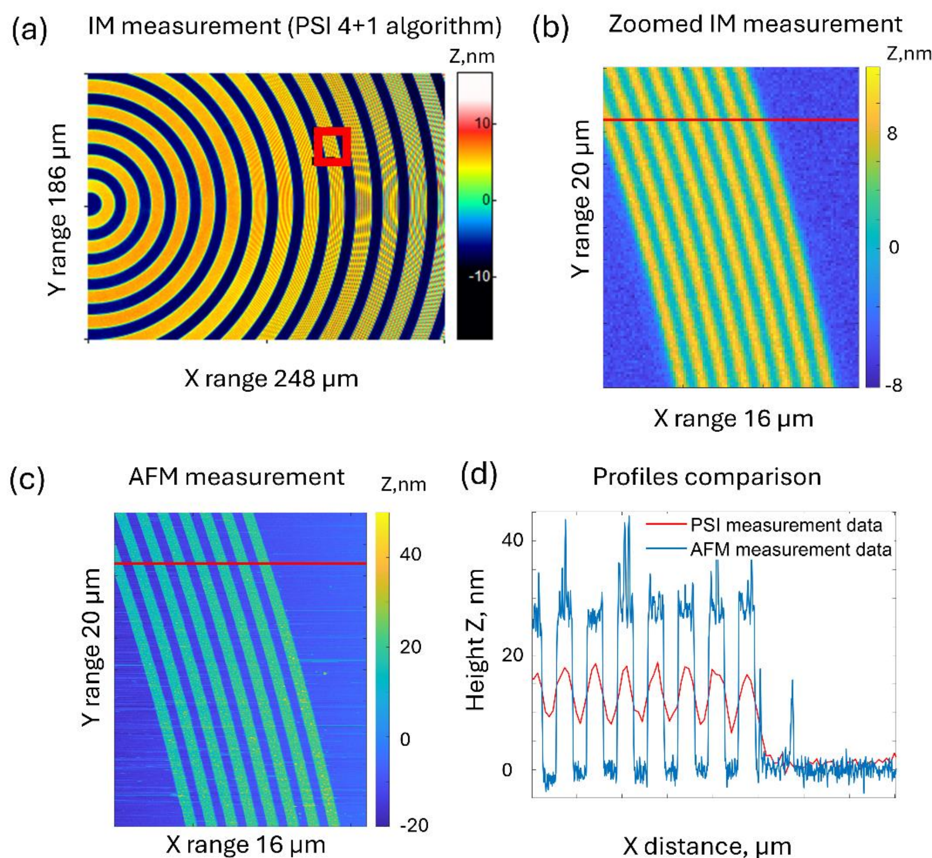

Figure 63 Measurement results of a N1 pattern of a CCS sample (a) The IM-mode measurement results in size of 248 µm x 186 µm (b) Cropped IM measurement in 16 µm x 20 µm (c) 16 µm x 20 µm AFM measurement, which measured at the same position as (b). (d) Cross-section profiles comparison between IM and AFM measurements. Red rectangular marked in (a) indicates the location of cropped image (b). This location is also where the AFM measurement (c) is taken placed. Horizontal red lines in (b) and (c) represent the same position on the sample. They are indicating where the profiles shown in (d) are extracted from both measurement results.

https://doi.org/10.7795/110.20260421A

Both application examples demonstrate great potential for using the AFM-mode of the developed HM for enhancing the lateral resolution of its IM measurements and meanwhile providing the reference measurement. However, two problems should be mentioned when using higher resolution AFM measurement from the AFM-mode of the HM as reference measurement:

1. Tip-convolution (dilation) effect. The recorded AFM topography represents the convolution of the AFM probe geometry with the true surface, rather than the surface itself [186–188]. Therefore, accurate surface reconstruction requires prior calibration of the tip geometry and subsequent deconvolution of its contribution from the AFM measurement results. Detailed procedures for tip calibration and correction have been developed in previous work by our research group [189].

2. Contamination effect (particle pick-up). Particles adhering to the AFM probe during scanning influence its effective geometry and introduce outliers into the measurement results [190]. Contact-mode AFM, as implemented in the current HM system, is especially sensitive to this effect due to its operating principle. Pick-up and drop-off events are stochastic; therefore, this type of outlier is hard to avoid. Post-processing algorithms are generally applied to suppress outliers caused by pickup effect and improve data quality. From an instrumentation standpoint, integrating non-contact or tapping-mode AFM into the HM would markedly reduce contamination effects. Development of such modes is ongoing.

6.2. Roughness investigations with a 20x objective

Surface roughness is commonly measured using optical or tactile methods. In most practical applications, the tactile approach refers to stylus profilometry rather than AFM, primarily due to the limited measurement range and slow measurement speed of early AFM systems. However, with modern advancements in AFM, which continues to push beyond its previous limitations, the use of AFM for characterizing industrial surface has significantly increased.

The HM can be well applied for addressing this task. To fulfill different needs in surface roughness investigations, the HM can provide its measurement abilities in both optical and AFM-modes with different objectives.

As application examples, the HM system equipped with 20x and 100x Nikon Mirau objectives is employed in surface roughness investigations conducted on a collection of samples (Figure 64). These samples differ in both material composition and surface finishing processes,

reflecting a broad range of real-world manufacturing conditions. For clarity and consistency in the discussion, each sample is referred to by the name of its base material. The standard experimental procedure involves randomly selecting an AOI on each sample. This AOI is first measured using the IM-mode with the PSI algorithm, followed by measurement using the AFM-mode to provide *in-situ* reference data. Both measurement results are subsequently post-processed, and the spatial correlation between the measurements is established using the phase correlation algorithm.

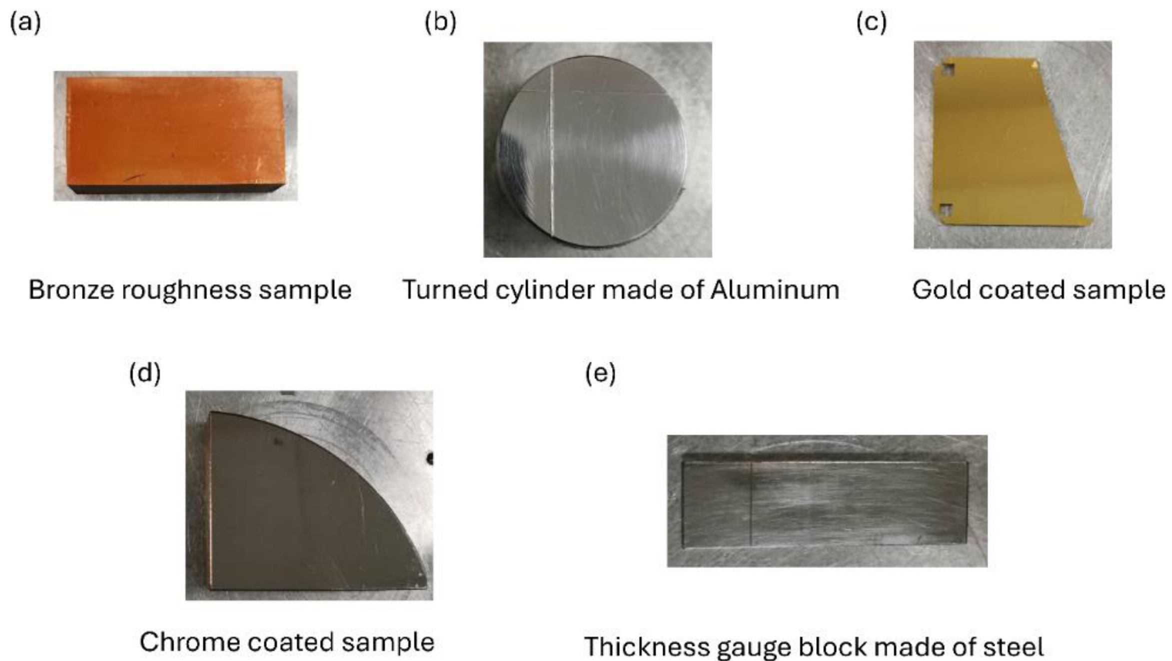

Figure 64 A collection of samples whose surfaces are made by different material and processed by different surface finishing methods (a) an old roughness sample made of bronze (b) an aluminum cylinder manufactured by turning (c) gold coated chip sample (d) chrome coated roughness sample and (e) thickness gauge block made of steel

The measurement results, each covering a uniform area of 12 µm x 20 µm, obtained using both the IM- and AFM-modes of the HM system, are summarized in Figure 65. The data are organized into five correlated pairs. These results demonstrate that the correlative metrology functions effectively and independently across different samples, regardless of material type or surface finishing technique.

The first impression of these measurement results is quite positive. Although the samples have different roughness from smooth (gold surface demonstrated in Figure 65c) to rough (steel surface demonstrated in Figure 65e) and have different surface characteristics, the IM measurements show good similarity with that of the AFM reference data in an overall view. Big features such as scratches, local peaks, and valleys are visible in IM measurements. This observation is supported by the profile comparisons diagrams demonstrated in Figure 66.

https://doi.org/10.7795/110.20260421A

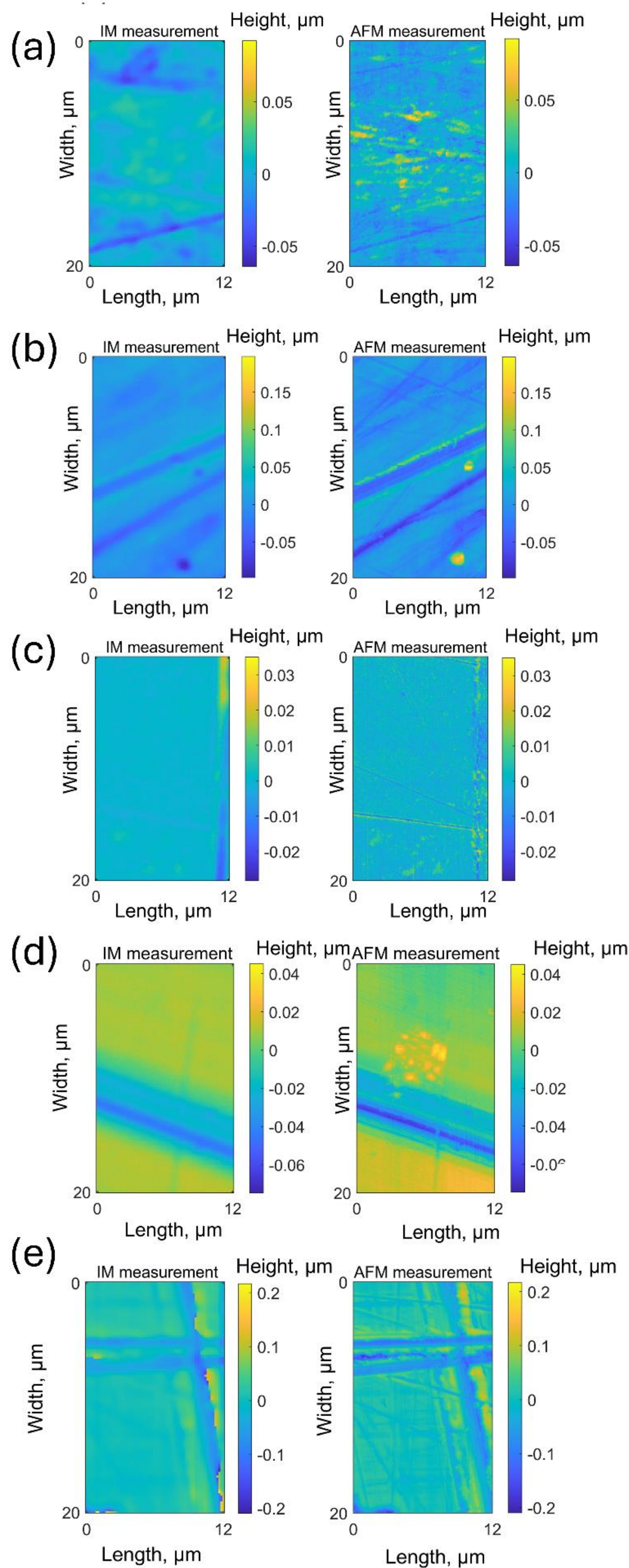

Figure 65 Correlative topographical measurement results using both AFM- and IM-modes of the HM equipped with a 20x objective over samples: (a) an old roughness sample made of bronze (b) an aluminum cylinder manufactured by turning machine (c) gold coated ship sample (d) chrome coated roughness sample and (e) thickness gauge block made of steel

https://doi.org/10.7795/110.20260421A

However, a more careful comparison reveals that the IM and AFM measurement results differ in several important respects. First, high spatial frequency features, such as fine surface roughness, are invisible in IM measurement results due to their limited lateral resolution. Second, even some low spatial frequency features captured by the IM-mode (e.g., the peaks and valleys shown in Figure 66b, Figure 66d, and Figure 66e) are not measured accurately. These features often appear with attenuated amplitudes, resulting in a less reliable representation of the actual surface compared to AFM measurement. These observations are also quantitatively verified by comparing their spectrums analyzed using the FFT algorithm (Figure 67).

Generally speaking, it is expected that the amplitudes of spatial topography signals measured by the IM-mode are lower than those obtained from the AFM-mode. Additional characteristics that are consistently observed in all profiles shown in Figure 67 are described below. First, there is a good overlap between the IM and AFM spectra in the low frequency range, from 0 to 0.3 μm^{-1}. Second, beginning at around 0.5 μm^{-1}, the IM spectrum begins to deviate significantly from the AFM spectrum. These findings align well with the ITF curve calibrated using the 20x objective in the previous chapter, where a 50% amplitude reduction begins at the cutoff frequency of 0.38 μm^{-1}. A third type of discrepancy involves the misrepresentation of local surface features. For example, as shown in the lower right corner of Figure 65b, the AFM measurement clearly indicates a peak (represented by a yellow colored area), whereas the IM measurement incorrectly identifies a valley at the same location (represented by a blue colored area).

The causes of these discrepancies are different. The first and second types are primarily attributed to the limited lateral resolution of the IM-mode, as previously discussed. In contrast, the third type of discrepancy, commonly referred to as an optical artifact, is a well-documented issue in optical surface metrology. A widely studied example is the so called "batwing effect" observed in WLI measurements [97]. Optical artifacts can arise from various sources. In the case of the batwing effect, the error is mainly caused by variations in the correlogram induced by multiple reflections. These interactions distort the recorded intensity patterns, resulting in a loss of fidelity in the IM signal and reducing its ability to accurately represent the actual surface topography. A more detailed discussion of this phenomenon will be provided in the following sections.

https://doi.org/10.7795/110.20260421A

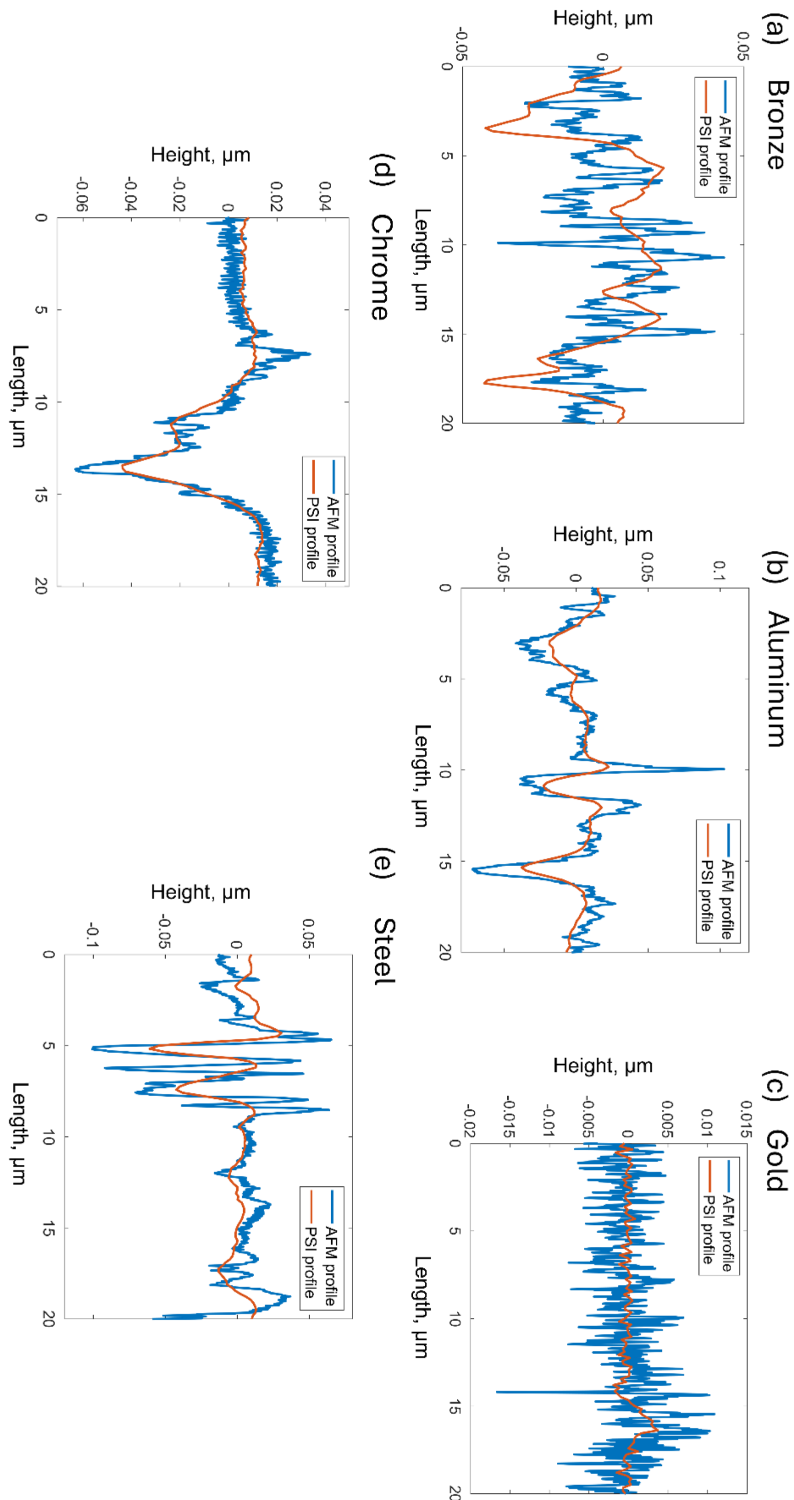

Figure 66 Correlative measurement results using both AFM- and IM-modes of the HM equipped with a 20x objective demonstrated as comparison of vertical profiles extracted at the same randomly selected position over samples: (a) an old roughness sample made of bronze (b) an aluminum cylinder manufactured by turning machine (c) gold coated ship sample (d) chrome coated roughness sample and (e) thickness gauge block made of steel

https://doi.org/10.7795/110.20260421A

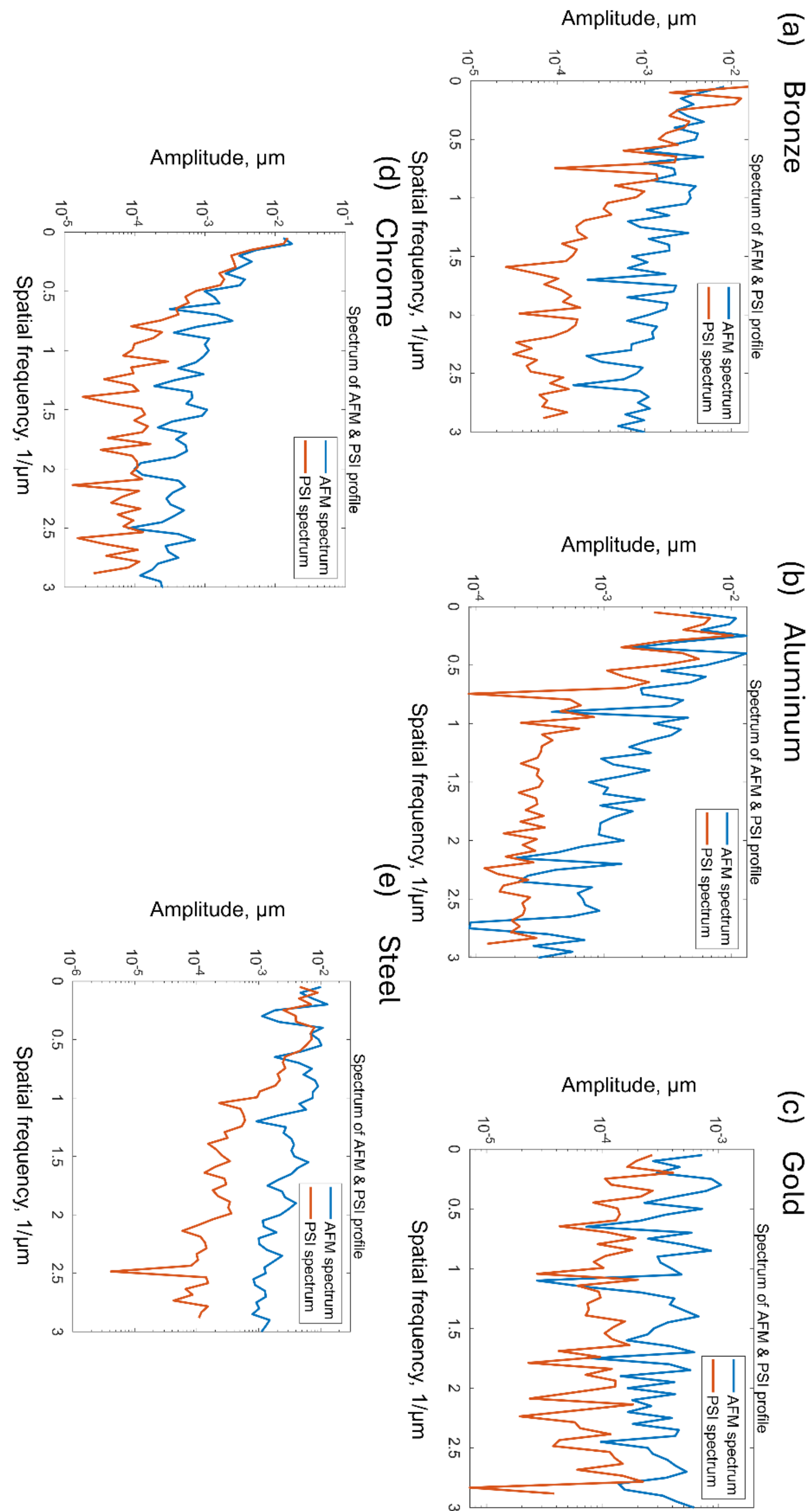

Figure 67 Spectrums of correlative profiles demonstrated in Figure 66 measured by the AFM- and IM-modes of the HM equipped with a 20x objective over (a) an old roughness sample made of bronze (b) an aluminum cylinder manufactured by turning machine (c) gold coated ship sample (d) chrome coated roughness sample and (e) thickness gauge block made of steel

https://doi.org/10.7795/110.20260421A

Furthermore, surface roughness is quantified from both AFM and IM measurements using height-based parameters. For example, two commonly used parameters [191] include the root mean square height, denoted as S_q:

$$S_q = \sqrt{\frac{1}{A_m} \iint z^2(x, y)\, dx\, dy}, \qquad \text{(Equ. 6.1)}$$

and arithmetical mean height S_a:

$$S_a = \frac{1}{A_m} \iint |z(x, y)|\, dx\, dy. \qquad \text{(Equ. 6.2)}$$

Here, x and y represent the lateral positions of the measured point. Parameter z is the height of the measured point. Parameter A is the evaluation related measurement area.

In general, surface roughness investigations using optical instruments are conducted with objectives of 20x and 50x magnification, while 100x objectives are used whenever possible to improve lateral resolution and reveal finer surface features. However, since each magnification level corresponds to a different measurement bandwidth, the evaluated roughness parameters can vary significantly [192]. As a result, it becomes difficult to determine whether the obtained parameters truly reflect the true surface roughness characteristics.

To address these challenges, filtration techniques are employed in roughness analysis. By applying appropriate filters, such as the S-filter and L-filter defined in ISO 25178-2 [191,193], the raw measurement data can be processed in a standardized manner. These filters are designed to attenuate the amplitudes of short wavelength and long wavelength surface features, respectively. Through this process, the bandwidth of the measured data is uniformly adjusted across different instruments, enabling meaningful comparison of roughness parameters. In addition, filtration allows the separation of surface roughness from form, waviness, and measurement noise, leading to more reliable roughness evaluation results.

The application of filtering techniques in roughness measurements requires the definition of two key parameters specified in roughness analysis: the long wavelength cutoff in the L-filter, denoted by λc, and the short wavelength cutoff in the S-filter, denoted by λs [194]. In this study, two cutoff wavelengths are selected to construct a bandpass filter used for preprocessing the measurement data. Specifically, λc is selected as 10 µm and λs is selected as 2.6 µm.

The choice of 10 µm as the long wavelength cutoff is based on the measurement ranges of the two modes. The AFM measurements cover a length of 12 µm, whereas the original IM measurements span a much larger area of 248 µm. By removing the low frequency content

https://doi.org/10.7795/110.20260421A

from the IM measurement, which cannot be captured by the AFM-mode, the two measurement methods are aligned to share the same lower spatial frequency boundary.

Table 8 Comparison of the evaluated roughness parameters S_a and S_q based on IM and AFM measurements of five samples (measured by the HM equipped with a 20x objective)

		Filtered only with absolute L-Filter ($\lambda c = 10.0\ \mu m$)		Filtered only with relative L-Filter ($\lambda c = 2.6\ \mu m$)		Filtered with L-Filter ($\lambda c = 10.0\ \mu m$) and S-Filter ($\lambda s = 2.6\ \mu m$)	
		IM	AFM	IM	AFM	IM	AFM
Al	S_a/nm	9.3	15.8	3.7	9.3	6.7	9.8
	S_q/nm	12.3	22.0	5.5	14.0	8.4	13.3
Steel	S_a/nm	18.2	25.2	9.1	16.8	10.7	12.6
	S_q/nm	29.4	36.2	18.4	24.9	15.9	17.6
Cu	S_a/nm	7.2	9.6	2.8	7.7	3.9	4.6
	S_q/nm	9.6	13.2	4.0	10.7	5.1	5.9
Au	S_a/nm	0.6	2.6	0.5	2.5	0.2	0.4
	S_q/nm	0.8	3.4	0.6	3.3	0.3	0.5
Cr	S_a/nm	0.7	2.5	0.5	2.1	0.4	1.2
	S_q/nm	0.9	3.4	0.7	2.9	0.5	1.5

Similarly, the short wavelength cutoff of 2.6 µm is selected to ensure a fair comparison between IM and AFM measurements by aligning their spatial frequency ranges. Due to the limited sampling resolution of the IM-mode, approximately 172 nm per pixel, the AFM-mode, with a sampling resolution of 20 nm per pixel, is better able to resolve high-frequency surface features. The upper frequency limit is therefore set to correspond to the lateral spatial period determined from the ITF calibration. This corresponds to a wavelength of 2.6 µm, at which at

https://doi.org/10.7795/110.20260421A

least 50% of the signal amplitude can still be reliably captured by the IM-mode. Under these conditions, the roughness parameters evaluated from both measurement methods become more directly comparable.

It should be noted that the focus of this section is on surface roughness measurement. As demonstrated in earlier discussions, optical topography measurements can be affected by optical artifacts, which may negatively influence the evaluation of roughness parameters. To remove such impacts, areas measured with such artifacts should be trimmed out so that they will not be involved in roughness evaluation. Also, this section mainly discusses the roughness results obtained with the 20x objective. Results from the 100x objective will be presented in the next section.

A total of three groups of roughness evaluations, each based on different spatial filters, are carried out. The corresponding evaluation results, expressed through roughness parameters S_a and S_q, are summarized in Table 8. In the first two columns of Table 8, the measured topographies are filtered using high-pass filters with cutoff wavelengths of $\lambda c = 10$ µm or $\lambda c = 2.6$ µm respectively. The results in the third column are evaluated using both filters with a lower limit $\lambda c = 10.0$ µm and an upper limit $\lambda s = 2.6$ µm.

The evaluation results are broadly consistent with expectations. Significant discrepancies in the of S_a and S_q values are observed when comparing measurements obtained from the IM-mode with those from the AFM-mode. Overall, both methods confirm that the Au and Cr samples exhibit smoother surfaces than the other three materials, namely Al, Steel, and Cu. These deviations are primarily attributed to the limited lateral resolution of the IM-mode, which is unable to capture high spatial frequency components of surface roughness. In contrast, the AFM-mode provides better spatial resolution, allowing accurate detection of fine surface features.

Although the roughness values obtained through AFM measurements are generally higher than those measured by IM-mode, a closer agreement is observed in the third column where a bandpass filter is applied during pre-processing of both measured datasets. This consistency can be explained by the fact that, within the selected low-frequency range, both measurement techniques are capable of detecting topographical features with comparable accuracy. As a result, the influence of lateral resolution limitations in the IM-mode becomes less significant in this specific frequency domain.

6.3. Roughness investigations with a 100x objective

Surface roughness investigations using the HM system with the 100x objective follow the same procedure as those conducted with the 20x objective, as described in Section 6.2. The only distinction in the instrumental configuration between these two investigations concerns the light source. As previously explained, the output power of the amber LED is insufficient for both measurement modes when using the 100x objective, primarily due to its smaller objective aperture. To address this, a red LED with a central wavelength of 620 nanometers and an effective wavelength of approximately 710 nanometers [184] is employed. The corresponding measurement results are presented in Figure 68.

In general, the IM measurement results obtained using the 100x objective reveal finer topographical details and exhibit greater similarity to the AFM reference measurements compared to those acquired with the 20x objective. These similarities are so pronounced that, even without using a correlation algorithm, one can visually observe a strong correspondence between the IM and AFM measurements.

Consistent with the observations presented in the previous section, low spatial frequency features such as scratches, local peaks, and valleys are effectively captured by IM measurements. This is further supported by the similarities identified through the comparison of randomly selected surface profiles, as shown in Figure 69. The previously discussed phenomena, including the low pass filtering behavior of the IM-mode and the presence of three characteristic types of discrepancies, remain evident in the results obtained using the 100x objective.

More detailed surface features are observed in the IM measurements shown in Figure 68 and Figure 69 when using the 100x objective. This is due to the improved lateral resolution of the 100x objective compared to the 20x objective, resulting from its higher NA (0.7 versus 0.4). As a consequence, improvements are evident in the first two types of discrepancies discussed earlier. In particular, the amplitude of low spatial frequency features is measured with greater accuracy and shows closer agreement with the reference data than that of 20x objective. However, complete elimination of any of the three identified discrepancies is not achieved with the 100x high-NA objective.

https://doi.org/10.7795/110.20260421A

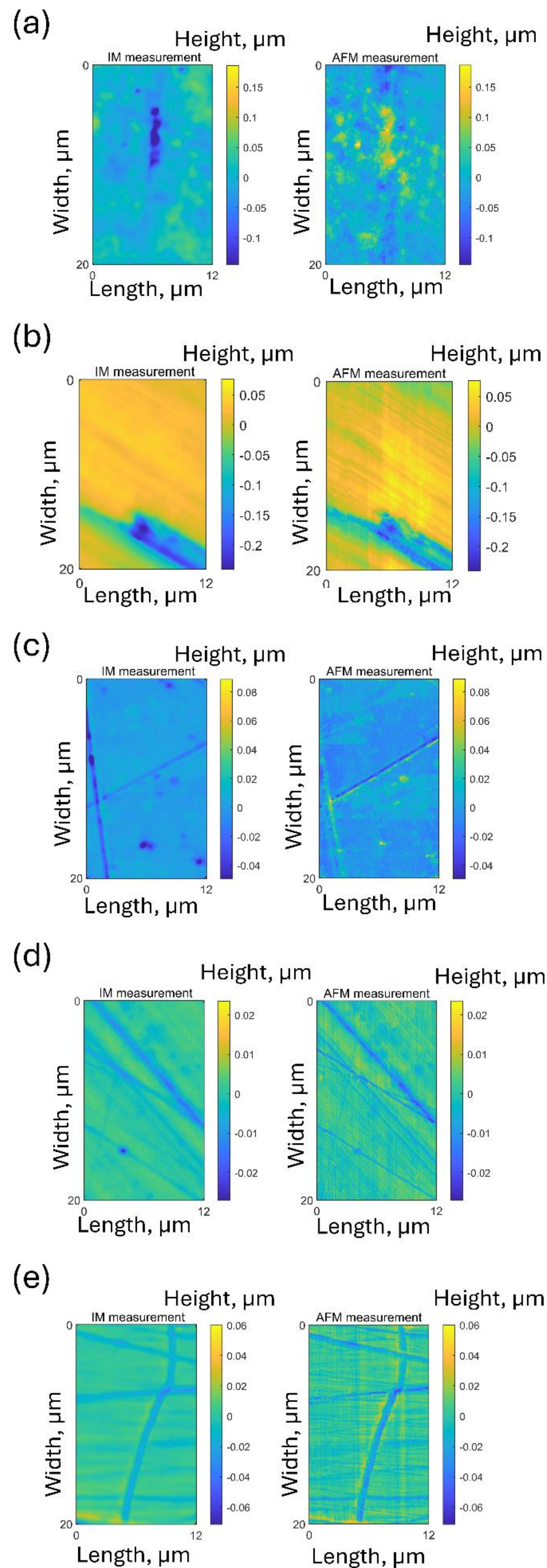

Figure 68 Correlative topographical measurement results using both AFM- and IM-modes of the HM equipped with a 100x objective over samples: (a) an old roughness sample made of bronze (b) an aluminum cylinder manufactured by turning machine (c) gold coated ship sample (d) chrome coated roughness sample and (e) thickness gauge block made of steel

https://doi.org/10.7795/110.20260421A

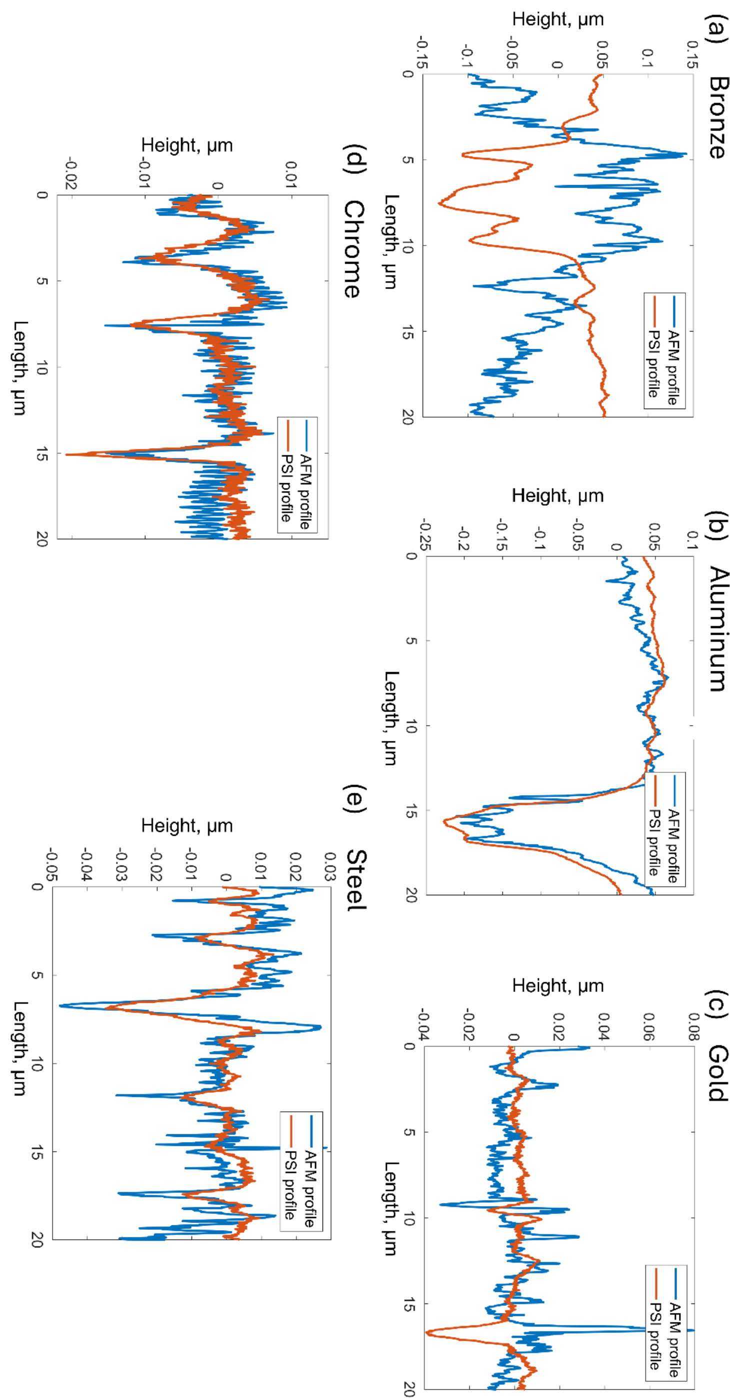

Figure 69 Correlative measurement results using both AFM- and IM-modes of the HM equipped with a 100x objective demonstrated as comparison of vertical profiles extracted at the same randomly selected position over samples: (a) an old roughness sample made of bronze (b) an aluminum cylinder manufactured by turning machine (c) gold coated ship sample (d) chrome coated roughness sample and (e) thickness gauge block made of steel

https://doi.org/10.7795/110.20260421A

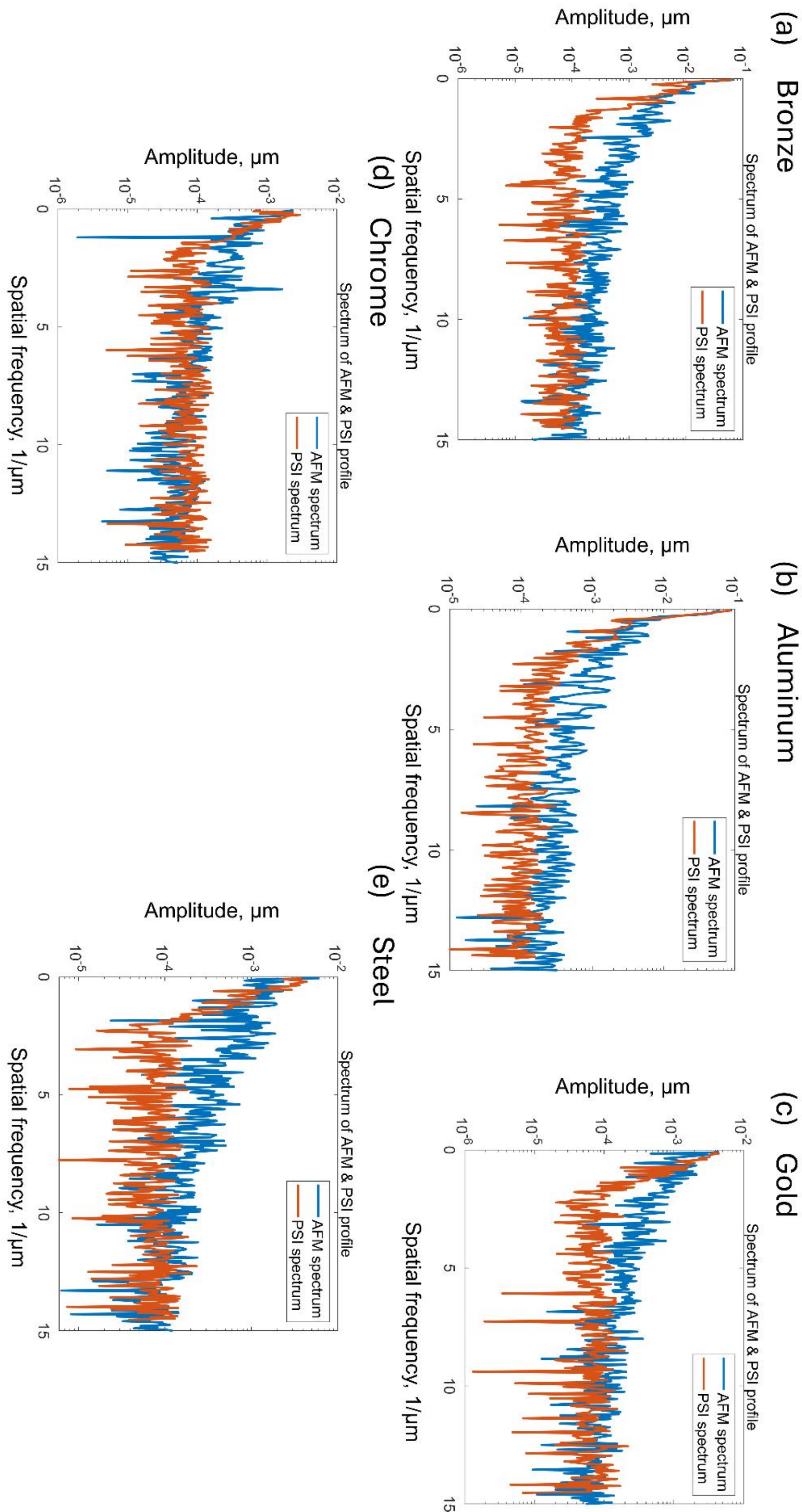

Figure 70 Spectrums of correlative profiles demonstrated in Figure 69 measured by the AFM and IM-modes of the HM equipped with a 100x objective over (a) an old roughness sample made of bronze (b) an aluminum cylinder manufactured by turning machine (c) gold coated ship sample (d) chrome coated roughness sample and (e) thickness gauge block made of steel

https://doi.org/10.7795/110.20260421A

Table 9 Comparison of the evaluated roughness parameters S_a and S_q based on IM and AFM measurements of five samples (measured by the HM equipped with a 100x objective)

		Filtered only with absolute L-Filter ($\lambda c = 10.0\ \mu m$)		**Filtered only with relative L-Filter ($\lambda c = 2.6\ \mu m$)**		**Filtered with L-Filter ($\lambda c = 10.0\ \mu m$) and S-Filter ($\lambda s = 2.6\ \mu m$)**	
		IM	AFM	IM	AFM	IM	AFM
Al	S_a/nm	14.7	17.4	4.3	7.8	12.5	13.4
	S_q/nm	26.5	28.1	7.8	12.3	21.6	21.3
Steel	S_a/nm	4.6	7.5	3.0	6.5	2.4	2.5
	S_q/nm	6.4	10.6	4.2	9.0	3.1	3.3
Cu	S_a/nm	7.2	9.6	2.8	7.7	3.9	4.6
	S_q/nm	9.6	13.2	4.0	10.7	5.1	5.9
Au	S_a/nm	4.0	7.0	2.8	5.6	2.3	3.0
	S_q/nm	7.5	10.7	5.5	9.0	3.4	3.9
Cr	S_a/nm	2.1	3.2	1.3	2.6	1.2	1.2
	S_q/nm	3.0	4.8	1.8	4.1	1.6	1.7

From a spectral perspective, the conclusion remains the same. Although the IM-mode with the 100x objective benefits from a higher NA value, it still operates based on the same underlying optical measurement principles. The increase in NA primarily results in a positive shift of the lateral period limit [61] from 2.6 µm to 1.0 µm. As a result, the IM measurement spectrum continues to exhibit the behavior of a low pass filter when compared to the AFM spectrum, as shown in Figure 70. In the low frequency range, the IM spectrum closely resembles the AFM reference. However, as the spatial frequency increases, especially beyond the lateral period

https://doi.org/10.7795/110.20260421A

limit, the amplitude gradually decreases until both measurement modes reach a frequency range dominated by measurement noise.

Surface roughness evaluations are also conducted using the measured topography data, following the same methodology previously applied with the 20x objective. To ensure comparability, the same filtering procedures are applied across all datasets, thereby maintaining consistent pre-processing conditions. The resulting roughness parameters are summarized in Table 9.

The evaluated roughness parameters show strong similarity to those from the 20x objective investigation. Specifically, although significant differences are observed in the first two columns of Table 9, where the topography data are processed using only a high-pass filter, the results converge closely in the third column, where both AFM and IM data are processed with a bandwidth filter (2.6–10.0 μm). More impressively, comparing to Table 8 (results of using the 20x objective), the roughness parameter differences between IM and AFM measurement are much smaller than that in Table 9, especially those in the third column. This observation indicates that as the NA increases, lateral resolution improves, the IM measured results are more closely related to the true topography, which is represented by the AFM reference data.

However, it must be emphasized that even when the roughness parameters and the spectral curve appear reasonable, as shown in Figure 70a, the reliability of the IM measurements cannot be guaranteed in the absence of a reference topography. This limitation becomes evident in the case of the Bronze (Cu) surface. Without the AFM measurement, it would not be apparent that the IM data are severely distorted due to the presence of an optical artifact. As shown in Figure 68a, the IM measurements incorrectly indicate a local valley structure where a local peak actually exists. This reversal is further demonstrated in Figure 69a, where the optical profile exhibits a shape similar to that of the AFM profile but with inverted height values. Under the influence of this optical artifact, the IM and AFM measurements are negatively correlated across the entire area of interest.

This observation reveals two notable peculiarities. First, optical artifacts have not previously appeared in the measured topography with such large dimensions, approximately 10 μm in length and 4 μm in width. Second, despite this significant deviation in surface structure, neither the spectral comparison shown in Figure 70a nor the roughness parameters listed in Table 9 are able to reveal its presence. These findings reveal a critical limitation of relying solely on roughness parameters and spectral analysis, without reference data, for evaluating the accuracy of optical measurements.

https://doi.org/10.7795/110.20260421A

In the absence of reference topography data, estimated quantities such as the PSD or Fourier spectrum may still closely match expected or reference values, even though the underlying measurements themselves are unreliable. This further demonstrates the strength of the HM system, which provides *in-situ* reference topography data based on direct measurements rather than relying exclusively on processed or derived reference values.

6.4. Investigation of optical artifacts using the hybrid microscope

Although the term "optical artifact" is generally used to describe measurement errors associated with optical principles in surface metrology, the underlying causes can vary significantly depending on factors such as the specific measurement technique employed. Examples include overshooting errors in confocal microscopy, the batwing effect in white-light interferometry, and the phase ambiguity in phase-shifting interferometry. These phenomena have been extensively studied from a theoretical perspective. However, when optical instruments are used to investigate unknown surfaces with complex topographies composed of randomly distributed features, such as those found on engineering surfaces, it remains challenging to distinguish between accurate and erroneous measurements without access to reference data. This challenge illustrates why reference data are essential for distinguishing true topography from artifact impacted measurement results in surface metrology.

Furthermore, this issue becomes particularly critical when artifact impacted measurements exhibit high repeatability. In such cases, the resulting artifacts, unlike random measurement noise, behave as systematic errors that can consistently mislead interpretation. Their repeatable nature makes them especially difficult to detect, particularly in the absence of prior knowledge about the true surface topography. Classical methods for suppressing optical artifacts, such as the application of filtering techniques (for example, frequency-based filters or local topography masks) or the exclusion of affected data from evaluation (such as the W/3 method used in step height analysis [180]), have demonstrated promising results in specific contexts. However, a major limitation of these approaches is their lack of general applicability across diverse measured topographies. This limitation arises because, first, these methods are typically developed for well-defined measurement tasks, such as step height evaluation, and second, they rely on prior knowledge of the surface topography, including the location and nature of the artifacts. Therefore, one of the key unresolved issues is: distinguishing between true surface features and artifact induced structures is inherently difficult, particularly when artifacts exhibit the same degree of repeatability as genuine surface characteristics.

https://doi.org/10.7795/110.20260421A

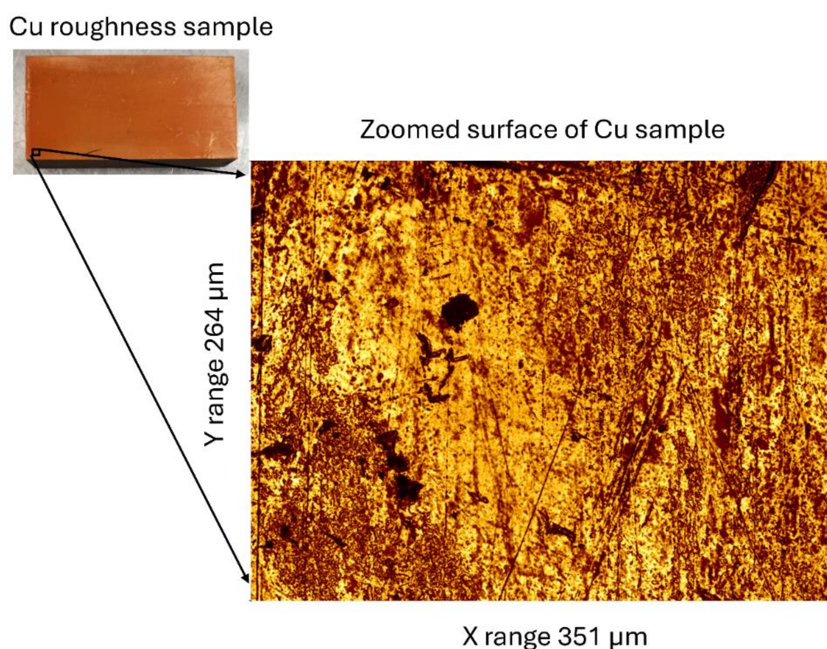

Figure 71 Overview of the Cu roughness sample. Surface pictured with digital camera in a size of 351 µm x 264 µm.

For example, in a surface investigation of the area illustrated in Figure 71, it is nearly impossible to predict the location or nature of potential optical artifacts in the measured topography without access to reference data. The difficulty in identifying artifacts is further highlighted by the comparison of topographies obtained from eight PSI measurements across different days at the same location, all of which display highly consistent features, as shown in Figure 72. Specifically, each measurement indicates that the area of interest contains a narrow valley structure.

In addition, when these consistent measurement results are compared with topographies obtained using different instrument configurations, such as a PSI mode with a 20x objective from the HM and another commercial PSI or WLI instrument (referred to hereafter as S) equipped with a 50x objective, the narrow valley structure remains clearly identifiable. Although slight variations exist, for example in the measured depth of the valley, all four measurements qualitatively confirm the presence of a valley at the same location, as illustrated by the green tone profile curves in Figure 73. This agreement across different instruments supports the interpretation of the structure as a genuine topographical feature rather than an optical artifact.

However, despite the apparent agreement among the optical measurements, they do not represent the true surface structure. Subsequent measurements performed at the same position using three independent methods, namely the contact AFM-mode of the HM, the tapping AFM-mode of a commercial AFM (referred to hereafter as ICON), and the confocal mode of instrument S equipped with a 50x objective, confirm that the actual structure of the

selected area of interest consists of peaks rather than a valley. These three reference measurements are presented in Figure 73 with red tone profile curves.

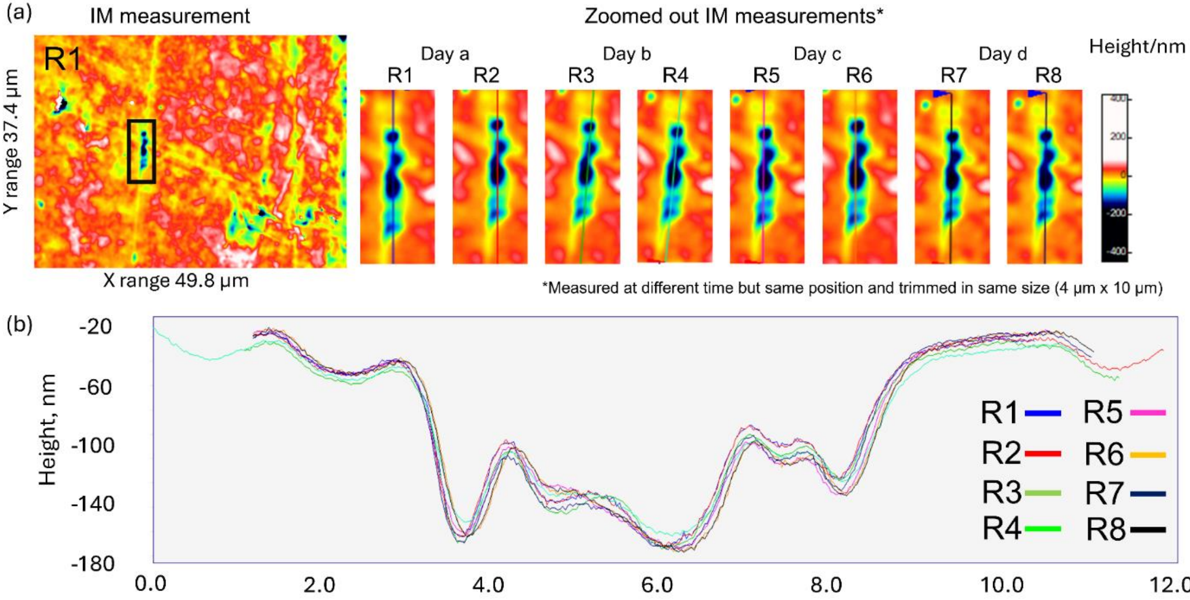

Figure 72 (a) PSI measurements using the IM-mode of the HM over the same sample position acquired at different dates. (b) Profile comparison over the same position extracted from the topographies shown in (a)

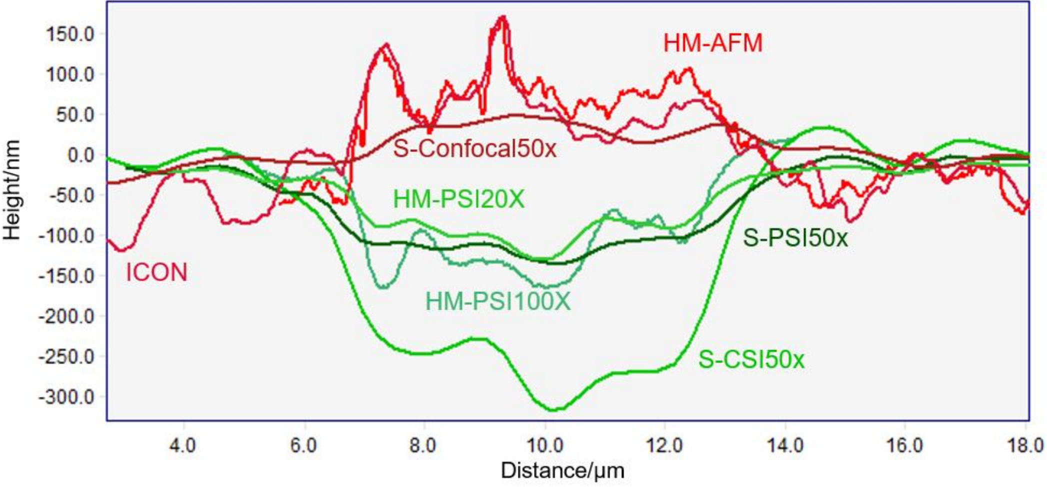

Figure 73 Comparison of the profiles measured by different instruments on the same location of the Cu sample

In Figure 73, the measured profiles can clearly be divided into two distinct groups based on the type of structure observed. The red tone profiles, obtained using noninterference measurement techniques, indicate that the actual surface structure consists of a narrow peak. In contrast, the green tone profiles, measured using interference-based techniques (no matter PSI or WLI), consistently but incorrectly represent this location as a valley. The primary reason for this discrepancy is likely related to the principles of phase-based interferometric

https://doi.org/10.7795/110.20260421A

measurements, where the phase information can be distorted by material properties of the surface, such as composition or the degree of oxidation.

Additional support for this interpretation comes from limited investigations conducted in the course of this doctoral work, which suggest that optical artifacts occur less frequently on silicon-based samples compared to metallic surfaces. Nevertheless, the detailed relationship between optical artifacts and surface material characteristics remains under investigation.

This observation raises fundamental concerns about the reliability of measurement results obtained from areal surface instruments based on interferometry, particularly when characterizing unknown surfaces. In such cases, it is difficult to determine whether repeatable measurement features reflect true surface structures or are in fact artifacts. As a result, such artifacts may easily go undetected in the absence of complementary reference measurements, potentially leading to incorrect conclusions regarding surface characteristics.

To address this challenge, we propose the use of a correlated reference topography that can be acquired with minimal additional effort, for example through the AFM-mode of the developed HM system. This approach enhances measurement reliability and enables accurate detection of artifacts in interferometric measurements.

https://doi.org/10.7795/110.20260421A

7. Conclusions and outlook

In this dissertation, a novel concept for *in-situ* reference areal surface metrology has been developed and demonstrated through the design and implementation of a hybrid microscope (HM) that integrates both interferometric microscopy- (IM) and atomic force microscopy-(AFM) modes. This hybrid system addresses critical challenges in optical surface metrology, namely the limitations in lateral resolution and overall measurement fidelity. By combining the fast and non-contact nature of the interferometric microscopy with the high resolution and high fidelity of the AFM technique, the hybrid microscope enables accurate, reliable, and traceable reference measurements, particularly for complex surface topographies.

The AFM-mode of the HM system is realized by introducing an AFM cantilever into the optical path of the IM-mode through a switching mechanism that allows the cantilever to be inserted into or removed from the beam path. This enables the system to switch between the two measurement modes and reflects the hybrid concept of combining IM- and AFM-based measurements within a single instrument. One of the key features of the design is its ability to achieve effective synergy between the two measurement modes. In the IM-mode, the system performs rapid, non-contact surface measurements. In the AFM-mode, the cantilever is positioned within the camera's field of view at the focal plane of the objective. At this position, interference fringes, which generated between the measurement beam reflected from the back side of the cantilever and the reference beam from the reference mirror of the Mirau objective, will be captured by the camera. The resulting interference fringes encode the topography of the cantilever's back surface. As the AFM tip interacts with the sample, tip sample forces cause deflection of the cantilever, which is detected through variations in the interference fringe, thereby enabling AFM measurement. This optical readout eliminates the need for a conventional optical-lever system. Therefore, this design offers two major advantages: it reduces system complexity and cost, and it enhances usability by significantly minimizing the effort required for AFM signal alignment and calibration.

A major contribution of this work is the demonstration of reliable and high-performance measurement capabilities in both developed IM- and AFM-mode. Comprehensive theoretical and experimental investigations were carried out to characterize the system's noise behavior and spatial bandwidth characteristics. In the IM-mode, several noise reduction strategies were successfully implemented, including advanced PSI algorithms, interferogram averaging technique, and topography averaging technique. As a result, the system achieved a root mean square noise level of 0.27 nm using a 20-step linear phase-shifting method, with further improvements possible through continued optimization. In addition to its low noise performance, the IM-mode of the HM demonstrates a highly uniform spatial response, with

https://doi.org/10.7795/110.20260421A

angular variation in bandwidth remaining below 8%. It also shows excellent measurement repeatability, evidenced by a standard deviation of less than 0.5 nm across five repeated measurements. These specifications of the developed interferometric mode confirm both the precision and consistency of the interferometric mode, highlighting its capability for high quality surface characterization.

In the AFM-mode of the HM, the system achieved a measurement noise level of 0.63 nm, where the dominant noise contribution is no longer from the sensor but from the piezo stage (0.48 nm). Notably, the sensor noise was reduced from approximately 0.52 nm to 0.04 nm through the application of averaging-based noise suppression techniques. To ensure the traceability of AFM measurements to the SI-Units (meter), a traceability chain was established for the AFM-mode by performing traceability calibrations using certified step height and lateral standards. Furthermore, repeatability investigations demonstrated excellent stability, with long-term repeatability reaching values as low as 2.5 nm. These results confirm the robustness, precision, and traceability of the developed HM and indicate its potential as a reliable instrument for high fidelity areal surface metrology.

Beyond the development of the instrument itself, this dissertation emphasizes the critical role of reference metrology in evaluating the fidelity of optical measurements. The HM offers a practical and efficient approach to acquiring correlated reference data *in-situ*, which is essential for distinguishing true surface features from repeatable but misleading optical artifacts. This capability is particularly important when investigating unknown complex surfaces, where identifying artifacts without reference data is inherently difficult. The high fidelity and traceable topography provided by the AFM-mode have been shown to enhance both lateral resolution and overall measurement fidelity for the interferometric measurement results. This has been demonstrated through a series of application examples conducted on various surface types, which confirmed the effectiveness of the HM and validated the practical value of the developed concept.

Moreover, the developed HM can be improved with following advancements:

1. Implementation of array measurements through parallel detection using multiple AFM probes within a single field of view, enabling faster measurement and reduced noise.

2. Realization of true 3D surface characterization using an isotropic AFM probe developed by PTB, which offers equal sensitivity to both torsion and bending related deformations. This will enable the capability of the HM in critical dimension measurement as well.

3. Reduction of tip-sample contact loss issue through the development of a real time control system to shorten the response time of each control loop.

https://doi.org/10.7795/110.20260421A

4. Implementation of non-contact AFM mode using a stroboscopic approach, which reduces the risk of tip damage and wear while increasing measurement speed and probe lifetime.
5. Comprehensive uncertainty analysis of the hybrid microscope to quantitatively assess the reliability and accuracy of its measurement results.

https://doi.org/10.7795/110.20260421A

Appendix

Details of phase correlation algorithm for realization of surface align function

The phase correlation algorithm leverages the complementary characteristics of both atomic force and interferometric measurements in the frequency domain to identify corresponding regions within the topographies. Assuming AFM measurement z_{AFM} has the same size as the IM measurement z_{IM}, but differs in its coordinate origin, the relationship between the two datasets can be mathematically expressed as:

$$z_{AFM}(m, n) = z_{IM}(m - t_m, n - t_n) \quad (1)$$

Where m and n are coordinates index and the t_m and t_n denote translations in x and y directions respectively. Their Fourier transforms (Z_{AFM}, Z_{IM}) can be expressed as follows:

$$Z_{AFM}(\xi, \eta) = Z_{IM}(\xi, \eta)e^{-j2\pi(\xi t_m + \eta t_n)} \quad (2)$$

Equation 2 shows that, in the frequency domain, the two measurements share identical amplitude spectra but differ by a phase shift of $e^{-j2\pi(\xi t_m + \eta t_n)}$. This phase shift can be isolated and quantified through the calculation of the normalized cross power spectrum, which is defined as:

$$e^{-j2\pi(\xi t_m + \eta t_n)} = \frac{Z_{AFM}(\xi,\eta)Z_{IM}*(\xi,\eta)}{|Z_{AFM}(\xi,\eta)Z_{IM}*(\xi,\eta)|} \quad (3)$$

Where $Z_{IM} * (\xi, \eta)$ is the complex conjugate of $Z_{IM}(\xi, \eta)$. Since the phase shift corresponds to a spatial translation, its inverse Fourier transform results in a shifted peak, typically represented as a Dirac delta function. Therefore, the translation between the two measurements can be determined by applying the inverse Fourier transform to the normalized cross power spectrum and identifying the position of the resulting peak:

$$F^{-1}\left[e^{-j2\pi(\xi t_m + \eta t_n)}\right] = \delta(m + t_m, n + t_n) \quad (4)$$

https://doi.org/10.7795/110.20260421A

Bibliography

1. Dai, G., Felgner, A., Koenders, L., & Fluegge, J. (2016, May). Reference areal surface metrology by high speed metrological large range AFM. In euspen's 16th International Conference & Exhibition, Nottingham, UK. https://www.euspen.eu/knowledge-base/ICE16-P1.35.pdf accessed 07.2025
2. Poon, C. Y., & Bhushan, B. (1995). Comparison of surface roughness measurements by stylus profiler, AFM and non-contact optical profiler. Wear, 190(1), 76–88. https://doi.org/10.1016/0043-1648(95)06652-2
3. Kühle, A., Rosén, B.-G., & Garnaes, J. (2003). Comparison of roughness measurement with atomic force microscopy and interference microscopy. In A. Duparré & B. Singh (Eds.), Advanced characterization techniques for optics, semiconductors, and nanotechnologies (Vol. 5188, pp. 154–161). SPIE. https://doi.org/10.1117/12.507374
4. Vorburger, T. V., Rhee, H.-G., Renegar, T. B., Song, J.-F., & Zheng, A. (2007). Comparison of optical and stylus methods for measurement of surface texture. Precision Engineering, 31(2), 129–138. https://doi.org/10.1016/j.precisioneng.2006.01.001
5. International Organization for Standardization. (2017). ISO 25178-600:2017 Geometrical product specifications (GPS)—Surface texture: Areal—Part 600: Metrological characteristics for areal-topography measuring methods.
6. Giusca, C. L., Leach, R. K., Helery, F., Gutauskas, T., & Nimishakavi, L. (2012). Calibration of the scales of areal surface topography-measuring instruments: Part 1. Measurement noise and residual flatness. Measurement Science and Technology, 23(3), 035008. https://doi.org/10.1088/0957-0233/23/3/035008
7. Giusca, C. L., Leach, R. K., Helery, F., Gutauskas, T., & Nimishakavi, L. (2012). Calibration of the scales of areal surface topography measuring instruments: Part 2. Amplification, linearity and squareness. Measurement Science and Technology, 23(6), 065005. https://doi.org/10.1088/0957-0233/23/6/065005
8. Giusca, C. L., & Leach, R. K. (2013). Calibration of the scales of areal surface topography measuring instruments: Part 3. Resolution. Measurement Science and Technology, 24(10), 105010. https://doi.org/10.1088/0957-0233/24/10/105010
9. Wyss, S., Krüger, J., Grundmann, J., Bodermann, B., Gao, S., Fu, L., Birk, A., Frenner, K., & Reichelt, S. (2023). Rigorous modeling of a confocal microscope. In B. Bodermann & K. Frenner (Eds.), Modeling Aspects in Optical Metrology IX (Proc. SPIE Vol. 12619, 126190Q). SPIE. https://doi.org/10.1117/12.2673784
10. de Groot, P., Colonna de Lega, X., Su, R., Coupland, J., & Leach, R. (2021). Modeling of coherence scanning interferometry using classical Fourier optics. Optical Engineering, 60(10), 104106. https://doi.org/10.1117/1.OE.60.10.104106
11. Lehmann, P., Pahl, T., & Riebeling, J. (2023). Universal Fourier optics model for virtual coherence scanning interferometers. In B. Bodermann & K. Frenner (Eds.), Modeling Aspects in Optical Metrology IX (Proc. SPIE Vol. 12619, 126190O). SPIE. https://doi.org/10.1117/12.2673292
12. Dai, G., Jiao, Z., Xiang, L., Seeger, B., Weimann, T., Xie, W., & Tutsch, R. (2020). A novel material measure for characterising two-dimensional instrument transfer functions of areal surface topography measuring instruments. Surface Topography: Metrology and Properties, 8(4), 045025. https://doi.org/10.1088/2051-672X/abc9d2
13. Munechika, K., Cabrini, S., Chao, W., Lacey, I., Pina-Hernandez, C., Rochester, S., & Yashchuk, V. V. (2021). Binary pseudo-random array test standard optimized for characterization of interferometric microscopes. In E. Novak, J. D. Trolinger, & C. C. Wilcox (Eds.), Applied Optical Metrology IV (Proc. SPIE Vol. 11817, 1181704). SPIE. https://doi.org/10.1117/12.2594995
14. Yashchuk, V. V., Lacey, I., Arnold, T., Paetzelt, H., Rochester, S., Siewert, F., & Takacs, P. Z. (2019). Investigation on lateral resolution of surface slope profilers. In L. Assoufid, H. Ohashi, & A. Asundi (Eds.), Advances in Metrology for X-Ray and EUV

https://doi.org/10.7795/110.20260421A

Optics VIII (Proc. SPIE Vol. 11109, 111090M). SPIE. https://doi.org/10.1117/12.2539527
15. Samanta, K., & Joseph, J. (2021). An overview of structured illumination microscopy: Recent advances and perspectives. Journal of Optics, 23(12), 123002. https://doi.org/10.1088/2040-8986/ac3675
16. Hell, S. W., & Wichmann, J. (1994). Breaking the diffraction resolution limit by stimulated emission: Stimulated-emission-depletion fluorescence microscopy. Optics Letters, 19(11), 780–782. https://doi.org/10.1364/OL.19.000780
17. Leach, R., Evans, C., He, L., Davies, A., Duparré, A., Henning, A., Jones, C. W., & O'Connor, D. (2015). Open questions in surface topography measurement: A roadmap. Surface Topography: Metrology and Properties, 3(1), 013001. https://doi.org/10.1088/2051-672X/3/1/013001
18. Leach, R., & Haitjema, H. (2010). Bandwidth characteristics and comparisons of surface texture measuring instruments. Measurement Science and Technology, 21(3), 032001. https://doi.org/10.1088/0957-0233/21/3/032001
19. Koumoulos, E. P., Tofail, S. A. M., Silien, C., De Felicis, D., Moscatelli, R., Dragatogiannis, D. A., Bemporad, E., Sebastiani, M., & Charitidis, C. A. (2018). Metrology and nano-mechanical tests for nano-manufacturing and nano-bio interface: Challenges & future perspectives. Materials and Design, 137, 446–462. https://doi.org/10.1016/j.matdes.2017.10.035
20. Whitehouse, D. J. (2008). Nanometrology. Contemporary Physics, 49(5), 351–374. https://doi.org/10.1080/00107510802611251
21. Binnig, G., & Rohrer, H. (1987). Scanning tunneling microscopy from birth to adolescence. Reviews of Modern Physics, 59(3), 615–625. https://doi.org/10.1103/RevModPhys.59.615
22. Meyer, E. (1992). Atomic force microscopy. Progress in Surface Science, 41, 3–49. https://doi.org/10.1016/0079-6816(92)90004-J
23. Voigtländer, B. (2015). Scanning probe microscopy: Atomic force microscopy and scanning tunneling microscopy (NanoScience and Technology). Springer. https://doi.org/10.1007/978-3-662-45240-0
24. Bian, K., Gerber, C., Heinrich, A. J., Scheuring, S., & Jiang, Y. (2021). Scanning probe microscopy. Nature Reviews Methods Primers, 1, Article 36. https://doi.org/10.1038/s43586-021-00033-2
25. Binnig, G. K. (1988). Atomic force microscope and method for imaging surfaces with atomic resolution (U.S. Patent No. 4,724,318). U.S. Patent and Trademark Office.
26. Bhushan, B. (Ed.). (2007). Springer handbook of nanotechnology (2nd ed., revised and extended). Springer. https://doi.org/10.1007/978-3-540-29840-3
27. Minsky, M. (1988). Memoir on inventing the confocal scanning microscope. Scanning, 10, 128–138. https://doi.org/10.1002/sca.4950100403
28. de Groot, P. J. (2017). Interference microscopy for surface structure analysis. In T. Yoshizawa (Ed.), Handbook of optical metrology: Principles and applications (2nd ed., pp. 791–828). CRC Press.
29. Sommargren, G. E. (1981). Optical heterodyne profilometry. Applied Optics, 20(4), 610–613. https://doi.org/10.1364/AO.20.000610
30. Artigas, R. (2011). Imaging confocal microscopy. In R. Leach (Ed.), Optical measurement of surface topography (pp. 237–285). Springer. https://doi.org/10.1007/978-3-642-12012-1_11
31. Leach, R. (2011). Introduction to surface texture measurement. In R. Leach (Ed.), Optical measurement of surface topography (pp. 1–13). Springer. https://doi.org/10.1007/978-3-642-12012-1_1
32. Feynman, R. P. (1959). There's plenty of room at the bottom. Talk presented at the American Physical Society meeting, Pasadena, CA. Reprinted in Caltech Engineering and Science, 23(5), 22–36. https://web.pa.msu.edu/people/yang/RFeynman_plentySpace.pdf accessed 07.2025

33. Jones, L., Wang, S., Hu, X., Rahman, S. U., & Castell, M. R. (2018). Maximising the resolving power of the scanning tunneling microscope. Advanced Structural and Chemical Imaging, 4, Article 6. https://doi.org/10.1186/s40679-018-0056-7
34. Gross, L., Mohn, F., Moll, N., Liljeroth, P., & Meyer, G. (2009). The chemical structure of a molecule resolved by atomic force microscopy. Science, 325(5944), 1110–1114. https://doi.org/10.1126/science.1174290
35. Stedman, M. (1987). Basis for comparing the performance of surface-measuring machines. Precision Engineering, 9(3), 149–152. https://doi.org/10.1016/0141-6359(87)90042-1
36. De Chiffre, L., Kunzmann, H., Peggs, G. N., & Lucca, D. A. (2003). Surfaces in precision engineering, microengineering and nanotechnology. CIRP Annals, 52(2), 561–577. https://doi.org/10.1016/S0007-8506(07)60204-5
37. Rosén, S., Thomas, T. R., & Rosén, B.-G. (2014). The Stedman diagram revisited. Surface Topography: Metrology and Properties, 2(1), 014005. https://doi.org/10.1088/2051-672X/2/1/014005
38. Fan, K.-C., Cheng, F., Wang, H.-Y., & Ye, J.-K. (2012). The system and the mechatronics of a pagoda type micro-CMM. International Journal of Nanomanufacturing, 8(1/2), 67–77. https://doi.org/10.1504/IJNM.2012.044656
39. Ruijl, T. (2002, January). Ultra precision coordinate measuring machine – Design, calibration and error compensation. Retrieved from https://www.researchgate.net/publication/27351970
40. Wu, Y. (2022). Großflächige Topographiemessungen mit einem Weißlichtinterferenzmikroskop und einem metrologischen Rasterkraftmikroskop [Doctoral dissertation, Friedrich-Alexander-Universität Erlangen-Nürnberg]. FAU University Press.
41. Fan, K.-C., Fei, Y.-T., Wang, W., Chen, Y., & Chen, Y.-C. (2008). Micro-CMM. In Micro-Manufacturing Engineering and Technology (pp. 305–325). Springer. https://doi.org/10.1007/978-1-84800-147-3_13
42. Fang, C. Y., & Sung, C. K. (n.d.). Measurement uncertainty analysis of CMM with ISO GUM. National Tsing Hua University, Hsinchu, Taiwan. https://www.demarcheiso17025.com/private/Measurement%20uncertainty%20analysis%20of%20CMM%20with%20ISO%20GUM.PDF accessed 07.2025
43. Ito, S., Kikuchi, H., Chen, Y., Shimizu, Y., Gao, W., Takahashi, K., Kanayama, T., Arakawa, K., & Hayashi, A. (2016). A micro-coordinate measurement machine (CMM) for large-scale dimensional measurement of micro-slits. Applied Sciences, 6(5), 156. https://doi.org/10.3390/app6050156
44. Spaan, H. A. M., & Widdershoven, I. (2011). Isara 400 ultra-precision CMM. In A. Duparré & R. Geyl (Eds.), Optical fabrication, testing, and metrology IV (Proc. SPIE Vol. 8169, 81690T). SPIE. https://doi.org/10.1117/12.902237
45. Jäger, G., Manske, E., Hausotte, T., & Büchner, H.-J. (2009). The metrological basis and operation of nanopositioning and nanomeasuring machine NMM-1. tm – Technisches Messen, 76(5). https://doi.org/10.1524/teme.2009.0960
46. Hausotte, T. (2010). Nanopositionier- und Nanomessmaschinen: Geräte für hochpräzise makro-bis nanoskalige Oberflächen- und Koordinatenmessungen [Habilitationsschrift, Technische Universität Ilmenau].
47. KLA Corporation. (2021). Topography sensor technology for stylus profilers. KLA Corporation. https://www.kla.com/wp-content/uploads/KLA_AppNote_Stylus_Sensor_Technology-1.pdf accessed 07.2025
48. Mahr GmbH. MarSurf LD 130 / LD 260: Das universelle Konturen- und Oberflächenmesssystem als Kompaktmessplatz. https://metrology.mahr.com/fileadmin/assets/files/MarSurf--3766245--FL--LD%20130_LD%20260--DE--2015-11-11.pdf accessed 07.2025
49. Taylor Hobson. Form Talysurf PGI 1240 aspherics measurement system. https://img1.17img.cn/17img/old/literature/C16151.pdf accessed 07.2025
50. Voigtländer, B. (2019). Atomic force microscopy (2nd ed.). Springer. https://doi.org/10.1007/978-3-030-13654-3

https://doi.org/10.7795/110.20260421A

51. Martin, Y., Williams, C. C., & Wickramasinghe, H. K. (1987). Atomic force microscope-force mapping and profiling on a sub 100 Å scale. Applied Physics Letters, 51(2), 144–146. IBM T. J. Watson Research Center. https://doi.org/10.1063/1.338807
52. Morita, S., Giessibl, F. J., Meyer, E., & Wiesendanger, R. (Eds.). (2015). Noncontact Atomic Force Microscopy (Vol. 3). Springer. https://doi.org/10.1007/978-3-319-15588-3
53. West, P. E. (n.d.). Introduction to Atomic Force Microscopy: Theory, Practice, Applications (pp. 1–138).
54. Gotszalk, T., Grabiec, P., & Rangelow, I. W. (2000). Piezoresistive sensors for scanning probe microscopy. *Ultramicroscopy*, *82*(1-4), 39-48. https://doi.org/10.1016/S0304-3991(99)00171-0
55. Paolino, P., Aguilar Sandoval, F. A., & Bellon, L. (2013). Quadrature phase interferometer for high resolution force spectroscopy. Review of Scientific Instruments, 84(9). https://doi.org/10.1063/1.4819743
56. Jones, C. N., & Gonçalves, J. (2010). A cost-effective atomic force microscope for undergraduate control laboratories. IEEE Transactions on Education, 53(2), 240–247. https://doi.org/10.1109/TE.2009.2021390
57. Dai, G., Koenders, L., Fluegge, J., & Hemmleb, M. (2018). Fast and accurate: High-speed metrological large-range AFM for surface and nanometrology. Measurement Science and Technology, 29, 054012. https://doi.org/10.1088/1361-6501/aaaf8a
58. Young, T. (1803). Experiments and calculations relative to physical optics. Philosophical Transactions of the Royal Society of London, 94, 1–16.
59. Hering, E., Martin, R., & Stohrer, M. (n.d.). Physik für Ingenieure (12th ed.). Springer. https://doi.org/10.1007/978-3-662-49355-7
60. Born, M., & Wolf, E. (1999). Principles of optics: Electromagnetic theory of propagation, interference and diffraction of light (7th ed., 60th anniversary ed.). Cambridge University Press.
61. de Groot, P. J. (2011). Chapter 8: Phase-Shifting Interferometry.In Optical measurement of surface topography. Springer. https://doi.org/10.1007/978-3-642-12012-1
62. de Groot, P. J. (2011). Chapter 9: Coherence scanning interferometry. In Optical measurement of surface topography. Springer. https://doi.org/10.1007/978-3-642-12012-1
63. de Groot, P. J. (2015). Chapter 31 Interference microscopy for surface structure analysis. Handbook of Optical Metrology Principles and Applications (pp.791-828)
64. Petzing, J., Coupland, J., & Leach, R. (2010). Measurement Good Practice Guide No. 116: The measurement of rough surface topography using coherence scanning interferometry. National Physical Laboratory. https://eprintspublications.npl.co.uk/4833/1/mgpg116.pdf accessed 07.2025
65. Schulz, G., & Elssner, K.-E. (1991). Errors in phase-measurement interferometry with high numerical apertures. Applied Optics, 30(31), 4465–4470. https://doi.org/10.1364/AO.30.004500
66. Sheppard, C. J. R., & Larkin, K. G. (1995). Effect of numerical aperture on interference fringe spacing. Applied Optics, 34(22), 4731–4735. https://doi.org/10.1364/AO.34.004731
67. de Groot, P. (2015). Principles of interference microscopy for the measurement of surface topography. Advances in Optics and Photonics, 7(1), 1–65. https://doi.org/10.1364/AOP.7.000001
68. Bruning, J. H., Herriott, D. R., Gallagher, J. E., Rosenfeld, D. P., White, A. D., & Brangaccio, D. J. (1974). Digital wavefront measuring interferometer for testing optical surfaces and lenses. Applied Optics, 13(11), 2693–2703. https://doi.org/10.1364/AO.13.002693
69. Malacara, D., Servín, M., & Malacara, Z. (2018). Interferogram analysis for optical testing (2nd ed.). CRC press. https://doi.org/10.1201/9781315221021
70. de Groot, P. J. (1995). Vibration in phase-shifting interferometry. JOSA A, 12(2), 354–365. https://doi.org/10.1364/JOSAA.12.000354

71. Dai, G., Jiao, Z., Rao, X., Wolff, H., & Tutsch, R. (2024). Novel hybrid interference and atomic force microscopy. Measurement Science and Technology, 35, 125905. https://doi.org/10.1088/1361-6501/ad76ce
72. Schwider, J., Burow, R., Elssner, K.-E., Grzanna, J., Spolaczyk, R., & Merkel, K. (1983). Digital wave-front measuring interferometry: Some systematic error sources. Applied Optics, 22(21), 3421–3432. https://doi.org/10.1364/AO.22.003421
73. P.Hariharan, B.F.Oreb and T. Eiju(1987). Digital phase-shifting interferometry: A simple error-compensating phase calculation algorithm. Applied Optics, 26(13), 2506–2510. https://doi.org/10.1364/AO.26.002504
74. Ghiglia, D. C., & Pritt, M. D. (1998). Two-dimensional phase unwrapping: Theory, algorithms, and software. Wiley-Interscience.
75. Larkin, K. G. (1996). Efficient nonlinear algorithm for envelope detection in white-light interferometry. JOSA A, 13(4), 832–843. https://doi.org/10.1364/JOSAA.13.000832
76. Paddock, S. W. (2000). Principles and practices of laser scanning confocal microscopy. *Molecular biotechnology*, *16*(2), 127-149. https://doi.org/10.1385/MB:16:2:127
77. Elliott, A. D. (2020). Confocal microscopy: Principles and modern practices. Current Protocols in Cytometry, 92(1), e68. https://doi.org/10.1002/cpcy.68
78. International Organization for Standardization. (2019). ISO 25178-607: Geometrical product specifications (GPS)—Surface texture: Areal—Part 607: Nominal characteristics of non-contact (confocal microscopy) instruments.
79. Hagemeier, S., Pahl, T., Breidenbach, J., & Lehmann, P. (2023). A novel cubic-exp evaluation algorithm considering non-symmetrical axial response signals of confocal microscopes. Journal of Microscopy, n/a. https://doi.org/10.1002/jemt.24376
80. Wilson, T., & Juskaitis, R. (1995). The axial response of confocal microscopes with high numerical aperture objective lenses. Bioimaging, 3, 35–38. https://doi.org/10.1002/1361-6374(199503)3:1<35::AID-BIO4>3.0.CO;2-M
81. Helmli, F. (n.d.). Chapter 7: Focus Variation Instruments. In R. Leach (Ed.), Optical Measurement of Surface Topography. Springer. https://doi.org/10.1007/978-3-642-12012-1
82. Hagemeier, S. (2022). Comparison and investigation of various topography sensors using a multisensor measuring system [Doctoral dissertation, University of Kassel]. https://doi.org/10.17170/kobra-202208186691
83. S-neox 3D optical profiler, specifications https://www.sensofar.com/metrology/industry-research/sneox/specifications/ accessed 07.2025
84. Park Systems. (2023). Enabling Nanoscale Advances: Park NX-Hybrid WLI. Park Systems Corp. https://www.parksystems.com accessed 07.2025
85. Nanosurf. (n.d.). LensAFM – Extend the resolution of optical microscopes. https://www.nanosurf.com/en/products/lensafm accessed 07.2025
86. S.I.S. Surface Imaging Systems Ultra Objective https://www.novusferro.com/shop/microscopes/objectives/s-i-s-surface-imaging-systems-ultra-objective/ accessed 07.2025
87. International Organization for Standardization. (2014). ISO 25178-70:2014: Geometrical product specification (GPS) – Surface texture: Areal – Part 70: Material measures. ISO.
88. Leach, R., Haitjema, H., Su, R., & Thompson, A. (2021). Metrological characteristics for the calibration of surface topography measuring instruments: A review. Measurement Science and Technology, 32(3), 032001. https://doi.org/10.1088/1361-6501/abb54f
89. de Groot, P., & Colonna de Lega, X. (2005) Interpreting interferometric height measurements using the instrument transfer function. Zygo Corporation. https://doi.org/10.1007/3-540-29303-5_3
90. Mínguez Martínez, A., Gómez Pérez, C., Pérez-Caballero, D. C., Carcedo Cerezo, L., & de Vicente y Oliva, J. (2020). Design of industrial standards for the calibration of optical microscopes. Materials, 14(01), 29. https://doi.org/10.3390/ma14010029

91. Leach, R. K., Giusca, C. L., Haitjema, H., Evans, C., & Jiang, X. (2015). Calibration and verification of areal surface texture measuring instruments. CIRP Annals - Manufacturing Technology, 64(2), 797–820. https://doi.org/10.1016/j.cirp.2015.05.010
92. Yashchuk, V. V., Rochester, S., Lacey, I., & Babin, S. (2020). Super-resolution surface slope metrology of x-ray mirrors. Review of Scientific Instruments, 91, 075113. https://doi.org/10.1063/5.0005556
93. Su, T., Maldonado, A., Su, P., & Burge, J. H. (2015). Instrument transfer function of slope measuring deflectometry systems. Applied Optics, 54(10), 2981-2990. https://doi.org/10.1364/AO.54.002981
94. de Groot, P. J. (2019). A review of selected topics in interferometric optical metrology. Reports on Progress in Physics, 82, 056101. https://doi.org/10.1088/1361-6633/ab092d
95. Lehmann, P., Niehues, J., & Tereschenko, S. (2014). 3-D optical interference microscopy at the lateral resolution. International Journal of Optomechatronics, 8(4), 231–241. https://doi.org/10.1080/15599612.2014.942924
96. Dullemond, K. (2024), Atmospheric turbulence effects + signal theory, https://www.ita.uni-heidelberg.de/ ~dullemond/lectures/obsastro_2010/ Chapter_Diffraction.pdf accessed: 03.2025
97. Xie, W. (2017). Transfer characteristics of white-light interferometers and confocal microscopes [Doctoral dissertation, University of Kassel].
98. Lloret, T., Morales-Vidal, M., Beléndez, A., Navarro-Fuster, V., Pascual, I., & Ramírez, M. G. (2022). Holographic lens resolution using the convolution theorem. Instituto Universitario de Física Aplicada a las Ciencias y las Tecnologías, Universidad de Alicante. https://doi.org/10.3390/polym14245426
99. Goodman, J. W. (1996). Introduction to Fourier Optics (2nd ed.). McGraw-Hill.
100. Gomez, C., Su, R., de Groot, P., & Leach, R. (2020). Noise reduction in coherence scanning interferometry for surface topography measurement. Nanomanufacturing and Metrology, 3, 68–76. https://doi.org/10.1007/s41871-020-00057-4
101. Van Wingerden, J., Frankena, H. J., & Smorenburg, C. (1991). Linear approximation for measurement errors in phase-shifting interferometry. Applied optics, 30(19), 2718-2729. https://doi.org/10.1364/AO.30.002718
102. JCGM 100:2008. (2008). Evaluation of measurement data — Guide to the expression of uncertainty in measurement (GUM 1995 with minor corrections). Joint Committee for Guides in Metrology. https://www.bipm.org/documents/20126/2071204/JCGM_100_2008_E.pdf accessed 07.2025
103. Tolmon, F. R., & Wood, J. G. (1956). Fringe spacing in interference microscopes. Journal of Scientific Instruments, 33, 236. https://doi.org/10.1088/0950-7671/33/6/310
104. Creath, K. (1989). Calibration of numerical aperture effects in interferometric microscope objectives. Applied Optics, 28(15), 3134–3140. https://doi.org/10.1364/AO.28.003333
105. Biegen, J. F. (1989). Calibration requirements for Mirau and Linnik microscope interferometers. Applied Optics, 28(11), 1973–1975. https://doi.org/10.1364/AO.28.001972
106. Dubois, A., Selb, J., Vabre, L., & Boccara, A. C. (2000). Phase measurements with wide-aperture interferometers. Applied optics, 39(14), 2326-2331. https://doi.org/10.1364/AO.39.002326
107. Schulz, G. (1954). Über Interferenzen gleicher Dicke und Längenmessung mit Lichtwellen. Annalen der Physik, 14(6), 1–5. https://doi.org/10.1002/andp.19544490309
108. Carré, P. (1966). Installation et utilisation du comparateur photoélectrique et interférentiel du Bureau International des Poids et Mesures. Metrologia, 2(1), 13–18. https://doi.org/10.1088/0026-1394/2/1/005
109. Aguilar, J. F., & Méndez, E. R. (1995). On the limitations of the confocal scanning optical microscope as a profilometer. Journal of Modern Optics, 42(9), 1785–1794. https://doi.org/10.1080/09500349514551551

110. ISO/TC 213/SC/WG 16. (2016). ISO/WD 25178-700.3: Geometrical product specifications (GPS) – Surface texture: Areal – Part 700: Calibration and verification of areal topography measuring instruments. International Organization for Standardization.
111. Eifler, M., Hering, J., von Freymann, G., & Seewig, J. (2018). Calibration sample for arbitrary metrological characteristics of optical topography measuring instruments. Optics Express, 26(13), 16609–16624. https://doi.org/10.1364/OE.26.016609
112. Koenders, L. (2005, November 28). Supplementary comparison according to the rules of CCL key comparisons: EUROMET Project 707 step height standards final report (EUROMET.L-S15 - Project No. 707). Physikalisch-Technische Bundesanstalt. https://www.bipm.org/documents/20126/45452492/EUROMET.L-S15.pdf/9207964d-993a-c7f3-30b5-1ee20d408188 accessed 07.2025
113. Bauer, W., Hüser, D., & Gerbert, D. (2020). Simple method to determine linearity deviations of topography measuring instruments with a large range axial scanning system. Precision Engineering, 65, 31–36. https://doi.org/10.1016/j.precisioneng.2020.04.005
114. de Groot, P., & DiSciacca, J. (2020). Definition and evaluation of topography measurement noise in optical instruments. Optical Engineering, 59(6), 064110. https://doi.org/10.1117/1.OE.59.6.064110
115. European Machine Vision Association. (2021, March 15). EMVA standard 1288: Standard for characterization of image sensors and cameras (Release 4.0, General Release Candidate). https://www.emva.org/wp-content/uploads/EMVA1288-3.0.pdf accessed 07.2025
116. Healy, N., Lagonigro, L., Sparks, J. R., Boden, S., Sazio, P. J. A., Badding, J. V., & Peacock, A. C. (2011). Polycrystalline silicon optical fibers with atomically smooth surfaces. Optics Letters, 36(13), 2517–2519. https://doi.org/10.1364/OL.36.002517
117. Schmitt, D.-R., Kratz, F., Ringel, G. A., Mangelsdorf, J., Creuzet, F., & Garratt, J. D. (1995). Fabrication and characterization of optical super-smooth surfaces. In Proc. SPIE 2576, International Conference on Optical Fabrication and Testing (pp. 118–127). https://doi.org/10.1117/12.215614
118. Sheglov, D. V., Sitnikov, S. V., Fedina, L. I., Rogilo, D. I., Kozhukhov, A. S., & Latyshev, A. V. (2020). From self-organization of monoatomic steps on the silicon surface to subnanometer metrology. Optoelectronics, Instrumentation and Data Processing, 56(5), 533–544. https://doi.org/10.3103/S8756699020050118
119. de Groot, P. J. (2021). The instrument transfer function for optical measurements of surface topography. Journal of Physics: Photonics, 3(2), 024004. https://doi.org/10.1088/2515-7647/abe3da
120. de Groot, P. J., & Colonna de Lega, X. (2020). Fourier optics modeling of interference microscopes. Journal of the Optical Society of America A, 37(9), B1–B8. https://doi.org/10.1364/JOSAA.390746
121. Deck, L. L., & de Groot, P. J. (2017). Using the instrument transfer function to evaluate Fizeau interferometer performance. In Design and Fabrication Congress 2017 (IODC, Freeform, OFT). Optical Society of America. https://doi.org/10.1364/OFT.2017.OM2B.7
122. Zhang, X., Kashti, T., Kella, D., Frank, T., Shaked, D., Ulichney, R., Fischer, M., & Allebach, J. P. (2012). Measuring the modulation transfer function of image capture devices: What do the numbers really mean? In F. Gaykema & P. D. Burns (Eds.), Image Quality and System Performance IX (Vol. 8293, 829307). SPIE. https://doi.org/10.1117/12.912989
123. de Groot, P., Colonna de Lega, X., Sykora, D., & Deck, L. (2012). The meaning and measure of lateral resolution for surface profiling interferometers. Optics and Photonics News, 23(4).
124. Yashchuk, V. V., Munechika, K., Rochester, S., Chao, W., Lacey, I., Pina-Hernandez, C., & Takacse, P. Z. (2022). Reliability investigation of the instrument transfer function calibration technique based on binary pseudo-random array standards. SPIE Proceedings, 12121. https://doi.org/10.1117/12.2633476

https://doi.org/10.7795/110.20260421A

125. Krüger-Sehm, R., Bakucz, P., Jung, L., & Wilhelms, H. (2007). Chirp-Kalibriernormale für Oberflächenmessgeräte. Technisches Messen, 74(11), 572–578. https://doi.org/10.1524/teme.2007.74.11.572
126. de Groot, P. J., & Colonna de Lega, X. (2010). Spatially resolved height response of phase-shifting interferometers measured using a patterned mirror with varying spatial frequency. Optical Engineering, 49(9), 095601. https://doi.org/10.1117/1.3488052
127. de Groot, P. J., & Colonna de Lega, X. (2008). Binary pseudorandom grating standard for calibration of surface profilometers. Optical Engineering, 47(7), 073602. https://doi.org/10.1117/1.2955798
128. International Organization for Standardization. (2019). ISO 10110-8:2019 – Optics and photonics — Preparation of drawings for optical elements and systems — Part 8: Surface texture.
129. de Groot, P. J., Daouda, Z., Deck, L. L., & Colonna de Lega, X. (2024). Linear systems characterization of the topographical spatial resolution of optical instruments. Applied Optics, 63(15), 4201–4210. https://doi.org/10.1364/AO.521868
130. M. S. C. Almeida and M. Figueiredo, "Deconvolving Images With Unknown Boundaries Using the Alternating Direction Method of Multipliers," in *IEEE Transactions on Image Processing*, vol. 22, no. 8, pp. 3074-3086, Aug. 2013, https://doi.org/10.1109/TIP.2013.2258354.
131. Babin, S., Gaevski, M., Joy, D., Machin, M., & Martynov, A. (2006). Technique to automatically measure electron-beam diameter and astigmatism: BEAMETR. Journal of Vacuum Science & Technology B: Microelectronics and Nanometer Structures Processing, Measurement, and Phenomena, 24(6), 2956–2959. https://doi.org/10.1116/1.2387158
132. Coupland, J., Sheppard, C., Leach, R., Su, R. (2021). Scattering and three-dimensional imaging in surface topography measuring interference microscopy. Journal of the Optical Society of America A, 38(2), A27–A38. https://doi.org/10.1364/JOSAA.411929
133. de Groot, P. J., & Colonna de Lega, X. (2004). Signal modeling for low-coherence height-scanning interference microscopy. Appl. Opt. 43, 4821-4830 https://doi.org/10.1364/AO.43.004821
134. Hooshmand, H., Pahl, T., de Groot, P. J., Lehmann, P., Pappas, A., Su, R., Leach, R., & Piano, S. (2024). Comparison of Fourier optics-based methods for modeling coherence scanning interferometry. Optical Engineering, 63(4), 044102. https://doi.org/10.1117/1.OE.63.4.044102
135. Lehmann, P., Xie, W., Allendorf, B., & Tereschenko, S. (2018). Coherence scanning and phase imaging optical interference microscopy at the lateral resolution limit. Optics Express, 26(6), 7376–7392. https://doi.org/10.1364/OE.26.007376
136. P. E., Pahl, T., Fu, L., Nielsen, I., Rosenthal, F., Reichelt, S., ... & Rømer, A. T. (2025). Digital Twins for 3D Confocal Microscopy: Near-Field, Far-Field, and Comparison with Experiments. Sensors, 25(7), 2001. https://doi.org/10.3390/s25072001
137. Lehmann, P., Künne, M., & Pahl, T. (2021). Analysis of interference microscopy in the spatial frequency domain. Journal of Physics: Photonics, 3(1), 014006. https://doi.org/10.1088/2515-7647/abda15
138. Dändliker, R., & Weiss, K. (1970). Reconstruction of the three-dimensional refractive index from scattered waves. Optics communications, 1(7), 323-328. https://doi.org/10.1016/0030-4018(70)90032-5
139. Coupland, J. M., & Lobera, J. (2008). Holography, tomography and 3D microscopy as linear filtering operations. Measurement science and technology, 19(7), 074012. https://doi.org/10.1088/0957-0233/19/7/074012
140. Thomas, M., Su, R., Nikolaev, N., Coupland, J., & Leach, R. (2019). Modelling of coherence scanning interferometry for complex surfaces based on a boundary element method. SPIE Proceedings, 11057, 1105713. https://doi.org/10.1117/12.2526015
141. Xie, W., Lehmann, P., Niehues, J., & Tereschenko, S. (2016). Signal modeling in low coherence interference microscopy on example of rectangular grating. Optics Express, 24(13), 14283–14297. https://doi.org/10.1364/OE.24.014283

142. Pahl, T., Breidenbach, J., & Lehmann, P. (2022). Quasi-analytical and rigorous modeling of interference microscopy. EPJ Web of Conferences, 266, 10013. https://doi.org/10.1051/epjconf/202226610013
143. de Groot, P., Colonna de Lega, X., Su, R., & Leach, R. (2019). Does interferometry work? A critical look at the foundations of interferometric surface topography measurement. In Proc. SPIE 11102, Applied Optical Metrology III (111020G). https://doi.org/10.1117/12.2526654
144. Xie, W., Lehmann, P., & Niehues, J. (2012). Lateral resolution and transfer characteristics of vertical scanning white-light interferometers. Applied Optics, 51(10), 1450–1457. https://doi.org/10.1364/AO.51.001450
145. Coupland, J., Mandal, R., Palodhi, K., & Leach, R. (2013). Coherence scanning interferometry: Linear theory of surface measurement. Applied Optics, 52(16), 3662–3671. https://doi.org/10.1364/AO.52.003662
146. EMPIR TracOptic Project. (2024). Good practice guides. Physikalisch-Technische Bundesanstalt (PTB). https://www.ptb.de/empir2021/tracoptic/information-communication/good-practice-guides/ accessed 07.2025
147. de Groot, P., Colonna de Lega, X., Liesener, J., & Darwin, M. (2008). Metrology of optically-unresolved features using interferometric surface profiling and RCWA modeling. Optics Express, 16(6), 3970–3982. https://doi.org/10.1364/OE.16.003970
148. Török, P., Munro, P. R. T., & Kriezis, E. E. (2008). High numerical aperture vectorial imaging in coherent optical microscopes. Optics Express, 16(2), 507–523. https://doi.org/10.1364/OE.16.000507
149. Pahl, T., Hagemeier, S., Künne, M., Yang, D., & Lehmann, P. (2020). 3D modeling of coherence scanning interferometry on 2D surfaces using FEM. Optics Express, 28(26), 39807–39821. https://doi.org/10.1364/OE.411167
150. Ansys Inc. ANSYS Lumerical FDTD: Industry's leading choice for versatile and scalable photonic design. https://www.lumerical.com/products/fdtd/ accessed 07.2025
151. Dai, G., Wolff, H., Pohlenz, F., & Danzebrink, H.-U. (2009). A metrological large range atomic force microscope with improved performance. Review of Scientific Instruments, 80(4), 043702. https://doi.org/10.1063/1.3109901
152. Schmit, J. (2003, May). High-speed measurements using optical profiler. In Optical measurement systems for industrial inspection III (Vol. 5144, pp. 46-56). SPIE. https://doi.org/10.1117/12.501035
153. You, J., Kim, C., Joo, K.-N., Tan, A. S., Dietrich, F., Pietscher, H.-G., ... & Rangelow, I. W. (2025). Ultra-fast correlative chemical-mechanical-polishing (CMP) metrology: Integrating phase-shifting interferometry with active probe scanning probe microscopy. https://doi.org/10.1117/12.3050140
154. Homepage of the working group 5.23 "3D Nanometrology" at Physikalisch-Technische Bundesanstalt https://www.ptb.de/cms/ptb/fachabteilungen/abt5/fb-52/ag-523.html accessed 06.2025
155. CF IC EPI Plan DI. Double beam interference objectives that have large numerical aperture, long working distance and high optical performance. accessed 06.2025
156. Physik Instrumente. N-216 NEXLINE® linear actuator: Nanopositioning over long travel ranges, with high forces, PiezoWalk principle. accessed 06.2025
157. Sawyer, L. C., Grubb, D. T., & Meyers, G. F. (2008). Polymer microscopy (3rd ed.). Springer. https://doi.org/10.1007/978-0-387-72628-1
158. Advanced Illumination. SL162 Spot/Coaxial Light (Product Revision "A"). https://www.advancedillumination.com accessed 06.2025
159. Homepage of the working group 4.11 "Spektroradiometrie" at Physikalisch-Technische Bundesanstalt https://www.ptb.de/cms/ptb/fachabteilungen/abt4/fb-41/ag-411.html accessed 06.2025
160. Specification of the CMOS camera of IDS UI-3040CP-M-GL Rev.2 https://en.ids-imaging.com/store/ui-3040cp-rev-2.html accessed 07.2025
161. Physik Instrumente. M-545 microscope XY stage: Compact, stable, long travel range. https://www.physikinstrumente.com/en/products/xy-stages/m-545-open-frame-microscope-stage-201525 accessed 07.2025

https://doi.org/10.7795/110.20260421A

162. Physik Instrumente. P-545.xR8S PInano XY(Z) piezo system. https://www.physikinstrumente.com/en/products/nanopositioning-piezo-flexure-stages/pifoc-objective-pinano-sample-scanners-for-microscopy/p-545xr8s-pinano-xyz-piezo-system-2015201 accessed 07.2025
163. Physik Instrumente. PiezoWalk piezo motors: Nanometer precision with a high feed force. https://www.physikinstrumente.com/en/expertise/technology/piezoelectric-drives/piezowalk-piezo-motors 07.2025
164. Newport. 8302 Picomotor piezo linear actuator. https://www.newport.com/p/8302 accessed 07.2025
165. González, A., Servin, M., Estrada, J. C., & Rosu, H. C. (2011). N-step linear phase-shifting algorithms with optimum signal-to-noise phase demodulation. Journal of Modern Optics, 58(14), 1278–1284. https://doi.org/10.1080/09500340.2011.604735
166. BudgetSensors. ContDLC contact mode AFM probe with diamond-like-carbon tip coating. https://www.budgetsensors.com/contact-mode-afm-probe-diamond-like-carbon-contdlc accessed 07.2025
167. Thiesler, J., Tutsch, R., Fromm, K., & Dai, G. (2020). True 3D-AFM sensor for nanometrology. Measurement Science and Technology, 31, 074012. https://doi.org/10.1088/1361-6501/ab7efd
168. Specification of alignment chip developed by NANOSENSORS™ https://www.nanosensors.com/uploads/media/files/0001/05/9b167f854a220675268c562c1fd457fdb1358638.pdf accessed 06.2025
169. Specification of DC-Getriebemotoren by Dr. Fritz Faulhaber GmbH & Co. KG. https://www.faulhaber.com/de/produkte/serie/1512sr/ accessed 06.2025
170. ADLINK Technology Inc. (n.d.). PCIE-1824/L: 32/16 high-density analog output channels. https://www.advantech.com/en/products/1-2mlk8x/pcie-1824/mod_8a74e675-9676-4b26-b514-08881b58ecbf accessed 06.2025
171. Xu, M., Zhou, Z., Ahbe, T., Peiner, E., & Brand, U. (2022). Using a tip characterizer to investigate microprobe silicon tip geometry variation in roughness measurements. Sensors, 22(3), 1298. https://doi.org/10.3390/s22031298
172. Åström, K. J., & Hägglund, T. (1995). PID controllers (2nd ed.). Instrument Society of America.
173. Franklin, G. F., Powell, J. D., & Emami-Naeini, A. (2009). Feedback control of dynamic systems (6th ed.). Pearson.
174. Degenhardt, J., Jiao, Z., Kuhlmann, C., Tutsch, R., & Dai, G. Novel hybrid AI-PID controller Poster presented at Euspen 2025 9-13.06 Zaragoza,Spain
175. Degenhardt, J., & Bounaim, M. W. (2024). A new kind of atomic force microscopy scan control enabled by artificial intelligence: Concept for achieving tip and sample safety through asymmetric control. Nanomanufacturing and Metrology, 7, 11. https://doi.org/10.1007/s41871-024-00229-6
176. Degenhardt, J. (2019). Untersuchung und Verbesserung der metrologischen Eigenschaften eines tilting-tip AFM [Studienarbeit, Technische Universität Braunschweig].
177. Minus K Technology. (2017). WS-4 compact vibration isolation table [Product datasheet]. https://www.minusk.com/products/ws4-vibration-isolation-tables-workstations.html accessed 07.2025
178. Herzan. (2023). Acoustic enclosures: Protect your microscope from disruptive acoustic noise [Product information]. https://www.herzan.com/products/acoustic-enclosures.html accessed 07.2025
179. Dai, G., Zhu, F., and Fluegge, J. (2015). High-speed metrological large range AFM. Measurement Science and Technology, 26(9), 095402. https://doi.org/10.1088/0957-0233/26/9/095402
180. International Organization for Standardization. (2000). Geometrical product specifications (GPS) – Surface texture: Profile method – Part 1: Parameters, their values and general rules for specifying requirements (ISO 5436-1:2000).
181. Dai, G., Pohlenz, F., Dziomba, T., Xu, M., Diener, A., Koenders, L., & Danzebrink, H.-U. (2007). Accurate and traceable calibration of two-dimensional gratings.

Measurement Science and Technology, 18(2), 415–421. https://doi.org/10.1088/0957-0233/18/2/S13
182. Simetrics. Roughness standard ARS (areal), Type ADT [Technical specification]. http://www.simetrics.de/pdf/ARS.pdf accessed 07.2025
183. Johnson, J. (2024, April 11). CMOS structure and architecture: Understanding noise and noise reduction in CMOS imaging sensors (Release Version One). Steward Observatory, University of Arizona.
184. Thorlabs. High-power LED for microscopy, 620 nm, SOLIS-620D (MTN024556-S01, Rev C). https://www.thorlabs.de/newgrouppage9.cfm?objectgroup_id=8986 accessed 07.2025
185. Deng, T. (2025). Roughness measurements using a novel hybrid interferometrical and atomic force microscopy (Master’s thesis, Technische Universität Braunschweig, Institut für Halbleitertechnik).
186. Dixson, R., Orji, N., Misumi, I., & Dai, G. (2018). Spatial dimensions in atomic force microscopy: Instruments, effects, and measurements. Ultramicroscopy, 195, 85–97. https://doi.org/10.1016/j.ultramic.2018.08.011
187. Canet-Ferrer, J., Coronado, E., Forment-Aliaga, A., & Pinilla-Cienfuegos, E. (2014). Correction of the tip convolution effects in the imaging of nanostructures studied through scanning force microscopy. Nanotechnology, 25(39), 395703. https://doi.org/10.1088/0957-4484/25/39/395703
188. Zhang, K., Bai, Y., & Zhang, Z. (2024). Compensation method for correcting the topography convolution of the 3D AFM profile image of a diffraction grating. Machines, 12(2), 126. https://doi.org/10.3390/machines12020126
189. Dai, G., Xu, L., & Hahm, K. (2020). Accurate tip characterization in critical dimension atomic force microscopy. Measurement Science and Technology, 31, 074011. https://doi.org/10.1088/1361-6501/ab7fd2
190. Gołek, F., Mazur, P., Ryszka, Z., & Zuber, S. (2014). AFM image artifacts. Applied Surface Science. https://doi.org/10.1016/j.apsusc.2014.01.149
191. International Organization for Standardization. (2012). Geometrical product specifications (GPS) — Surface texture: Areal — Part 2: Terms, definitions and surface texture parameters (ISO 25178-2:2012).
192. Badami, V. G., Liesener, J., Evans, C. J., & de Groot, P. (2011). Evaluation of the measurement performance of a coherence scanning microscope using roughness specimens. https://www.academia.edu/97709132/Evaluation_of_the_measurement_performance_of_a_coherence_scanning_microscope_using_roughness_specimens accessed 07.2025
193. Leach, R. (2014). Measurement good practice guide No. 37: The measurement of surface texture using stylus instruments (Updated ed.). National Physical Laboratory. ISSN 1368-6550. https://eprintspublications.npl.co.uk/2041/1/mgpg37.pdf accessed 07.2025
194. Vorburger, T. V., Renegar, T. B., Zheng, A. X., Song, J.-F., Soons, J. A., & Silver, R. M. (n.d.). NIST surface roughness and step height calibrations: Measurement conditions and sources of uncertainty. National Institute of Standards and Technology. https://www.nist.gov/system/files/documents/pml/div683/grp02/nistsurfcalib.pdf accessed 07.2025

https://doi.org/10.7795/110.20260421A

Die Physikalisch-Technische Bundesanstalt,
das nationale Metrologieinstitut, ist eine
wissenschaftlich-technische Bundesoberbehörde
im Geschäftsbereich des Bundesministeriums für
Wirtschaft und Energie.

Physikalisch-Technische Bundesanstalt
Nationales Metrologieinstitut
ISNI: 0000 0001 2186 1887

Bundesallee 100
38116 Braunschweig

Presse- und Öffentlichkeitsarbeit

Telefon: (0531) 592-93 21
Fax: (0531) 592-30 08
E-Mail: presse@ptb.de
www.ptb.de